

# HIGH-TIME RESOLUTION ASTROPHYSICS USING DIGITAL BEAMFORMING

A THESIS SUBMITTED TO THE UNIVERSITY OF MANCHESTER  
FOR THE DEGREE OF DOCTOR OF PHILOSOPHY  
IN THE FACULTY OF ENGINEERING AND PHYSICAL SCIENCES

2015

By  
Monika Karolina Obrocka  
School of Physics and Astronomy

# Contents

|  |           |
|--|-----------|
| <b>Declaration</b>   | <b>11</b> |
| <b>Copyright</b>   | <b>12</b> |
| <b>Acknowledgements</b>  | <b>13</b> |
| <b>1 Introduction</b>  | <b>18</b> |
| 1.1 Objectives . . . . .   | 18        |
| 1.1.1 MUST . . . . .   | 18        |
| 1.1.2 Time-domain beamforming . . . . .                              | 19        |
| 1.1.3 Detection and localisation of transient phenomena . . . . .    | 19        |
| 1.2 Thesis Outline . . . . .   | 19        |
| 1.3 Contributions . . . . .  | 20        |
| 1.3.1 The MUST array . . . . .                                       | 20        |
| 1.3.2 Digital Back-end . . . . .                                     | 21        |
| 1.3.3 Transient Source Location Estimation Method . . . . .          | 22        |
| <b>2 Background</b>  | <b>23</b> |
| 2.1 Transient Background . . . . .                                   | 24        |
| 2.1.1 Pulsar Background . . . . .                                    | 26        |
| 2.1.2 Fast Radio Bursts . . . . .                                    | 30        |
| 2.1.3 Spectral Index and Flux density of transient sources . . . . . | 32        |
| 2.2 Observing Strategies . . . . .                                   | 35        |
| 2.2.1 Single Dish Instruments . . . . .                              | 36        |
| 2.2.2 Interferometers . . . . .                                      | 38        |
| 2.3 Future of High-Time Resolution Radio Astronomy . . . . .         | 46        |
| 2.3.1 SKA Pathfinders . . . . .                                      | 46        |
| 2.3.2 SKA Precursors . . . . .                                       | 47        |

|          |  |            |
|----------|--|------------|
| <b>3</b> | <b>The Manchester University Student Telescope</b>       | <b>51</b>  |
| 3.1      | Introduction . . . . .                                   | 51         |
| 3.1.1    | Scientific justification . . . . .                       | 54         |
| 3.2      | Array Design . . . . .                                   | 55         |
| 3.3      | Radio Frequency Interference Challenges . . . . .        | 56         |
| 3.4      | The MUST-1 Receiver . . . . .                            | 62         |
| 3.4.1    | Architecture . . . . .                                   | 62         |
| 3.4.2    | Test Results . . . . .                                   | 65         |
| 3.5      | MUST-4 . . . . .   | 67         |
| 3.5.1    | Array Configuration . . . . .                            | 71         |
| 3.5.2    | Back-end System . . . . .                                | 74         |
| 3.6      | MUST Performance Estimation . . . . .                    | 83         |
| 3.6.1    | First Light . . . . .                                    | 84         |
| 3.7      | Discussion . . . . .                                     | 87         |
| <b>4</b> | <b>Digital Beamformer for the MUST array</b>             | <b>90</b>  |
| 4.1      | Beamforming . . . . .                                    | 90         |
| 4.1.1    | Time-domain Beamforming . . . . .                        | 91         |
| 4.1.2    | Frequency-domain Beamforming . . . . .                   | 94         |
| 4.1.3    | Multibeaming in the Time and Frequency Domain . . . . .  | 96         |
| 4.1.4    | Beamformers in Radio Astronomy . . . . .                 | 98         |
| 4.2      | Interpolation Filter Architecture . . . . .              | 99         |
| 4.2.1    | Direct-form . . . . .                                    | 100        |
| 4.2.2    | Polyphase Form . . . . .                                 | 102        |
| 4.2.3    | Multistage Form . . . . .                                | 102        |
| 4.3      | Interpolation Filter Implementation . . . . .            | 104        |
| 4.4      | Fractional filter . . . . .                              | 107        |
| 4.5      | Polyphase Filter Bank . . . . .                          | 111        |
| 4.5.1    | Implementation . . . . .                                 | 111        |
| 4.5.2    | Simulating a Pulsar Signal . . . . .                     | 113        |
| 4.6      | Discussion . . . . .                                     | 119        |
| <b>5</b> | <b>FRBs and Interferometric Arrays</b>                   | <b>124</b> |
| 5.1      | Spectral sensitivity of interferometric arrays . . . . . | 124        |
| 5.1.1    | Simple Example . . . . .                                 | 131        |
| 5.2      | Simulation Parameters . . . . .                          | 134        |

|          |  |            |
|----------|--|------------|
| 5.2.1    | Uncertainties and Error Propagation . . . . .                  | 136        |
| 5.3      | Simulation Results . . . . .                                   | 138        |
| 5.3.1    | The MUST array . . . . .                                       | 140        |
| 5.3.2    | LOFAR Superterp . . . . .                                      | 150        |
| 5.3.3    | The MeerKAT Core . . . . .                                     | 160        |
| 5.4      | Discussion . . . . .   | 170        |
| 5.4.1    | Detection Rates . . . . .                                      | 170        |
| 5.4.2    | Location Estimation Accuracy . . . . .                         | 174        |
| 5.4.3    | Intrinsic Spectral Index Recovery . . . . .                    | 178        |
| <b>6</b> | <b>Conclusions</b>   | <b>180</b> |
| <b>A</b> | <b>The derivation of Equation 2.1</b>                          | <b>185</b> |
| <b>B</b> | <b>Position Estimation Methodology</b>                         | <b>187</b> |
| B.1      | Simulation . . . . .   | 187        |
| B.1.1    | Input File . . . . .   | 187        |
| B.1.2    | Beam Pattern . . . . .   | 188        |
| B.1.3    | Sensitivity $\mathcal{S}$ Map . . . . .                        | 188        |
| B.1.4    | Instrumental Spectral Index $\mathcal{A}$ Map . . . . .        | 188        |
| B.1.5    | Output file . . . . .  | 189        |
| B.2      | Data Analysis . . . . .  | 189        |
| <b>C</b> | <b>The MUST array beam pattern without the primary element</b> | <b>191</b> |

Word Count: 43041



# List of Tables

|      |   |     |
|------|---|-----|
| 2.1  | Fast Radio Bursts discovered to date . . . . .  | 31  |
| 3.1  | MUST bandpass filter specification . . . . .  | 58  |
| 3.2  | The UK frequency allocation in the MUST frequency band . . . . .  | 60  |
| 3.3  | HPBW for the MUST array . . . . .   | 73  |
| 4.1  | Interpolation filter requirements . . . . .   | 94  |
| 4.2  | Summary of the computational cost for the interpolation filter . . . . .                                      | 104 |
| 4.3  | Summary of the computational cost for the fractional delay filter . . . . .                                   | 111 |
| 4.4  | The relationship between the number of taps per filter component and<br>quality of channelised data . . . . . | 116 |
| 5.1  | Glossary of symbols. . . . .  | 129 |
| 5.2  | Values used in Equation 2.7. . . . .  | 135 |
| 5.3  | Number of TABs per spatial sampling for each array . . . . .  | 139 |
| 5.4  | HPBW for the LOFAR Superterp and the MeerKAT core . . . . .   | 139 |
| 5.5  | The MUST undersampling of the FoV results . . . . .   | 141 |
| 5.6  | The MUST Nyquist sampling of the FoV results . . . . .  | 145 |
| 5.7  | The MUST oversampling of the FoV results . . . . .  | 146 |
| 5.8  | The LOFAR undersampling of the FoV results . . . . .  | 150 |
| 5.9  | The LOFAR Nyquist sampling of the FoV results . . . . .   | 153 |
| 5.10 | The LOFAR oversampling of the FoV results . . . . .   | 157 |
| 5.11 | The MeerKAT undersampling of the FoV results . . . . .  | 161 |
| 5.12 | The MeerKAT Nyquist sampling of the FoV results . . . . .   | 163 |
| 5.13 | The MeerKAT oversampling of the FoV results . . . . .   | 167 |
| 5.14 | Detection rates for the MUST, LOFAR and MeerKAT arrays. . . . .   | 170 |
| B.1  | Input files description . . . . .   | 187 |

# List of Figures

|      |  |    |
|------|--|----|
| 2.1  | The transient ‘phase space’ . . . . .  | 25 |
| 2.2  | $P - \dot{P}$ diagram . . . . .  | 27 |
| 2.3  | Illustration of the apparent flux density variations with frequency . . .              | 33 |
| 2.4  | Illustration of the frequency-dependent gain pattern . . . . .                         | 39 |
| 2.5  | Illustration of phase shifts . . . . .   | 40 |
| 2.6  | Illustration of the pattern synthesis . . . . .  | 43 |
| 2.7  | Array configuration for the LOFAR Superterp and MeerKAT core . .                       | 48 |
| 3.1  | The MUST array original frame concept . . . . .  | 53 |
| 3.2  | The MUST array chronology . . . . .  | 54 |
| 3.3  | The first RFI test at Jodrell Bank Observatory . . . . .                               | 57 |
| 3.4  | Graphical representation of the MUST bandpass filter for 33 MHz<br>bandwidth . . . . . | 58 |
| 3.5  | The second RFI scan at Jodrell Bank Observatory . . . . .                              | 59 |
| 3.6  | RFI spectrum from a single MUST tile . . . . .   | 61 |
| 3.7  | The MUST-1 signal chain . . . . .  | 63 |
| 3.8  | A detailed block diagram of the chassis with the first LO . . . . .                    | 64 |
| 3.9  | The Crab pulsar observation with the MUST-1 back-end . . . . .                         | 66 |
| 3.10 | The MUST array Yagi antenna beam pattern . . . . .                                     | 68 |
| 3.11 | The MUST-4 array tile . . . . .  | 69 |
| 3.12 | Modified MUST Yagi . . . . .   | 70 |
| 3.13 | The MUST array location at the JBO . . . . .   | 70 |
| 3.14 | The Yagi antenna test range set-up . . . . .   | 71 |
| 3.15 | The MUST array configuration . . . . .   | 72 |
| 3.16 | The MUST-4 array and tile radiation patterns . . . . .                                 | 75 |
| 3.17 | The MUST normalised array beam patterns . . . . .                                      | 76 |
| 3.18 | The MUST array beam patterns (vertical cut) . . . . .                                  | 77 |
| 3.19 | The MUST-4 signal chain . . . . .  | 79 |

|      |  |     |
|------|--|-----|
| 3.20 | Illustration of the sub-sampling concept . . . . .   | 80  |
| 3.21 | Illustration of the sub-sampling concept . . . . .   | 81  |
| 3.22 | ADC dynamic range . . . . .  | 83  |
| 3.23 | Sensitivity maps for the MUST array . . . . .  | 85  |
| 3.24 | Predicted rates for FRBs . . . . .   | 86  |
| 3.25 | The Sun drift scan . . . . .   | 88  |
| 4.1  | The time-domain beam output $B(t)$ . . . . .   | 92  |
| 4.2  | The discrete time-domain beam output $B(n)$ . . . . .  | 93  |
| 4.3  | Illustration of the interpolation process . . . . .  | 101 |
| 4.4  | The polyphase decomposition . . . . .  | 103 |
| 4.5  | Magnitude Response (dB) of an interpolation filter . . . . .   | 105 |
| 4.6  | The relationship between the number of beams and the sampling time . . . . .   | 106 |
| 4.7  | Magnitude Response (dB) of an interpolation filter . . . . .   | 106 |
| 4.8  | Simulink model of interpolate-by-4 FIR . . . . .   | 108 |
| 4.9  | Signal interpolation on ROACH-1 . . . . .  | 109 |
| 4.10 | Magnitude and phase delay responses of Lagrange FDF . . . . .  | 112 |
| 4.11 | Magnitude and phase response of the prototype filter . . . . .   | 114 |
| 4.12 | Frequency response of a 64-band filter bank . . . . .  | 115 |
| 4.13 | The dynamic spectrum of a simulated pulsar . . . . .   | 116 |
| 4.14 | Spectra from 64 channels polyphase 2-tap filter bank . . . . .   | 117 |
| 4.15 | Spectra from 64 channels polyphase 11-tap filter bank . . . . .  | 118 |
| 4.16 | A pulse profile of a 500 Hz pulsar with 16 MHz bandwidth processed<br>with a 2-tap and 11-tap filter . . . . .                           | 120 |
| 4.17 | The steps in the interpolation process with polyphase decomposition . . . . .  | 121 |
| 4.18 | Polyphase components . . . . .   | 122 |
| 5.1  | Flux ratio of two overlapping TABs . . . . .   | 125 |
| 5.2  | The sensitivity $\mathcal{S}$ map and the flux density ratio $\mathcal{S}_1/\mathcal{S}_2$ map . . . . .                                 | 127 |
| 5.3  | The instrumental spectral index map $\mathcal{A}$ and the spectral index differ-<br>ence $(\mathcal{A}_2 - \mathcal{A}_1)$ map . . . . . | 130 |
| 5.4  | Illustration of detection in five TABs . . . . .   | 132 |
| 5.5  | Example $\mathfrak{s}_1/\mathfrak{s}_2$ and $(\mathfrak{a}_2 - \mathfrak{a}_1)$ maps for the MUST array . . . . .                        | 133 |
| 5.6  | An example of the cumulative error range for the LOFAR array . . . . .   | 138 |
| 5.7  | Graphical representation of $P$ , $D$ and $\delta\phi$ . . . . .   | 140 |
| 5.8  | The MUST array spatial TAB sampling . . . . .  | 142 |

|      |   |     |
|------|---|-----|
| 5.9  | The mean total area $\overline{D}$ covered by the estimated positions for the MUST<br>TABs . . . . .    | 144 |
| 5.10 | Detection examples for the MUST array . . . . .   | 148 |
| 5.11 | The estimated $\overline{\alpha}_l$ for sources detected in the MUST TABs . . . . .                     | 149 |
| 5.12 | The LOFAR Superterp spatial TAB sampling . . . . .  | 152 |
| 5.13 | The mean total area $\overline{D}$ covered by the estimated positions for the LO-<br>FAR TABs . . . . . | 155 |
| 5.14 | Detection examples for the LOFAR array . . . . .  | 156 |
| 5.15 | The estimated $\overline{\alpha}_l$ for sources detected in the LOFAR TABs . . . . .                    | 159 |
| 5.16 | The MeerKAT Core spatial TAB sampling . . . . .   | 162 |
| 5.17 | The mean total area $\overline{D}$ covered by the estimated positions for the MeerKAT<br>TABs . . . . . | 165 |
| 5.18 | Detection examples for the MeerKAT array . . . . .  | 166 |
| 5.19 | The estimated $\overline{\alpha}_l$ for sources detected in the MeerKAT TABs . . . . .                  | 169 |
| 5.20 | HPBW contours of the MUST, LOFAR and MeerKAT arrays. . . . .  | 171 |
| 5.21 | The LOFAR and the MeerKAT 3-D beam patterns . . . . .   | 172 |
| 5.22 | Detection rates for the MeerKAT array . . . . .   | 173 |
| 5.23 | Hierarchy of positional accuracy within a TAB . . . . .   | 175 |
| 5.24 | Summary of results . . . . .  | 177 |
| 5.25 | MeerKAT oversampled TABs comparison . . . . .   | 178 |
| 5.26 | Accuracy of $\overline{\alpha}_l$ in relation to the number of TABs . . . . .                           | 179 |
| B.1  | The location estimation flow chart . . . . .  | 190 |
| C.1  | The MUST-4 array beam pattern without the primary element . . . . .                                     | 192 |

# **The University of Manchester**

ABSTRACT OF THESIS submitted by Monika Karolina Obrocka  
for the Degree of Doctor of Philosophy and entitled  
“High-time Resolution Astrophysics using Digital Beamforming”, January 2015.

In the past few years, a possible new population of sources emitting fast and bright transient radio bursts have been discovered. To explore this new transient phase space, the next generation of radio telescopes, typically interferometers, provide wide observing bandwidths in order to achieve high sensitivity for the detection of weak sources and multi-beaming capabilities to increase the field of view. In comparison to a traditional single beam radio dish, these telescopes collect vast volumes of data and still rely on the traditional observing techniques. Localising transient events during their discovery is essential as these events might not be repeatable by nature.

I describe the development and construction of a prototype phased array, the Manchester University Student Telescope (MUST), capable of multi-beam operation. I present results of the Yagi antenna beam measurements and the optimum antenna separations; the investigation of the radio frequency interference spectrum around the preferred observing band and setting the subsequent bandpass filter specifications; simulations of the optimum configurations of the MUST tiles; and finally I describe implementation of the digital back-end.

For the joint task of discovery and simultaneous localisation, the advantages of single dishes and interferometers are combined in a beamforming approach. I present an investigation into the wide-bandwidth time-domain signal processing techniques for time-domain beamforming that can be used in transient and pulsar observations. I discuss the efficient polyphase decomposition for interpolation digital filters and multiplication-free fractional delay filters that can be used to reduce the complexity of the beamformer implementation and avoid high sampling rates. This reduced complexity allows more simultaneous beams to be formed using time-domain techniques. This analysis was performed for the MUST array, but is applicable to a wide range of interferometers.

I have developed and analysed a new proof-of-concept non-imaging method to localise transient sources observed with interferometers or phased array feeds. It utilises the additional spectral and comparative spatial information obtained from multiple overlapping tied array beams. This allows us to estimate a transient source location

with up to arcsecond accuracy in almost real time and allows the required high time resolution to be preserved. We demonstrate that this method can work for a variety of interferometric configurations, including for LOFAR and MeerKAT, and that the estimated angular position may be sufficient to identify a host galaxy, or other related object, without reference to other simultaneous or follow-up observations.

# **Declaration**

No portion of the work referred to in this thesis has been submitted in support of an application for another degree or qualification of this or any other university or other institute of learning.

# Copyright

- i. The author of this thesis (including any appendices and/or schedules to this thesis) owns certain copyright or related rights in it (the “Copyright”) and s/he has given The University of Manchester certain rights to use such Copyright, including for administrative purposes.
- ii. Copies of this thesis, either in full or in extracts and whether in hard or electronic copy, may be made **only** in accordance with the Copyright, Designs and Patents Act 1988 (as amended) and regulations issued under it or, where appropriate, in accordance with licensing agreements which the University has from time to time. This page must form part of any such copies made.
- iii. The ownership of certain Copyright, patents, designs, trade marks and other intellectual property (the “Intellectual Property”) and any reproductions of copyright works in the thesis, for example graphs and tables (“Reproductions”), which may be described in this thesis, may not be owned by the author and may be owned by third parties. Such Intellectual Property and Reproductions cannot and must not be made available for use without the prior written permission of the owner(s) of the relevant Intellectual Property and/or Reproductions.
- iv. Further information on the conditions under which disclosure, publication and commercialisation of this thesis, the Copyright and any Intellectual Property and/or Reproductions described in it may take place is available in the University IP Policy (see <http://documents.manchester.ac.uk/DocuInfo.aspx?DocID=487>), in any relevant Thesis restriction declarations deposited in the University Library, The University Library’s regulations (see <http://www.manchester.ac.uk/library/aboutus/regulations>) and in The University’s policy on presentation of Theses



# Acknowledgements

Undertaking a doctoral thesis is an endeavour, to be polite. You are given a vague deadline that is million years in the future, or so you thought, to announce to the world your *original contribution*. But research is not linear. Research is unpredictable and results are not guaranteed even if you work really, really hard. That is why the people around you are so important during this turbulent time. Simply, someone to stop you jumping off the bridge in the Alan Turing building.

First of all I would like to thank my PhD supervisors Ben Stappers and Peter Wilkinson for their guidance, support and encouragement. Most of all for putting up with my Eastern European grumpiness – this cheerful and sunny disposition we are known for. Ben, you have never given up on me, even though I did on many occasions, and for that I thank you.

The person that had been there for me through the worst times is Gemma Janssen. We both attended ERIS in Oxford, but only met at the Jodrell Bank two years later. She was there to talk and to offer guidance, she listen to my cries during a temporary deterioration in mental health. Thank you for all of the meetings and chats over the years. You are a mentor and a friend to me.

I would like to thank Prabu Thiagaraj for reminding me that there are still people with a genuine desire to share their knowledge. We all recognise the need to learn from the life experience and wisdom of others. I believe that if our paths crossed earlier, this PhD could have been an enjoyable experience. Prabu, you were never too busy to offer your invaluable advice and expertise. Thank you.

Without the pulsar group life would have been boring and dull. How better to spend an afternoon than to reorganise the office space? My weekly duty of driving you lot

to Jodrell was a chore that I enjoyed immensely. Our conversations about everything from science, Mancunian matters, politics to general nonsense I will cherish forever. I enjoyed every pub trip and every boat trip, but I am still waiting for the train driving experience.

To Sally and Simon – *"There is something wrong with you"*.

I owe my sincere thanks to the people from the Jodrell Bank Observatory, especially to Chris Jordan and Richard Whittaker. Thank you for all of your warm help and support during my PhD studies. I would also like to thank the digital team from the University of Oxford, namely Jack Hickish, Griffin Foster, David Sinclair and Danny Price for the weekly RadioLab chats. Thank you for making me feel welcome.

Finally, I would like to thank my husband Sebastian for showing me that the time you enjoy wasting is not wasted time. You are my best friend.

*I dedicate this work to my parents Zbigniew and Elżbieta Obrockich.*

*“So, where is my dream?  
It is a continuation of reality.  
But where is my reality?  
It is at the end of your dream.”*

Ikari Shinji and Ayanami Rei (Neon Genesis Evangelion)

# Acronyms

**LOFAR** LOw-Frequency ARray

**MUST** Manchester University Student Telescope

**SKA** Square Kilometre Array

**LNA** Low Noise Amplifier

**JBO** Jodrell Bank Observatory

**MSSGE** MATLAB-Simulink-Signal Generator-EDK

**DSP** Digital Signal Processing

**FoV** Field of View

**MeerKAT** Karoo Array Telescope

**TAB** Tied Array Beam

**ISM** Inter-Stellar Medium

**IGM** Inter-Galactic Medium

**RFI** Radio Frequency Interference

**FoM** Figure of Merit

**DM** Dispersion Measure

**FRB** Fast Radio Burst

**FFT** Fast Fourier Transform

**HPBW** Half Power Beamwidth

# Chapter 1

## Introduction

The great pace of technological developments in the areas of super-fast silicon chips, data transport and phased array antennas enables the construction of ever more powerful radio telescopes in the form of connected arrays. The next generation radio telescopes, like LOW-Frequency ARray (LOFAR), provide wide bandwidths and multi-beaming capabilities. These telescopes collect vast volumes of data, in comparison to a single beam radio dish, but still rely on evolutions of the traditional observing techniques. To unlock their full potential, new analysis techniques and observing strategies have to be developed.

### 1.1 Objectives

The principal goals of this thesis are to investigate transient phenomena detection strategies and to deliver a proof-of-concept time domain beamforming system for the Manchester University Student Telescope (MUST) in order to study the effects of processing, if any, on the pulsar data.

#### 1.1.1 MUST

A perceived need for an additional scientific instrument at the Jodrell Bank Observatory coincided with the digital TV switchover in the UK. This prompted the initial planning and prototyping of a new array suitable to test new analysis techniques of time domain astronomical data with reference to the Square Kilometre Array (SKA).

### 1.1.2 Time-domain beamforming

To achieve high sensitivity to detect weak noise-like signals the observing bandwidth often has to be increased. The processing of astronomical signals is often done in the frequency-domain, where they are decomposed into narrow-band frequency components by the means of fast Fourier transform (FFT). The aim is to investigate and compare the effects of frequency and time-domain signal processing techniques on pulsar data collected with the MUST telescope. We discuss each approach's own advantages and disadvantages. We also present investigation of the new time-domain implementations of digital filters.

### 1.1.3 Detection and localisation of transient phenomena

In the past few years, a possible new population of sources emitting transient radio bursts has been discovered. Follow up radio observations failed to find further bursts or identify a counterpart. Accurate localisation of a transient source (to arcsecond precision) has previously required an image produced with an interferometer. At the present time it is difficult to perform this in real time. The aim is to develop a method for localising a source as fast as possible without imaging and at the same time retain high time resolution.

## 1.2 Thesis Outline

This thesis is organised in the following manner:

Chapter 2 provides background information on pulsar physics and gives an introduction to the observing methods. Then the fast radio burst phenomenon and related recent discoveries are given. The concepts of interferometry and associated terminology are introduced. A short review of new and upcoming radio telescopes is also given.

Chapter 3 describes the development and construction of the first phase of the MUST array. The design decisions, regarding the array elements and back-end system, are justified. Various electrical tests are described. We also show extensive simulations of the MUST array beam patterns and discuss the potential scientific performance.

Chapter 4 presents an investigation into the time-domain signal processing techniques for the pulsar and transient sources data analysis. A short description of various beamforming techniques is given. In our work we propose the time domain processing for beamforming, thereby reducing the unnecessary artifacts in the signal being analysed which are inevitably introduced in frequency domain processing. This is of importance to the transient and pulsar observations that we propose to do with the phase 1 "MUST-4" instrument and we discuss the advantages of this approach.

Chapter 5 presents the development of a new non-imaging method for a fast localisation of transient sources. Employing multi-beam data simulated for several interferometric arrays, we investigate the possibility of localising a source with better accuracy than a single tied array beam width in real time; we use only the observed flux density and information about the array beam shapes. For arrays where the source is detected in more than one beam we demonstrate that the frequency-dependent variations in a telescope beam shape can be exploited to localise a source position with high accuracy – down to arcsecond levels in some cases. This would be sufficient to identify optical counterpart (if any) to transient source.

Chapter 6 concludes this thesis and provides remarks on the future work.

## **1.3 Contributions**

### **1.3.1 The MUST array**

The task to develop a low-cost and innovative system was shared by several departments at the University of Manchester, together with local companies that provided materials for the frames and aerials. As a result, a significant proportion of this work arises from collaborations with astronomers and engineers across the Faculty of Engineering and Physical sciences. The idea for the low-cost array originally came from Prof. Lyne, Prof. Kramer and Prof. Wilkinson in 2003. After the project was revived in 2011, Prof. Wilkinson has been responsible for overseeing its execution one of whose aims was to involve graduate students from across the Faculty of Engineering and Physical Sciences. The MUST frames were designed by Dr James Methven and students from the School of Mechanical Engineering. The initial Yagi array was designed by Prof. Zhipeng Wu and his students and was based on commercial antennas,



albeit these have now been redesigned and replaced. The initial Low Noise Amplifier (LNA) design was performed by a PhD student of Prof. Mohamed Missous from the School of Electronic and Electrical Engineering, again this LNA design has been replaced. The frame support were designed by a combination of Dr Adrian Bell and staff from the School of Civil Engineering, in particular by Mr Bob Wray.

The MUST analog heterodyne receiver was adapted from the 42 foot telescope back-end at the Jodrell Bank Observatory (JBO), both designed by Mr. Tim Ikin at Jodrell Bank. I conducted all RFI scans and was assisted by either Mr Tim Ikin, Dr Richard Whittaker or Dr Sarah Smith. The receiver tests that involved the signal from the 42 foot telescope were conducted with help from Dr Chris Jordan. I was also heavily involved in the process to determine the optimum Yagi spacings, described in Adam Davidson's MSc thesis (Davidson, 2013). In addition, the majority of Yagi antennas used for the tests were modified by me. The frames were constructed primarily by Prof. Wilkinson and Dr Ian Stevenson. Although I was not closely involved in all aspects of the commissioning, I contributed significantly work to, and took part in, several design decisions.

### 1.3.2 Digital Back-end

This thesis was envisaged from the start as focused on the MUST project and in particular the digital back-end signal processing; I was responsible for this part of the system. Due to delays in the construction (as explained in §3) and because of the funding-imposed limitations on the size of the prototype, the MUST array was over a year late. As a result, only half of the original envisaged array was built. I took part in the original specification and the purchase of the hardware from the USA. All the digital design work in this thesis was designed by me with the MATLAB-Simulink-Signal Generator-EDK (MSSGE) tool-flow and Digital Signal Processing (DSP) System Toolbox for the digital filter design. During the course of the project I benefited from technical help with hardware from Dr Richard Whittaker, Dr Chris Jordan and Dr Prabu Thiagaraj and the staff at the JBO. The digital receiver architecture was a result of a visit to the Digital Back End group at the SKA South Africa in Cape Town. I received assistance from Dr Matt Dexter from Berkeley's Radio Astronomy Laboratory with the QuadADC tests and from Dr Griffin Foster from Oxford University with the interpolation filter design.

### 1.3.3 Transient Source Location Estimation Method

The Matlab script that simulates and analyses the data I developed entirely by myself. There are two main Matlab programs, the first one simulates the transient sources in the Field of View (FoV) and calculates the sensitivity and spectral index maps for all beams. The second script analyses the data from the simulation programme, i.e. estimates the source location and the intrinsic spectral index. I also made use of various open software Matlab toolboxes and functions available from the Matlab Central website. For example, used an excellent *geom2d*<sup>1</sup> and *geom3d*<sup>2</sup> toolboxes for measuring distances and drawing of shapes written by David Legland. As the location estimation script requires a beam pattern for each telescope, I also extensively used the OSKAR-2 package. As an input, it uses a tree-like telescope model to generate a beam pattern that has to be provided by the user. Thus, the LOFAR telescope model was provided by Griffin Foster from Oxford University and the models for the Karoo Array Telescope (MeerKAT) and MUST arrays I generated myself. Prof. Ben Stappers provided the original inspiration for the method, and Prof. Peter Wilkinson provided advice and discussion on how to improve it.

---

<sup>1</sup><http://uk.mathworks.com/matlabcentral/fileexchange/7844-geom2d>

<sup>2</sup><http://uk.mathworks.com/matlabcentral/fileexchange/24484-geom3d>

# Chapter 2

## Background

High time resolution radio astronomy was, for a long time, dominated by large filled-aperture dishes. A dish size dictates an area of sky seen in a single pointing and a large dish would increase the sensitivity, but at the same time reduce the Field of View (FoV). To combine better sensitivity, preserve the FoV and have high angular resolution, next generation telescopes are typically interferometers made up of many relatively small elements, where the signals are correlated across the array to emulate a much larger dish. A 2-dimensional snapshot image of the sky made with a correlation interferometer can provide a large FoV and an accurate localisation of a radio source to less than a beamwidth of its primary element, where beamwidth is a function of the antenna dimension and the wavelength of the signal. The data from such a telescope are often coherently integrated over a time of a few seconds to reduce the massive data volumes; the information about the sub-second variability in the sky therefore is lost.

High-time resolution is retained in a process called beamforming, where the input signals from antennas are added coherently producing a narrow tied array beam. The relative localisation capabilities of a single Tied Array Beam (TAB) are similar to a single dish, except the beam is much narrower. To achieve a similar FoV, to a correlation interferometer, with a beamformer hundreds to many thousands of TABs may have to be formed. As a result the real-time signal processing of a multibeamforming beamformer can be prohibitively expensive. Furthermore, even with the addition of many sensitive TABs, it is commonly thought that without imaging a source position can only be approximated to an individual TAB. In §5 we develop a new method to get around this problem by including all the differential spatial and spectral information available from an array forming many TABs.

## 2.1 Transient Background

Transient emission is detected from flares, pulses and bursts on timescales that vary from nano-seconds to years. The extreme environments in the Universe can be observed in the X-ray, radio and  $\gamma$ -ray bands. So far, the observations using wide-field orbiting observatories, with all-sky monitors, in the X-ray and  $\gamma$ -ray bands have revealed a rich array of explosive events missed by optical telescopes due to their narrow FoV. From the ground one way to study those extreme events is using radio emission. We have been observing the transient sky for decades but due to a lack of wide-field instruments and the demanding signal processing, the exploration of the fast transient radio sky has been slow. This is best described in Figure 2.1 that plots the phase space of variable and transient radio sources (Keane et al., 2011; Cordes et al., 2004). It represents the time-luminosity phase space, where radio luminosity parameters; the product of peak flux density  $S$  and the square of the distance to the source  $D$ , are plotted against the product of a transient time-span  $W$  and the observing frequency  $\nu$ . In the Rayleigh-Jeans approximation, the source brightness temperature  $T$  of a radio source and flux density  $S$  are related using the following formula<sup>1</sup>:

$$\nu^2 W^2 \sim \frac{1}{2\pi k} \frac{SD^2}{T}. \quad (2.1)$$

As can be seen, the plot is scarcely populated and the empty spaces may soon be filled with new discoveries. The most studied group is represented by pulsars.

It is clear that our exploration of the transient sky has just started and the opportunity for new discoveries is enormous. We live in a new golden era for radio astronomy where new observing techniques and more importantly new wide FoV instruments are being commissioned. Throughout the rest of this work, the term *transient* refers to *radio transients* unless otherwise stated. In addition, we only consider fast transient (i.e. with durations from  $\sim$  milliseconds to  $\sim$  nanoseconds).

A transient signal propagating through the Inter-Stellar Medium (ISM) or Inter-Galactic Medium (IGM) is affected by propagation effects i.e. dispersion, scattering and scintillation (Rickett, 1990). Dispersion causes the low frequency components of a pulse to arrive later than the higher frequency components, proportional to  $\nu^{-2}$ . Scattering of the radio waves has an exponential broadening affect on the pulse shape,

---

<sup>1</sup>Derivation can be found in §A

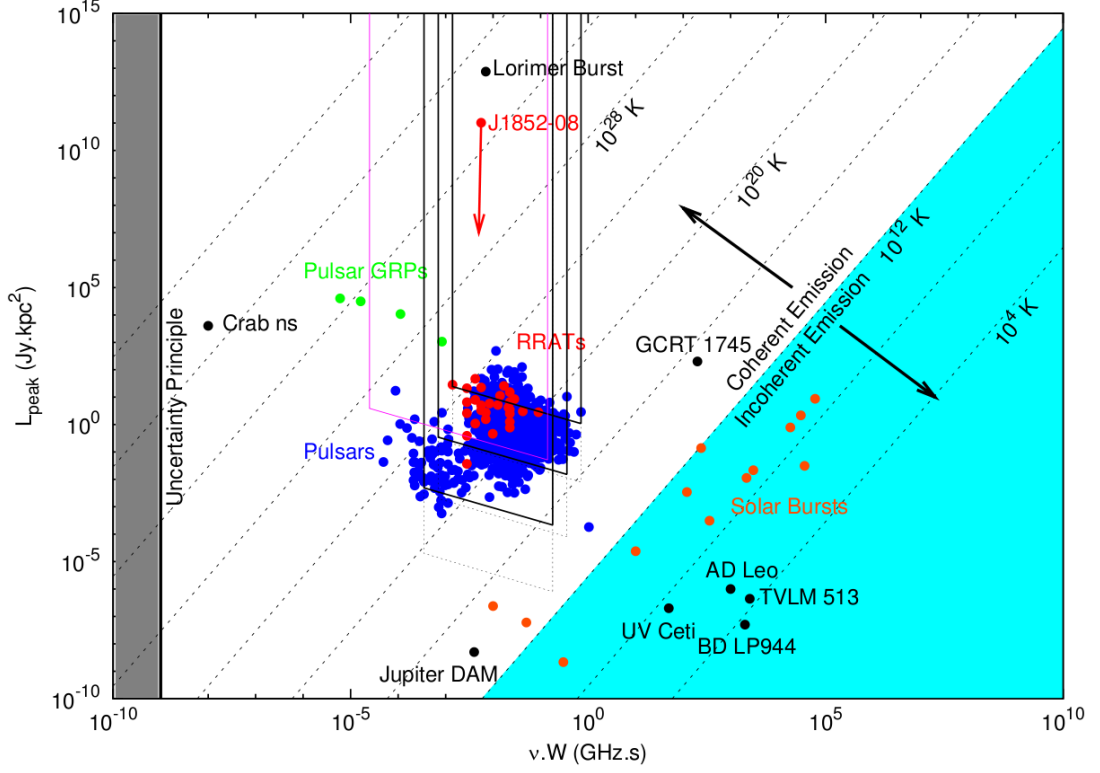


**Figure 2.1:** The transient "phase space". A plot of the radio pseudo-luminosity  $L = SD^2$  versus  $\nu W$ , where  $S$  is flux density,  $D$  is distance,  $\nu$  is observing frequency and  $W$  is pulse width. Plotted are lines of constant minimum brightness temperature  $T_B$  (credit Keane et al. (2011)).

proportional to  $\nu^{-4}$ . Scintillation contributes to changes in the received signal strength that manifest as brightening or dimming on a variety of time and frequency scales. This may lead to strong sources not being detected or weak sources temporarily being detectable; these changes in flux density can be rapid or take days or weeks. All these effects are frequency dependent and are stronger at the low frequencies<sup>2</sup>.

A simple Figure of Merit (FoM) (Bhat, 2011) describes the ability of a telescope to detect transient sources:

$$FoM \propto \left( \frac{A_{eff}}{T_{sys}} \right)^2 \frac{\Omega_i T_{obs}}{\Delta\Omega \Delta T}, \quad (2.2)$$

where  $A_{eff}$  is the effective collecting area of an array,  $T_{sys}$  is the system temperature,  $\Omega_i$  is the instantaneous field of view,  $\Delta\Omega$  is the localization radius,  $T_{obs}$  is the dwell time

<sup>2</sup>A positive effect of those propagation effects is in providing discrimination between real astrophysical signals and Radio Frequency Interference (RFI).

and  $\Delta T$  is the time resolution of the data. Thus to detect such events radio telescopes have to cover large areas of the sky with high time resolution. We can distinguish five general methods used to detect transient events:

- dedicated surveys focusing on wide field sensitive searches;
- multi-wavelength triggered detection, where a detection at one wavelength triggers an observation with a telescope operating at a different wavelength;
- archival studies, where many hours of data are searched for different parameters i.e. higher Dispersion Measure (DM);
- serendipitous, or accidental detection;
- commensal detections, where observing time is shared between multiple independent programs simultaneously.

Fortunately breakthroughs in radio astronomy follow technological advances and with the growing signal processing capabilities of today's electronic components radio astronomers can venture into the unknown. A review of periodic sources (pulsars), and non-periodic transient events, the Fast Radio Burst (FRB), will now be given. A broader introduction to transient sources can be found in Fender & Bell (2011) and Bhat (2011).

### 2.1.1 Pulsar Background

The existence of neutron stars was suggested 30 years before their discovery by Baade & Zwicky (1934) as one possible outcome for a star that burned all its nuclear fuel. Depending on the mass, the next stage of a star's life cycle will be a white dwarf, a neutron star or a black hole. A star with a mass below  $1.4 M_{\odot}$  will continue its life as a white dwarf, this is true for around 99% of stars. Only the most massive stars, i.e. with core masses above  $3 M_{\odot}$ , will become black holes. This mass limit is known as *the Oppenheimer-Volkoff (OV) limit* that lies somewhere in the range between  $1.4 M_{\odot}$  to  $3 M_{\odot}$ . A star that has a core mass in the OV limit are transformed into a neutron star. Neutron stars typically have a radius of 10 km, a mass of  $1.4 M_{\odot}$  and a mean density of  $6.7 \times 10^{14} \text{ gcm}^{-3}$ . For a star that emits very little visible light, as insufficient energy is produced in the optical range, and is only the size of a small city, the prospects of finding one were thought to be almost none. That is why pulsars were a serendipitous discovery by astronomers from Cambridge (Hewish et al., 1968) who built a low-cost phased array designed to survey the sky at 81.5 MHz to study interplanetary radio scintillation. The array consisted of full-wave dipoles arranged in a

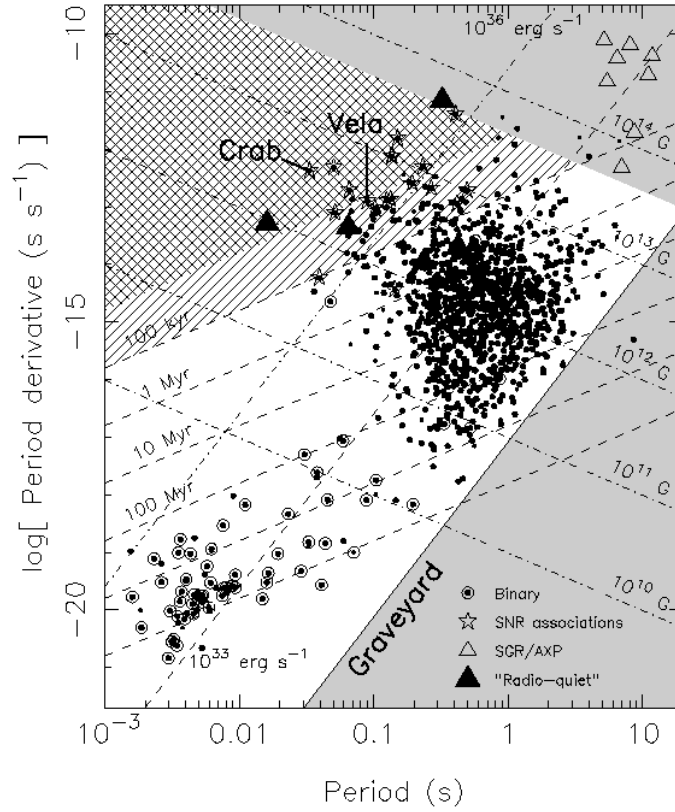


**Figure 2.2:**  $P - \dot{P}$  diagram, where the spin-down parameter  $\dot{P}$  is plotted against the spin period  $P$  (Lorimer & Kramer, 2004). Lines of constant magnetic field strength ( $B \propto \sqrt{P/\dot{P}}$ ) and characteristic age ( $\tau \propto P/\dot{P}$ ) are also plotted.

16 by 128 rectangular grid. It extended to 470 m in an East-West direction and 45 m in the North-South direction. All dipoles were phase aligned to form beams. Four receivers were used to produce four independent scanning beams in declination<sup>3</sup>. The array could also operate as an East-West interferometer. As well as studying scintillation, Hewish et al. (1968) stumbled upon regular series of pulses and initially mistook them for "Little Green Men". The connection between pulsars and neutron stars was made shortly after by Gold (1968).

Pulsars are highly magnetised rotating neutron stars that emit radio waves, X-rays and gamma rays. Although the radio emission is continuous it appears to be periodic as the radiation can be compared to a celestial radio lighthouse i.e. a narrow beam of radio emission is created at the poles of the magnetic field and radiation is observed with every rotation of a star. The spin axis and the magnetic poles are not necessarily

<sup>3</sup>More information about the beamforming mode can be found in §2.2.2.

aligned and therefore, as observed from the Earth, the pulsar appears to switch "on" and "on" as the beam sweeps over the Earth. The time between the "on" and "off" period is called the *spin period*  $P$  of a pulsar. The pulse periods range between 1.4 ms and 8.5 s. As a pulsar rotates, it slowly loses its rotational kinetic energy, i.e. it slows down. The *spin-down* parameter  $\dot{P}$  when plotted against the parameter  $P$  gives an insight into the spin evolution of a neutron star, Figure 2.2. Using this  $P - \dot{P}$  diagram the inferred age ( $\tau \propto P/\dot{P}$ ) and magnetic field strength ( $B \propto \sqrt{P/\dot{P}}$ ) can be estimated for each neutron star.

Pulsars can be viewed as a very precise natural clocks and their clock-like rotational stability enables tests of general relativity and can be used as a diagnostic of gravitational radiation using pulsars found in binary systems (Kopeikin, 1997; Taylor et al., 1992). They also have the potential to provide a time standard, in particular from the millisecond pulsars (e.g. van Straten et al. (2001)).

Pulsars can also be used as probes of the ISM, to study its structure and ionisation, due to the propagation effects described earlier. By estimating the distance to the pulsar, the distribution of the Galactic free electrons can be mapped. One of the methods to estimate the distance to a pulsar is to measure the frequency-dependent delay in the signal arrival time. This *dispersion delay*  $\Delta t$  depends on the number of free electrons  $n_e$  along the line of sight, the distance to a pulsar  $L$  and the observing frequency  $\nu$ :

$$\Delta t = \frac{\text{DM}}{2.410 \times 10^{-4} \nu_{\text{MHz}}^2} [\text{s}], \quad (2.3)$$

where DM, called the *dispersion measure*, is the measure of the number of free electrons between the pulsar and the Earth. DM can be expressed in the form of an integral:

$$\int_0^L n_e(l) dl [\text{cm}^{-3} \text{pc}]. \quad (2.4)$$

The Galactic electron density varies with the line-of-sight and distance. Thus, two sources observed along the same line-of-sight, where one is further away, will have different DMs. The great advantage of dispersion for the detection of transient sources is that we can efficiently discriminate between signals of Galactic origin and the signals of terrestrial origin<sup>4</sup>. Before any further processing, the effects of dispersion have

---

<sup>4</sup>Signals of terrestrial origin are in general not dispersed, but see §2.1.2.



to be corrected for using a technique called de-dispersion prior to data analysis.

Pulsar data can be dedispersed coherently or incoherently. Coherent dedispersion, called also *pre-detection dedispersion*, is applied to the voltage data from the receiver. The effect of dispersion can be modelled as a linear filtering operation. For known sources, where the DM is known a priori, the inverse filtering can remove the dispersion effect exactly. Thus, retaining the original time resolution of the full observational bandwidth  $BW$  (Hankins & Rickett, 1975). Incoherent dedispersion, also called *post-detection dedispersion*, is applied to the squared voltages (intensity). The bandwidth  $BW$  is split into many channels using a filter bank. The pulsar signal is detected in each of these channels. Then, a delay, calculated with Equation 2.3, is applied to the detected data to correct for the dispersion. Appropriately shifted channels are summed to form a dedispersed time series. For the study of known pulsars coherent dedispersion is the preferred method as it accurately recovers the intrinsic shape of the observed source, whereas incoherent dedispersion is used in surveys as it is less demanding in computational power.

Recent discoveries of new pulsar phenomena are the *Rotating Radio Transients* *RRATs* (McLaughlin et al., 2006) and *the intermittent pulsars* (Kramer et al., 2006). Predominantly, searches for pulsars have been carried out using Fourier domain searches that look for a periodicity in the received signal. In a periodicity search, a Fast Fourier Transform (FFT) is applied to the dedispersed time series. Many harmonics are summed together and then averaged ("folded") to increase sensitivity and to produce a pulse profile (Ransom et al., 2002). *RRATs*, and other transient and one-off pulses, cannot be found using the FFT<sup>5</sup> technique since they emit short radio bursts sporadically and are missed by periodicity searches. The intervals between the bursts vary from source to source and range from 4 min to 3 hours while the bursts themselves last from 2 to 30 ms. Instead single pulse detection is used (McLaughlin & Cordes, 2003), where a dedispersed time series is searched for pulses with an amplitude above some  $S/N$  threshold. Each time series has a known mean and standard deviation and any event that deviates from that mean is treated as a possible transient source. Single pulse searches may also be used when observing intermittent pulsars as they experience periods of inactivity. However, they are generally formed using FFT searches. An intermittent pulsar could be ON for a week and OFF for a month, where the radio emission shut-off

---

<sup>5</sup>Fast Fourier Transform

takes less than 10 s. Due to the nature of these sources "traditional" observations could easily miss them, either because they were in their OFF phase during observation or during follow-up observations.

Usually pulses emitted from pulsars vary in intensity by an order of magnitude, but some pulses can vary by as much as 1000 times the mean pulse intensity. They are called "giant" pulses and were first observed in the Crab pulsar (Lundgren et al., 1995). So far, the majority of all discovered pulsars are located in our Galaxy, with some discovered in the Magellanic Clouds (Crawford et al., 2001), dwarf galaxies orbiting our Milky Way. With the *Square Kilometer Array (SKA)* (§2.3) giant pulses from pulsars will be detectable out to the Virgo cluster. Using extragalactic pulsars we could explore the baryon density and magnetic field in the Local Group via studies of rotation measure and dispersion. Apart from the erratic pulsars already described, sources that are expected to emit radio pulses are annihilating black holes, blitzars<sup>6</sup>, supernovas and transient sources of unknown origin such as FRBs, described in detail next.

### 2.1.2 Fast Radio Bursts

In the past few years, a possible new population of sources emitting fast and bright transient radio bursts has been discovered. In August 2001 an isolated pulse of radio emission was recorded but only discovered during the analysis of archival survey data of the Magellanic clouds (Manchester et al., 2006) by an undergraduate student David Narkevic. The discovery was published in 2007 (Lorimer et al., 2007) and has since been called the *Lorimer Burst (LB)*. It had a duration of 5 ms and intensity of at least 30 Jy at 1.4 GHz and at a very high  $DM = 375 \text{ cm}^{-3} \text{ pc}$  that Lorimer et al. took to indicate an extra-galactic origin. The pulse was observed in 3 out of 13 beams of the Parkes multi-beam receiver. The strongest detection with SNR of at least 23, saturated beam 6 in the single-bit digitisers. The team conducted 90 hours of follow-up observation with no subsequent detection and concluded that it was a one-off event. The non-terrestrial origin of the *LB* has been questioned by Burke-Spolaor et al. (Burke-Spolaor et al., 2011). They studied the same Parkes data set and identified 16 bursts that, they claim, represent a new class of broadband terrestrial sources of radio emission that they called

---

<sup>6</sup>Imploding neutron star.

*Perytons*<sup>7</sup>. Perytons also exhibit an apparent dispersive delay characteristics of a non-terrestrial source with pulse width between 30 and 50 ms. All detected Perytons were seen in all 13 Parkes beams. However it is noteworthy that all Peryton pulses from Parkes and all but one from Bleien Observatory (Saint-Hilaire et al., 2014), occurred during the day, whereas the *LB* occurred during the night. Work continues to understand the relationship (if any) between the *LB* and Perytons. So far 16 Perytons have been observed at Parkes and 5 at Bleien Observatory. A trend has also been identified that majority of the perytons occurred in June.

Another similar FRB transient was found 5 years later during reanalysis of the Parkes Multi-beam Pulsar Survey (PMPS) data (Keane et al., 2012). Four more FRBs were then found during the analysis of the High Time Resolution Universe (HTRU) survey conducted with Parkes telescope (Thornton et al., 2013). Recently, a new FRB has been discovered in the 1.4-GHz Pulsar ALFA survey conducted with the Arecibo Telescope (Spitler et al., 2014). It is the first FRB observed at a different geographical location than the Parkes telescope. Details of all published FRBs are presented in Table 2.1. One FRB that stands out, FRB 010621, originated close to the Galactic plane ( $b = -4^\circ$ ) and could be of Galactic origin as the DM is just over the maximum expected DM from NE2001<sup>8</sup> along this line-of-sight (Bannister & Madsen, 2014). FRB121102 also originated along the Galactic plane ( $b = 0^\circ$ ) but the Galactic DM contribution is much lower at around only 30%.

**Table 2.1:** Fast Radio Bursts discovered to date and in the open literature, where  $b$  is the galactic latitude,  $S$  is the flux density,  $W$  is the pulse width,  $DM_{Total}$  is the observed DM and  $DM_{EG}$  is the extra galactic DM.

| FRB    | $DM_{Total}$ | $DM_{EG}$ | $b$         | $S$ (Jy) | $W$ (ms) | Reference              |
|--------|--------------|-----------|-------------|----------|----------|------------------------|
| 010724 | 375          | 330       | $-42^\circ$ | 30       | 5        | Lorimer et al. (2007)  |
| 010621 | 746          | 213       | $-4^\circ$  | 0.4      | 8        | Keane et al. (2012)    |
| 110220 | 944          | 910       | $-55^\circ$ | 1.3      | 6        | Thornton et al. (2013) |
| 110627 | 723          | 677       | $-42^\circ$ | 0.4      | $<1.4$   | Thornton et al. (2013) |
| 110703 | 1104         | 1072      | $-59^\circ$ | 0.5      | $<4.3$   | Thornton et al. (2013) |
| 120127 | 553          | 521       | $-66^\circ$ | 0.5      | $<1.1$   | Thornton et al. (2013) |
| 121102 | 557          | 370       | $0^\circ$   | 0.3      | 3        | Spitler et al. (2014)  |

<sup>7</sup>Mythological Perytons are winged elk that cast the shadow of a man.

<sup>8</sup>Model for Galactic electron density Cordes & Lazio (2002)

The observed large DMs<sup>9</sup> and high galactic latitudes, for almost all detected FRBs, suggest an extragalactic origin for FRBs. The follow up radio observations failed to find further bursts at the same location, i.e. areas of sky covered by Parkes beams where an FRB occurred. It is therefore believed FRBs are one off events that "light-up" the radio sky at an estimated event rate of thousands per day (Thornton et al., 2013; Lorimer et al., 2013). As FRBs might represent a new class of highly compact and extreme events it is vital to find the source location using only the one available burst. This is especially true for when there is no afterglow present and thus to identify a host galaxy one has to rely on the original observation.

As well as identifying a new class of source, an exact determination of FRB positions and distance (via the redshift) will give a unique opportunity to study the magneto-ionic properties of the intergalactic medium (IGM) (Macquart & Koay, 2013). It is thought that a substantial fraction of the 60% of the missing baryons in the Universe reside in intergalactic gas (Cen & Ostriker, 1999). The location of the missing baryons is difficult to constrain if they occur at densities and temperatures that do not show significant absorption or emission. If, for example, there is an association between FRBs and Gamma-ray bursts (GRB) a new window on cosmology will open. From such an association two precise measurements can be made, namely the DM from the FRB and the redshift of the system from the GRB (Deng & Zhang, 2014). That will allow one to directly measure the IGM portion of the baryon mass fraction, which in turn will constrain the re-ionisation of He and H in the Universe. Achieving the required number of FRB discoveries will, however, require the development of a new FRB observing and discovery strategy. We describe it in §5.

### 2.1.3 Spectral Index and Flux density of transient sources

The observed flux density  $S_\nu$  of many radio sources has a power law dependency with the observing frequency  $\nu$ . That relationship differs for thermal and synchrotron emission. For pulsars it often follows a power law dependency to the first order<sup>10</sup>, e.g. Maron et al. (2000):

$$S(\nu) \propto \nu^\alpha, \quad (2.5)$$

---

<sup>9</sup>Values of DM that exceeds the contribution from our Galaxy.

<sup>10</sup>At this stage of the analysis we are considering only power laws.

where  $\alpha$  is the spectral index. The spectra represent intrinsic characteristics of pulsar emission and geometry. The typical flux density spectra of radio pulsars are known to be steep with a mean spectral index of  $-1.41$  (Bates et al., 2013). Although measurements of a significant number of spectral indices have been made (Maron et al., 2000; Lorimer et al., 1995), the study of the intrinsic distribution of pulsar spectra is limited; many pulsars are observed at only one frequency and hence there is inevitably a bias towards the strongest pulsars in the surveys. Gaining a better understanding of the intrinsic spectral index can have the implications for the understanding of pulsar's emission mechanism. The debate on the most probable emission mechanism is still ongoing (Manchester, 2009; Beskin & Philippov, 2012; Kontorovich & Flanchik, 2013).

So far the limited evidence available suggests that the spectra of FRBs are flat (Hassall et al., 2013), but due to the frequency-dependent gain pattern of telescopes, sources detected off-axis can have their spectral index distorted substantially. For example, Spitler et al. (2014) reported a spectral index of  $+7 \pm 1$  for FRB 121102 discovered with Arecibo. Spitler et al. created a map of the apparent instrumental spectral index for the ALFA receiver using the gain variation in units of  $\text{K Jy}^{-1}$ . The contribution of the apparent spectral index at the phase centre is zero for each horn. Moving away from the phase centre the apparent spectral index contribution becomes negative as the gain decreases (for a detailed explanation see §5.1). The only area of the map that could impose a positive apparent spectral index on FRB 121102 is the rising edge of the first sidelobe, as is suggested by the authors.

The observed (apparent) flux density of the same source can vary considerably at different frequencies, see Equation 2.5. Moreover, the sensitivity of a TAB is frequency and steering direction dependent (see §5). To illustrate this dependency, Figure 2.3 shows apparent flux density variations with frequency at different distances from the phase centre of a simulated TAB formed by an adding interferometer array. The simulated sources are equally spaced along a straight line, as shown in the top panel in Figure 2.3, where the first source is simulated at the phase centre of a TAB (bottom left corner) and the last in the first sidelobe (upper right corner). All sources are detected at 7 equally spaced frequencies  $\nu$ . Each source has identical characteristics and we analyse two different scenarios, where the intrinsic spectral index of a source is flat and where it varies according to a power law.

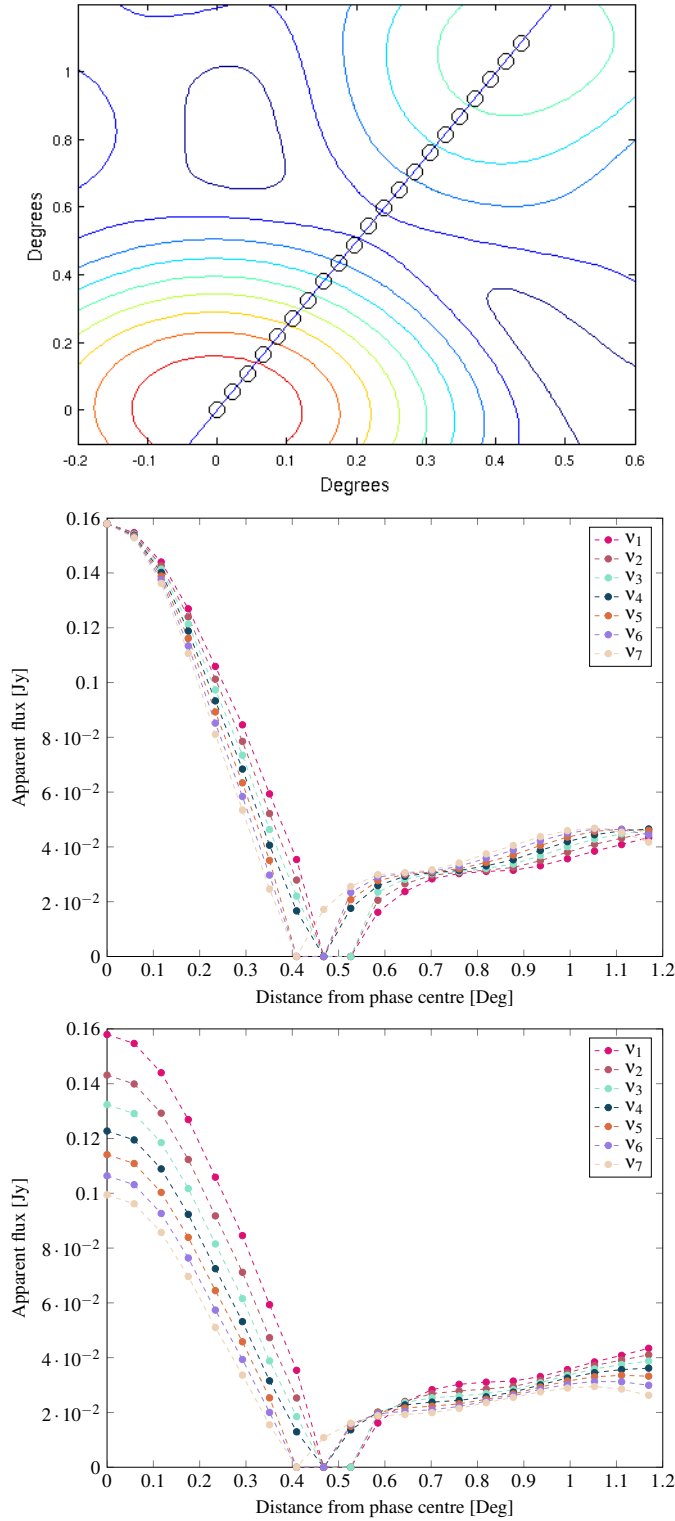


**Figure 2.3:** The apparent flux density variations with frequency at different distances from the phase center. (top) The apparent flux at 21 equally spaced locations (marked with circles) along a straight line is measured for seven different frequencies; (middle) The intrinsic  $S_v$  does not change with  $v$ ; (bottom) The intrinsic  $S_v$  changes with  $v$  according to Equation 2.5.

The middle panel in Figure 2.3, demonstrates the variations in the observed flux density  $S_\nu$ , when a detected source has a flat intrinsic spectrum. In this case, the observed flux density  $S_\nu$  does not change with  $\nu$ . This is best observed at the phase centre, where  $S_\nu$  stays constant at all  $\nu$ . The  $S_\nu$  starts to depart from the constant value at all  $\nu$  with increasing distance from the phase centre. The most pronounced changes can be seen for sources at the edge of the TAB. This is caused by the changing size of the beam shape with frequency  $\nu$ . For sources detected in a sidelobe, the changes in  $S_\nu$  reflects the change in sidelobe position relative to the TAB, i.e. sidelobes move closer to the TAB with increasing  $\nu$ .

In contrast, shown in the bottom panel in Figure 2.3 are sources for whom the intrinsic spectral index follow a power law. The observed variations in the values of  $S_\nu$  that intrinsically follow a power law dependency are much more visible due to the combined effects of the power-law spectrum and the TAB frequency dependent sensitivity. This can best be observed at the phase centre, where the  $S_\nu$  for the same source can vary drastically at the two furthest  $\nu$ . That trend continues throughout the TAB and only declines for sources detected in sidelobes. It is also interesting to note that the variations of  $S_\nu$  in sidelobes in both, the middle and the bottom panel, also differ.

As the observed  $S_\nu$  at different frequencies will give different values depending on the distance from the phase centre and on the intrinsic spectral index distribution, for both scenarios in Figure 2.3, that information can be used to locate a transient source as described in detail in §5.

## 2.2 Observing Strategies

Sensitivity is clearly of great importance for fast transient detection. A radio telescope measures radiation as units of flux density, i.e. the power per unit frequency interval that passes through a surface of unit area. This power can be compared with the thermal noise produced by a resistor at a given temperature. The output of a radio telescope randomly fluctuates about mean value determined by the total noise present in the system given as the radiometer equation, e.g. Lorimer et al. (2006):

$$\Delta T = \frac{k_B T_{\text{sys}}}{\sqrt{\tau \Delta \nu}}, \quad (2.6)$$

where  $T_{\text{sys}}$  is the system temperature (K),  $\tau$  is the integration time (s),  $k_B$  is the Boltzmann constant and  $\Delta\nu$  is the sampled bandwidth. Thus, a transient source is detected only if the power available from the source exceeds the output noise of the system. The sensitivity of the radio telescope is represented by the minimum detectable power flux density  $S_{\text{v,min}}$ :

$$S_{\text{v,min}} = K \frac{2k_B\beta T_{\text{sys}}}{A_{\text{eff}} \sqrt{N_p} \tau \Delta\nu} \quad (2.7)$$

where  $A_{\text{eff}}$  is the effective cross section of the antenna,  $N_p$  is the number of polarisations that can have a value of either 1 or 2,  $K$  is the detection threshold in units of rms flux density and  $\beta$  accounts for digitisation losses. To increase the sensitivity of a given telescope to short transients the obvious steps are to increase the gain, by either increasing the collecting area or improving the efficiency, the receiver bandwidth  $\Delta\nu$  and/or integration time  $\tau$ , unless it smears the pulse from the transient.

### 2.2.1 Single Dish Instruments

Traditionally, a single feed horn is placed at the antenna focus of a telescope and the beam is formed directly with physical optics. Survey observations are often done by performing a raster scan, i.e. by moving an antenna back and forth and hence imaging a small area of the sky at one time. This approach is very time consuming and when searching for transient events this type of observation is simply inadequate. Furthermore, the radio frequency interference (RFI) mitigation techniques used with single dish telescope might result in reduced observing efficiency and loss of data. For example, observing only at night, when the man made RFI is usually lower, stopping observing during bursts of radiation i.e. radar or cutting out the contaminated data during post-processing.

Such a single-pixel single-telescope system can be improved by an array of feed horns providing a multi-pixel (multi-beam) instrument, for example the Parkes multi-beam receiver, described below. This increases the survey speed by approximately the same factor as the number of pixels. The dish size also determines the angular resolution of a radio telescope and is a measure of how small details of an area in the sky can be seen. The angular resolution of a radio telescope is expressed as:

$$\theta_{3dB} = \text{const} \frac{\lambda}{l} \quad [\text{rad}] \quad (2.8)$$



where  $\lambda$  is the wavelength of incoming signal and  $l$  is the diameter of a dish. The value of *const* depends on the feed taper and typically has values between 1.15 and 1.25.

In radio astronomy, the location of a radio source has to be known, in general, to arcsecond accuracy to allow it to be observed reliably at different wavelengths across the EM-spectrum - especially to obtain a definitive optical identification. With today's techniques the location of a transient source can be known with an accuracy, roughly, of only within an area defined by the 3-dB beam-width  $\theta_{3dB}$  or a Half Power Beamwidth (HPBW). This contrasts sharply with the case of a continuously emitting source whose position can be found to  $\sim \text{HPBW}/\text{SNR}$ <sup>11</sup> by scanning the beam across the source. Even the biggest single dish radio telescope, the Five-hundred-meter Aperture Spherical radio Telescope (FAST) (Nan et al., 2011), currently being built in China, will achieve a HPBW of 2 arcminute. Hence, finding a transient position will be problematic. The two current leading telescopes for FRB searches are now briefly described.

### **The Arecibo Telescope**

In 2004 the Arecibo Telescope single-pixel receiver system was upgraded to a seven horn Arecibo L-band Feed Array (ALFA) receiver. The Arecibo Pulsar ALFA (PALFA) survey searches for pulsars and transients in the inner and outer Galactic plane regions started shortly after the installation of a new receiver (Deneva et al., 2009). Each horn of the receiver produces a beam with a HPBW of 3.5 arcminute. The seven horns are arranged into a hexagon and their combined HPBW is approximately  $24' \times 26'$ . The 100 MHz observing band, upgraded to  $\sim 300$  MHz recently, is centred at 1.4 GHz. Multi-channel (256) time series are recorded to disk every  $64 \mu\text{s}$  during an observation and decimated to 1 ms resolution. This allows a quick-look processing pipeline running in real time to search for periodic signals and single pulses. Millisecond pulsars and other short duration transients are searched for off-line in the full-resolution data.

### **The Parkes Telescope**

The Parkes telescope was upgraded to 13-feed receiver in 1996 with the principal aim to search for hydrogen from nearby galaxies and for pulsars in our Galaxy. The 13

---

<sup>11</sup>Signal to Noise ratio

feeds are arranged in a double hexagon pattern where the centre feed is surrounded by two rings of six feeds. The centre horn has a HPBW of 14 arcminute. The Parkes Multi-beam Pulsar Survey (PMPS) (Manchester et al., 2001) commenced in 1997 and discovered 600 pulsars in the first four years. The survey targeted a strip along the Galactic plane with  $|b| < 5^\circ$  and  $l = 260^\circ$  to  $l = 50^\circ$ . The 288 MHz band is centred at 1.374 GHz. This band, after down-conversion, is split into three equal parts which are then split into 96 3-MHz channels in a filter bank. In 2009 the Parkes telescope was equipped with a new digital back-end system, the Berkeley-Parkes-Swinburne Recorder (BPSR). This allowed recording of 400 MHz of bandwidth per beam. A new survey to scan the entire southern sky, the High Time Resolution Universe (HTRU) survey (Keith et al., 2010), was conducted using the new set-up. The BPSR spectrometer system is based on the IBOB<sup>12</sup> platform that samples the signal at 800 MHz with 8 bits per sample. The signal is then divided into 1024 channels of width 390 kHz. The time resolution is 64  $\mu$ s. The disk space is sufficient to record 3 days worth of data that is then written to magnetic tape.

### 2.2.2 Interferometers

A single-dish system cannot separate two radio sources if their separation is less than a HPBW beamwidth. The limiting factor  $l$  in the diffraction formula (Equation 2.8) was the original motivation for developing radio interferometry. The basic idea behind radio interferometry is to connect many radio dishes to form a large virtual radio telescope many times the collecting area and baseline resolution of the elemental dishes. The voltages from the array elements are combined together in various ways to provide the desired results. In radio astronomy two main types of radio interferometers are recognised based on the method of combining the appropriately delayed signals:

- multiplying interferometer;
- adding interferometer.

The main difference between the two is that the adding interferometer, or a *beam-former*, produces an instantaneous beam in the direction of interest, e.g. the blue and black beams in Figure 2.4. While the multiplying interferometer, called a *correlator*, produces correlation products, called *visibilities*, the Fourier components of the source brightness distribution from which an image over the entire FoV of a primary element can be computed, i.e the red beam in Figure 2.4.

---

<sup>12</sup>Internet Break-Out Board

### Adding Interferometers

An interferometer array can be generically viewed as a collection of individual sensors sampling the wave field at discrete spatial locations. A signal collected with a single radio dish represents the voltage generated in the receiver as a function of discrete instances of time sampled at a rate  $1/T$ , where  $T$  is the sampling time interval in samples per second. The same signal can be collected with multiple radio dishes separated by a sampling space interval  $d$ , Figure 2.5. Spatial sampling of a continuous signal with an array produces a sequence of temporal signals with the spatial sampling interval of  $d$ . Similarly to the sampling time rate of  $1/T$ , the array is sampling the signal at a rate of  $1/d$  samples per meter.

A time sampled signal is usually passed through a filter that effects the magnitude and phase in some desired way. In a filter, the signal is convolved with the filter impulse response  $h$ . The frequency response of this filter is described by:

$$H(e^{j\omega T}) = \sum_{n=0}^{N-1} h_n e^{-jn\omega T}, \quad (2.9)$$

where  $N$  is the length of the impulse response  $h$ . In an array, the excitation  $w$ , i.e. windowing function, and the geographic position of each element determines the array radiation pattern, called *the array factor AF*. The array factor can thus be compared to the frequency response  $H$  of a digital filter and the impulse response  $h$  to the array weighting<sup>13</sup> function  $w$ . For a linear array with  $N$  identical elements of regular spacings  $d$ , the array factor can be described as:

$$AF(u) = \sum_{n=0}^{N-1} w_n e^{-jn2\pi(u/\lambda)d}, \quad (2.10)$$

---

<sup>13</sup>In some sources also called tapering, apodization, windowing or shading.

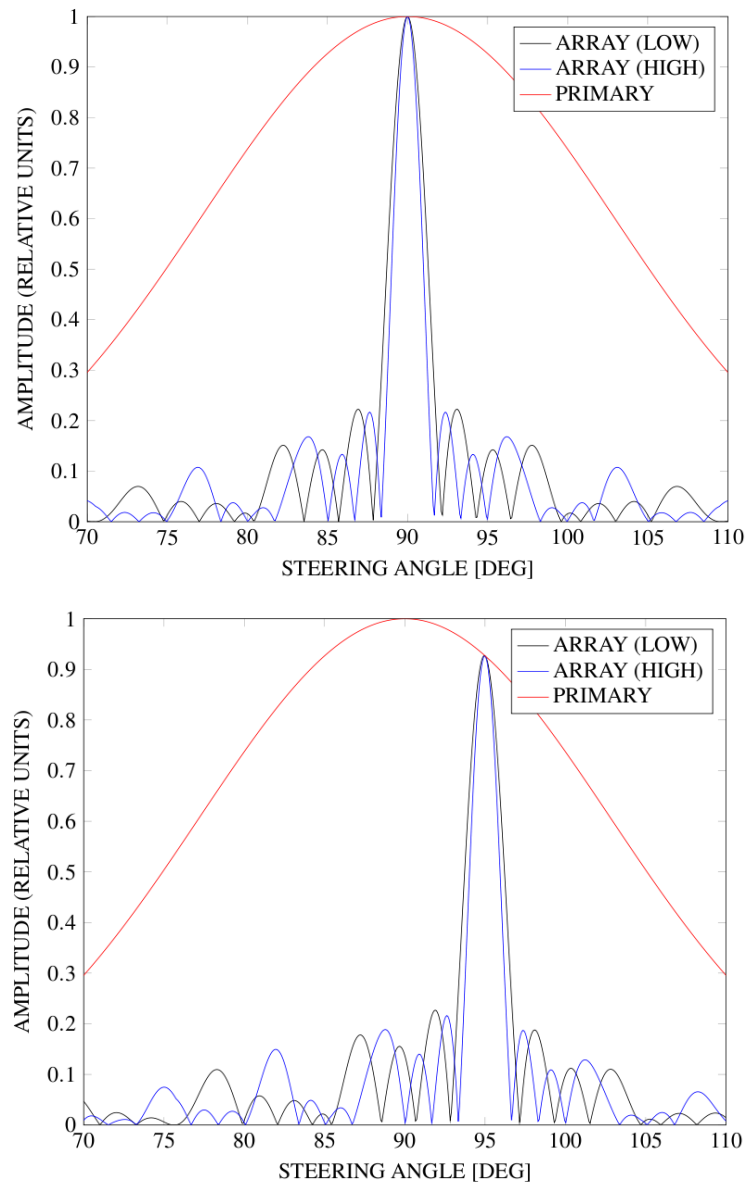


**Figure 2.4:** Illustration of the frequency-dependent gain pattern variations for an arbitrary array. The graph depicts a TAB, at the lowest frequency (black) and at the highest operational frequency (blue) and sidelobes. The primary beam is plotted only at the lowest frequency for clarity. (top) TAB pointed at the zenith. (bottom) TAB steered off the zenith.

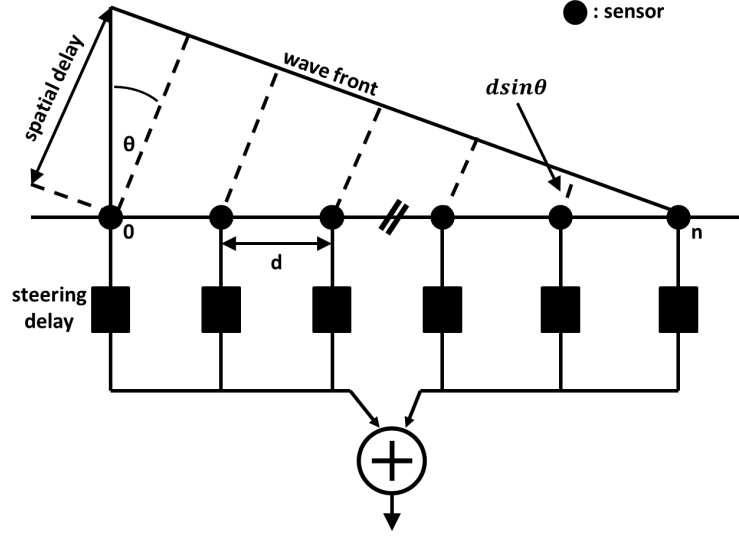


**Figure 2.5:** A linear array of antennas separated by distance  $d$ ;  $d \sin \theta$  represents a difference in travel-distance between neighboring elements in a linear array.

where  $\lambda$  is the signal wavelength and the variable  $u$  describes the direction of the incoming wavefront, described in a vector form as follows:

$$\mathbf{u} = \begin{bmatrix} \sin \theta \cos \phi \\ \sin \theta \sin \phi \\ \cos \theta \end{bmatrix} = \begin{bmatrix} u_x \\ u_y \\ u_z \end{bmatrix}, \quad (2.11)$$

where  $\theta$  and  $\phi$  are the azimuth and elevation angle respectively. For every direction other than the zenith, there will be a difference in travel-distance between neighboring elements in the array. For a linear array, this distance is equal to  $d \sin \theta$ . This can be converted to the inter-element phase shifts that have to be corrected for before the signals are processed further.

So far, it has been shown that the sampling time interval  $T$  is the corollary to the sampling space interval  $d$  and that the array weighing function  $w$  plays the same role in shaping the array response as the impulse response  $h$  in the digital filters. Another relationship can be found between the angular frequency  $\omega$  and the term  $2\pi(u/\lambda)$  in Equation 2.10, called *the wavenumber*  $k$ . For example, sampling in time introduces spectral copies in the frequency domain that repeat with a period equal to the sampling rate or at every integer multiple of sampling frequency  $f_s$ . Those copies are usually undesired components and the values of  $\omega T$  are restricted to the interval  $(-\pi \leq \omega T \leq \pi)$ ,

also called the Nyquist interval. In spatial sampling the same principles from the sampling theory apply, the spatial copies are called *the grating lobes*. If the grating lobes are not desirable, the sampling rate  $1/d$ , must satisfy the sampling theorem condition (Shannon, 1949):

$$\frac{1}{d} \geq \frac{2}{\lambda}. \quad (2.12)$$

Thus, the spacing between elements must be  $d \leq \lambda/2$  to avoid grating lobes and the values of  $kd$  are restricted to the interval  $(-\pi \leq kd \leq \pi)$ . The grating lobes are exploited in radio astronomy interferometry to achieve very fine spatial resolution, Figure 2.6.

Thus far, it has been assumed that all elements in the array are omnidirectional i.e. receive equal amount of energy from all directions. In reality, elements in the array have some directivity, called *the element factor*  $AF_e$ , that affects the array response. Hence the final array factor is a product of the element radiation pattern and the Discrete Fourier transform of the array geometry, sometimes in array theory called *the grating*  $AF_g$ :

$$AF = AF_e \times AF_g. \quad (2.13)$$

This process of multiplying the field patterns together is called *the pattern synthesis*. A thorough treatment of beamforming techniques is given in §4.

The above process of forming an output of an array by applying appropriate delays and weights to point the beam in the desired direction is also called *beamforming*. An adding interferometer incorporates this process as the coherent addition of signals maximises the detection sensitivity as the signal-to-noise ratio (SNR) is increased. The localisation capabilities of a single TAB are similar to a single dish, except it is narrower by a filling factor  $B/l$ , where  $B$  is the maximum baseline and  $l$  is the size of the primary element, Figure 2.6. The area of a TAB is smaller by a factor  $(B/l)^2$  therefore to achieve a similar FoV to a correlation interferometer i.e. FoV of a primary element, often hundreds to thousands of TABs have to be formed. The cost of the real-time signal processing of a multibeamforming beamformer can therefore be computationally expensive. Thus, only the elements contained in a smaller region of the array are used, often with a higher filling factor and sometimes referred to as the *core*. This leads to wider TABs but with reduced sensitivity. Optimising this combination, including the total number of TABs, one can form and subsequently process is an important aspect of time domain radio astronomy using interferometers (Janssen et al., 2009). But even

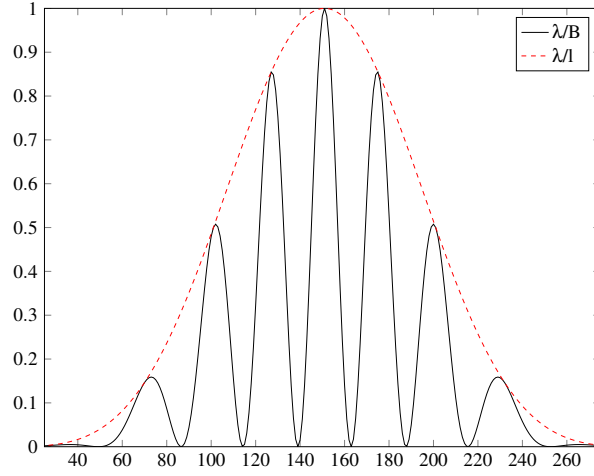


**Figure 2.6:** The pattern synthesis;  $B$  the maximum baseline;  $l$  is the size of the primary element.

with the addition of many sensitive TABs, without imaging and with only a single observation, a source position can only be approximated with the HPBW of a TAB if no other spatial information is collected. In the case of a strong source, it might even be detected in a sidelobe (Spitler et al., 2014). To overcome this limitation a new method that utilises the additional spectral and comparative spatial information from multiple TABs to estimate a source location with up to arcsecond accuracy in almost real time without imaging is presented in §5.

### Multiplying Interferometers

Multiplying interferometers combine data by cross-correlating between each pair of antennae in an array. Similarly to the adding interferometer, the signals have to be time aligned. The simplest form of a radio interferometer is a two-element system consisting of identical antennas. For an infinitely distant point radio source the time delay due to the late arrival of the wavefront at the second antenna, called the *geometric delay* is expressed in a form:

$$\tau_g = \mathbf{b} \cdot \hat{\mathbf{s}}/c, \quad (2.14)$$

where  $\mathbf{b}$  is the projected baseline i.e. a vector connecting reference points of two antennas,  $\hat{\mathbf{s}}$  is a unit vector in the apparent direction of the radio source and  $c$  is the speed of light. The projected baseline varies with time, due to the Earth's motion, and can be expressed as:

$$\mathbf{b}(t_1) = \mathbf{x}_2(t_1) - \mathbf{x}_1(t_1), \quad (2.15)$$

where  $\mathbf{x}_1$  and  $\mathbf{x}_2$  are locations of the two antennas and  $t_1$  is the time of arrival of the wave at the first antenna. The received voltages of the two antennas are denoted as  $V_1(t) = v_1 \cos(2\pi \mathbf{v} t)$  and  $V_2(t) = v_2 \cos(2\pi \mathbf{v}(t - \tau_g))$ , where  $\mathbf{v}$  is the mean frequency,  $v$  is the magnitude and subscripts 1 and 2 signify each antenna. The correlation processing involves the multiplication and integration (time averaging) of the signals. Thus, the cross-correlation of two voltages  $V_1(t)$  and  $V_2(t)$  is:

$$R_{V_1 V_2}(\tau) \equiv \langle V_1(t) V_2(t + \tau) \rangle, \quad (2.16)$$

where one is delayed by time  $\tau$ . In the cross-correlation the power received from the source is proportional to the effective antenna area  $A(\hat{\mathbf{s}})$  and the source flux  $S$ . We can write the cross-correlation  $R$  in the following form:

$$R_{V_1 V_2}(\tau_g) = A(\hat{\mathbf{s}}) S \cos(2\pi \mathbf{v} \cdot \mathbf{b} \cdot \hat{\mathbf{s}}/c). \quad (2.17)$$

The projected baseline vector  $\mathbf{b}$  can be measured in wavelengths  $\lambda$  to simplify the above equation, i.e.  $\mathbf{b}_\lambda = \mathbf{b}/\lambda$ . The cosine term expresses a sinusoidal interferometric *fringe pattern* on the sky that varies with the source direction. The cross-correlation function  $R_{V_1 V_2}(\tau)$  forms a Fourier transform pair with the cross-power spectrum density  $S_{V_1 V_2}(\mathbf{v})$ . The cross-power spectrum is given as the transform of  $V_1(t)$  and the complex conjugate of the transform of  $V_2(t)$ :

$$S_{V_1 V_2}(\mathbf{v}) \equiv X_1(\mathbf{v}) Y_2^*(\mathbf{v}). \quad (2.18)$$

The cross-power spectrum  $S_{V_1 V_2}(\mathbf{v})$  describes the interferometer output and, similarly to  $R_{V_1 V_2}(\tau)$ , can be expressed as:

$$S_{V_1 V_2}(\mathbf{v}) = A(\hat{\mathbf{s}}) S e^{(i2\pi \mathbf{v} \cdot \mathbf{b} \cdot \hat{\mathbf{s}}/c)}. \quad (2.19)$$

The voltage output of the antennas represent observed astronomical signals and are related to the brightness of the astronomical object  $I(\hat{\mathbf{s}})$  over a solid angle  $d\Omega$ . Thus, the observation contains information not only about a source but also from the solid angle denoted by  $d\Omega$ . For that reason we use a reference point known as the *phase tracking centre*  $\hat{\mathbf{s}}_0$  to distinguish the contributions coming from the offset directions  $\boldsymbol{\sigma}$  so that  $\hat{\mathbf{s}} = \hat{\mathbf{s}}_0 + \boldsymbol{\sigma}$ . The cross-power spectrum  $S_{V_1 V_2}(\mathbf{v})$  can be written in terms of the



direction vectors and  $\mathbf{b}_\lambda$ :

$$S_{V_1 V_2}(\hat{\mathbf{s}}_0) = \int A(\boldsymbol{\sigma}) I(\boldsymbol{\sigma}) e^{(i2\pi(\mathbf{b}_\lambda \cdot (\hat{\mathbf{s}}_0 + \boldsymbol{\sigma}) - \nu \tau_i))} d\Omega, \quad (2.20)$$

where  $\tau_i$  is the instrumental delay usually set to cancel the tracking centre delay. Now we define a function known as the *complex visibility* as follows:

$$\mathcal{V} = \int A(\boldsymbol{\sigma}) I(\boldsymbol{\sigma}) e^{(i2\pi \mathbf{b}_\lambda \boldsymbol{\sigma})} d\Omega. \quad (2.21)$$

The complex visibility describes a radiation energy incoming from a certain direction in the sky collected by a fringe pattern. Further, the visibility depends on the normalised projected baseline components  $u_\lambda$  and  $v_\lambda$ . Thus, the complex visibility is a two-dimensional Fourier transform of the source brightness distribution  $I_\nu$  at spatial frequencies corresponding to  $u_\lambda$  and  $v_\lambda$ . This Fourier transformation relation is called *van Cittert–Zernike Theorem*.

A 2D snapshot image of the sky, made with a correlation interferometer array, can provide a large FoV and an accurate localisation of many compact radio sources simultaneously. The slow transients can be observed using the techniques applied at optical wavelengths, like images synthesised from interferometric arrays. However since hundreds of measurements (baselines) may be acquired for the image the data are often integrated over times of a few seconds; the information about the sub-second variability in the sky is therefore lost. Fast imaging methods that integrate the data on time scales of less than one second have been shown (Law et al., 2011), or more recently, Law et al. (2014) demonstrated an interferometric imaging campaign tailored to searching for FRBs with 5 ms time resolution using the VLA. Still, the problem of data management and the high computational load remain. To determine location of a fast transient source using the non-imaging methods in the visibility domain, the channelisation has to be implemented as the signals have small duty cycle. Due to the reduced bandwidth the S/N of fringes will be also reduced. As the signals are dispersed, before averaging across channels to increase the S/N one needs to apply dedispersion. These effects limit the localisation capability using the fringe phase. Novel approaches to signal processing used for fast transient observations with interferometers include the 8gr8 mode (Janssen et al., 2009), V-FASTR (Wayth et al., 2011), Fly’s Eye (Siemion et al., 2012) and pulsar gating methods (Briskin et al., 2000; Roy & Bhattacharyya, 2013).

We note that the computational and data rates for different transient search methods are discussed in detail in papers such as Bannister & Cornwell (2011) and Law & Bower (2014). This limitation can be, to some extent, overcome with a transient buffer a storage facility allowing only data with a possible transient detection to be preserved for non-real-time analysis. However, to explore the transient phase space, it is necessary to search out to very high DMs, which places a demand on memory capacity to capture the fully dispersed transient event. As the dispersion grows with  $\nu^{-2}$  and the real DM is unknown, the transient buffer capacity requirements can be large, especially at low frequencies. There is also a significant delay between the detection and localisation for multi-wavelength identification of a transient source when the data are imaged. In short, the classical correlation approach to interferometry is not well suited to finding FRBs.

It is clear from this brief discussion that the classical correlation approach to astronomical interferometry is not well suited to *finding* FRBs. It is very useful for follow up after a trigger from another instrument.

## 2.3 Future of High-Time Resolution Radio Astronomy

How little we know about the dynamic radio sky is best illustrated in Figure 2.1. As can be seen, the plot is scarcely populated and two conclusions can be drawn from it. Either there are no sources present in that phase space or, quite the opposite, we just have not usefully explored it yet. The Square Kilometre Array (SKA) is the next generation giant radio telescope that will hopefully open up this parameter space. The SKA will be a coherently connected array, and at the time of writing is entering its final stages of the design process. Its main science goals mostly involve conducting very sensitive surveys over a wide FoV, with at least an order of magnitude improvement in sensitivity over a wide frequency range e.g. Dewdney et al. (2009). The SKA Precursors, described below, will form the base of the array and will be operational in 2016. The construction of the first stage of the SKA is expected to be complete by 2023. The SKA will eventually extend out to 3000 km with a combined aperture of one million square metres. The operational frequency band for the SKA, between 70 MHz ( $\lambda = 4.3$  m) and 15 GHz ( $\lambda = 2$  cm), will require multiple antenna technologies, to observe phenomena never seen before, particularly in the early Universe.

### 2.3.1 SKA Pathfinders

A pathfinder for the SKA can be defined as any new technology, any science case that tests or simulates observational capabilities and a scheduling/time allocation techniques scalable to the full SKA. The SKA pathfinders that are considered in this work will now be briefly described.

#### Low Frequency Array (LOFAR)

*The LOw-Frequency ARray* (LOFAR) is an interferometric array and the SKA Pathfinder constructed with the bulk of the collecting area in the Netherlands (van Haarlem et al., 2013) from thousands of low-cost and simple antennas operating in the 10 to 250 MHz frequency range. The core of LOFAR array, referred to as the Superterp, is a 320 m diameter island with 12 core stations, the top panel in Figure 2.7. The remainder of the collecting area consists of arms spreading from the core across Europe. The core stations are divided into the High Band Antenna (HBA) for the 120 to 240 MHz frequency range and Low Band Antenna (LBA) stations for the 10 to 80 MHz frequency range. Each station is equipped for initial processing by means of an *analog to digital converter* (ADC), filtering, frequency selection and combination of signals. All of the digital signal processing (DSP) is carried out on *field programmable gate arrays* (FPGAs) at the station level. In §5, the LOFAR Tied-Array All-Sky Survey (LOTAAS) (Coenen et al., 2014) specifications such as frequency range and number of participating stations, is used for the simulation purposes. LOTAAS is a pulsar and fast transient survey for the LOFAR array that operates in the 119 – 150 MHz range. Its main goal is to study the sky for pulsars and radio transients like FRBs.

#### Long Wavelength Array (LWA)

*The Long Wavelength Array* (LWA) is an aperture synthesis imaging array under development in New Mexico (Ellingson et al., 2009). LWA will operate in the 10 to 88 MHz frequency band with 53 stations distributed over a region of 400 km. A first station of LWA, called LWA1 (Ellingson et al., 2013), was completed in 2011. It consists of 260 pairs of wire-grid "bowtie" antennas, where 256 form the central core plus outriggers of five pairs. The area covered by the core is about a 100 m by 100 m ellipse.

For the LWA1, four independently-steerable beams are formed with time-delays using delay-and-sum beamforming architecture run on FPGA boards equipped with

Virtex-5 chips. The delays are applied in two stages, first an integer number of samples, representing a coarse delay, are applied using a first-in-first-out (FIFO) buffer. A 28-tap FIR filter is then used to implement a fractional sample delay<sup>14</sup>.

### 2.3.2 SKA Precursors

SKA precursors are located at the future SKA sites in the Karoo in South Africa's Northern Cape and the Murchison Shire of the mid-west of Western Australia. Both sites have been chosen due to the low population density and hence very low man made RFI. At present there are three arrays with an official SKA Precursor title, namely the MeerKAT, ASKAP and MWA that will now be briefly described.

#### The Karoo Array Telescope (MeerKAT)

*The Karoo Array Telescope*<sup>15</sup> (MeerKAT) is being built in South Africa's Northern Cape region, the first antenna was erected in March 2014, and will be the most sensitive radio telescope at centimetre wavelengths in the Southern Hemisphere. MeerKAT will consist of 64 dishes with wide-band single pixel feeds. Each dish has a 13.5 m diameter main reflector and a 3.8 m sub-reflector. The core will consist of 48 elements into an area of a diameter of 1 km, the bottom panel in Figure 2.7. The remaining dishes will be distributed out to a maximum baseline of 8 km, the middle panel in Figure 2.7 (Booth et al., 2009; Booth & Jonas, 2012). The array will operate in the range between 580 MHz and 14.5 GHz achieving a synthesised HPBW of 6 arcsecond at 1.42 GHz and ten times smaller at 14.5 GHz. The MeerKAT dishes will house several receivers that will operate simultaneously. The down conversion step with the intermediate frequency will be avoided and signals would be digitised after the LNA stage.

#### Australian SKA Pathfinder (ASKAP)

*The Australian SKA Pathfinder* (ASKAP) is a synthesis radio-telescope located at the Murchison Radio Astronomy Observatory in Western Australia. The full array will consist of 36 dishes, 12 meters in diameter, with a maximum baseline of 6 km. Each ASKAP dish is equipped with a *Phased Array Feed* (PAF) to increase survey speed. PAFs consist of densely packed small elemental antennas that can synthesise multiple

---

<sup>14</sup>Fractional sample represent a time delay that is a fraction of the ADC output sample. A complete explanation is given in §4

<sup>15</sup>The KAT-7 array is the seven-dish precursor array for the MeerKAT array. The addition of *meer* word translates as *more* in the English language.

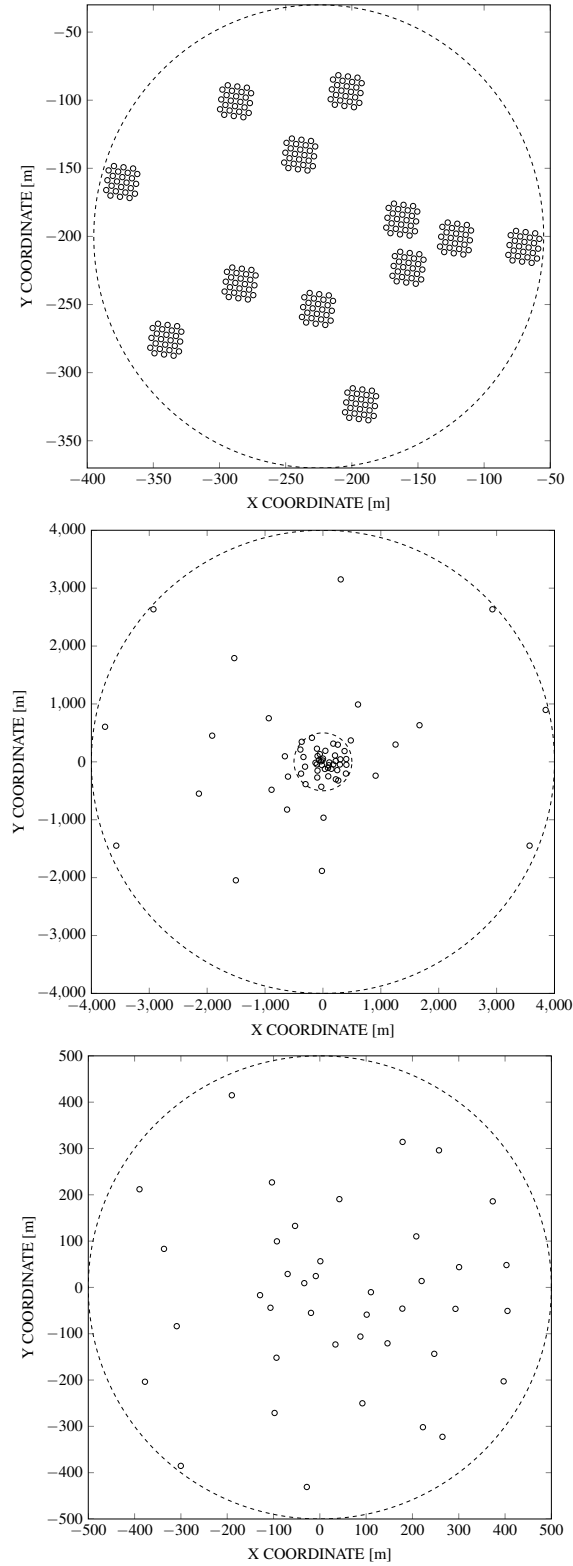


**Figure 2.7:** The LOFAR Superterp and MeerKAT array configurations used in the simulations presented in Section §5. (top) The LOFAR Superterp: shown with 12 HBA stations with 24 tiles (van Haarlem et al., 2013). (middle) The MeerKAT array. (bottom) The MeerKAT array core: the dashed circle represents the inner core of the array with 60% of the dishes (Booth et al., 2009).

simultaneous and overlapping beams to sufficiently cover the FoV while maintaining the angular resolution. ASKAP PAFs, connected-chequerboard arrays printed on a dielectric printed circuit board (PCB), are designed to operate from 700 MHz to 1.8 GHz. Each chequerboard arrays consists of 94 dual polarised conducting patches with the FoV of 30 square degrees.

A coarse filter bank that splits each digitised signal into 304 channels, 1 MHz wide, is oversampled by a factor of  $32/27$  (1.185). The beamformer combines channelised signals from all 94 PAFs into a maximum of 36 beams.

### **Murchison Widefield Array (MWA)**

The *Murchison Widefield Array* (MWA) is located at the Murchison Radio Astronomy Observatory in Western Australia (Tingay et al., 2013). MWA is a complementary array to ASKAP. MWA is an aperture array that consists of 128 tiles. Each tile holds 16 dual polarisation active antennas positioned on a rectangular grid. The array core combines about 25% of tiles in a densely packed region, 100 m in diameter. The remaining tiles have a smooth distribution out to 1.5 km in diameter. In addition, 16 tiles are located in an outer ring of 3 km in diameter.

The signals at a tile level are combined in an analog beamformer for each polarisation, giving 32 beamformers per tile. Each beamformer has an independent delay switch providing a discrete delay between 0 and 13.5 ns in discrete steps of 435 pico seconds. All 128 beams from all tiles can be steered independently up to  $30^\circ$  elevation. After the analog beamformer, signals are digitised, filtered and down converted before being passed to a correlator. The correlator main task is to spectral filter the data using the polyphase filter bank board (PFB), yielding a spectral resolution of 10 kHz, and to cross-multiply it using the correlator board (CBD). Both boards are different FPGA boards. The MWA correlator does not employ fringe stopping in its architecture as due to long wavelengths and small array extent, the phase difference between small data segments is negligible.

## Chapter 3

# The Manchester University Student Telescope

Having showed in the previous chapter that high time resolution radio astronomy can benefit from the development of interferometric arrays with multibeaming capabilities, the following chapter outlines the design process of the Manchester University Student Telescope (MUST) array. The medium-term goal of the MUST project is to design and construct an innovative radio telescope array on the Jodrell Bank Observatory (JBO) site to carry out world-leading science. Fortunately, recent hardware and software advances now enable the development of a high resolution and low frequency instrument that can be constructed from "off the shelf components" (COTS). During the period of this thesis the first phase of MUST was completed. This chapter describes the design and commissioning of a wide-field instrument to aid the exploration of the transient sky.

### 3.1 Introduction

The MUST programme, led by Prof. Peter Wilkinson, is a new incarnation of the Software and Multi-Beam Array (SAMBA) conceived by Prof. A. Lyne, Prof. M. Kramer and Prof. P. Wilkinson in 2003. SAMBA was aimed at being a part of the UK contribution to the SKA development. The goal of SAMBA was to develop a low-cost, low-maintenance instrument that could generate hundreds of independent beams which could train the next generation of radio astronomers in the areas of pulsar research with interferometer arrays to:

- Monitor the transient sky,

- Measure arrival times and flux densities of all pulsars in a  $10^\circ$  declination strip each day,
- Perform coherent de-dispersion on many pulsars simultaneously,
- Study pulsar astrophysics,
- Searches for extra-terrestrial intelligence (SETI) signals,
- Have an educational and "citizen science" role.

With a proposed collecting area of  $3600\text{m}^2$  SAMBA's multi-beaming concept would have been equivalent to many Lovell-class telescopes operating simultaneously. The design motivation for SAMBA was to investigate what can be observed with the cheapest RF arrangement per unit area. The initial centre frequency suggested for SAMBA was 600 MHz due to:

- extensive experience with the Crab pulsar observations with a 42 foot telescope and to complement the Lovell telescope;
- ready availability of low-cost components from the broadcast TV industry.

The initial cost estimates for a prototype array were higher than anticipated. The project was therefore sidelined until extra funds became available or the costs came down. In 2010 the basic design concept for SAMBA was revisited by Prof. Wilkinson in response to a perceived need for a scientific instrument at JBO to add to student training opportunities in the first instance. In addition, the digital TV switch over, starting in 2008 in the UK, offered a potential for a broader frequency band around 600 MHz than used in the 42 foot telescope system. The project was renamed, MUST, and officially re-started in 2011 with University funding.

An integral feature of the MUST concept is the engagement of a wide range of MSc, PhD, undergraduate and visiting students across the Schools in the Engineering and Physical Sciences Faculty in all aspects of the design, build and data analysis. Over the course of three years the MUST mechanical design concept had two iterations. The original design consisted of four *frame arrays* (FA), each measuring 6.7 m by 3 m, with approximately 60 Yagi antennas, see the top panel in Figure 3.1. The physical (not electrical) area of these four FAs would have been  $\sim 80\text{m}^2$ . The exact number of Yagis was not determined at this stage as the optimum spacing between the elements had to be investigated for the intended dual-polarisation layout. Each FA was intended to be electrically divided into two tiles each with  $\sim 30$  Yagi antennas, split between the two polarisations. The completed initial MUST FA and mounts can be seen in the bottom panel in Figure 3.1, erected on the roof of the Pariser building on



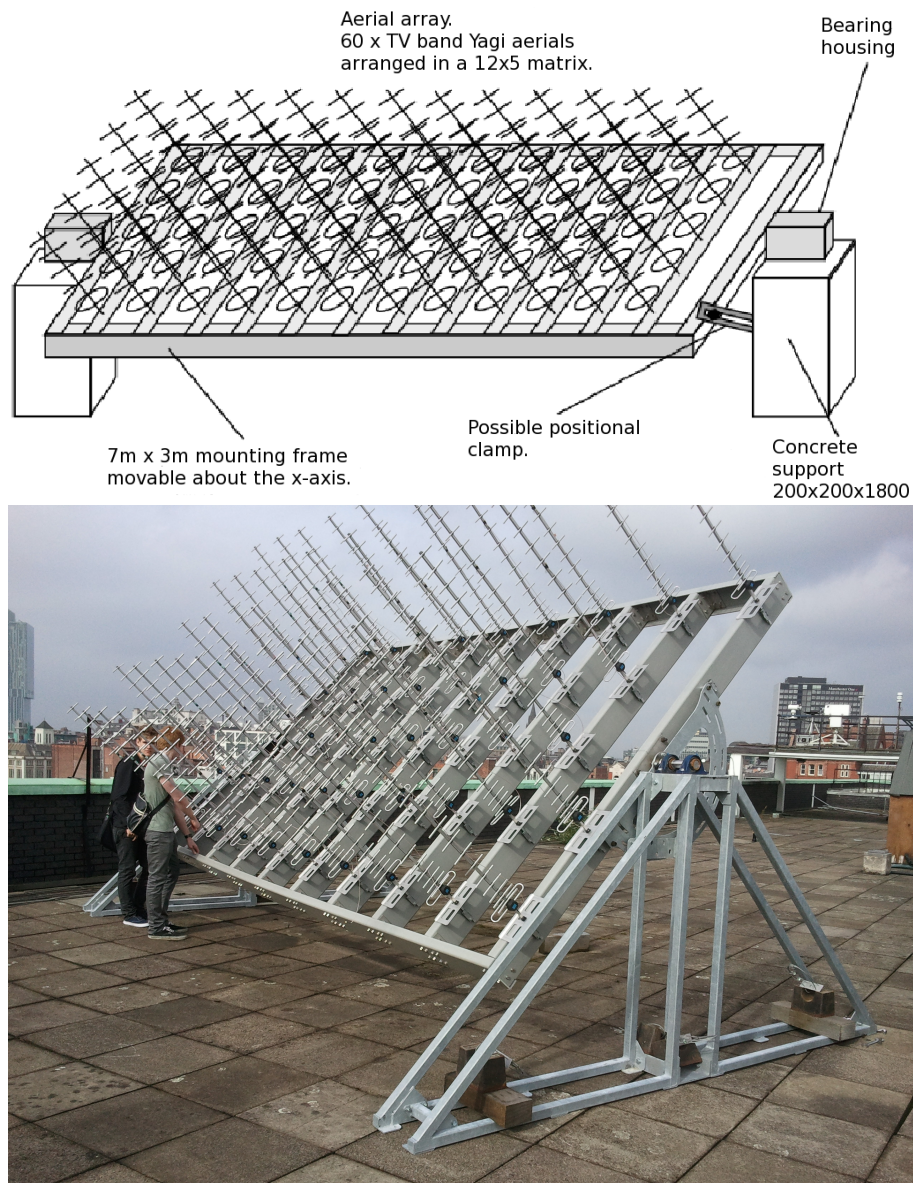


**Figure 3.1:** A MUST array original frame concept, the top panel, courtesy of J. Methven. The frames are largely constructed from GRP C-sections; (bottom) the first frame on a roof of the Pariser Building in October 2013, courtesy of Prof. P. Wilkinson. As seen in this picture, the mounts have changed in to steel A-frames, designed by Mr Bob Wray in the School of Civil Engineering.

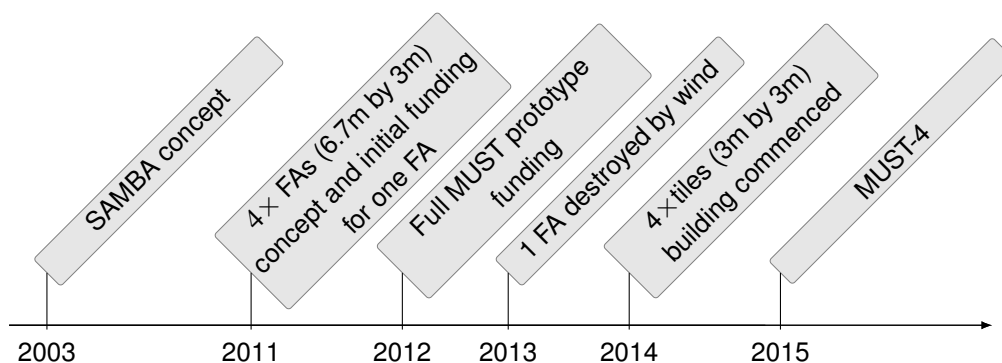


**Figure 3.2:** The MUST array chronology. In parallel the digital back-end being developed by the author.

the Manchester north campus. The reason for building the first FA in a (radio) noisy central Manchester was to give better access for the Civil and Mechanical Engineering staff for the mechanical testing purposes. Unfortunately the frame proved not robust enough and in a strong wind in October 2013 it twisted and split. The design response was to divide the FA into two 3 m by 3 m tiles and add straightening pieces near the mounting points. Due to a lack of available funds for an extra sets of mounts, the collecting area of the array had to be halved. Thus, instead of building four FAs, four individual *tiles* were erected at the JBO site, the bottom panel in Figure 3.11. The chronology of the MUST project is depicted in Figure 3.2.

The commissioning will be divided into two phases. Phase one involved building four tiles with a physical collecting area of  $\sim 36\text{m}^2$ . This configuration is referred to as the MUST-4 array throughout this work. In the second phase, it is envisaged that four more tiles will be added to achieve roughly the same collecting area as the original concept envisaged for the FAs; this is referred to as the MUST-8 array but currently awaits additional funding.

### 3.1.1 Scientific justification

The Jodrell Bank Observatory has been at the forefront of radio astronomy-related research almost since the field of radio astronomy came into existence. Like every science organisation, it needs new facilities to explore emerging phenomena in the ever expanding study of the radio universe and to provide learning opportunities for new generations of graduate students. The MUST array should prove to be an excellent investment when one considers the science that will potentially be returned once it

is fully realised. As already discussed in §2.1, the exploration of the transient sky has been slow due to a lack of wide field instruments and the demanding signal processing. Thus the potential for new discoveries is enormous and all new radio arrays designed for observations at meter wavelengths, either being commissioned or operational, are likely to be oversubscribed. An opportunity to host a low-cost phased array at the Jodrell Bank site will give researchers and students opportunities in the exploration of this new and exciting field.

Before the final stage of the MUST-4 array commissioning is completed, the existing tiles will be used to investigate the Peryton phenomenon, §2.1.2. The first Perytons observed at a different geographical location than the Parkes telescope were recently reported by Saint-Hilaire et al. (2014) at the Bleien Observatory in Switzerland. The observations were made around  $\sim 20$  cm wavelength with a single commercially available log-periodic dipole, later replaced by a 1 m diameter horn antenna. As even a single MUST tile has larger collecting area than these antennas and so with a similar 24 h observation time, the MUST telescope can contribute significantly to transient phenomenology by looking for new peryton events at a lower frequency and in a different location.

## 3.2 Array Design

As with all projects, the MUST array is constrained by a budget in its implementation. Thus, a robust antenna element and cost effective receiver system is of much importance. This places various constraints on the system design that has to achieve high performance at a low cost. The following section describes the array parameters that are largely dictated by the science goals and design choices that were dictated by the budget.

To utilise the available low-cost commercial component, the preferred frequency band is based on the UK TV band between 470 MHz and 854 MHz. The initial RFI tests pointed to a commercially unused band between 565 MHz and 620 MHz, see Figure 3.3, allowing for a bandwidth of 50 MHz. However, this band has subsequently had to be modified because of the developments of new sources of RFI, see §3.3.

To achieve a significant collecting area at low cost, the telescope frame should

be built with a lightweight, low maintenance material that can be produced in large numbers. As many people participated in the design process, the material had to be flexible enough to accommodate minor changes to the frame. A glass reinforced plastic material (GRP) was chosen and a full analysis can be found in the MSc thesis of Gokhale, S. D. (2011) from the school of Mechanical Engineering and supervised by Dr J. Methven. GRP is a robust, lightweight and strong material that can be formed using an extrusion-like process<sup>1</sup>. The GRP structure used for the frame is also electrically neutral, in contrast to a metal frame, and hence does not alter the performance of the Yagi array.

Typical sources in radio astronomy emit very weak, noise-like signals that require large amounts of collecting area coupled with the most sensitive receivers. There are two back-end systems designed for the MUST array. The first is the analog back-end for MUST-1, a single tile configuration, which is based on a heterodyne architecture, described in Chapter §3.4. The second, is the digital back-end, described in §4 and built entirely on CASPER/ROACH FPGA board for the MUST-4, and scalable to MUST-8. It directly samples the RF signal and employs sub-sampling techniques described later in this chapter and in Chapter §4.

### 3.3 Radio Frequency Interference Challenges

Radio frequency interference (RFI) is one of the biggest challenges radio astronomers and engineers face today. As the JBO site is located in a moderately populated area, interfering radio emission is common. The main operational mode of the MUST array is an adding interferometer; consequently we can not utilise the signal processing techniques used in aperture synthesis to suppress RFI. However, our main observing targets are pulsars and other transient sources, we can take advantage of the fact that terrestrial RFI has a DM close to zero. As discussed in §2.1.1, a signal travelling through space passes through electrons in the interstellar medium and when observed on the Earth propagation effects are noticeable. A signal that originates close to, or on the Earth, does not encounter too many electrons and its DM is close to zero. Thus, we can use a filter that removes the zero-DM signals. Other mitigation techniques, like shaping the beam by different antenna weights and hence placing nulls in the antenna pattern

---

<sup>1</sup>Material supplied specified section lengths by Excel Composites, Runcorn

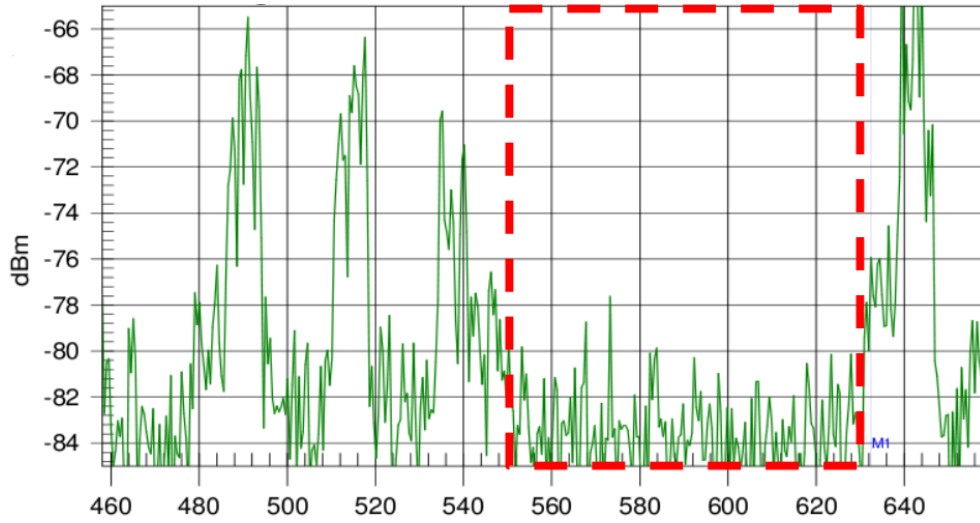


**Figure 3.3:** RFI at the Jodrell Bank site. Scan conducted on 11 November 2011 showing the frequency band between 550 and 630 MHz (dashed red line) to be relatively free of RFI.

to suppress RFI coming from a particular angle, can be explored further when the full array is operational. The main mitigation strategy is of course to choose a frequency band that is relatively free from strong interference and this method is investigated next.

The measurement system in the initial RFI scans, conducted in November 2011, consisted of an omnidirectional antenna and Anritsu S332D spectrum analyser. The antenna has a vertical sensitivity null, i.e. zenith of the antenna, as most strong RFI will be received from the sides from terrestrial transmitters. The measurements were conducted on the JBO field, where the MUST array was to be located, Figure 3.13. The initial RFI scans were short measurements, i.e. less than 15 minutes, designed to give a first order estimate of the RFI environment. The results of the November 2011 scans suggested that a bandwidth of 50 MHz centred at 590 MHz is RFI free, as is seen in Figure 3.3. Based on this result the specification for a bandpass filter was devised. A custom bandpass filter to this specification was then manufactured by Phase2Microwave Ltd<sup>2</sup> with a generous bandwidth of 56 MHz. A specification for the original bandpass filter  $H_{WB}$ , in terms of the lower  $T_{\omega_L}$  and the upper  $T_{\omega_H}$  width of the pass-band, is listed in Table 3.1.

A further, more detailed, one hour long scan was conducted in August 2012. The signal chain was similar to the scan from 2011 but with an inclusion of the bandpass

<sup>2</sup><http://www.phase2mw.co.uk/>

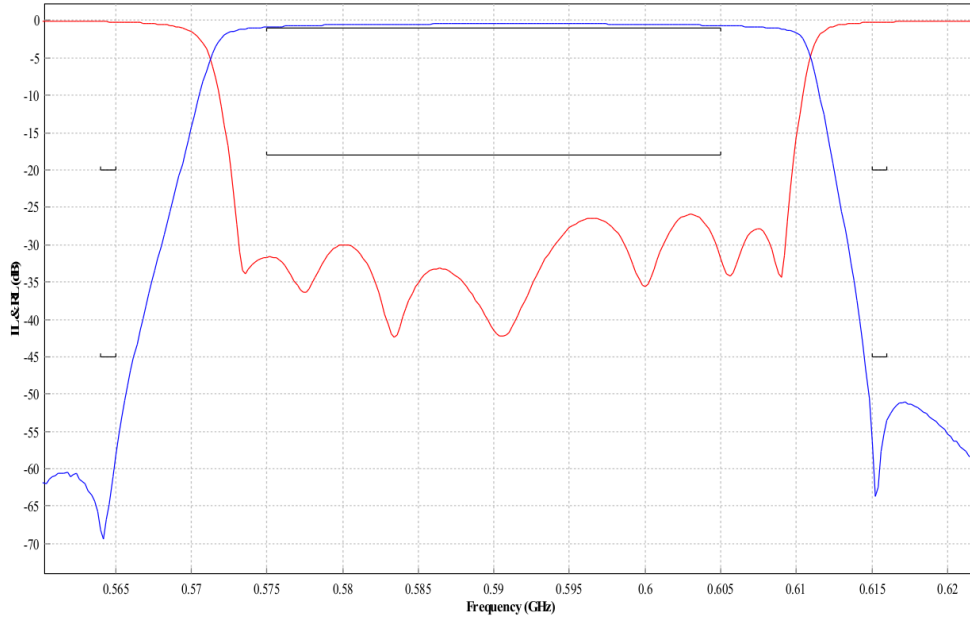


**Figure 3.4:** Graphical representation of the MUST bandpass filter for 33 MHz bandwidth. Courtesy of Phase2Microwave.

**Table 3.1:** MUST bandpass filter specifications for 56 MHz bandwidth  $H_{WB}$  and 33 MHz bandwidth  $H_{NB}$ ; the width of the lower transition band  $T_{\omega_L} = \omega_{L,\text{pass}} - \omega_{L,\text{stop}}$ ; the width of the upper transition band  $T_{\omega_H} = \omega_{H,\text{stop}} - \omega_{H,\text{pass}}$ , where  $\omega$  signify a cut-off frequency.

|                          | $H_{WB}$ [MHz] | $H_{NB}$ [MHz] |
|--------------------------|----------------|----------------|
| $\omega_{L,\text{stop}}$ | 554            | 565            |
| $\omega_{L,\text{pass}}$ | 564            | 575            |
| $\omega_{H,\text{stop}}$ | 630            | 618            |
| $\omega_{H,\text{pass}}$ | 620            | 608            |

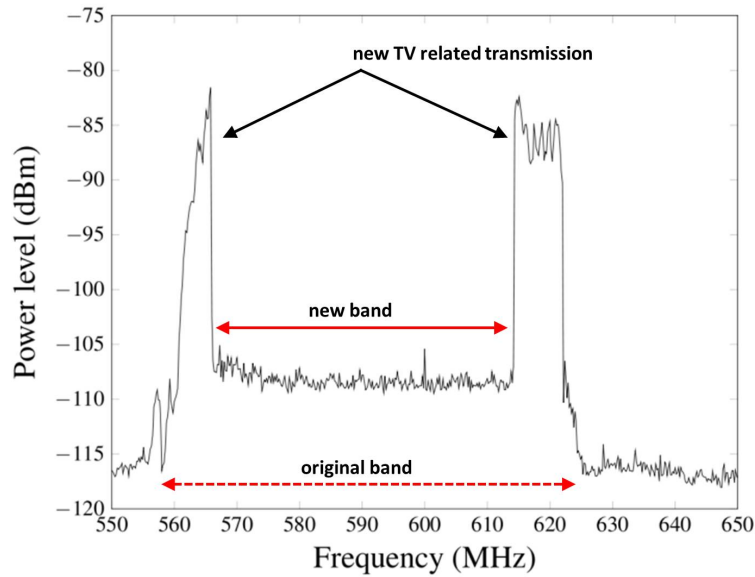


**Figure 3.5:** RFI scans at the Jodrell Bank site from 18 August 2014.

filter between the antenna and spectrum analyser. The second RFI scan helped to determine the required ADC dynamic range described in detail in §3.5.2. It also verified the bandpass filter performance and its ability to suppress the strong interference at the edges of the band below 560 MHz and above 620 MHz as in Figure 3.3.

A third RFI scan was conducted on the 18 August 2014 but this showed an unexpected appearance of new TV signals at the edges of the previously clear band, see Figure 3.5. Fortunately, a significant ( $\sim 35$  MHz) band could be used by re-engineering the bandpass filter to a narrower band. This work has also been carried out by Phase2Microwave. The appearance of the new TV signals adds an extra cost, and significant delay, to the project as retuning the filters down to 60% of the original band was non-trivial and was a significant fraction of their original cost. A new specification is shown in Table 3.1 under a symbol  $H_{NB}$  and plotted in Figure 3.4.

The current frequency spectrum allocations that potentially overlap the MUST band are presented in Table 3.2. Even though there is a radar and TV broadcast transmission present in the band, there are no strong transmitters in the vicinity of the array and its operation in the reduced 35 MHz band is currently not impaired, particularly when the antennas are pointed due South. It is however difficult to predict how the

<sup>3</sup><http://www.ofcom.org.uk/>

**Table 3.2:** The UK frequency allocation in the MUST frequency band. Source Ofcom<sup>3</sup> as of 28 of August 2014.

| Frequency         | Sector       | Product name  |
|-------------------|--------------|---|
| 606.6 - 606.8 MHz | PMSE         | Audio Distribution System                           |
| 590 - 598 MHz     | Aeronautical | Aeronautical Radar                                  |
| 470 - 606 MHz     | Broadcasting | Terrestrial TV Broadcast Transmission (UHF Digital) |
| 614 - 790 MHz     | Broadcasting | Terrestrial TV Broadcast Transmission (UHF Digital) |
| 470 - 606 MHz     | PMSE         | Audio Distribution System                           |
| 590 - 598 MHz     | Aeronautical | Aeronautical Radar                                  |
| 614 - 790 MHz     | PMSE         | Audio Distribution System                           |
| 470 - 606 MHz     | PMSE         | Programme Making and Special Events (Fixed Site)    |
| 470 - 606 MHz     | PMSE         | Programme Making and Special Events (Link)          |
| 470 - 606 MHz     | PMSE         | Programme Making and Special Events (Low Power)     |
| 606 - 614 MHz     | PMSE         | UK Wireless Microphone (Annual)                     |
| 606 - 614 MHz     | PMSE         | UK Wireless Microphone (Biennial)                   |
| 606.6 - 606.8 MHz | PMSE         | Audio Distribution System                           |
| 606.6 - 606.8 MHz | PMSE         | Programme Making and Special Events (Fixed Site)    |
| 606.6 - 606.8 MHz | PMSE         | Programme Making and Special Events (Link)          |
| 606.6 - 606.8 MHz | PMSE         | Programme Making and Special Events (Low Power)     |
| 606.9 - 607.1 MHz | PMSE         | Audio Distribution System                           |
| 606.9 - 607.1 MHz | PMSE         | Programme Making and Special Events (Fixed Site)    |
| 606.9 - 607.1 MHz | PMSE         | Programme Making and Special Events (Link)          |
| 606.9 - 607.1 MHz | PMSE         | Programme Making and Special Events (Low Power)     |

\*Programme making and special events (PMSE) - primarily providing time limited access to spectrum for the use by wireless cameras and microphones, and other PMSE applications.

MUST band will be used in the future as new RFI may appear with the implementation of new technology and new commercial requirements. Generally, the radio frequency spectrum utilisation by communications and navigation systems will increase. Therefore the band should be regularly checked for any new time-frequency distribution of RFI and its variations with the time of the day.

After successful mechanical tests of the tiles on the JBO site in the spring of 2014, one tile was phased up to conduct an electrical test. The results are shown in Figure 3.6 for an RFI scan done with the array without a bandpass filter, the top panel, with the original wideband bandpass filter  $H_{WB}$ , the middle panel, and with the re-tuned narrowband bandpass filter  $H_{NB}$ , the bottom panel.



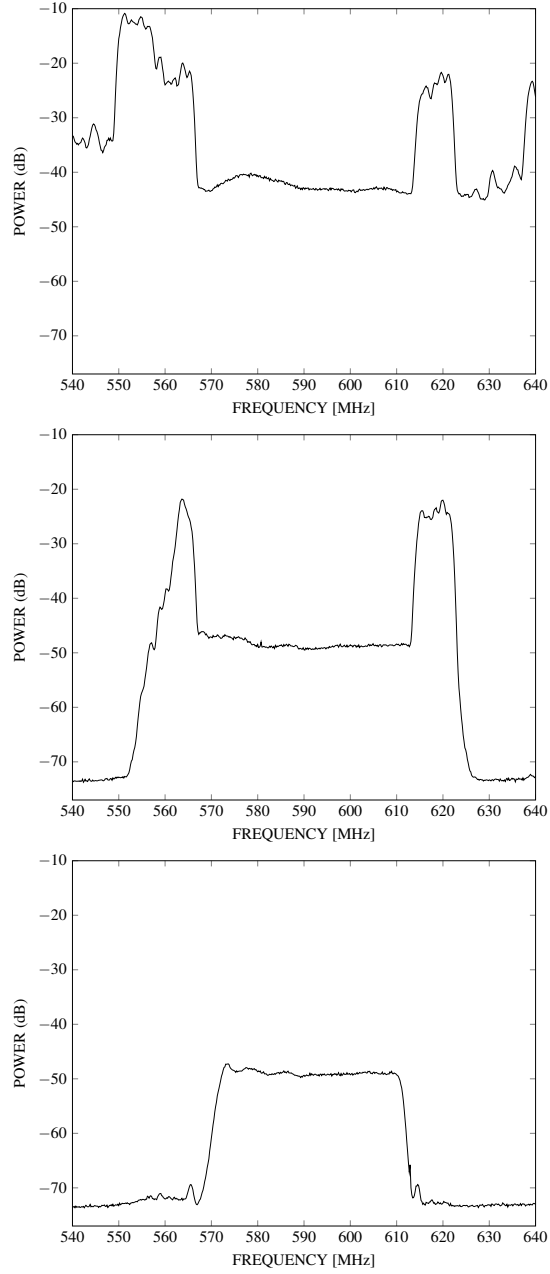


**Figure 3.6:** RFI spectrum from a single MUST tile; scans conducted in November 2014. (top) Spectrum measurements from a scan without a bandpass filter; (middle) Scan with  $H_{WB}$  filter (BW = 56 MHz); (bottom) Scan with  $H_{NB}$  filter (BW = 35 MHz).

### 3.4 The MUST-1 Receiver

MUST-1 is essentially a single element MUST tile. In order to test this and the other tiles individually a separate receiver, adapted from the 42 foot telescope back-end at JBO, was constructed. The 42-foot telescope regularly observes about 20 pulsars at  $\sim 600$  MHz, thus this MUST-1 back-end was aimed at being a field tested set-up that would allow for an easy performance comparison between different tiles in the array. Moreover, observations can be done concurrently with the 42-foot telescope and the MUST-1, to analyse and inspect collected data simultaneously. Thus, the MUST-1 receiver was designed as a test-bed/calibration facility and potentially to monitor RFI for the array as a whole in a “sniffer” mode simultaneously with the MUST-4 array operation.

#### 3.4.1 Architecture

The MUST-1 heterodyne receiver converts, amplifies and bandpass filters the RF signals of frequency  $\nu_{RF}$  MHz to a lower intermediate frequency (IF)  $\nu_{IF}$ . In the heterodyne receiver, the RF signal is mixed with a *local oscillator* (LO) frequency  $\nu_{LO}$  creating two new signals, the sum  $(\nu_{RF} + \nu_{LO})$  and the difference  $(\nu_{RF} - \nu_{LO})$ . The difference signal represents the lower intermediate frequency and is usually kept for further processing, while the sum is discarded. Thus, the intermediate frequency is equal to  $\nu_{IF} = (\nu_{RF} - \nu_{LO})$ . This completes the first stage of down-conversion (RF to IF). The first down-conversion stage is depicted as the blue box on the left side in Figure 3.7 and more details regarding the actual components used in the MUST-1 heterodyne receiver are given in Figure 3.8.

In the second stage, right hand box in Figure 3.7, this intermediate signal  $\nu_{IF}$ , centred at a frequency  $\nu_c$  with a bandwidth  $BW$ , is converted to a baseband signal. The signal is effectively shifted down in frequency so that it is now centred about zero Hz, i.e. the frequencies of the IF and the second LO signals are equal. The down-conversion to baseband requires both *in-phase* (I) and *quadrature* (Q) components of the signal to achieve maximum information, as one part of the signal now resides on the negative frequency half-axis. This process is called the *quadrature conversion* and is depicted in the purple box on the right side in Figure 3.7. First, the signal is split into two channels and down-converted with the second LO signal, which has a phase shift of  $90^\circ$  with respect to another. The advantage of the *quadrature conversion* is

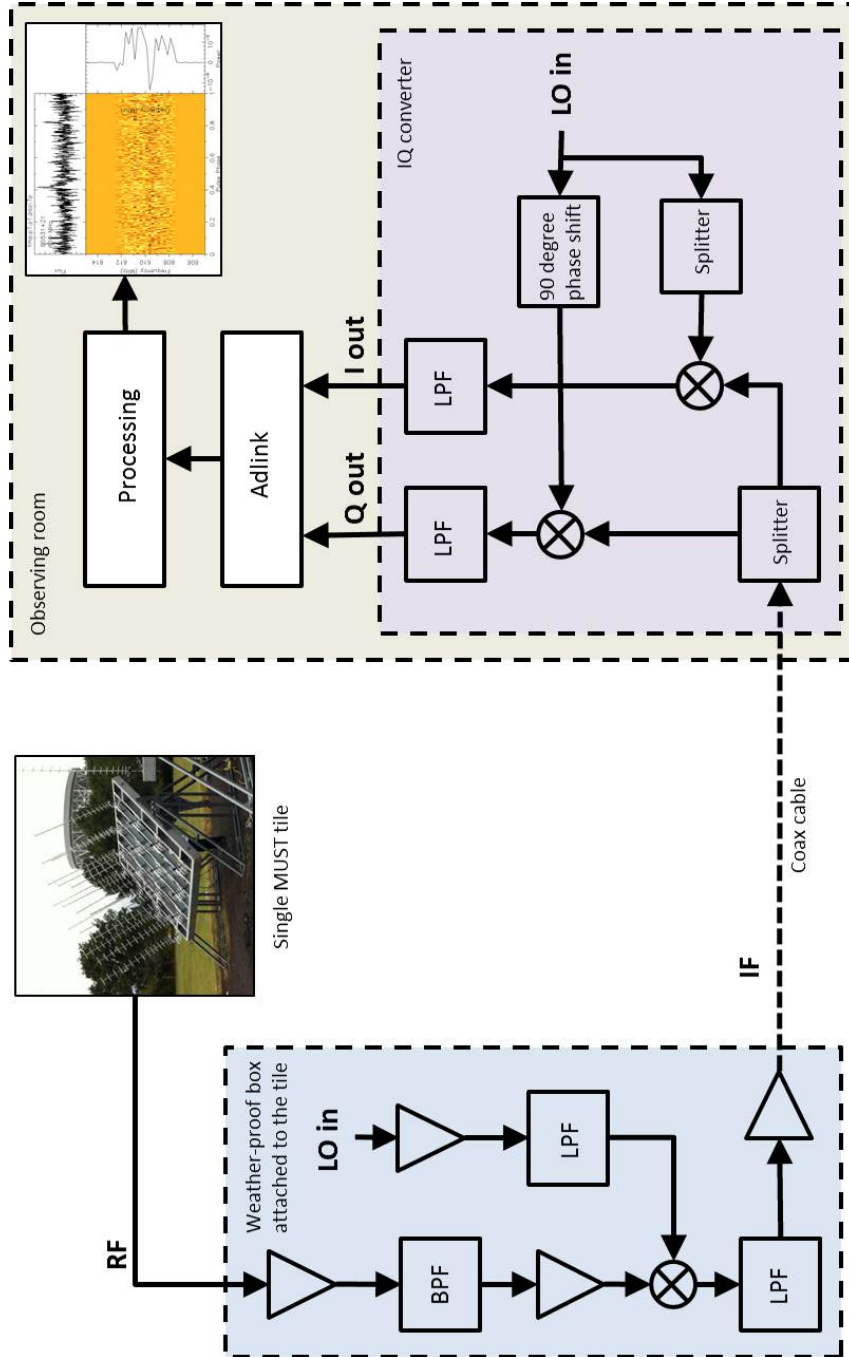


**Figure 3.7:** The MUST-1 signal chain. Listed frequencies are taken from §3.4.2. First, the amplified signal  $v_{RF} = 603$  MHz is passed through a bandpass filter and mixed down with the first LO<sub>1</sub> signal,  $v_{LO_1} = 633$  MHz, to an intermediate frequency  $v_{IF} = 30$  MHz. This process is depicted in the blue box on the left side. More detail is given in Figure 3.8. Then, the signal is sent over a coaxial cable to the baseband box, the box on the right hand side, in the processing station where it is further down converted, using a second LO<sub>2</sub> signal,  $v_{LO_2} = 30$  MHz, to baseband  $v_{BB}$  and digitised. Sampled data is processed in a digital back-end system. Various amplifiers (triangle shape) were omitted for clarity.

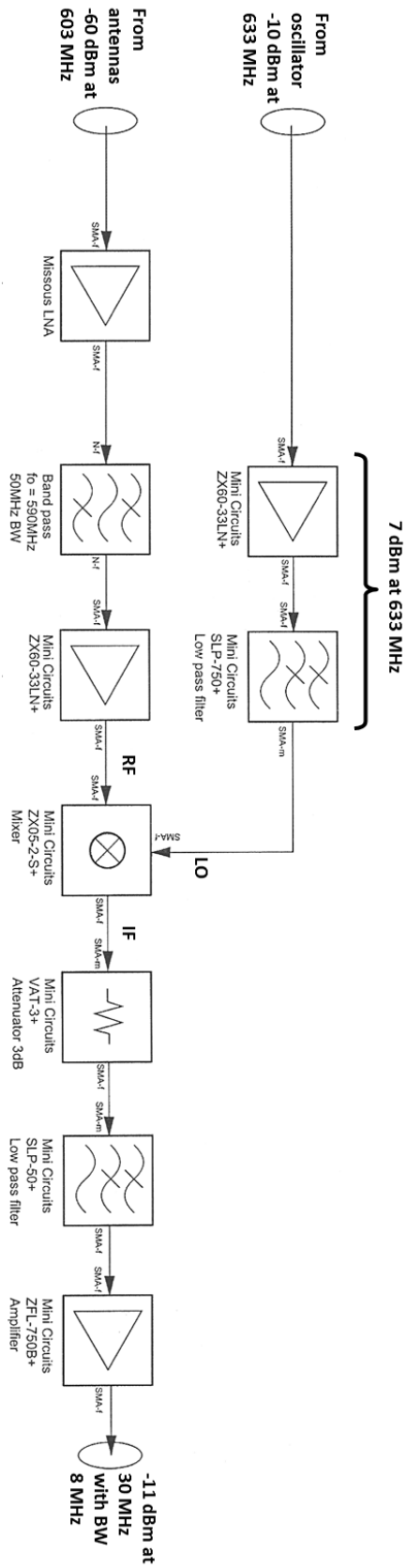


**Figure 3.8:** A detailed block diagram of the chassis with the first LO in Figure 3.7. The system has been tested with the input of -60 dBm at 603 MHz. The RF signal from the antennas is mixed with the LO signal at 633 MHz. The resulting IF is centred at 30 MHz with 8 MHz bandwidth. The circuit under test conditions amplified the incoming RF to -11 dBm, an amplification of 50 dB. Components are listed below each box diagram.

that it is much easier to measure the magnitude and the phase of a signal as a complex number is represented by a phasor with magnitude  $|M| = \sqrt{I^2 + Q^2}$  and the direction  $\phi = \tan^{-1}(Q/I)$  degrees. A detailed diagram of the signal chain is shown in Figure 3.7.

By converting the RF signal to a lower frequency, the noise and linearity performance of the ADC can be best utilised as the signal can now be sampled at the lower rate consistent with the signal bandwidth  $BW$ . In addition, the loss of signal during transport through the cable can be lowered, as the loss goes up with increasing frequency.

### 3.4.2 Test Results

The first test was to confirm that sufficient amplification is provided for the digitiser, the blue box on the left side in Figure 3.7 housing the only amplification stage. The signal chain was tested in the lab with a single tone input of -60 dBm at  $\nu_{RF} = 603$  MHz. The resulting IF is centred at 30 MHz with an 8 MHz bandwidth and the signal was amplified to -11 dBm; this was passed the baseband box. An Adlink<sup>4</sup> card is used to digitise the signal. As the Adlink card can digitise a bandwidth of up to 20 MHz the intermediate frequency  $\nu_{IF}$  has to be down-converted further, in this case to baseband. Thus, the second LO is centred at 30 MHz and after the mixer the I and Q components both span from zero to 4 MHz selected by a narrow set of filters.

The baseband box is tested separately to verify the operation of the filters and to verify operations of the MUST-1 receiver on an actual astronomical source. This test was conducted using the data from the 42 foot telescope. The data was collected simultaneously with two different back-ends. One polarisation ( $p_1$ ) from the 42 foot telescope went through its usual signal chain and the other polarisation ( $p_2$ ) through the MUST signal chain from the second chassis, the purple box on the right side in Figure 3.7. The RF signal was mixed with  $\nu_{LO_1} = 580$  MHz and  $\nu_{LO_2} = 30$  MHz. The resulting baseband signal is filtered with 8 MHz and 5 MHz bandpass filter for  $p_1$  and  $p_2$  respectively. The data was sampled and digitised using the JBO COBRA2<sup>5</sup> sampler/dedisperser. The results of a 25 minute observation of the Crab pulsar can be seen in Figure 3.9,  $p_1$  is plotted in the top panel and  $p_2$  in the bottom panel. Due to the lower bandwidth of the MUST baseband box of 5 MHz, we expect the SNR to be

---

<sup>4</sup><http://www.adlinktech.com>

<sup>5</sup>Coherent Baseband Receiver for Astronomy

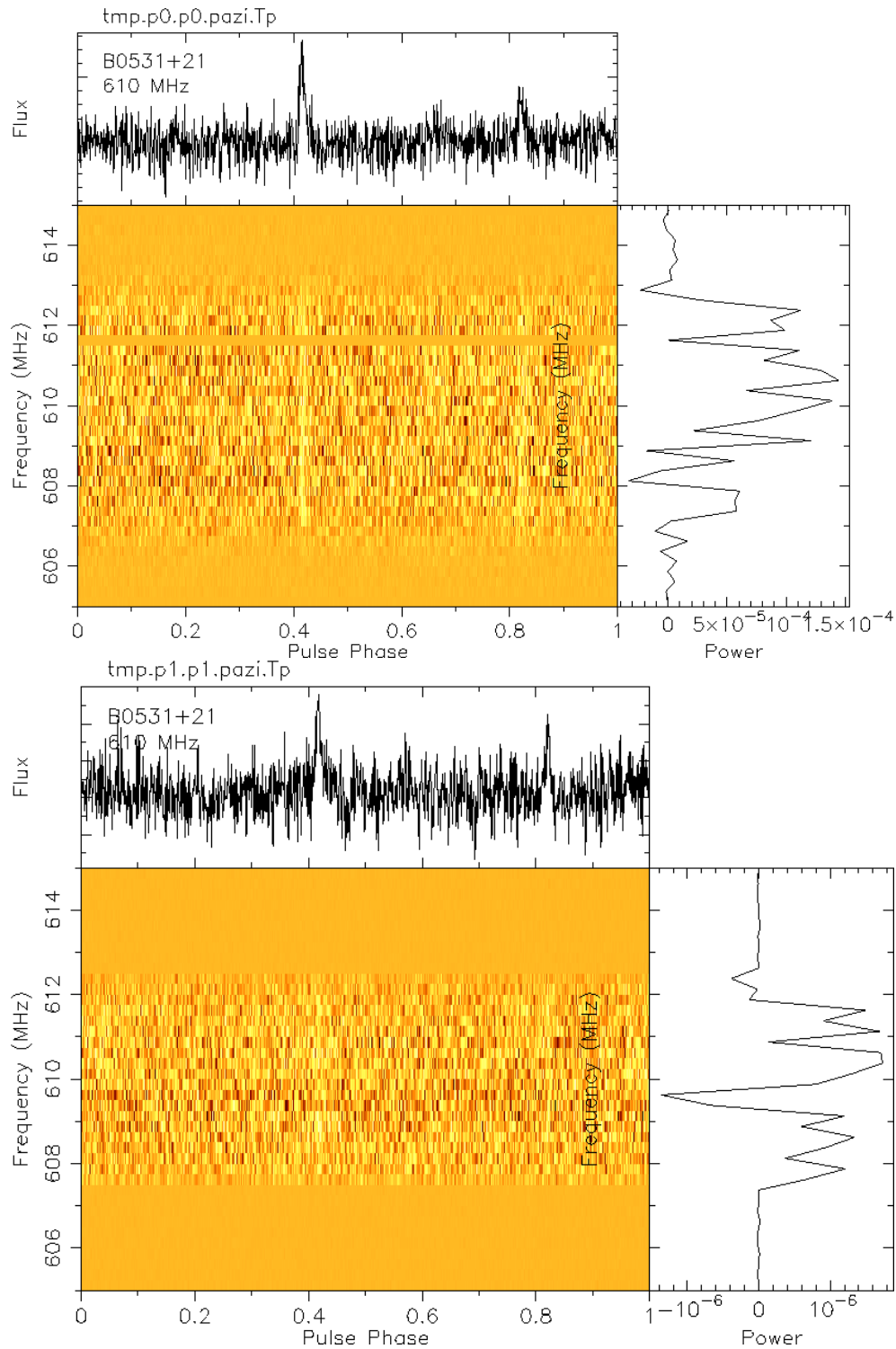


**Figure 3.9:** Dynamic spectra, time series (top), and average bandpass (right) of a 25 minute observation of the Crab pulsar. Both plots show the same observation. (top) Polarisation  $p_1$  collected with the signal chain used with the 42 foot telescope. (bottom) Polarisation  $p_2$  collected with the baseband box intended for the MUST-1 system (see Figure 3.7 for reference).

around  $\sqrt{5/8} \approx 79\%$  of the SNR of the original box with 8 MHz bandwidth<sup>6</sup>. The SNR from  $p_1$  is equal to 4.56 and from  $p_2$  to 3.3, which is approximately 28% less.

### 3.5 MUST-4

The MUST-4 array with sets of 16 single-polarisation Yagi antennas arranged in an equally spaced  $4 \times 4$  grid is shown in Figure 3.11. The signals from all elements in each tile are combined with equal length cables in a 16-way analogue RF combiner feeding a single low noise amplifier (LNA), followed by a power amplifier to compensate for the loss of signal ( $\sim 8$  dB for 75 m of cable). The signal is then sent over a 75 m coaxial cable to the RFI proof building ("Moon Hut") that will be used to house the array electronics, see Figure 3.13.

The initial Yagi aerials used in the project, the CR18WB model<sup>7</sup>, covered the full TV band i.e. 470-854 MHz, and were bought "off the shelf". These commercial Yagis have a very broad beam pattern and the horizontal and vertical polarisations were not symmetrical, see the top panel in Figure 3.10. In addition, standard TV antennas are matched to 75 ohms impedance in contrast to the standard of 50 ohms impedance used in preference throughout the MUST project. The same company (Blake Antennas of Chesterfield) that supplied the CR18WB model, therefore designed a Yagi antenna optimised for the narrow band  $590 \pm 25$  MHz with an impedance as close to 50 ohms as possible. The bottom panel in Figure 3.10 shows the much improved beam pattern. The new Yagis were also equipped with a 25 cm rear extension to the boom, behind the reflector, to simplify the attachment to the frame. Despite the fact that the Yagi antennas were custom made for the MUST telescope, some modifications to each Yagi were necessary, see Figure 3.12. Namely, a balun<sup>8</sup> on each Yagi was supplied with a feedline meant for carrying the TV signal in standard 75 ohm cable. As the MUST project uses low-loss cables with a larger outer diameter plus a thicker inner conductor, the plastic casing and central conductor clamp hole had to be drilled out to accommodate a thicker cable. In addition, the cable clamp screws needed replacing for a longer equivalents. Finally, the reflector made up of two separate sub-elements had to be assembled onto the antenna.

---

<sup>6</sup>Wider filters were not available at the time.

<sup>7</sup><http://www.blake-uk.com/>

<sup>8</sup>A impedance matching transformer.

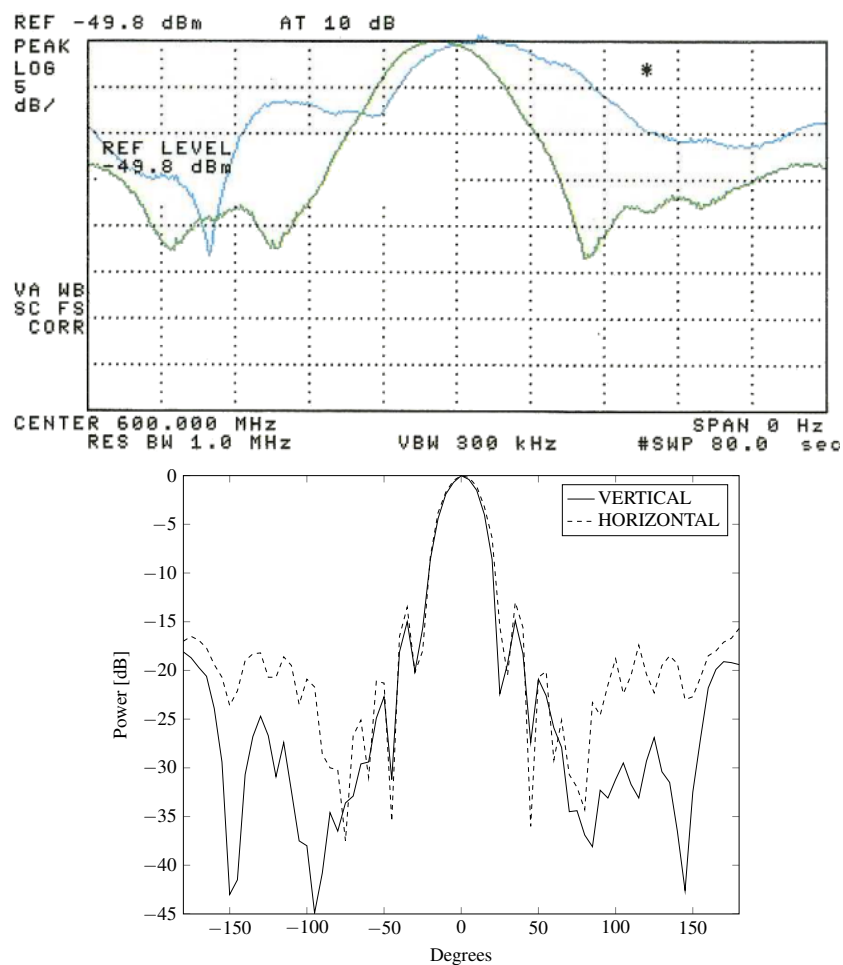


**Figure 3.10:** The MUST array Yagi beam patterns; (top) CR18WB Yagi where blue line depicts horizontal polarisation and green line vertical polarisation (figure courtesy of Blake UK). (bottom) A measurement of the beam pattern of the custom MUST Yagi at 575 MHz from Blake Antennas taken in the field at the JBO.





**Figure 3.11:** The MUST-4 array (second iteration); (top) single tile; (bottom) in a linear array configuration. At this time only the vertical polarisation Yagis were installed.



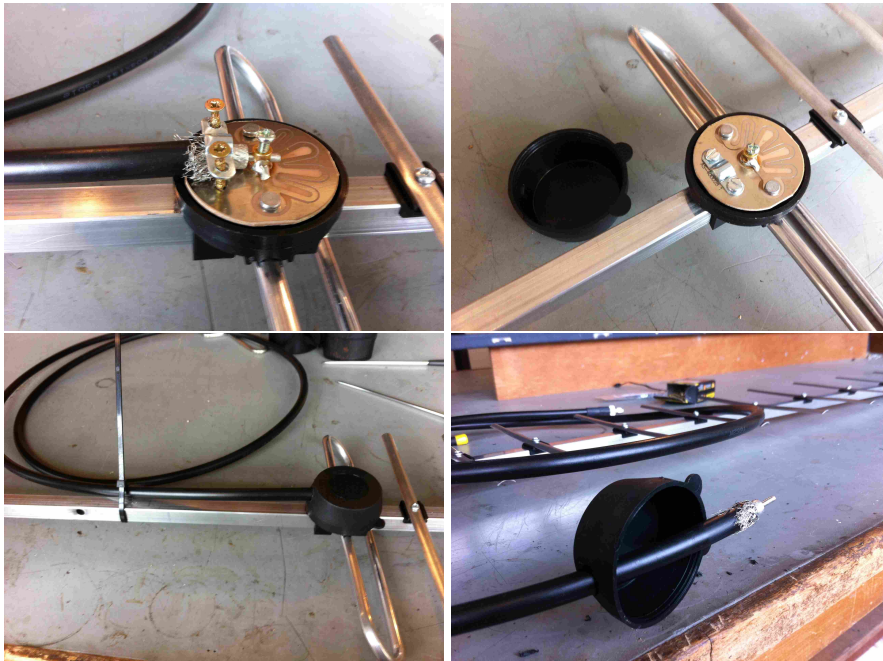


**Figure 3.12:** Modified MUST Yagi; (top right) original balun; (top left) low-loss cable fitted to a plastic casing; (bottom left) longer screws; (bottom right) modified Yagi with a low-loss cable attached.



**Figure 3.13:** Location of the MUST array at the JBO site.



**Figure 3.14:** The antenna test range set-up. The Yagi array under test is on the left and the transmitter is on the right; it uses an identical Yagi and transmits in the far field, i.e. Rayleigh distance. The antenna array under test can be rotated through  $360^\circ$  to produce the power pattern; the wooden cross beam enabled a linear array of four Yagis to be mounted. The author is shown with the antenna under test but would step away while the power reading was taken. Picture courtesy of Prof. P. Wilkinson.

The electromagnetic interaction between antennas in an array is called *mutual coupling*. Mutual coupling tends to have an undesirable effect on the array radiation pattern and changes the input impedance. For that reason the optimum Yagi spacings on the tile, for both polarisations, had to be carefully examined quantitatively. The extensive test observations of Yagi arrays at the JBO site carried out in Summer 2013 suggested an optimum separation between 0.8 m and 0.9 m at 590 MHz. More details can be found in the MSc dissertation of Davidson (2013). Eventually, a separation of 0.8 m was chosen in part for practical reasons associated with the available GRP sections which had been cut down to make the smaller tiles.

### 3.5.1 Array Configuration

The MUST-4 array has been built on the central field area at the JBO, see Figure 3.11 and Figure 3.13. The frames are currently arranged on an East-West line with approximately one metre separation between the tiles' edges, see the bottom panel in Figure 3.15. The spacing between the tiles is partly dictated by the size of the tarmac area and partly to avoid grating lobes in the FoV of the primary element. The linear configuration is being used for testing purposes as every tile can "see" the Sun in the South and the tower, with test signals transmitters, in the North; otherwise the tiles would shadow

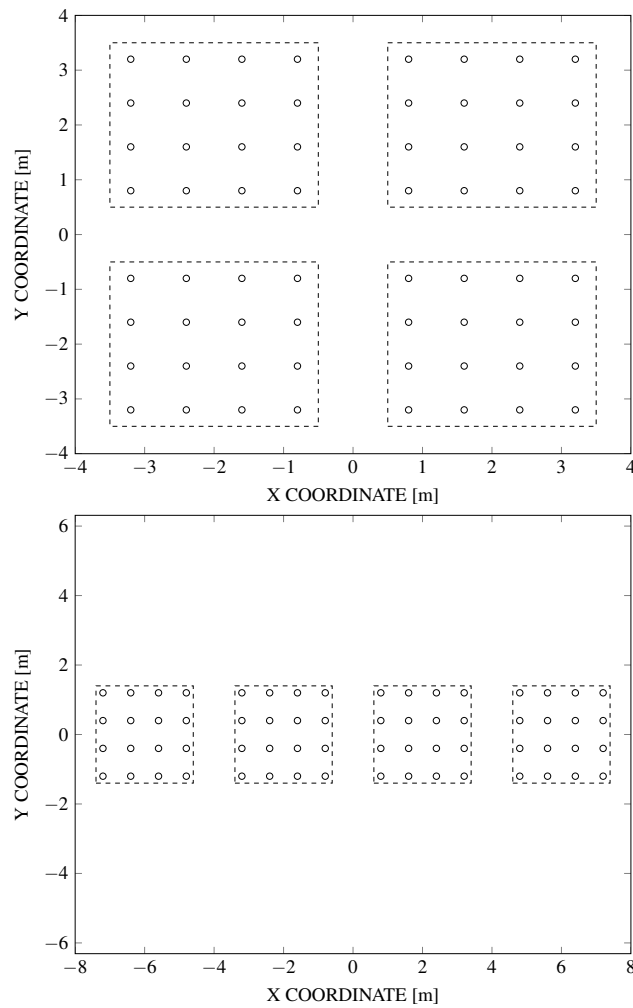


**Figure 3.15:** The MUST array configurations for the simulations where each Yagi is considered as a separately amplified channel. Figure depicts two possible configurations of the MUST-4 tiles (dashed rectangles), where Yagi aeriels are marked as circles. Only one polarisation is plotted for clarity. (top)  $2 \times 2$  grid. (bottom)  $1 \times 4$  grid.

each other. The final configuration will be a regular  $2 \times 2$  grid ensures a symmetrical directive beam, unlike a linear array where a wide fan beam is formed. The rectangular array configuration is assumed for the analysis of the beam shape given below.

### Tied Array Beam

*For these simulations only*, which are also used in §5, it is assumed that every Yagi antenna is independently connected to the beamformer system, i.e. each is a separately

**Table 3.3:** Calculated and simulated values of a TAB for the MUST array, where  $HPBW_T$  and  $HPBW_S$  are the theoretical and simulated half power beamwidths respectively,  $D_{max}$  is the maximum baseline,  $\nu_L$  and  $\nu_H$  are the lowest and the highest operating frequencies and  $S_{min}$  (Equation 2.7) is the minimum detectable flux.

| Array  | $D_{max}$ [m] | Frequency [MHz] | $HPBW_T$ | $HPBW_S$ | $S_{min}$ [Jy] | Location [Lat,Long] |
|--------|---------------|-----------------|----------|----------|----------------|---------------------|
| MUST-4 | 5.65          | $\nu_L$ 575     | 5.28°    | 5.39°    | 13.03          | +53°28'04.28"       |
|        |               | $\nu_H$ 625     | 4.86°    | 4.96°    | 12.84          | −02°13'52.6"        |

amplified channel. In reality, to reduce cost each Yagi in a given polarisation is connected through a 16-way combiner to a single LNA and a further amplifier chain, see Appendix C. It is hoped to evolve the MUST-4 system to the much more flexible simulated configuration as costs allow.

The simulated MUST-4 array TAB pattern ( $AF_{MUST-4}$ ) is a product<sup>9</sup> of the radiation pattern of a single Yagi antenna ( $AF_{Yagi}$ ), the tile factor of the  $4 \times 4$  Yagi array ( $AF_{Tile}$ ) and the array factor of  $2 \times 2$  tile array ( $AF_{Array}$ ):

$$AF_{MUST-4} = AF_{Yagi} \times AF_{Tile} \times AF_{Array}. \quad (3.1)$$

For simulation purposes the Yagi radiation pattern is modelled as a Gaussian beam with a HPBW of 27° with no sidelobes present. Apart from the sidelobes this is similar to the actual Yagi beam in the bottom panel in Figure 3.10. In the simulation the lower limit for Yagi spacings is assumed, i.e.  $d = 0.8m$ .

The beam patterns for the  $AF_{Tile}$  and  $AF_{Array}$  simulated in MATLAB for the lower edge of the MUST original bandwidth, i.e. 575 MHz, is plotted in uv coordinate system<sup>10</sup> in Figure 3.16. Both,  $AF_{Tile}$  and  $AF_{Array}$ , exhibit grating lobes, as Equation 2.12 is not satisfied and the sampled signal is spatially aliased. To avoid grating lobes in the  $AF_{Tile}$ , the spacing  $d$  for  $\sim f = 575$  MHz should be less than  $\lambda/2$ , i.e. 26 cm. Thus is both impractical, due to mutual coupling, and difficult due to the physical size of each Yagi. The number of grating lobes in the  $AF_{Array}$  pattern increases with increasing frequency. This is not unexpected as each tile, in the simulation, is treated as a point receiver separated by approximately 4 m, resulting in the beam pattern in the bottom

<sup>9</sup>See §2.2.2 for more details on the pattern synthesis.

<sup>10</sup>The uv coordinate is a way of plotting the antenna radiation pattern using a transformation of the azimuth  $\theta$  and elevation  $\phi$  angle coordinates, where u and v are defined as  $\sin\theta\cos\phi$  and  $\sin\theta\sin\phi$  respectively.

panel in Figure 3.10.

The effect of multiplying  $AF_{\text{Tile}}$  and  $AF_{\text{Array}}$  is shown in Figure 3.17 at 575 MHz in linear (normalised beam pattern) and in dB units. The simulated HPBW is  $5.28^\circ$ , using the longest baseline of 5.65 m, see Table 3.3. The simulated HPBW is a closer approximation for the real beam pattern. To achieve a fully realistic beam, beam pattern for each Yagi and the exact spacings for the frames would have to be taken into account.

The array beam pattern exhibits four strong sidelobes close to the main lobe. The attenuating effect of the ideal Gaussian beam corresponding to an individual Yagi can be seen in the top panel in Figure 3.17, showing that the majority of the grating lobes have been reduced. The pattern synthesis process (§2.2.2) is also illustrated with the vertical cuts through the simulated MUST array beam pattern (Figure 3.18) in linear and logarithmic units.

### 3.5.2 Back-end System

As the MUST project was always regarded as a test bed for a much bigger array, equipping the array with heterodyne receivers for each tile would be too expensive. In addition, hardware based components could limit the flexibility of this constantly evolving project. By performing certain receiver functionality, like down-sampling in software, the array design can become cost-effective and flexible. Moreover, a global collaboration of astronomers and engineers, called the *Centre for Astronomy Signal Processing and Electronics Research* (CASPER), provide support and platform-independent, open-source hardware and software for radio astronomy instrumentation. Thus, an early design decision was made to implement the digital processing system on CASPER hardware. The signal chain is shown in Figure 3.19 and the subsystem is described below.

#### FPGA board

CASPER FPGA boards, called *Reconfigurable Open Architecture Computing Hardware* (ROACH), are built around a Xilinx Virtex 5 chip (ROACH-1) and a Virtex 6 chip (ROACH-2). The CASPER collaboration has been working on making FPGA



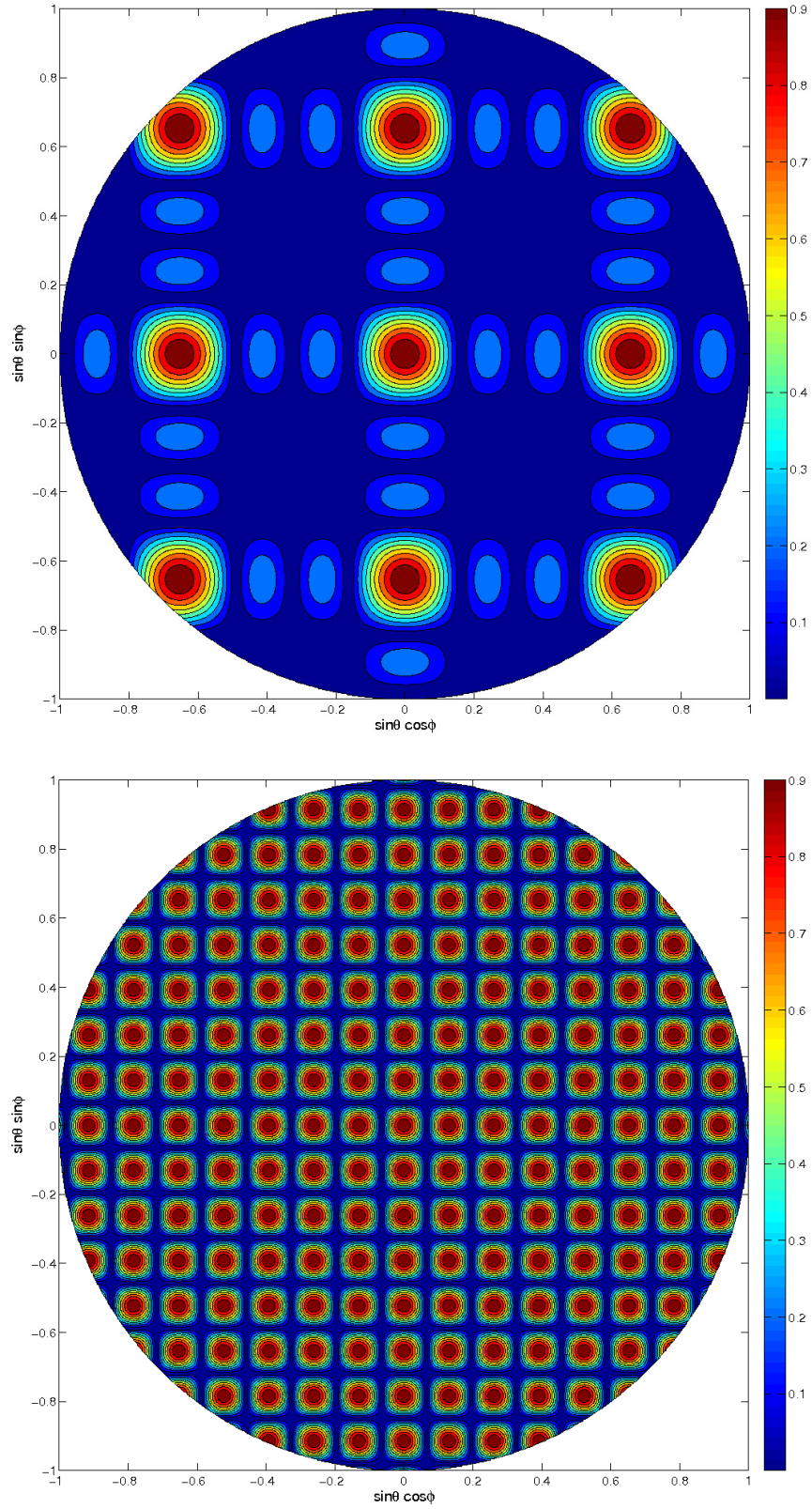


**Figure 3.16:** The MUST-4 array and tile radiation patterns (normalised). (top)  $AF_{\text{Tile}}$  for the  $4 \times 4$  Yagi array beam pattern of a single tile; (bottom)  $AF_{\text{Array}}$  for the  $2 \times 2$  tile array.

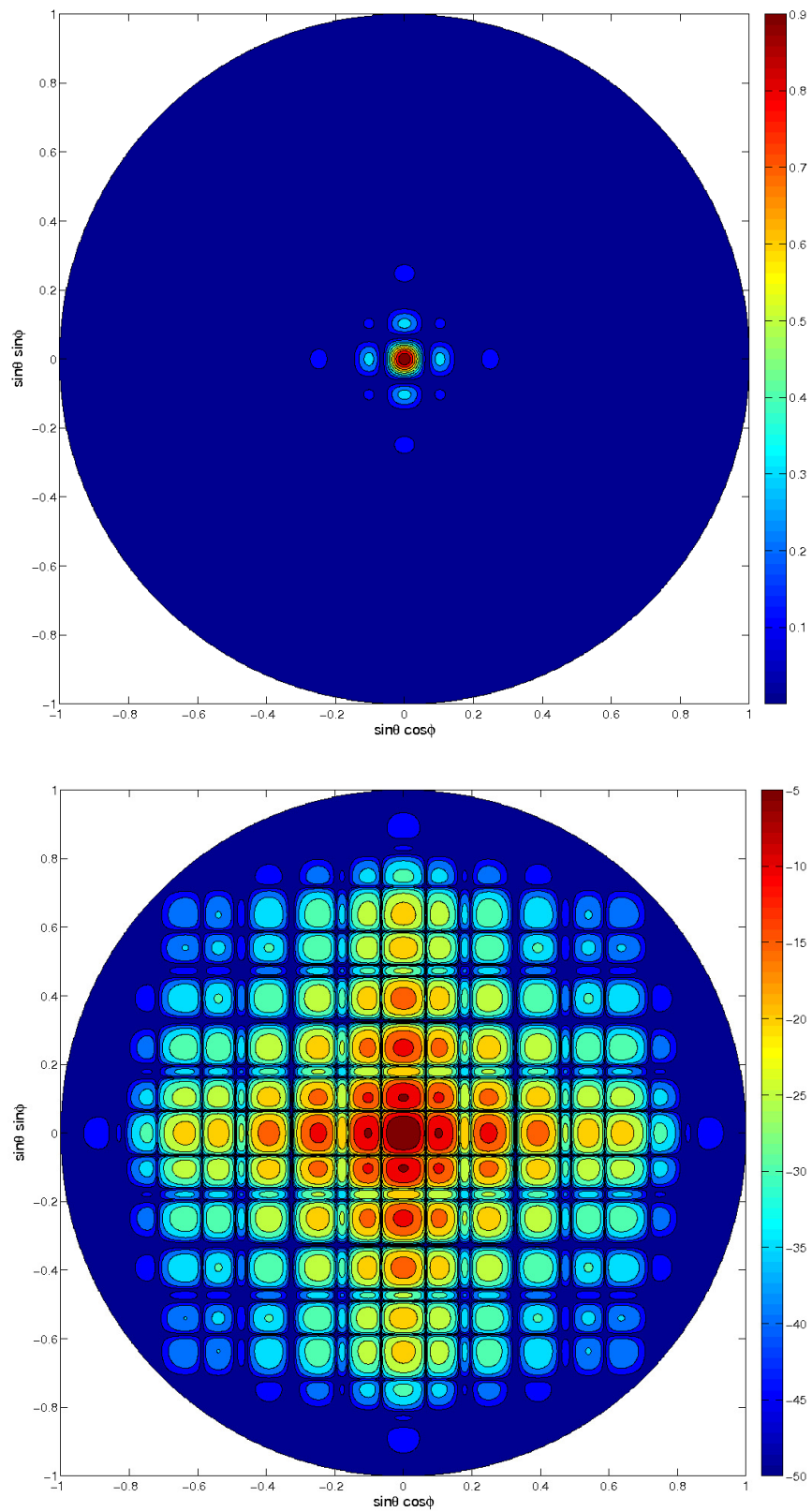


**Figure 3.17:** The MUST array normalised beam pattern AF. (top) Linear units. (bottom) Log units.



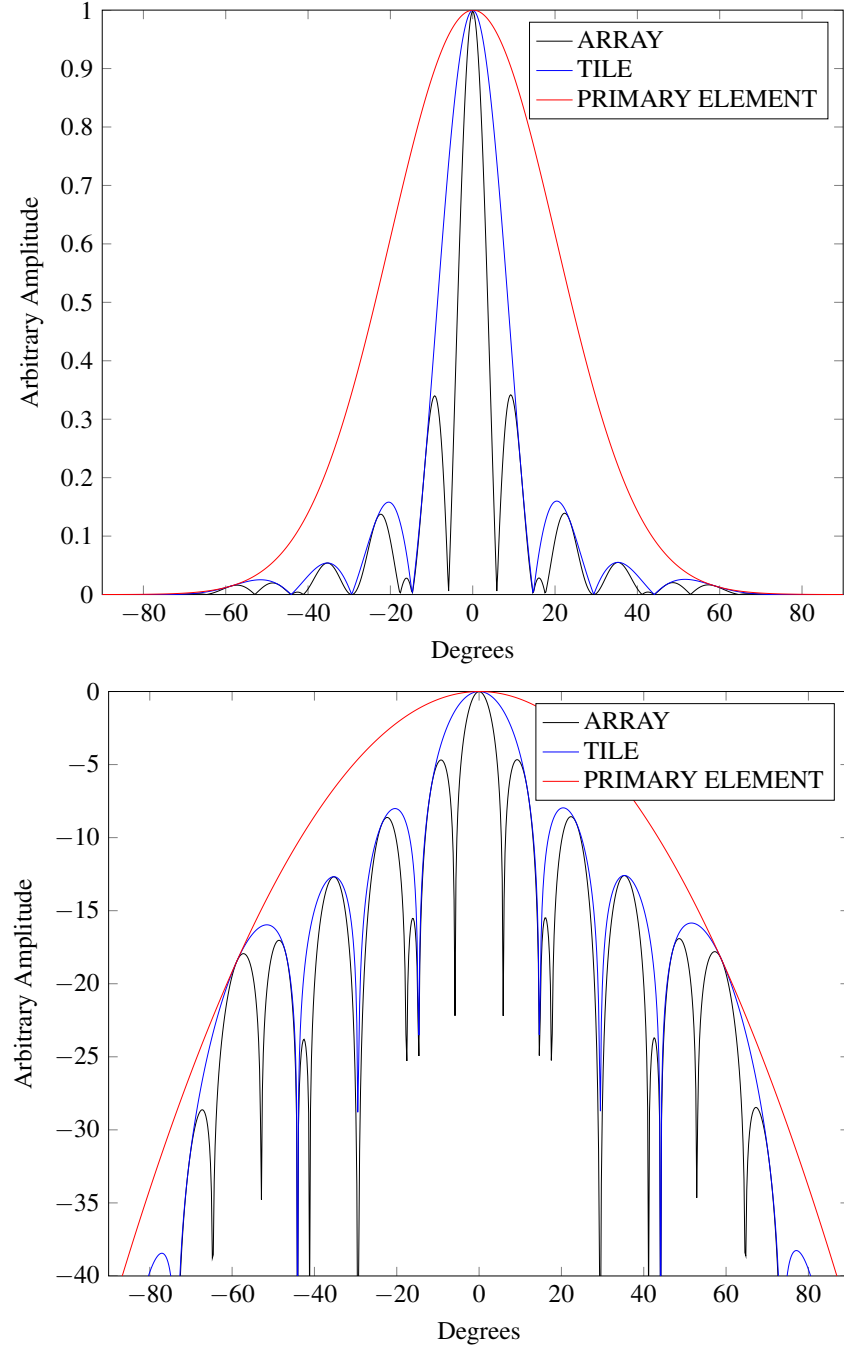


**Figure 3.18:** A vertical cut through of the simulated MUST array beam pattern. Red: primary element. Blue:  $AF_{Yagi} \times AF_{Primary}$ . Black:  $AF_{Primary} \times AF_{Yagi} \times AF_{Tile}$  (top) Linear units. (bottom) Log units.

technology more accessible with its MSSGE tool-flow<sup>11</sup>. MSSGE provides a user with the high-level straight forward graphical approach to design, simulation and test environment without the need of expertise in HDL<sup>12</sup> required to programme FPGAs directly.

The MUST project will use ROACH-1 boards, as it was the most powerful board available from the CASPER collaboration in 2011, when the initial design decision was made. The main components of ROACH-1 are:

- Virtex 5 chip is a high-performance logic device that contains approximately 95,000 logic cells and can be clocked at up to 550 MHz.
- Power PC, a command/control mechanism with a Debian GNU/Linux BORPH<sup>13</sup> kernel installed. Its main task is to handle FPGA resources.
- Monitor/Management subsystem that provides automated shut-down, remote power on/off and monitors the voltages and temperature.

The analog to digital converter (ADC) boards and the digitisation are described below.

## Sampling

The advantage of the heterodyne receiver is that the IF signal can be sampled at the lowest rate after analog down conversion to baseband. The disadvantage of this approach is that each signal path requires two mixers, each with a local oscillator, making it cost prohibitive for a many-tile array. An alternative approach is to shift the analog processing to the digital domain to increase the receiver flexibility, effectively creating a *software radio* design, e.g. Mitola (1995).

The essential point is that, the RF signal need only be sampled at a rate that is greater than twice the signal bandwidth rather than twice the highest signal frequency content, by taking advantage of the repeating spectrum of a sampled signal. This concept is called *sub sampling*. Sampling of continuous signals introduces spectral replicas, or shifted versions, centred at integer multiples of the sampling frequency  $f_s$  and makes the signal periodic in the frequency domain. If the signal is band limited, the spacing between the spectral replicas is dictated by  $f_s$ . To avoid aliasing, i.e. overlapping of the two spectral replicas, the sampling frequency has to be at least twice

---

<sup>11</sup>MATLAB-Simulink-Signal Generator-EDK

<sup>12</sup>Hardware Description Language

<sup>13</sup>Berkeley Operating system for ReProgrammable Hardware

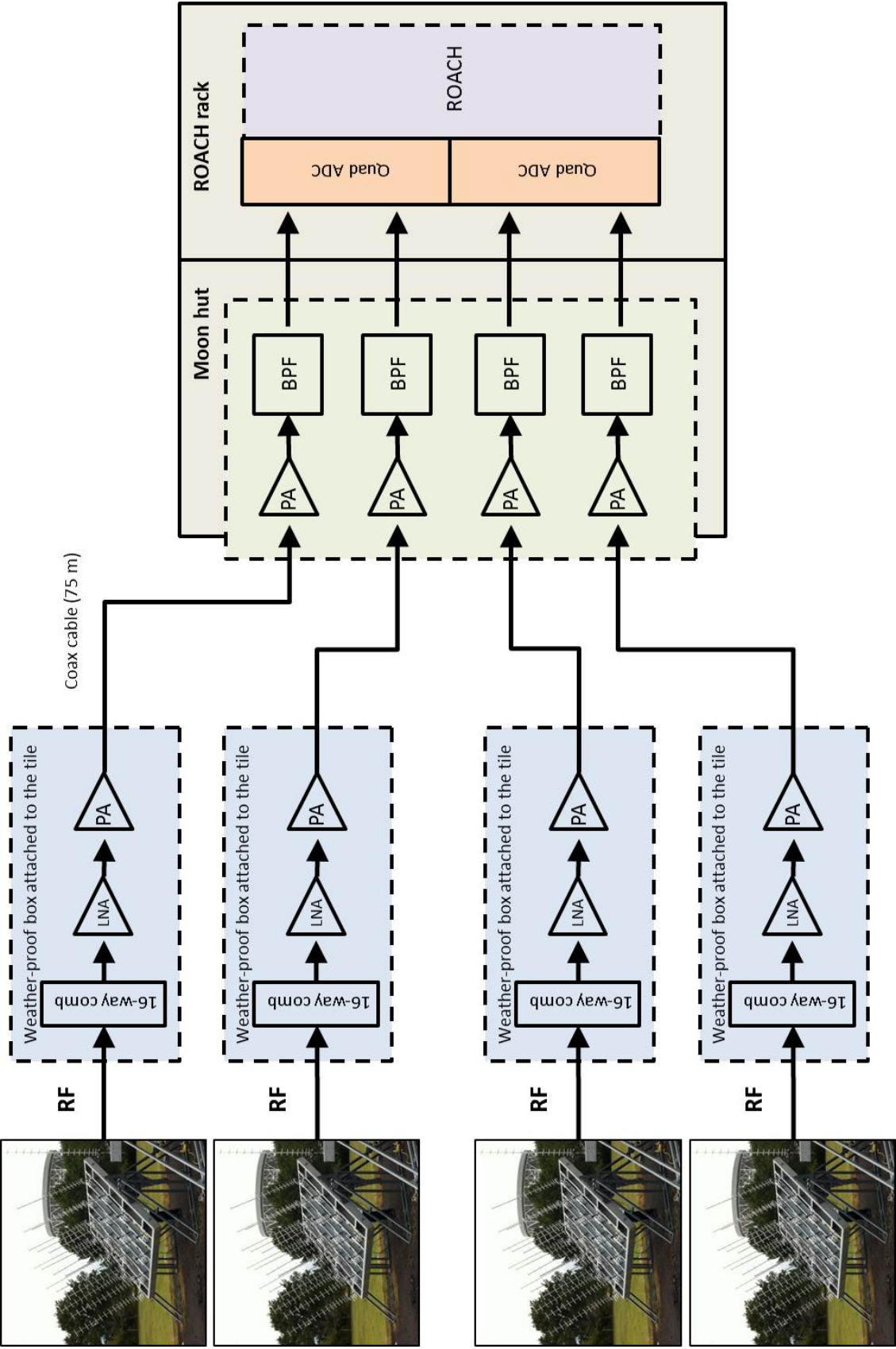


**Figure 3.19:** The MUST-4 signal chain. The signals from four tiles are filtered, sampled with Quad QDC and processed on ROACH-1 board.

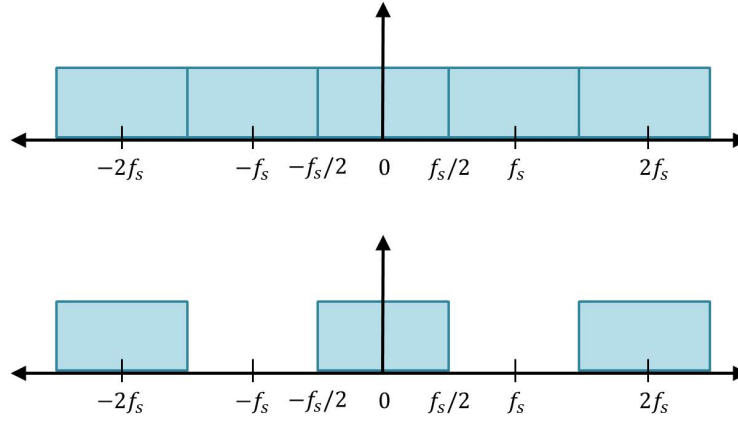


**Figure 3.20:** Illustration of the sub-sampling concept.; (top) spectrum of the critically sampled signal; (bottom) spectrum of an oversampled signal.

the bandwidth  $BW$ . Otherwise the recovery of the original signal would be impossible. Mathematically the optimum frequency for desired separation can be expressed as:

$$\frac{2f_h}{k+1} \leq f_s \leq \frac{2f_l}{k}, \quad (3.2)$$

where  $f_h$  is the highest frequency in the band,  $f_l$  is the lowest frequency in the band and  $1 \leq k \leq f_l/BW$  signify the *Nyquist zone* in which the replica resides. If a bandlimited signal is sampled at exactly  $f_s = 2 \times BW$ , is *critically sampled*, the resulting spectral replicas are adjacent to each other but do not overlap in theory, see the top panel in Figure 3.20. In reality, for critically sampled signal there will be some overlap as not all filters have steep transition band. By increasing the sampling frequency the replicas spread further apart relaxing the requirements on the transition width of a filter used to remove them. The spaces between replicas are sometimes called *guard* or *idle bands*, see the bottom panel in Figure 3.20. Due to the periodicity of the spectral images, any operation performed on a replica that resides in an interval  $[-f_s/2, f_s/2]$ , called the *Nyquist interval*, will be mirrored on all replicas instantly. Thus, the processing can be done on a lower frequency replica and the original bandpass can be reconstructed by passing the sampled signal through a bandpass filter. A good practise is to ensure that the centre frequency  $f_c$  is placed at the centre of each Nyquist zone as follows (Lyons, 2010) hence:

$$f_s = \frac{4f_c}{2k-1}, \quad (3.3)$$

where  $k$  is the Nyquist interval.

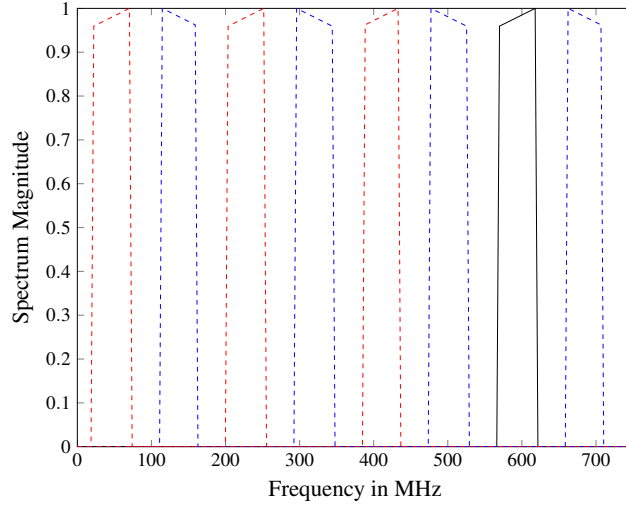


**Figure 3.21:** Spectrum of a bandpass signal sampled at 182.46 MHz; the original spectrum (solid black), the frequency reversed spectra (dashed blue) and images (dashed red).

The MUST frequency band is centred at about 590 MHz and has the revised bandwidth of 35 MHz bandwidth. In order, to satisfy the Nyquist criterion, the classical sampling frequency would have to be in the region of 1.2 GHz. With the application of sub-sampling we only have to sample at a rate  $\geq 2 \times 35$  MHz, i.e. twice the bandwidth. Using Equation 3.3, the optimum sampling frequency  $f_s$  is 182.46 MHz which places the original bandpass signal in the 7<sup>th</sup> Nyquist zone. The spectrum of the sampled signal is shown in Fig 3.21.

### Digitisation

The very low-level signals in radio astronomy and the potential for strong RFI requires a large dynamic range of the system. The dynamic range is the difference between the weakest and the strongest signal amplitude that can be simultaneously effectively digitised without saturating the digitisation levels. The strongest signal is determined by the presence of RFI ( $P_{max}$ ). Thus, the RFI signal strength relates to the noise which dictates how large the dynamic range has to be. Estimating the dynamic range is not a trivial task as the noise contribution from all components in the system, like amplifiers and filters, have to be taken into account. Here, we present an estimate the number of bits needed to represent the range between the strongest RFI encountered and the weakest astronomical signal. The system under test, for which the dynamic range is

measured below, comprises of a digital spectrum analyser and an omnidirectional antenna<sup>14</sup>. We use it as an example to demonstrate the process.

The performance of a radio system depends on the SNR at the receiver's input and the antenna can contribute significantly to this figure. To measure the SNR at the receiver's input, here the spectrum analyser, we used the antenna described in §3.3. As the antenna has a vertical sensitivity null most RFI will be received from the sides from terrestrial transmitters. The noise power ( $P_A$ ) at the input port of the spectrum analyser from the antenna can be calculated via the power-temperature relation:

$$P_A = k_B T_a \Delta\nu, \quad (3.4)$$

where  $k_B$  is the Boltzmann constant,  $T_a$  can be taken as the ambient temperature due to the antenna's vertical null and  $\Delta\nu$  is the input bandwidth as seen by the spectrum analyser. For a bandwidth  $\Delta\nu$  we chose a range of 100 MHz in the scan. Thus the  $P_A$  is equal to  $4.14 \times 10^{-13}$  mW, or -123.8 dBm. The peak noise power, i.e. the peak RFI, is equal to  $P_{max} = -92$  dBm, shown as a black line in Figure 3.22. To calculate the dynamic range we subtract  $P_{max}$  from  $P_A$ , which gives 31.8 dB of signal range. The maximum achievable dynamic range is limited by quantisation error and the minimum number of bits required is expressed with a formula:

$$DR_{ADC} = 20 \log_{10}(2^Q) = 6.02 \times Q \text{ (dB)}, \quad (3.5)$$

where  $Q$  is the number of bits. Thus, for dynamic range of 31.8 dB, the minimum  $Q$  is 6 bits. We stress again that this is simply a numerical example, not band on the MUST configuration.

The dynamic range required for astronomical sources, such as pulsars, require some headroom to accommodate strong RFI. For the MUST project, two commercial ADCs were considered, namely the iADC<sup>15</sup> and Quad ADC<sup>16</sup>, both with 8 bits of quantisation. The iADC offers higher sampling rates, from 10 MHz to 1 GHz, but can sample a maximum of two input streams. Whereas the QuadADC offers a maximum

---

<sup>14</sup>It later surfaced that the digital spectrum analyser produced regular strong spikes that do not exist as a real RFI. RFI scan conducted in August 2012, §3.3, with an unscreened digital spectrum analyser which emitted a comb of frequencies.

<sup>15</sup><https://casper.berkeley.edu/wiki/ADC2x1000-8>

<sup>16</sup><https://casper.berkeley.edu/wiki/ADC4x250-8>

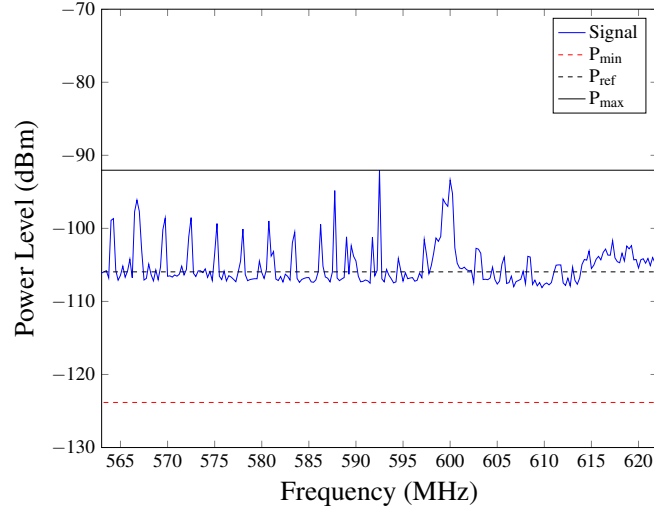


**Figure 3.22:** ADC dynamic range calculations with data from RFI scan conducted in August 2012. The comb of frequencies was generated by the unscreened digital spectrum analyser used in the test. It serves as an example of potential future RFI from outside sources.

of four inputs but at much lower sample rates, maximum of 250 MHz. To keep most of the system on one board, the QuadADC with four inputs was used in the design. An 8 bit quantisation provided by CASPER ADC boards we hope will provide sufficient range to allow for further RFI incursions into the 35 MHz band. In reality, the current RFI environment resembles the one shown in the bottom panel in Figure 3.6.

### 3.6 MUST Performance Estimation

The MUST-4 performance can be estimated using recent findings on the detectability of fast radio transients published by Lorimer et al. (2013). We will explore whether, even at the prototype MUST-4 stage, interesting scientific data on FRBs can be obtained.

To calculate the minimum array sensitivity  $S_{v,\min}$  we used Equation 2.7. The value of the digitisation loss  $\beta$  was taken from Kouwenhoven & Voûte (2001) and is equal to 0.999 for 8 bits. The sky temperature values vary as a function of Galactic latitude and longitude. To account for the sky noise variability we used the Haslam et al. (1982) 408-MHz all-sky survey, where the sky temperature  $T_{\text{sky}}$  is scaled to 575 MHz and 625 MHz using a scaling with a spectral index of synchrotron radiation of  $\alpha = -2.6$  (Reich

& Reich, 1988) via:

$$T_v = T_{408} \left( \frac{\nu}{408} \right)^\alpha \quad (3.6)$$

where  $T_v$  is the scaled sky temperature,  $T_{408}$  is the sky temperature from the Haslam survey and  $\nu$  is the observing frequency. The MUST-4 basic parameters used in Equation 2.7 are:

- System temperature:  $T_{sys} + T_{sky} \sim 120 [K] + 10 [K]$ ;
- Bandwidth:  $\Delta\nu \sim 35 [MHz]$  (§3.3);
- Effective area of four individual tiles:  $A_{eff} \sim 30 [m^2]$ ;
- Integration time:  $\tau = 5 \times 10^{-3} [s]$ .

The integration time is chosen so as not to significantly smear out an FRB signal similar to the Lorimer burst. The resulting sensitivity maps are plotted in Figure 3.23.

For the MUST-4 system  $S_{v,min}$ , adopting a threshold detection of  $8\sigma$ , is approximately 160 Jy. Consulting Figure 3.24 for the predicted burst rates above some threshold flux density  $S$ , the sensitivity of 160 Jy at 575 MHz would give us a rate of  $\sim 10^{-5}$  sources per hour per square degree. We are designing our system so that it will be able to fill the primary Yagi beam with at least 10 array beams giving us 50 square degrees of sky coverage with closely packed frames. That in turn will give us a rate of  $\sim 0.0005$  sources per hour. This calculation demonstrates that the MUST-4 system should be able to detect one transient<sup>17</sup> source after three months of constant observing, if the published rate estimates are correct. This rate is not very encouraging. Currently therefore MUST-4 is more suited for peryton searches (§2.1.2), which can be much stronger (Saint-Hilaire et al., 2014) than FRBs.

### 3.6.1 First Light

The investigation of the performance of Yagi arrays gradually build up to the capability to perform a first measurement on an astronomical source, the Sun. The first tiles were completed in Summer 2014 and are currently undergoing electrical tests while commissioning continues. We used the Sun to determine the beamwidth of a single tile using *Sun transit time*, i.e. the moment when the Sun transits the celestial meridian. This *drift scan* was conducted on the 31<sup>st</sup> of July 2014 at the JBO with a single tile, shown in the top panel in Figure 3.11.

---

<sup>17</sup> Assuming a typical radio spectral index  $\alpha = -1.4$ .



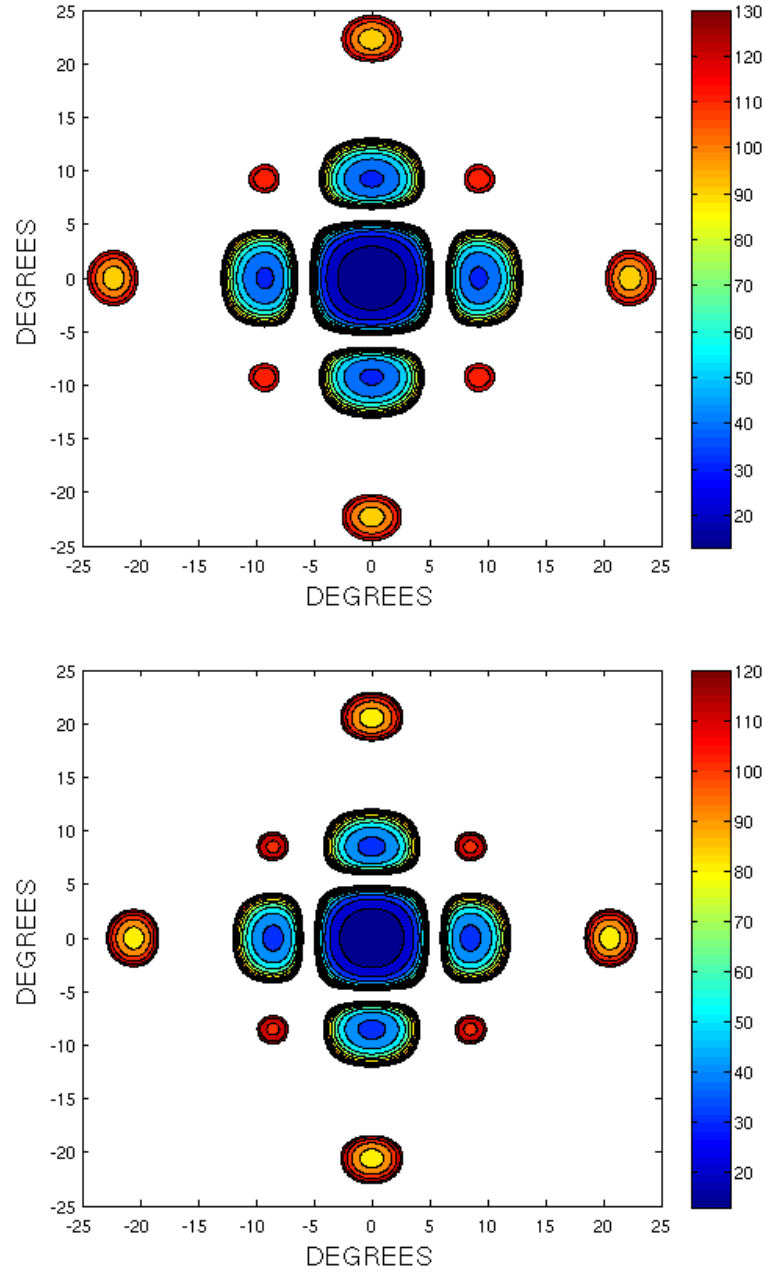


**Figure 3.23:** Sensitivity maps in units of [Jy] for the MUST array. Sensitivity maps at frequency  $\nu_1 = 575$  MHz the top panel, and frequency  $\nu_2 = 625$  MHz, the bottom panel, demonstrate the frequency dependent change in the beam shape. Due to the small fractional bandwidth the difference is small. For the purpose of simulation in §5 we have taken a 50 MHz band centred at 600 MHz. The peak values are listed in Table 3.3.

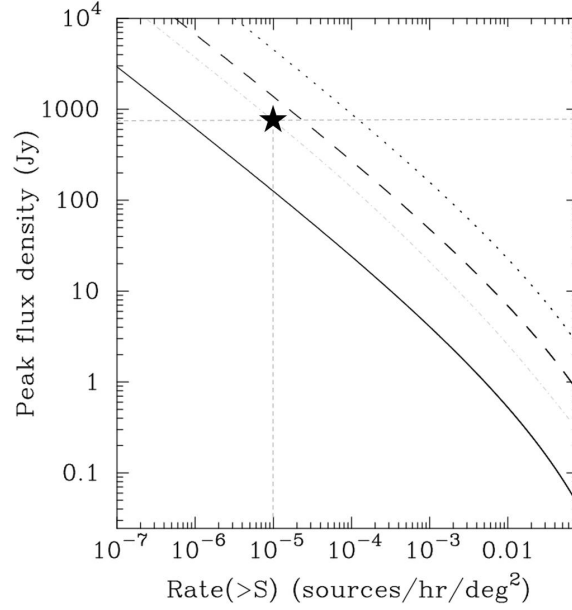


**Figure 3.24:** Predicted burst rates above some threshold flux density  $S$  at 1400 MHz (solid line), 350 MHz (dashed line) and 150 MHz (dotted line) and adapted from Lorimer et al. (2013). The black star indicates the estimated burst rates for FRBs detectable with the MUST-4 array.

To perform a drift scan observation the tile is positioned ahead of the Sun so it can drift through the tile beam. The experimental setup consisted of, starting from the tile, LNA<sup>18</sup>, narrow band-pass filter  $H_{NB}$  and FUNcube Dongle<sup>19</sup>, a simple USB receiver covering approximately 60 MHz to 1.7 GHz band. The scan was conducted at 585 MHz frequency and the results are plotted in Figure 3.25, where the power (dBm) is plotted against a time stamp in GMT (BST-1). On the 31<sup>st</sup> of July 2014, the Sun was predicted for a transit at 12h 07m GMT. The level of the main lobe peak in Figure 3.25 is -20.35 dBm at 12h 08m, which implies that the positional error is negligible. For sources on the celestial equator the rotation of the Earth causes the source to move at a rate of  $360^\circ$  every 24 hours. To achieve best estimation of the half-power beam width we have to apply a correction for the actual solar declination, where the rate of motion is about  $(360^\circ/24)\cos(\delta^\circ)$  per 24 hours, where  $\delta$  is the declination of the source. From the measurement, the 3-dB point before and after transit occurred at 11h 41m and 12h 36m respectively. The Sun's declination on that day was  $18.2^\circ$  which results in a beamwidth of  $12.36^\circ$ . This result is consistent with our simulations described in §3.5.1. To compare this result with a theoretical beamwidth, described with Equation

<sup>18</sup><http://www.researchcomms.com/>

<sup>19</sup><http://funcubedongle.org.uk/>

2.8, for  $\lambda = 0.513$  m and  $l = 2.4$  m is equal to  $12.25^\circ$ . The HPBW test was conducted using the Sun with the apparent angular size of  $0.5^\circ$  the beam broadening effect has to be taken into account. As the HPBW of a single MUST tile is much larger than the Sun apparent angular size, the measurement is a good approximation. To demonstrate that we add the two in quadrature, which gives  $12.37^\circ$ . Again, the broadening effect is negligible.

### 3.7 Discussion

We have discussed the design of a radio telescope suited which is for expanding our knowledge about the transient phase space, specifically the perytons. It takes advantage of consumer off the shelf components and low-cost student labour. In addition, its potential for training the next generation of radio astronomers and engineers has also been demonstrated during the design stage and the first phase of commissioning. The MUST project will be an unique platform for graduate students across many disciplines to acquire hands-on experience in radio astronomy technology.

The cross disciplinary nature, relevant for physics, engineering, computer science as well as astronomy students, of the MUST array means that it was susceptible to unexpected delays and design changes. We also cite:

- wind breakage of the original large frame, which delayed the project by 4 to 6 months;
- the redesign of the RF filters necessitated by increased RFI, which also delayed the project by some months.

The majority of the available funds had to be allocated for the raw materials and much of the work was carried out by Prof. P. Wilkinson and graduate students including the author.

The experience of construction MUST-4 helped to highlight that an array built using many Yagi aerials requires many man-hours to test, construct and attach each Yagi antenna to the frame and then to "connect up" the system generally. As a result, it has become clear that at the originally chosen frequency of  $\sim 600$  MHz, small dish antennas would have been more suitable. This was a frequency driven conclusion. For example, if 300 MHz has been chosen for MUST, then four times fewer Yagis and analogue components would be needed and the Yagi array approach would still be the

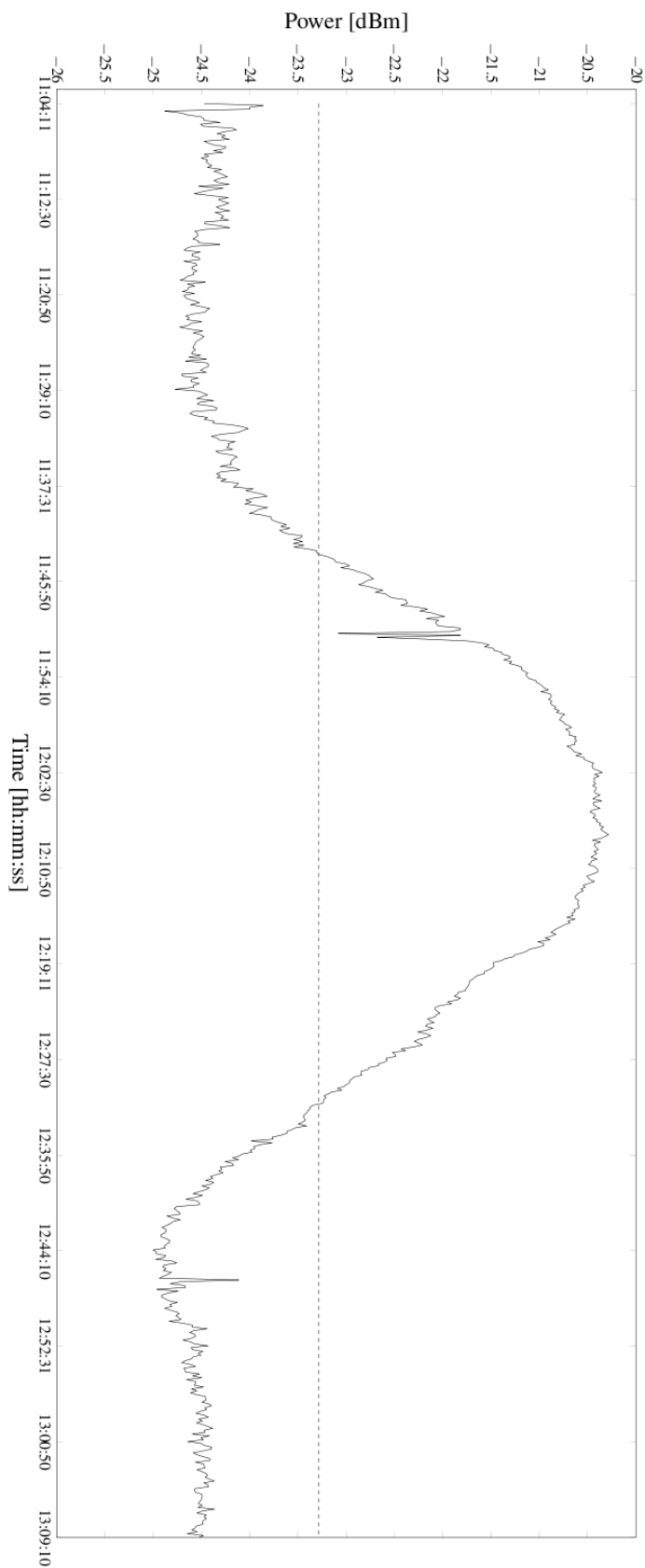


**Figure 3.25:** The Sun drift scan conducted on the 31<sup>st</sup> of July 2014 at the JBO with a single MUST tile. The scan was conducted at 585 MHz frequency. The power (dBm) is plotted against a time stamp in GMT (BST-1). The level of the main lobe peak is -20.35 dBm at 12h 08m and the 3-dB point before and after transit occurred at 11h 41m and 12h 36m respectively. The black line indicates the HPBW points.

most appropriate solution. However, for 600 MHz there are too many components and connections for scaling up to a much larger array, even though they are available commercially from the TV industry. The same arguments have resulted in the SKA-low, using wire antennas for frequencies  $\simeq 400$  MHz whereas SKA-mid operating at higher frequencies utilises dishes array.

As well as a search instrument for perytons the MUST-4 array in its current form remains useful for testing new observing methods, such as that developed in §5 and the bi-spectrum (Papadopoulos & Nikias, 1988) or chimageator method (Bannister & Cornwell, 2011). In addition, new RFI mitigation strategies can be tested. If funds allow, the second commissioning phase of adding another four tiles will begin in 2015/16 so that the same collecting area as the original concept envisaged can be achieved. The development of the monitor and control software as well as data acquisition and inspection will also extend the student involvement and overall use of the telescope.

## Chapter 4

# Digital Beamformer for the MUST array

Radio sources emit weak noise-like signals that can be corrupted with interference. To achieve high sensitivity, the ability to observe and study weak radio sources, the time of the observation and the observing bandwidth needs to increase. For transient events, like FRBs, increasing the observing time is impractical. Thus, to achieve good sensitivity is to increase the bandwidth so that more emission can be received. The processing of astronomical signals is often done in the frequency-domain. As the frequency-domain processing of wide-bandwidth signals requires channelisation, decomposing data into several smaller channels, the spectral leakage of unwanted energy to neighbouring channels can only be minimised but not avoided. Moreover, many astronomical science cases require the data to be transformed back to the time domain to achieve the required high time resolution. An advantage of the time domain processing is that the signals are processed in their light curve form or "as received". As there is no comprehensive study available on the effects of the frequency and the time domain signal processing techniques on the pulsar data, in the following chapter we presents an investigation into the wide-bandwidth time-domain signal processing techniques and on the effects of channelisation and filtering on the pulsar pulse profile.

### 4.1 Beamforming

As introduced in §2.2.2, beamforming is a process of spatial filtering, where elements in an array are made more sensitive to the signals coming from a particular direction while others are attenuated. Beamforming utilises the differences in the propagation

times that cause the signal wavefront to reach different antennas at different times. To enhance the signal strength from a particular direction, appropriate time delays are applied to compensate for the geometrical delay  $\tau_m$  expressed as:

$$\tau_m = \mathbf{r}_m \cdot \mathbf{k} / c, \text{ for } m = 1, 2, \dots, M, \quad (4.1)$$

where  $c$  is the speed of light,  $M$  is the number of antennas in an array,  $\mathbf{r}_m = [r_x, r_y, r_z]$  is the antenna position vector in the local coordinate system,  $\mathbf{k} = 2\pi/\lambda \mathbf{u}$  is the wave vector describing the direction of the wavefront, where  $\lambda$  is the wavelength and the unit vector  $\mathbf{u}$  is defined in Equation 2.11. The wave vector  $\mathbf{k}$  is specified relative to the reference antenna. In addition, the signals are weighted with a beam shaping function  $a_m$  and summed. The beamformer output  $B(t)$  can then be described as follows:

$$B(t) = \sum_{m=0}^{M-1} a_m x_m(\omega t - \omega \tau_m), \quad (4.2)$$

where  $x_m$  is the antenna output and  $\omega = 2\pi f$  is the analog angular frequency. An example of the continuous beam pattern for an eight element array is plotted in Figure 4.1.

In the analog domain, the delay compensation can be accomplished by switching between different signal path lengths. For broadband applications such a system can be lossy due to cable lengths<sup>1</sup>. The longer the cable, the greater the loss. For multibeamforming arrays each beam would need a separate switching board making this cost higher. For narrowband applications the delay compensation can be approximated with phase shifts. However, the drawback is that phase shifts are correct only for very narrow channels. As the channels are of finite width, phase shifts will introduce smearing, i.e. amplitude reduction. Digital implementations of the time and frequency domain beamforming will now be briefly introduced for completeness.

### 4.1.1 Time-domain Beamforming

For a digitised signal, the delay compensation is approximated by skipping or advancing over an integer number of samples. A discrete form of Equation 4.2 is obtained by sampling the signals every  $T$  seconds or at a rate  $f_s = 1/T$ . Then the discrete

---

<sup>1</sup>As radio frequency signal travels through a coaxial cable it gets attenuated. The power loss is defined in terms of decibels per unit length for a given frequency and is usually given in the data sheet.

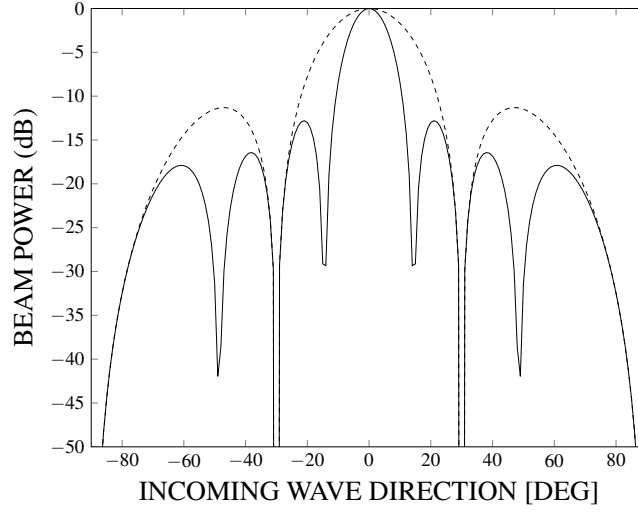


**Figure 4.1:** The time-domain beam output  $B(t)$  as a function of incoming wave direction for a linear array with all  $M = 8$  separated by  $\lambda/2$  (Equation 4.2) shown in solid black line. For completeness, a four element array is shown in dashed line.

time-domain beam output  $B(n)$  is as follows:

$$B(n) = \sum_{m=0}^{M-1} a_m x_m(\omega T(n - q_\tau)), \quad (4.3)$$

where  $t$  in Equation 4.2 was replaced with  $nT$ ,  $n$  is the time domain index of the input sample that lies in the range  $(1 \leq n \leq N)$ , where  $N$  is the number of samples of the input sequence. The propagation delay  $\tau_m$ , that also determines the beam pointing direction, is now an integer multiple of the sample period  $q_\tau = \tau_m/T$ . Thus, it is clear that the beam direction is also quantised and depends on the sampling rate. An example of a discrete beam pattern is plotted in Figure 4.2 (solid line).

### Delay-Sum

The architecture described so far, i.e. delaying and summing signals, is commonly referred to as a delay-sum architecture. For an array with  $M$  elements, each sampled and delayed signal is buffered or stored until the last sample needed for beamforming arrives. Only then the beam output can be computed. Depending on the sampling frequency  $f_s$  and the number of elements  $M$  the storage requirements can be very large. A memory saving can be achieved with a *partial-sum beamformer*, where groups of partial sums are produced that can be summed together at a later stage. For example, a partial sum is performed for a coarse delays, i.e. integer multiples of the sampling



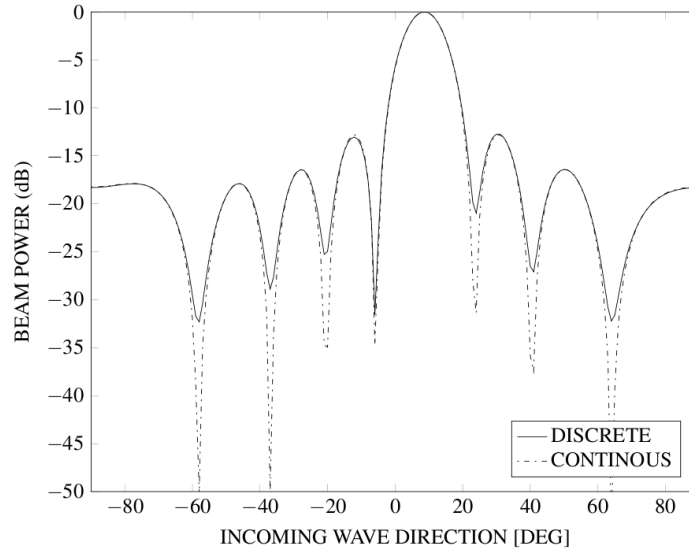


**Figure 4.2:** The discrete time-domain beam output  $B(n)$  example of a linear array with  $M = 8$  separated by  $\lambda/2$  (Equation 4.3) steered off boresight. As the values of  $B(n)$  are discrete, i.e. are restricted to certain values, the nulls in the beam pattern are not as deep as for the continuous beam output  $B(t)$ .

rate. Often the sampling period is too coarse to approximate the steering delays. For example, a delay equal to 2.1 samples can only be approximated to 2 samples. This will introduce errors in the steered beam pattern. To achieve finer delay resolution, the sampling rate has to be increased to at least several times the Nyquist rate. The storage requirements can thus be minimised but the high data rates remain so as to achieve high accuracy delay adjustment.

### Interpolation

Interpolation is a process of increasing the sampling frequency  $f_s$ , or decreasing the sampling period  $T$ , by an integer factor  $L$  so the new sampling period  $T'$  is equal to  $T/L$ . The additional samples thus produced can be used with the time-domain beamforming to achieve finer delay adjustment. The simplest form of interpolation is linear interpolation, where the point of interest lies on a straight line drawn between two known points. In this implementation, the beamformer output rate is less than the input rate. The interpolation filter can be positioned before or after the delay-sum operation as the summation and filtering are linear operations, e.g. Pridham & Mucci (1978). When the order is swapped, the beamforming operation is performed

on the zero-padded sequence. The fundamental difference between the two implementation is that for this beamformer structure the output rate is greater than the input rate. The implementation choice is also driven by the desired number of beams formed simultaneously, as indicated in Table 4.1 (Pridham & Mucci, 1979a). Thus for arrays where the number of beams is greater than the number of elements in the array the pre-beamformer interpolation is computationally efficient. As the MUST array design requirements are 10 beams for the initial four elements (§3), implementation of the pre-beamformer interpolation is discussed in more details in §4.2.

**Table 4.1:** Interpolation filter requirements for pre-beamforming and post-beamforming implementations, where  $N_B$  is the number of beams,  $N_C$  is the number of filter coefficients,  $N_E$  is the number of elements in the array and  $f_s$  is the sampling frequency. Table assumes symmetrical filter coefficients.

| Type             | Interpolation Filter Requirements |                     |
|------------------|-----------------------------------|---------------------|
|                  | MPIS                              | APIS                |
| Pre-beamforming  | $N_E N_C f_s / 2$                 | $N_E (N_C - 1) f_s$ |
| Post-beamforming | $N_B N_C f_s / 2$                 | $N_B (N_C - 1) f_s$ |

### Shifted-sideband

The *Shifted-sideband* (SSB) (Pridham & Mucci, 1979b) is a time-domain technique that incorporates elements used in frequency domain processing. The SSB is used with the bandpass signals that occupy a frequency band from  $f_c - BW/2$  to  $f_c + BW/2$ , where  $f_c$  is the centre frequency and  $BW$  is the signal bandwidth. In the process of quadrature sampling, described in 3.4.1, the signal is shifted down in frequency and sampled at a rate consistent with the signal bandwidth  $BW$ . After the quadrature sampling, the data is processed further by the interpolation beamformer. The beam output of the SSB beamformer is as follows:

$$\hat{B}(n) = \sum_{m=0}^{M-1} a_m \hat{x}_m(n - q_\tau) e^{-j\Omega_c q_\tau}, \quad (4.4)$$

where  $\Omega_c = \omega T$ . The SSB provide hardware savings in form of ADC and data transmission and storage. The complex data  $\hat{x}_m$  can be sampled at rates higher than Nyquist to achieve more steering directions if the interpolation beamformer is not used.

### 4.1.2 Frequency-domain Beamforming

In the discrete-frequency domain, the application of a discrete Fourier Transformed (DFT) outputs are compensated for the delay by means of a phase shift. The frequency domain equivalent of the time domain waveform from each sensor output  $x_n(t)$  is obtained from its *Fourier transform*:

$$x_m(t) \xrightarrow{\mathcal{F}} X_m(f).$$

Similarly, the Fourier transform can be applied to the beamforming process:

$$B(t) \xrightarrow{\mathcal{F}} B(f, \tau_m) = \sum_{m=0}^{M-1} a_m X_m(f) e^{-j2\pi f \tau_m}.$$

where the phase  $2\pi f \tau_m$  is the phase equivalent of the geometric time delay  $q_\tau$ .

#### Discrete Fourier Transform (DFT)

The discrete form of the beam output can be obtained with the use of *the Discrete Fourier Transform* (DFT), where the discrete frequency domain sequence  $X_m(k)$  is described as follows:

$$X_m(k) = \sum_{n=0}^{N-1} x_m(n) e^{-j2\pi nk/N}, \quad (4.5)$$

where  $k$  is the index of the DFT output in the frequency domain, also called *the frequency bin index*,  $n$  is the time domain index of the input samples,  $N$  is the number of samples of the input sequence, which also describes the number of frequency points in the DFT output. The DFT frequency resolution is determined by the number of samples  $N$  and by the sampling rate  $f_s$ :

$$\frac{f_s}{N}. \quad (4.6)$$

$f_s/N$  also determines *the fundamental frequency* of the DFT, where each frequency bin of the DFT is the integer multiple of this fundamental frequency:

$$f_k = k \frac{f_s}{N}, \quad (4.7)$$

where  $0 \leq k \leq N-1$ . The resolution can also be improved with the zero-padding technique. In contrast to interpolation, the zero-valued samples are appended to the end of

the time sequence. This method will improve the DFT output resolution, as the continuous Fourier transform is sampled more often, but the spectral resolution remains the same. To improve spectral resolution more non-zero value samples are needed. The DFT gives correct values only when the input samples contain energy at the centre of the  $m^{\text{th}}$  frequency bin. If the input sample contains energy at the intermediate frequency, this signal will leak into the neighbouring DFT output samples. This phenomenon is called *DFT leakage*, which can be minimised with windowing functions but cannot be completely eliminated.

Each frequency bin of the DFT can be treated as a narrow bandpass filter whose frequency is centred at the analysis frequency  $f_s/N$ . By decreasing the bandwidth of the bandpass filter (increasing  $N$ ) the frequency resolution can be improved and the DFT magnitude<sup>2</sup> raise above the average background noise. This ability of the DFT to pull out the weak signals from the background noise is called *the DFT processing gain*. The  $N$ -point DFT requires  $N^2$  complex multiply-additions making it inefficient and expensive. In 1965 an algorithm was published to compute the DFT with only  $N \log_2(N)/2$  multiply-addition operations, called *the Fast Fourier Transform FFT* (Cooley & Tukey, 1965). It allows one to break the  $N$ -point DFT into smaller components. Finally, the frequency domain representation of the time domain beam output is:

$$B(k, \tau_m) = \sum_{m=0}^{M-1} a_m X_m(k) e^{-j\omega_k \tau_m}. \quad (4.8)$$

It can be readily observed that the steering directions are no longer limited by the sampling frequency and the beam output will resemble the continuous beam output in Figure 4.1 rather than the quantised beam output in Figure 4.2. Hence, the sampling frequency has to only satisfy the Nyquist criterion. The limiting factor comes from the number of samples  $N$  of the input sequence that describes the number of frequency points in the DFT output. As the beams are formed in the frequency domain, no time delays are inserted during the beamforming process. The steering is accomplished by multiplying the Fourier transformed input signals by the complex steering factor matrix of size  $M \times N$  times the number of beams.

---

<sup>2</sup>For real inputs with frequency  $f$  less than half of the sampling frequency  $f_s$ , with  $N$  samples and peak amplitude of  $A_0$  the DFT magnitude  $M_r$  is defined as  $A_0 N/2$ . For complex sinusoid, the output magnitude  $M_c$  of the DFT is  $A_0 N$ .

### 4.1.3 Multibeaming in the Time and Frequency Domain

In modern radio astronomical observations, multibeaming allows telescope arrays to have a sensitive system with a FoV comparable to the size of primary element. As astronomical sources have to be tracked, due to the Earth's movement, pointing and tracking accuracy to retain sensitivity is of high importance. Creating multiple independent beams, that can be steered in any direction within the view of primary element, in either the frequency or time domain has its advantages and disadvantages that will be briefly reviewed now.

As discussed earlier, the steering directions in time-domain beamforming are quantised by the sample period  $t_s$ . For a linear array with equally spaced elements, the geometric delay can be expressed as:

$$\tau_m = \mathbf{r}_m \cdot \mathbf{k}_b / c = (m-1) \frac{d}{c} \sin \psi_b, \quad (4.9)$$

where  $\psi_b$  is the steering angle in direction  $\mathbf{k}_b$ . The quantised form of this equation is as follows:

$$q\tau = (m-1) \left\lfloor \frac{df_s}{c} \sin \psi_b \right\rfloor, \quad (4.10)$$

where symbol  $\lfloor \cdot \rfloor$  maps a real number to the largest previous integer, i.e.  $\text{floor}(x) = \lfloor x \rfloor$ . The number of beams  $N_B$  that can be synthesised with the given sample period  $t_s$ :

$$N_B = 2 \left\lfloor \frac{1}{\sin \frac{c}{df_s}} \right\rfloor + 1. \quad (4.11)$$

From that, the beam index  $b$  lies in the range  $-\lfloor N_B/2 \rfloor \leq 0 \leq \lfloor N_B/2 \rfloor$ , where  $b = 0$  signifies the broadside direction and is called *the main response axis* (MRA). The realisable pointing directions are:

$$\psi_b = \sin^{-1} \left( b \frac{c}{df_s} \right). \quad (4.12)$$

For a planar array with sensor spacing  $d_x$  along the x-axis and  $d_y$  along the y-axis, the number of beams formed is simply  $N_B = N_{B_x} \times N_{B_y}$ . To increase  $N_B$  the sampling frequency  $f_s$  would have to be increased, or for arrays with a large number of elements, the spacing between elements  $d$  can be varied by excluding some number of the antennas.

The minimum number of beams  $N_B$  that can be synthesised in frequency-domain for a linear array with equally spaced elements is equal to the number of elements in that array. Thus, the beam steering resolution is not affected by the sampling frequency  $f_s$ . As described in §4.1.2, the FFT can be used to compute the multidimensional DFT over space and time<sup>3</sup>. The first N-point FFT is performed on the time samples of each sensor to transform the signals to the frequency domain called the temporal FFT. The second M-point FFT is performed on the frequency bins for all sensors to transform the signals to the frequency-wavenumber domain called the spatial FFT. Each element data represents a beam in a direction:

$$\psi_b = \sin^{-1} \left( b \frac{c}{df_k M} \right), \quad (4.13)$$

where the beam index  $b$  is in the range  $-M/2 \leq b \leq M/2$ . The number of realisable beams can be increased by zero-padding the spatial FFT.

#### 4.1.4 Beamformers in Radio Astronomy

Beamforming has been used for the last century in applications of wireless communication, radar and sonar and are considered matured technology in those fields. The wide-spread use of beamformers in radio astronomy has been challenged by the demanding requirements for very low system noise and use of wide bandwidths. Fortunately recent hardware and software advances enable the development of beamformers for radio astronomy and a few relevant for this work will be reviewed here.

##### LOFAR Pipeline Software Beamformer

The LOFAR array is introduced in §2.3.1. At the station level, the data are split into 195 kHz or 156 kHz sub-bands that are then filtered by a Poly-Phase Filter (PPF) bank that consists of a number of 16 Finite Impulse Response Filters (FIR). The PPF produces up to 256 narrowband frequency channels of 763 Hz. These are typical values and can be modified since the filter bank specification is chosen in software at run time. Next the delays due to the signal arriving at different time at each sensor are compensated for and bandpass corrected, i.e. corrected for the filtering effects that cause channel-to-channel amplitude variations. What distinguishes LOFAR from other radio telescopes

---

<sup>3</sup>The signal is represented as a linear combination of frequency, direction, amplitude and phase.

is that the final array signal processing was done in software in real-time using an IBM Blue Gene/P supercomputer (Romein et al., 2011), which was recently upgraded to a graphic processing unit (GPU) based cluster, called COBALT. Beamforming is optional in the LOFAR processing. The signals from stations might be added together to form a virtual "superstation" with increased sensitivity. The beam can be formed coherently (phase correction) and incoherently (adding the amplitudes), i.e. (Mol & Romein, 2011; Stappers et al., 2011).

### **EMBRACE ASIC Beamformer**

*The Electronic Multi-Beam Radio Astronomy ConcEpt* (EMBRACE) is a array demonstrator for the SKA. The EMBRACE beamformer has a four level hierarchical architecture combining analog and digital phasing (Bosse et al., 2010). The digital custom-built <sup>4</sup> beamforming chip phases four elements from the aperture plane in 45° steps. The chip outputs two independent beams and constitutes the basic building block in the beamformer architecture. The analog summation of signals has three steps. First, the signals from three beamforming chips are combined. Then, summation of six of those signals create a tile beam. Finally, four tiles are connected together to form a beam from a station or a tile set.

### **LWA Delay-sum Beamformer**

*The Long Wavelength Array* (LWA) is an aperture synthesis imaging array under development in New Mexico. The LWA telescope utilises digital "true time delay" beamforming (Soriano et al., 2011). Each element pair of the array is equipped with a beam forming unit that computes a partial sum (§4.1.1) and forms four independent beams. This partial sum is next passed to another pair to add further partial sums. Thus, the LWA utilises the partial sum delay-sum beamformer described earlier in this chapter. The final sum is sent to four digital receivers (DRX). Phasing of elements is accomplished by delaying samples by the appropriate integer number of delays using a first-in-first-out (FIFO) buffer. Finer delays are computed with a finite impulse response (FIR) interpolation filter. Interpolation filters will be discussed in more details later in this chapter.

---

<sup>4</sup>Application Specific Integrated Circuit (ASIC)

## 4.2 Interpolation Filter Architecture

Interpolation is used with the time-domain beamforming to increase the number of *synchronous beams* i.e. beams that can be formed with integer number of delays as  $\tau_m = mT$ , where  $m$  is integer and  $T$  is the sampling time. Interpolation involves two steps:

- inserting  $L - 1$  zero-valued samples between each sample of the original signal called *up-sampling*. This step increases the Nyquist interval to contain  $L$  times larger bandwidth;
- passing the up-sampled signal through a digital lowpass filter that will pass only the baseband image and all images that reside on the multiples of the new sampling frequency  $Lf_s$ , in the bottom left panel in Figure 4.3. This lowpass filter is sometimes referred to as *the anti-imaging filter*.

For example Figure 4.3 depicts interpolation by  $L = 3$ , frequencies used in the MUST array and described in §3. A signal containing three tones, at  $f_L = 568$  MHz,  $f_c = 593$  MHz and  $f_H = 618$  MHz, is sampled at  $f_s = 182.46$  MHz, the top panel in Figure 4.3. The signal is up-sampled by  $L = 3$  i.e. two zero-valued samples are inserted between every pair of the original samples, the middle left panel in Figure 4.3. The spectrum of the up-sampled signal is shown in the middle right panel in Figure 4.3. The next step is to filter the up-sampled signal using the anti-imaging filter with the normalised stop frequency edge at  $\pi/L$ , the bottom left panel in Figure 4.3.

The anti-imaging filter is the most expensive stage computationally to implement. When designing a FIR lowpass filter, three characteristics can be varied in order to achieve the desired performance at affordable cost. First, is the filter order, or the length of the truncated impulse response<sup>5</sup>, example in the top left panel in Figure 4.4. The longer the filter length the better the approximation of the input samples. Second, is the transition width of a filter i.e. the difference between the stop-band and pass-band frequencies. Short transition width means better frequency selectivity and is usually achieved with longer filter length. Last, is the stop-band and pass-band ripple. Small ripples signify a small error between the ideal and actual filter. Various FIR filter architectures and design algorithms can also aid the implementations and a few will be reviewed in this chapter.

---

<sup>5</sup>The impulse response of the ideal lowpass filter is infinitely long sinc function.



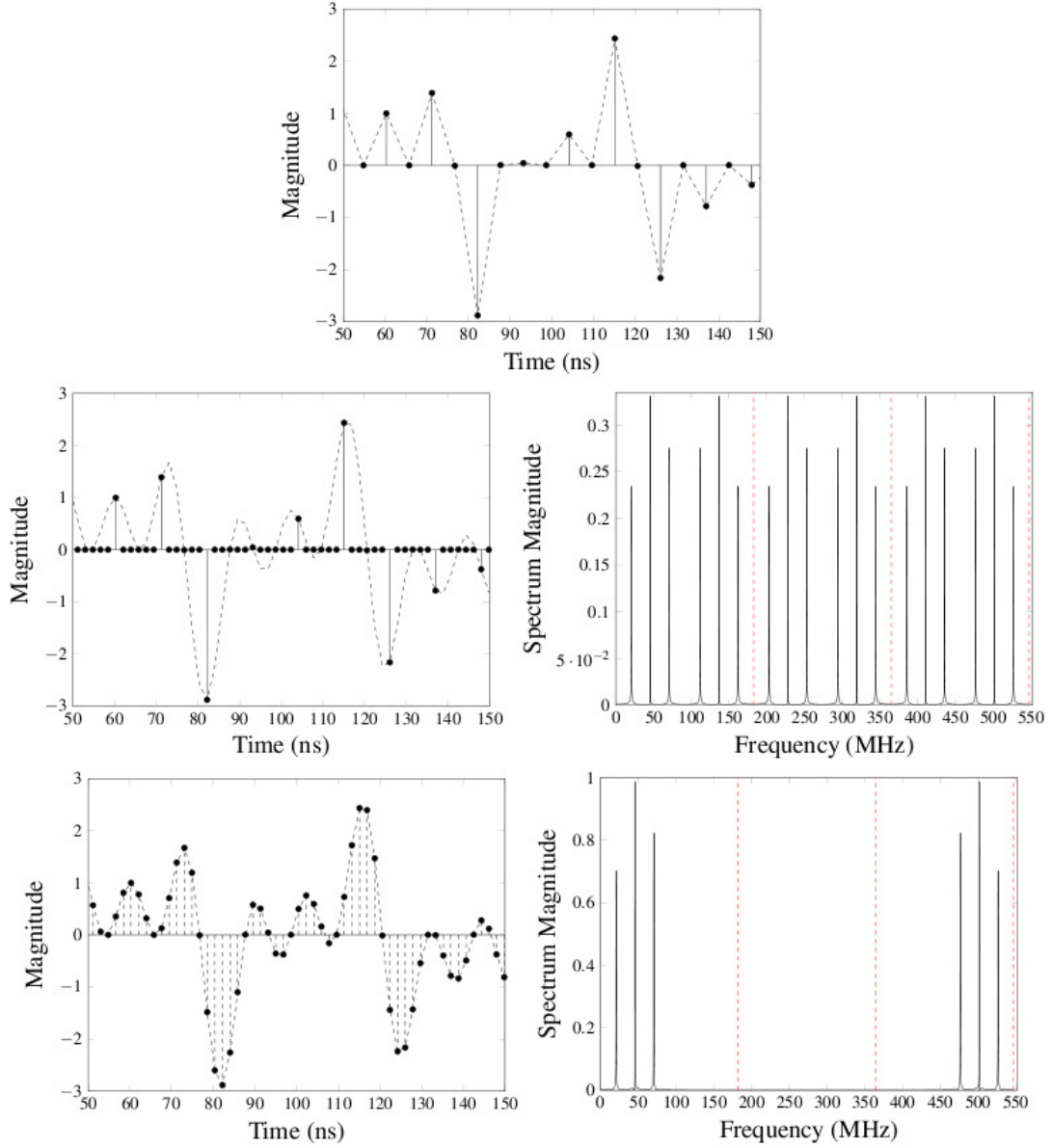


**Figure 4.3:** Illustration of the interpolation process. Red dashed lines indicate the multiples of the sampling frequency. (Top) The original discrete-time signal; (middle left) discrete-time signal up-sampled by  $L = 3$ ; (middle right) frequency-domain representation of the up-sampled signal; (bottom left) up-sampled discrete-time signal passed through the anti-imaging filter; (bottom right) frequency-domain representation of the filtered signal. Only the one-sided spectrum of the baseband image is shown for clarity.

### 4.2.1 Direct-form

The direct-form filter, also called a *tapped delay line*, is the most basic and the most expensive FIR filter design technique. The filter order is dictated by the number of delay elements in the filter and filter length is equal to the number of coefficients, or tap weights. Each sample is multiplied with a coefficient and accumulated to form an output sample<sup>6</sup>. The direct-form implementation does not take advantage of the coefficient symmetry. Thus, the implementations costs are highest for the direct-form filter. The cost can be improved with the symmetric direct-form implementation, where the coefficient symmetry<sup>7</sup> is exploited halving the filter length as a result. For FIR filters implemented on FPGAs, the transposed direct-form structure is often used as the multiplications and additions are performed in a parallel fashion.

### 4.2.2 Polyphase Form

In practise, the interpolation filters are less often realised in the form described in §4.2.1 as the multiplication by zero, in the top left panel in Figure 4.3, are a waste of resources. Instead, a much more efficient approach is the *polyphase decomposition* of the direct-form filter transform function, in the top left panel in Figure 4.4. Effectively, the interpolate-by- $L$  filter transfer function is split into  $L$  sub-filters<sup>8</sup>  $H_l(z) = z^{l/L}$ , where  $l = 0, 1, \dots, L-1$  and  $H$  is the  $z$ -transform of the impulse response, Figure 4.4 top right and bottom panels. The impulse response is effectively decimated by  $L$ . The interpolated signal is produced with a commutator that operates at the sampling frequency  $Lf_s$  or with a direct filter structure. Hence, the multiply-accumulate operation (MAC) operations can be performed at the lower sample rate. Each sub-filter is an all-pass filter with different phase shifts, see §4.4. In practice, only the sub-filter  $H_0(z)$  is truly all-pass as it is a pure delay, in the top right panel in Figure 4.4. Thus, the sub-filters are only approximations of the ideal FIR filters.

### 4.2.3 Multistage Form

To make the design more optimum in term of number of multipliers, adders and overall complexity, a filter can be implemented using many smaller order filters of different architectures in cascade. For example, the interpolate-by-4 FIR can be implemented

---

<sup>6</sup>Multiply-accumulate operation (MAC)

<sup>7</sup>When the coefficients are symmetrical around the centre coefficient.

<sup>8</sup>Fractional advance filters.

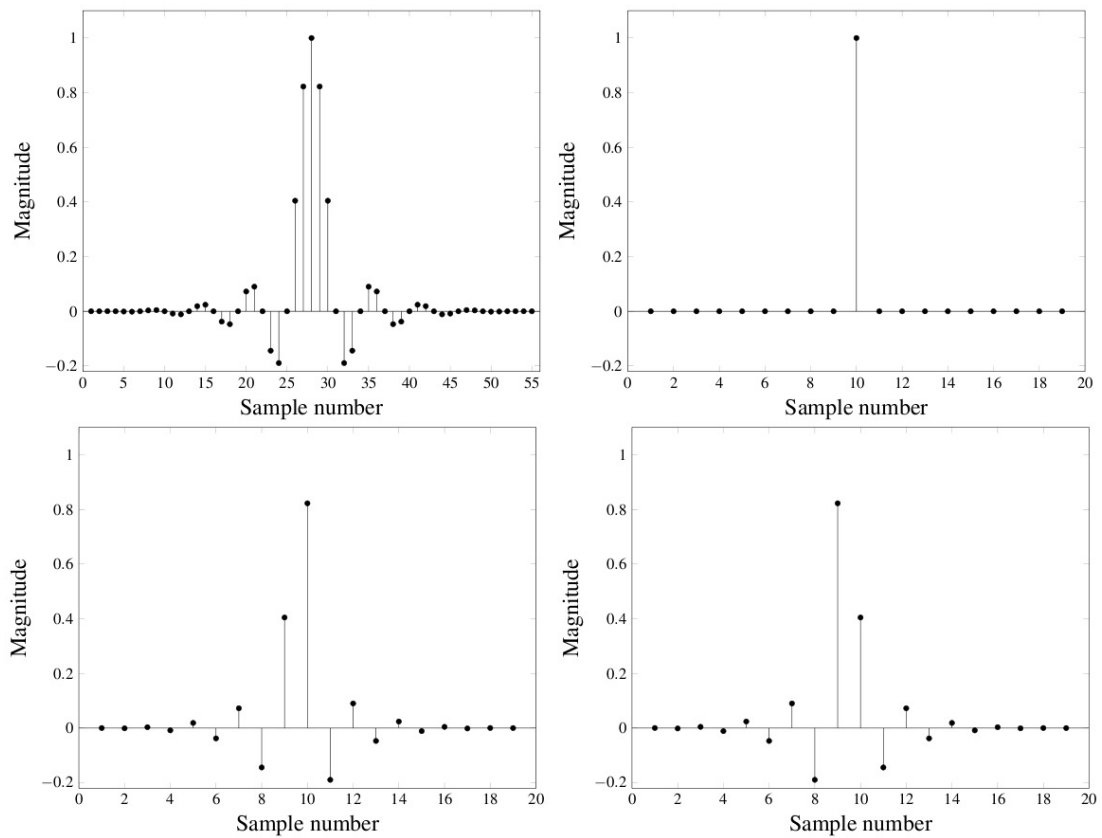


**Figure 4.4:** The polyphase decomposition of the interpolate-by- $L$  filter, here  $L = 3$ . (top left) The impulse response of the interpolate-by-3 filter; (top right) Sub-filter  $H_0(z)$ ; (bottom left) Sub-filter  $H_1(z)$ ; (bottom right) Sub-filter  $H_2(z)$ .

with two halfband<sup>9</sup> filters in cascade. The reduction in the number of multipliers and adders between the single (Direct) and multistage ( $H_{HB}$ ) design is listed in Table 4.2.

To reduce the number of multipliers and adders, a cascaded integrator–comb (CIC) filter can be used as the last stage of the multistage design. The advantage of CIC filters is that they are implemented without multipliers as only addition and subtraction are used. In addition, there are no coefficients to store. CIC filters provide better attenuation in designs with multiple sections, i.e. more than two. We show an example here for completeness. Figure 4.5 shows two realisations of interpolate-by-4 filter, two half-band  $H_{HB}$  (solid) and halfband with CIC filter  $H_{CIC}$  (dashed). The hardware savings are also listed in Table 4.2. It is evident that for this design, two halfband filters provide more attenuation than the combination of halfband and CIC filters. However, for the halfband and CIC combination the savings in multipliers and adders are substantial and this solution should be considered for designs with higher degree of interpolation.

**Table 4.2:** Summary of the computational cost of the direct and multistage implementation interpolate-by-4 FIR. Two different multistage implementations are analysed. Namely, two halfband filters in cascade  $H_{HB}$  and a halfband and a CIC filter in cascade  $H_{CIC}$ .  $N_M$  is the number of multipliers,  $N_A$  is the number of adders,  $N_S$  is the number of states, MPIS is the multiplications per input sample and APIS is the additions per input sample.

|           | $N_M$ | $N_A$ | $N_S$ | MPIS | APIS |
|-----------|-------|-------|-------|------|------|
| Direct    | 42    | 39    | 13    | 42   | 39   |
| $H_{HB}$  | 28    | 26    | 26    | 44   | 41   |
| $H_{CIC}$ | 12    | 17    | 17    | 12   | 20   |

### 4.3 Interpolation Filter Implementation

Taking into account the above discussion, the chosen architecture for the interpolation filter is the polyphase decomposition of the transfer function to reduce the implementation cost. As discussed in the §3, the signal is sampled at only three times the original bandwidth rate. Thus, some degree of interpolation is required for accurate delay adjustments. From Equation 4.11, the sampling period  $T_s$  of 5.5 ns for the MUST array, allows one to form five synchronous beams, i.e. at  $0^\circ$ ,  $\pm 24.3^\circ$  and  $\pm 55.3^\circ$ . To uniformly sample the sky, the sampling has to be fine enough to allow us to form TABs in steps equal to the  $HPBW/2$ . From §3, the  $HPBW_{vL}$ , at the lower edge of the frequency

<sup>9</sup>Nyquist filter where every second coefficient of the impulse response is equal to zero.

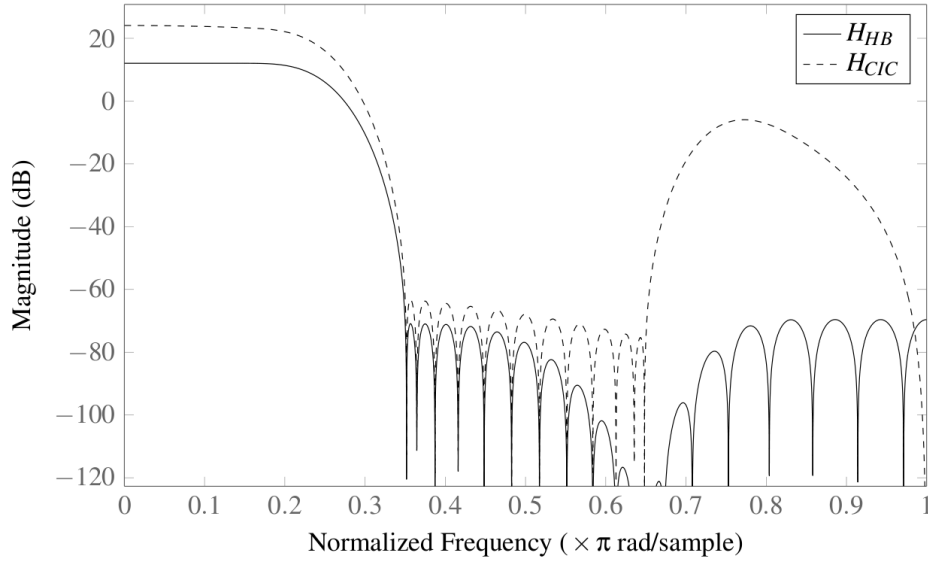


**Figure 4.5:** Magnitude Response (dB) of a multistage interpolate-by-4 filter; (dashed black) a halfband and a CIC filter in cascade  $H_{CIC}$ ; (solid black) two halfband filters in cascade  $H_{HB}$ .

band, is equal to  $5.28^\circ$ . From Equation 4.12, to steer a TAB to  $2.64^\circ$  off the zenith the sampling period  $T_s$  need to be decreased to 1.2 ns. This fine sampling would allow us to synthesise 25 beams along one axis of the array, as plotted in Figure 4.6. However, as stated in §3.5.2, a ROACH-1 board can be clocked at up to 550 MHz. This is a theoretical limit and can be reduced to a lower value depending on the complexity of the design implemented on the ROACH. With the design constraints, an interpolation by a factor of three already reaches the theoretical limit of the ROACH clock speed. Thus, to implement the interpolation filter on the ROACH board the bandwidth has to be decreased.

To demonstrate this multi-rate<sup>10</sup> processing for the time-domain beamforming on the ROACH board, the original bandwidth of a signal is decreased by a factor of 10, from  $f_c \pm 25$  MHz to  $f_c \pm 2.5$  MHz. This way, the sampling frequency requirements are also lower. The optimum determined  $f_s$ , for this lower bandwidth example, is 40.2 MHz. The centre frequency  $f_c$  will then shift down (aliased) to 10 MHz, or  $0.125\pi$  in terms of the normalised frequency. As explained in §3.5.2, the idle bands between the spectral replicas are chosen to be wide enough so that the transition band width can also be relaxed, saving FPGA resources.

<sup>10</sup>Systems where the input signal has a different sampling rate than the output signal.

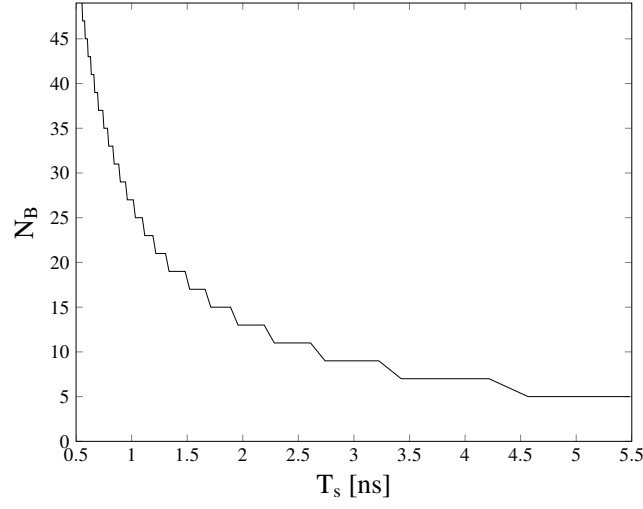


**Figure 4.6:** The relationship between the number of beams  $N_B$ , i.e. realisable directions, and the sampling time  $T_s$ .

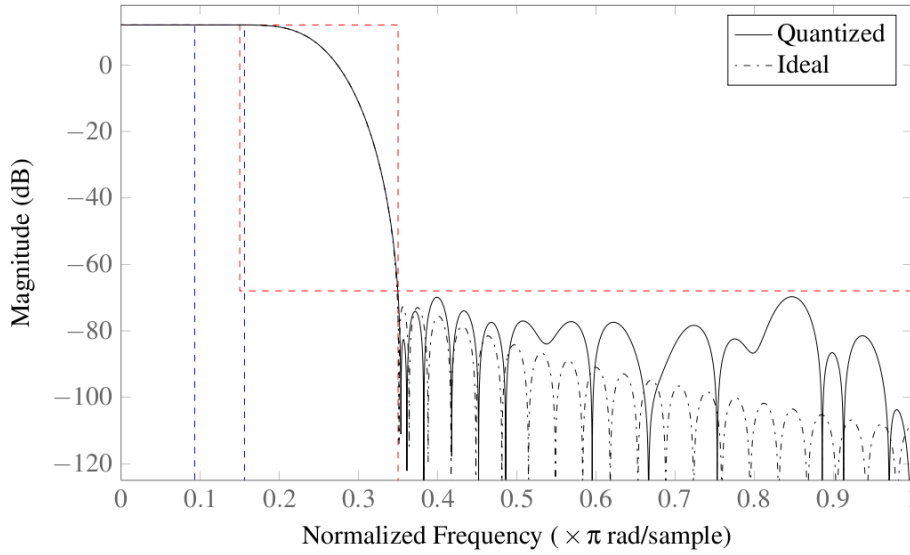


**Figure 4.7:** Magnitude Response (dB) of an interpolate-by-4 filter; (dashed red) shows the transition band; (dashed blue) illustrates the frequency range; (dashed black) double-precision floating point magnitude response; (solid black) fixed-point magnitude response plotted for normalised frequencies.

The coefficients for the interpolate-by-4 FIR were optimised for the transition band of length  $0.2\pi$  and the stop-band attenuation of 80 dB. Moreover, the interpolate-by-4 FIR is a Nyquist filter with a cut-off frequency equal to  $\pi/4$ , i.e. where every  $4^{th}$  sample is equal to zero. The reasoning for that is given in §4.2.2. The magnitude response of this filter is shown in Figure 4.7 (dashed black line). The highest frequency in the band  $f_H$  after sampling will be positioned just at the start of the transition band, i.e. at  $0.156\pi$ . As the impulse response values, i.e. coefficients, have to be represented in a fixed-point format for the ROACH, the number of bits that represent the fractional values has to be chosen carefully. Most of the impulse responses follow a sinc shape, as illustrated in the top left panel in Figure 4.4. For long impulse responses, the values at the edges are very close to zero. Thus, with too little bits the fractional values might not be represented with enough precision affecting the magnitude response. For example increasing the sidelobes level, as illustrated in Figure 4.7 (solid black line).

To follow the CASPER tool-flow, §3.5.2, the interpolation-by-4 FIR was implemented in Simulink using CASPER and Xilinx blocks, shown in Figure 4.8. Continuous sinusoidal signal, a single tone of frequency 590 MHz, is used to simulate a source. Data, represented as signed integers with 8 bit precision, is digitised with the QuadADC block with a sampling frequency of 40.2 MHz and fed to a FIR with coefficients calculated with a Matlab script. Each signal colour in the figure signifies different data rates. For example, a signal entering the FIR (green) has a sample time of 24.8 ns. The interpolated signal (red) sample time is four times finer at 6.21 ns, as expected. The model from Figure 4.8 was tested on the ROACH-1 to verify the interpolation. Figure 4.9 shows the results of that test, where the top panel shows the input samples to the FIR and the bottom one the interpolated signal with extra samples are indeed inserted in between the original samples.

## 4.4 Fractional filter

So far in this work, the term interpolation was used in relation to the process of up-sampling a data stream and then passing it through a low-pass filter. When a design is constrained with a maximum sample clock rate, like MUST, a signal has to be fractionally delayed without changing the sampling rate. Usually, the delay  $\Gamma$  is composed of an integer part  $\lfloor \Gamma \rfloor$  and a fractional part  $\mu$ ,  $\Gamma = \lfloor \Gamma \rfloor + \mu$ . The  $\lfloor \Gamma \rfloor$  part is implemented

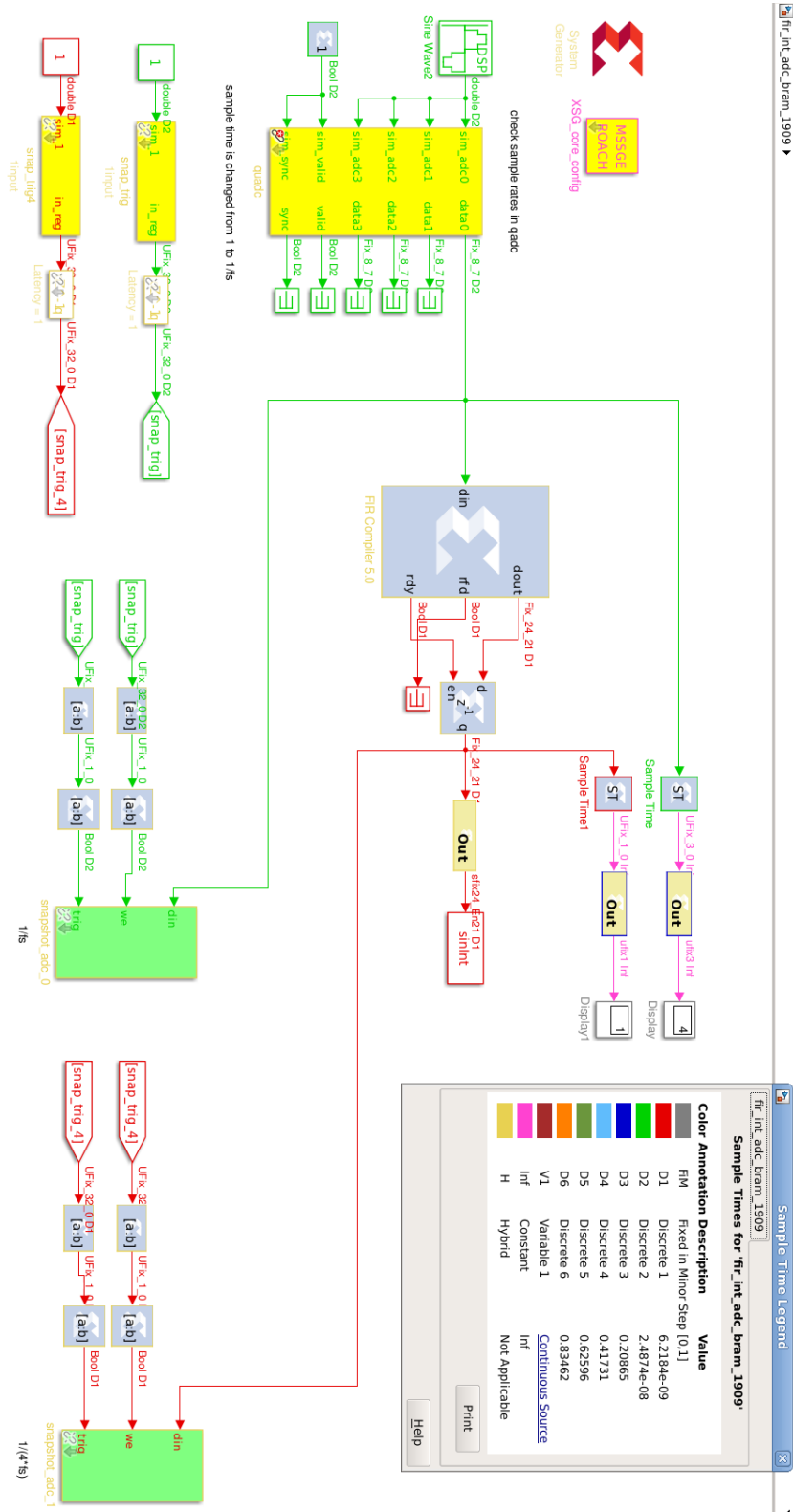


**Figure 4.8:** Simulink model of interpolate-by-4 FIR. Each signal colour in the figure signifies different data rates, values shown in the top right window. First, the data is digitised using the QuadADC block. Next, the digitised stream passes through a FIR interpolation filter. The data is acquired after the QuadADC block and after the interpolation stage for testing purposes.



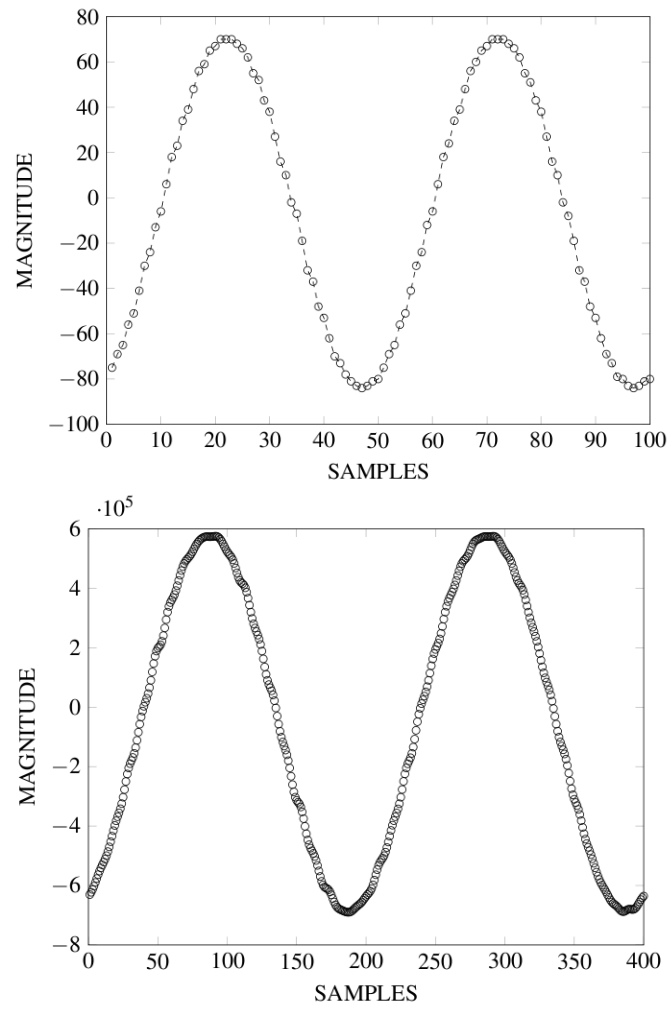


**Figure 4.9:** Signal interpolation on ROACH-1; (top) original; (bottom) interpolated signal. The increase in the number of samples can be clearly seen

with memory elements by storing the signal for  $\lfloor \Gamma \rfloor$  number of samples. To fractionally delay a digital signal, i.e. delay by a fraction of the sampling period time, we use fractional delay filters (FDF). The ideal frequency response of the FDF is defined as follows:

$$H_{id}(\omega) = e^{-j\omega(\lfloor \Gamma \rfloor + \mu)}. \quad (4.14)$$

The ideal impulse response is then a shifted and sampled sinc function,  $h_{id}[n] = \text{sinc}(n - \Gamma)$ , i.e. is infinite and has to be approximated with a FIR filter<sup>11</sup>. The important requirements for the FDF are unity magnitude response,  $|H(e^{j\omega})| = 1$  for all  $\omega$ , and a linear phase function, i.e. a linear frequency phase response  $\arg(H(e^{j\omega})) = -\Gamma\omega$  and a constant phase delay  $\tau_p(\omega) = \Gamma$ . So that the FDF resembles a pure delay.

To achieve those characteristics, we can compute new samples from the existing samples using interpolation techniques in the time domain, e.g. the Lagrange interpolation (Laakso et al., 1996). The Lagrange interpolation method is based on polynomial algebra and states that an  $N^{\text{th}}$ -order polynomial can be matched to  $(N + 1)$  arbitrary points to calculate FDF coefficients  $h(n)$ :

$$h(n) = \prod_{\substack{k=0 \\ k \neq n}}^N \frac{\Gamma - k}{n - k}, \text{ for } n = 1, 2, \dots, N, \quad (4.15)$$

where  $N$  is the order of the FIR filter. For example, top panel in Figure 4.10 shows magnitude and phase delay responses of a first-order Lagrange FDF for different values of delay  $\mu$ . The magnitude lines, left panel, decrease with frequency and the phase delay lines, right panel, at low frequencies are almost constant but approach the nearest integer delay at high frequencies<sup>12</sup>. It is clear that a low-order Lagrange FDF is only applicable when the signals are heavily oversampled. Moreover, the filter order  $N$  is the only design parameter, which makes the design goals like stop-band attenuation or pass-band ripple difficult to meet. The flat magnitude response and a linear frequency phase response are difficult to control in the time domain, as demonstrated above. In frequency domain, the filter characteristics can be specified in terms of the desired magnitude and phase responses using, for example, magnitude frequency response approximation (Laakso et al., 1996). As shown in the bottom panel in Figure

<sup>11</sup>FDF can also be approximated with the infinite impulse response (IIR) filters, but are not reviewed here.

<sup>12</sup>Apart from  $\mu = 0.5$  due to the  $h(n)$  symmetry mimicking a linear-phase filter.

4.10, the magnitude and phase delay responses of a third-order Lagrange<sup>13</sup> FDF for different values of delay  $\mu$ . The magnitude lines, left panel, and the phase delay lines, right panel, now remain constant for 75% of the band only approaching the nearest integer delay at very high frequencies. The computational cost of the first-order and third-order Lagrange FDF filters are listed in Table 4.3.

**Table 4.3:** Summary of the computational cost of a first-order  $H_1$  and third-order  $H_3$  implementation of Lagrange fractional interpolator.  $N_M$  is the number of multipliers,  $N_A$  is the number of adders,  $N_S$  is the number of states, MPIS is the multiplications per input sample and APIS is the additions per input sample.

|       | $N_M$ | $N_A$ | $N_S$ | MPIS | APIS |
|-------|-------|-------|-------|------|------|
| $H_1$ | 1     | 2     | 1     | 1    | 2    |
| $H_3$ | 65    | 59    | 9     | 65   | 59   |

Despite those disadvantages the Lagrange method is very popular for implementation of FDF on FPGA. This is because the Lagrange FDF can be decomposed into parallel sub-filters with fixed coefficients for a given order  $N$ , called the Farrow structure (Farrow, 1988). The only parameter that changes is the delay  $\mu$  and there is no need for updating the sub-filter coefficients. For a fractional delay  $\mu$  that changes often, even with every sample, the Farrow structure is advantageous.

## 4.5 Polyphase Filter Bank

The processing of astronomical signals is often done in the frequency-domain, where signals require channelisation. However, data quality may deteriorate due to the leakage during the transformation to the frequency domain. In radio astronomy signal processing, an assumption is often made that the frequency bins in the FFT are independent. As introduced in §4.1.2, if the signal does not exactly lie on a frequency bin, spectral leakage will be introduced causing localized spreading of frequency components. Next, we investigate the effects of frequency and the time domain signal processing techniques on pulsar data.

<sup>13</sup>Matlab script adapted from <http://legacy.spa.aalto.fi/software/fdtools/>

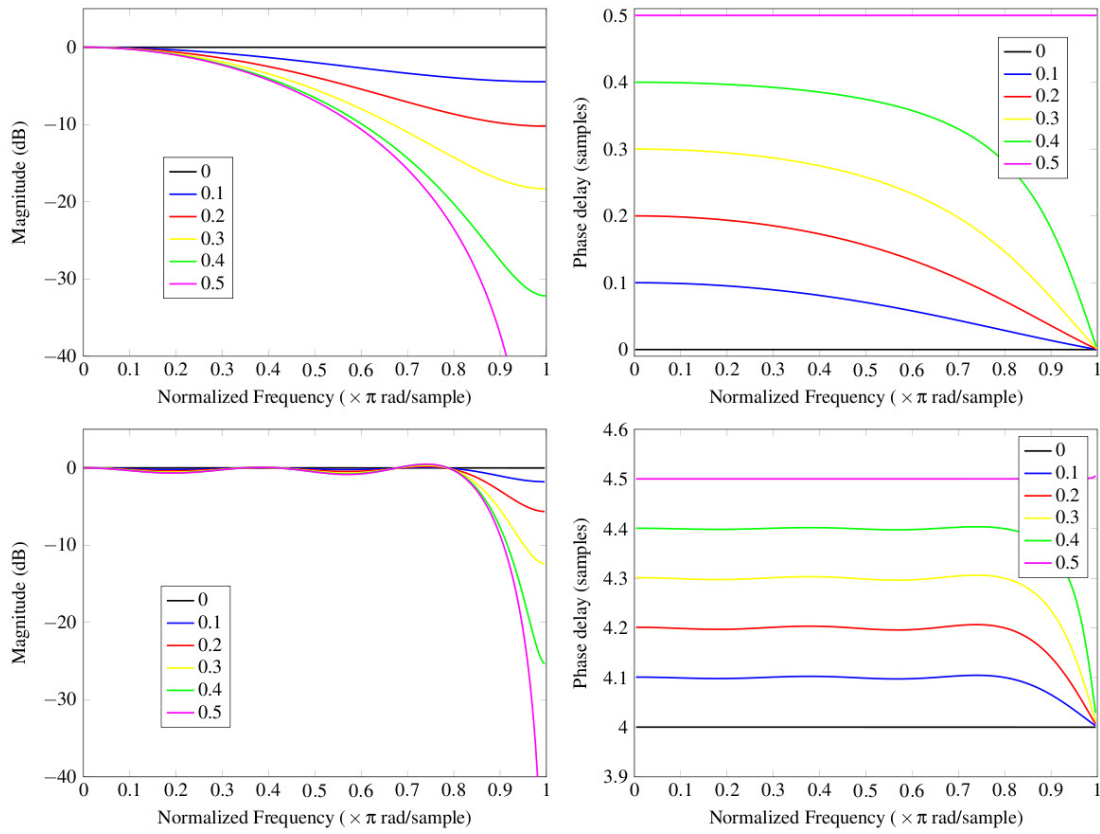


**Figure 4.10:** Magnitude and phase delay responses, left and right panel respectively, of a first-order Lagrange fractional interpolator (top) and for a third-order Lagrange fractional interpolator (bottom) for different values of delay  $\mu$ .

### 4.5.1 Implementation

A filter bank is a collection of filters that share common input and a summed output. First, the original signal is passed through a set of  $K$  filters where it is decomposed into  $K$  channels, or sub-bands. If all sub-bands are of equal width, then the filter bank is called *uniform*. The number of output samples from each sub-filter is the same as the number of input samples and as a result there is  $K$  times more samples. Thus, the sub-band streams have to be decimated<sup>14</sup> by  $K$ . This first step of decimation and channelisation is called the *analysis filter bank*. Splitting the signal bandwidth into smaller chunks allows for better treatment of more important frequencies. Next, the processed sub-bands have to be combined into a single data stream. This set of filters have to provide the near perfect reconstruction of the original signal. Also, sub-band streams have to be interpolated to return to the original number of samples. This is called the *synthesis filter bank*. The applications of filter banks include providing frequency-selective separation between the channels and convenient processing on smaller bandwidths.

There are several techniques for designing filter banks, but here only a polyphase uniform DFT filter bank will be reviewed<sup>15</sup>. First, a low-pass *prototype filter* is designed with an approximate bandwidth of  $\pi/K$ . Here, we use the classical windowed-based method for the design of a linear-phase prototype filter<sup>16</sup>. The desired characteristics of the filter are a sharp transition width and a minimum stop-band attenuation of at least 40 dB, so that the leakage from neighbouring channels can be minimised. The magnitude and phase responses of the prototype low-pass filter, with  $h_k[n]$  of 704 coefficients, are plotted in Figure 4.11, where  $K = 64$ . Next, the impulse response is decimated into  $K$  polyphase components, similar to the polyphase decomposition in §4.2.2, to save resources. The frequency responses of the  $K$  filters are uniformly shifted responses of the prototype filter by an amount  $2\pi k/K$ , where  $k = 0, 1, \dots, K - 1$ , see Figure 4.12.

<sup>14</sup>Decimation is the reverse process of interpolation where instead of computing new samples every  $L^{\text{th}}$  sample is discarded.

<sup>15</sup>The simplest method of implementing a filter bank is with the use of the DFT. The application of the DFT on an input signal suffers from leakage (§4.1.2) and from the loss in energy between frequency bin centres, i.e. scalloping loss. The polyphase filter bank suffers from the same drawbacks, but provides superior suppression of out-of-band signals.

<sup>16</sup><http://uk.mathworks.com/help/signal/ref/firl.html>

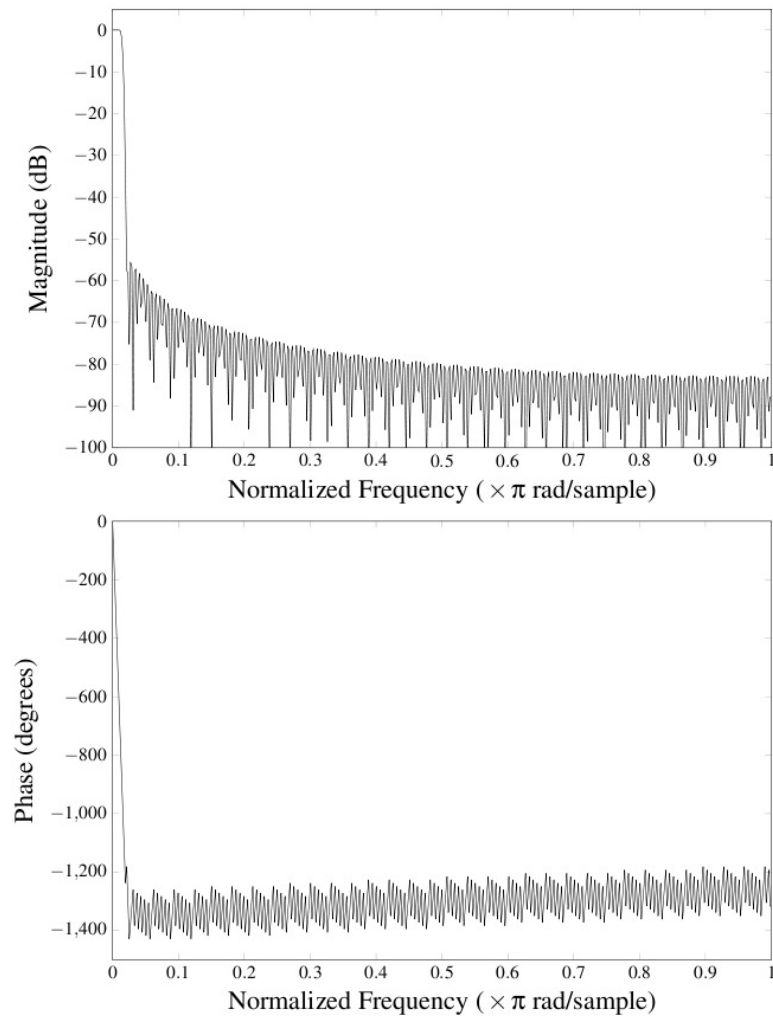


**Figure 4.11:** Magnitude and phase response of the prototype filter, the top and the bottom panel respectively, with a bandwidth of  $\pi/64$  and 704 coefficients.

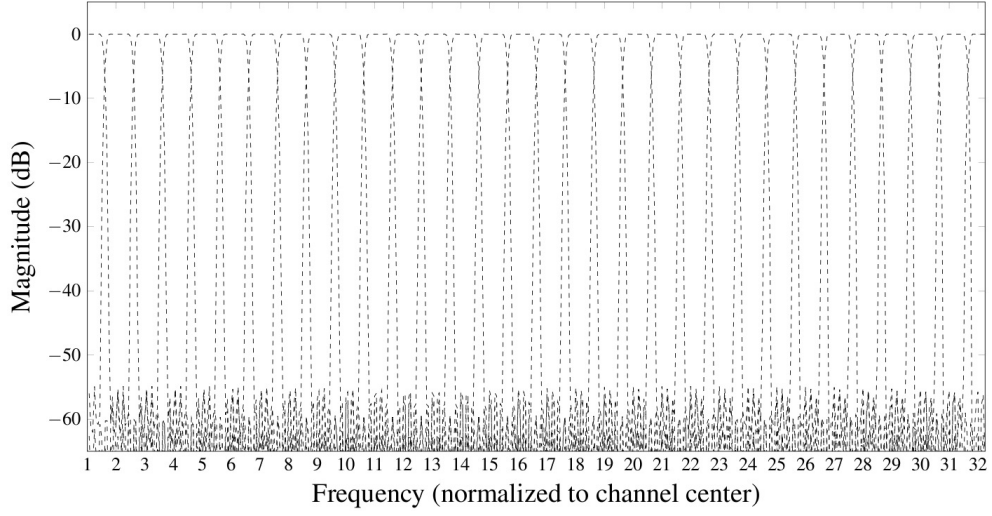


**Figure 4.12:** Frequency response of a 64-band polyphase filter bank. Frequencies are normalised to the channel centre. Only half of the polyphase filter bank is shown for clarity.

### 4.5.2 Simulating a Pulsar Signal

To investigate the effect of the frequency domain signal processing techniques on the pulsar data, we simulated<sup>17</sup> a 5 Hz pulsar observed at 1420 MHz with an observation bandwidth of 16 MHz for a duration of 2 seconds, see Figure 4.13. The data are modelled to be complex sampled at 16 MHz. We will call it the *original* data. This data set was split into 64 channels using six different filter banks, implemented using the technique described in §4.5.1, each with a different number of taps per filter component. We will call this the *channelised* data. As discussed earlier, better frequency selectivity can be achieved with more taps in the filter, i.e. sharp transition band. This can be observed when comparing Figure 4.14 and Figure 4.15, showing spectra from a 64 channel polyphase 2-tap filter bank and an 11-tap filter bank respectively. For the 11-tap filter component, the bandpass edges are much sharper than for the 2-tap equivalent. It can also be seen that the signal in each channel represents the actual bandpass shape. This is a general result and is not only applicable to the MUST telescope.

Next, we compare the data quality of the full un-channelised bandwidth with the data channelised with the six different filter banks. In Table 4.4 we list the error  $\Delta\tau_{\text{ToA}}$ , in the estimated arrival time (ToA), when we correlate the pulse profile of the original with the channelised data and the time delay  $\Delta\tau_{\text{GD}}$  between the original and the channelised data against the number of taps in the polyphase filter bank component. It can

<sup>17</sup>C. Bassa, private communication.

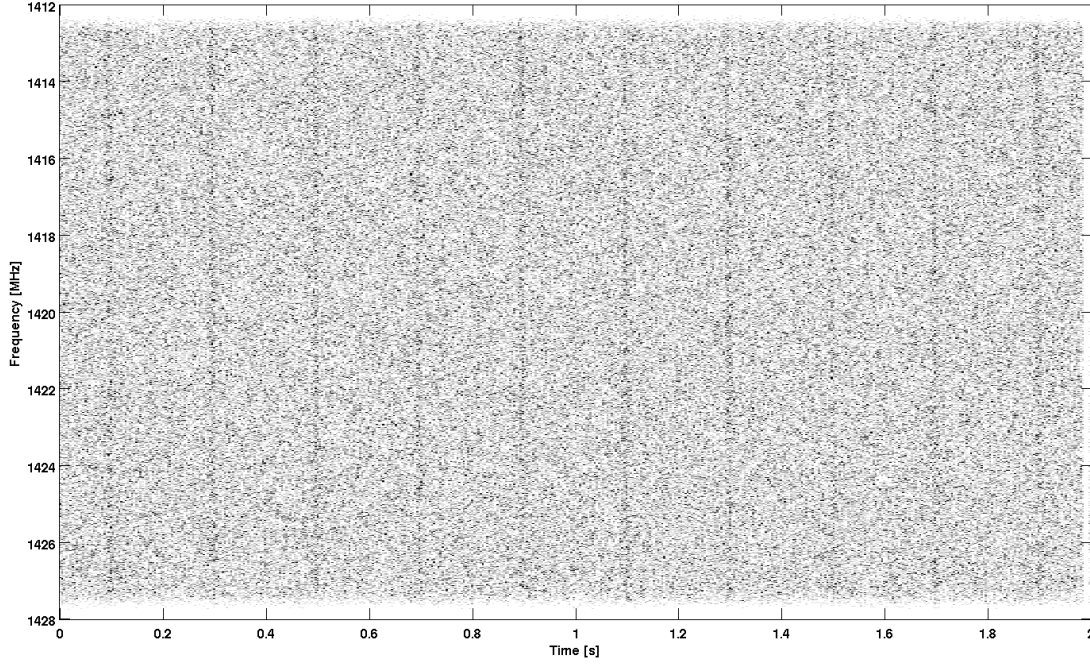


**Figure 4.13:** The dynamic spectrum of the 1420 MHz observation of a simulated 5 Hz pulsar with 16 MHz bandwidth.

be observed that as the number of taps increases, the error  $\Delta\tau_{\text{ToA}}$  decreases. This illustrates that more taps helps to preserve the data closer to its original form. Whereas, the delay  $\Delta\tau_{\text{GD}}$  is getting larger with the increasing number of taps. This is associated with the processing chain and the delay elements present in the filter structure. For example, for a given FIR filter with  $N$  taps, the delay is equal to  $(N - 1)/(2f_s)$ , where  $f_s$  is the sampling frequency. Thus, as the number of taps increases the delay associated with the additional stages in the processing chain will also increase. To obtain better statistics, we filtered a 60 second observation of the same pulsar with an 11-tap polyphase filter. The resulting error on the estimated arrival time  $\Delta\tau_{\text{ToA}}$  is  $52.4 \pm 0.8 \mu\text{s}$ , still within the error bounds when comparing to the 11-tap entry in Table 4.4. Moreover, the correlation of the pulse profiles of the original with the channelised data is consistent with the noise.

To determine whether the observed time delay  $\Delta\tau_{\text{GD}}$  is relatively constant for a chosen number of taps, we processed a 60 second observation of a 500 Hz pulsar with a 2-tap and 11-tap polyphase filters. The time delay  $\Delta\tau_{\text{GD}}$  between the original and the channelised data for a 2-tap and 11-tap filters is  $38.2 \mu\text{s}$  and  $56.2 \mu\text{s}$  respectively. While the  $\Delta\tau_{\text{GD}}$  is still in the same range as  $\Delta\tau_{\text{GD}}$  for the 5 Hz pulsar, the difference of



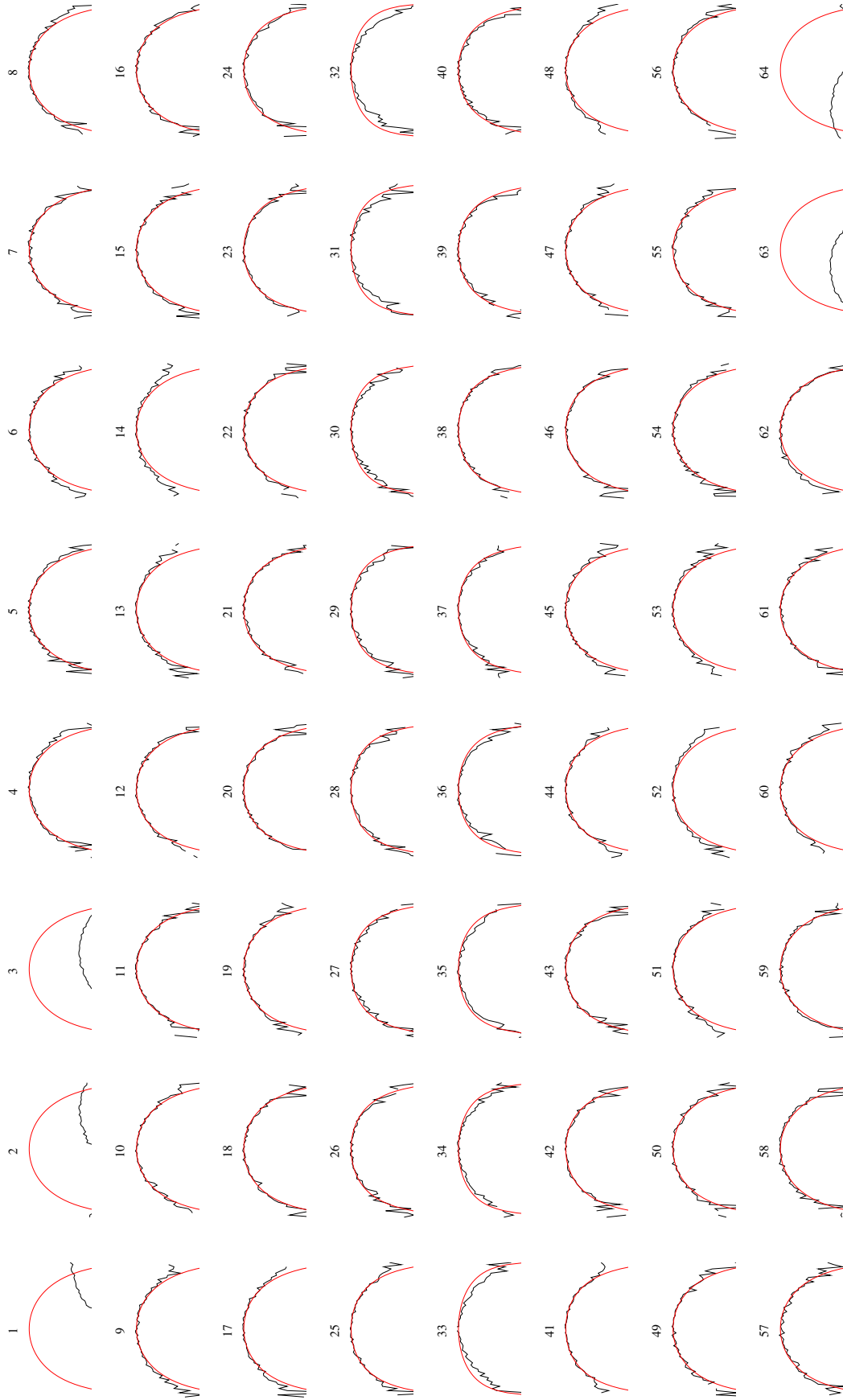


**Figure 4.14:** Spectra from 64 channels polyphase 2-tap filter bank. The figure shows a 16 MHz bandwidth partitioned into 64 250 kHz sub-channels. A bandpass shape of simulated sub-filter and the filtered data, red and black line respectively, can be compared.

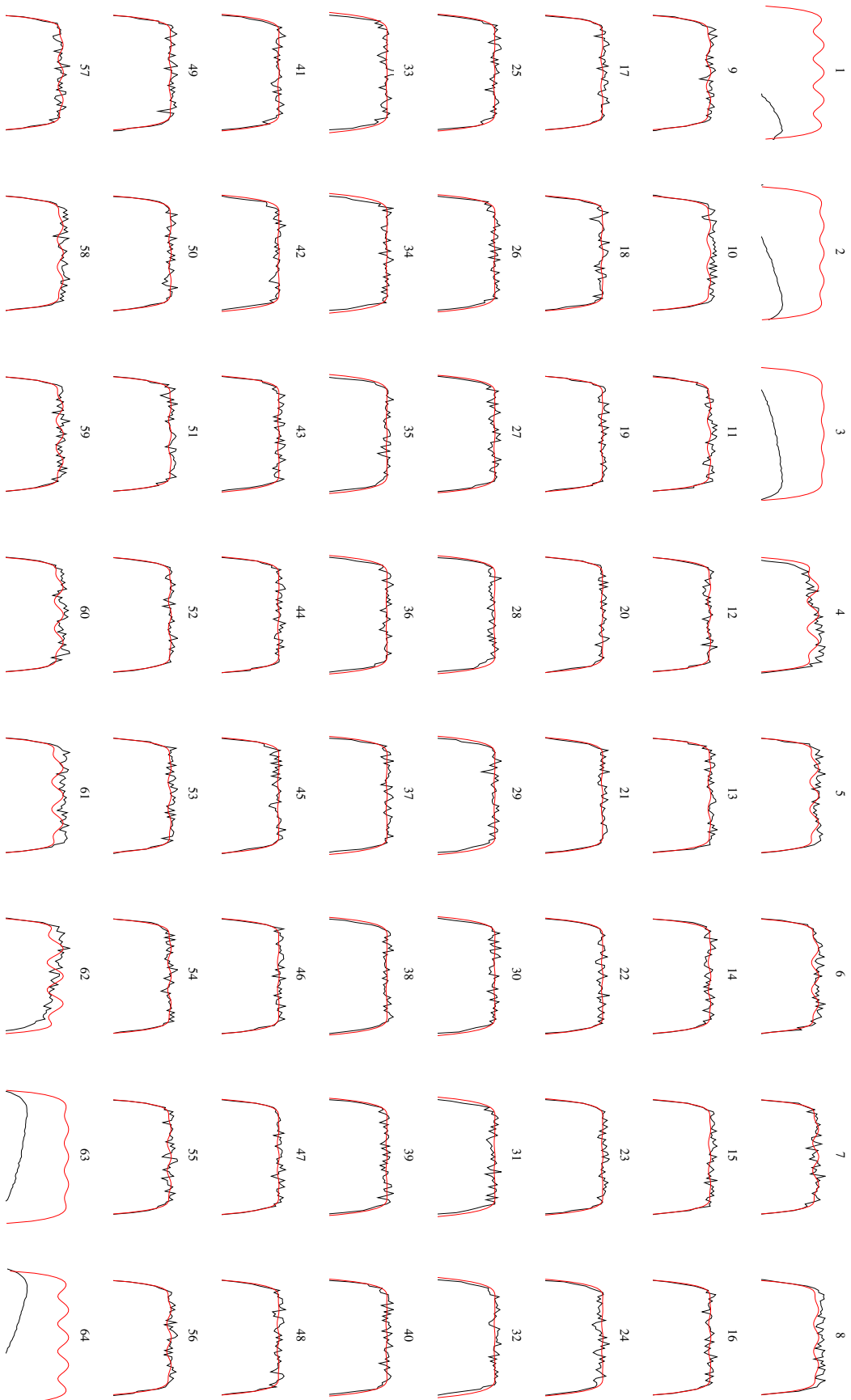


**Figure 4.15:** Spectra from 64 channels polyphase 11-tap filter bank. The figure shows a 16 MHz bandwidth partitioned into 64 250 kHz sub-channels. A bandpass shape of simulated sub-filter and the filtered data, red and black line respectively, can be compared.

**Table 4.4:** The relationship between the number of taps per filter component against the error  $\Delta\tau_{\text{ToA}}$  in the estimated arrival time (ToA) and the time delay  $\Delta\tau_{\text{GD}}$  between the original and the channelised data.

| Taps | $\Delta\tau_{\text{ToA}}$ | $\Delta\tau_{\text{GD}} [\mu\text{s}]$ |
|------|---------------------------|--|
| 2    | 2.51                      | 36.71                                  |
| 4    | 2.25                      | 39.27                                  |
| 6    | 2.23                      | 42.13                                  |
| 8    | 2.21                      | 45.60                                  |
| 10   | 2.11                      | 48.43                                  |
| 11   | 2.08                      | 51.04                                  |

the pulse profiles of the original with the channelised data no longer resembles noise. As the correlation is sensitive to the change in shape, the largest difference of around 5% of amplitude can be seen for the signal processed with a 2-tap polyphase filter. This distortion in the pulse shape, namely at the base, can be seen in the left panel in Figure 4.16. The pulse profile of the signal processed with an 11-tap polyphase filter has a lower amplitude difference of less than 1%, the middle panel in Figure 4.16.

## 4.6 Discussion

The main disadvantage of time-domain beamforming is the high implementation cost of the interpolation and/or fractional delay filters, as each beam requires its own chain of filters. By reducing the filter complexity, more filters can be implemented on a single board. We showed in §4.2 that by using polyphase decomposition a certain level of savings in terms of multiplications/additions per input sample can be achieved. It has been reported by Schobben & Sommen (1996) that polyphase decomposition can be exploited to further reduce the complexity when high angular resolution is needed, compared to the number of sensors used and the number of simultaneously formed beams. To introduce this idea, we plot the steps in the interpolation process with polyphase decomposition in Figure 4.17. The top panels show two signals, where the one in the top right panel lags by  $\omega T_s/2$ . The two signals have to be aligned before summation. Thus, interpolation<sup>18</sup> by  $L = 4$  is performed on both signals, Figure 4.17 middle. The new sampling time is equal to  $T'_s = T_s/L$ . Next, the delayed signal can be delayed by  $2T'_s$ , the right middle panel, and decimated by  $M = 4$ . The signal after

<sup>18</sup>Padding by zero and filtering.

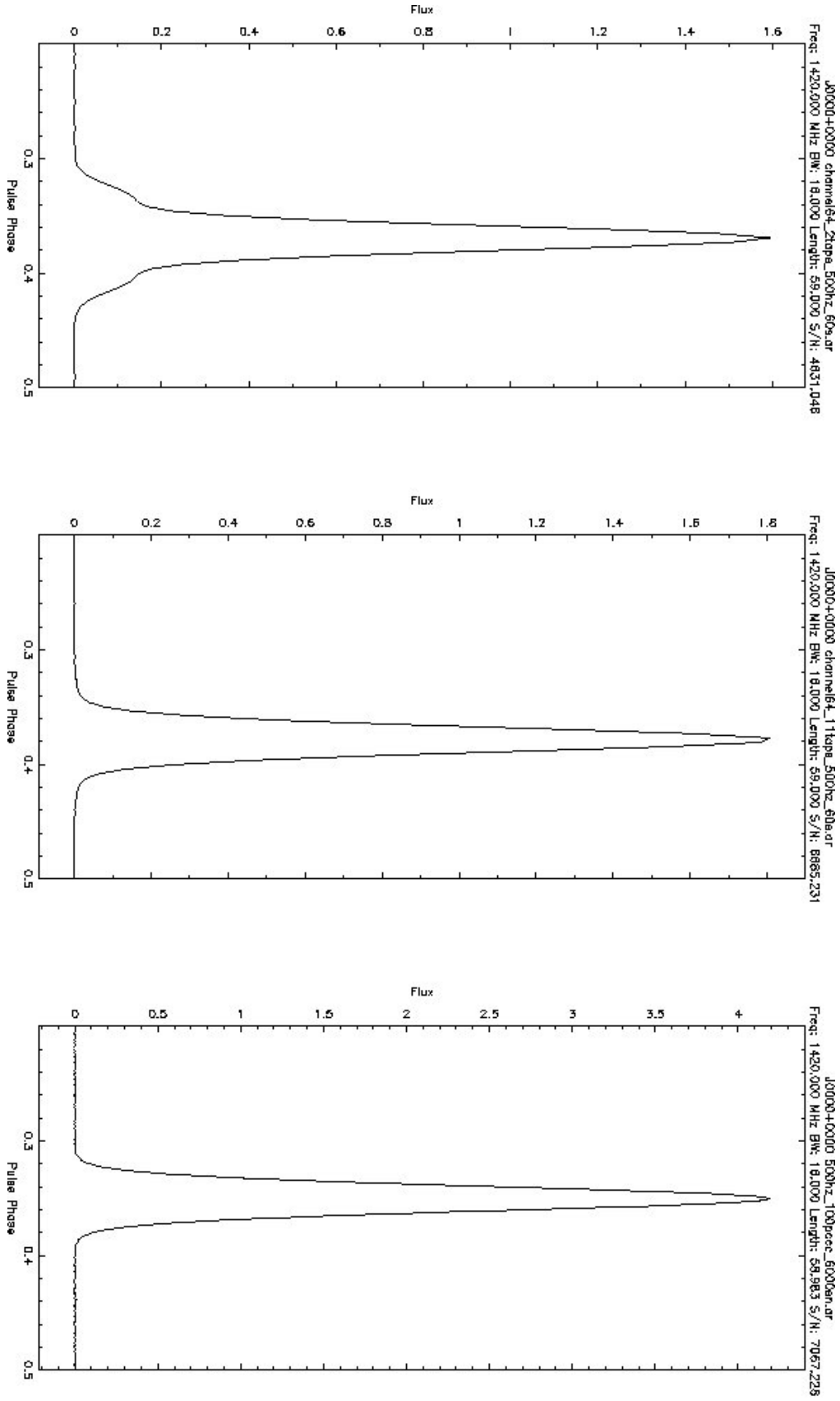


**Figure 4.16:** A pulse profile of a 500 Hz pulsar with 16 MHz bandwidth processed with a 2-tap and 11-tap per polyphase filters component; (left) 2-tap filter; (middle) 11-tap filter; (right) unfiltered.

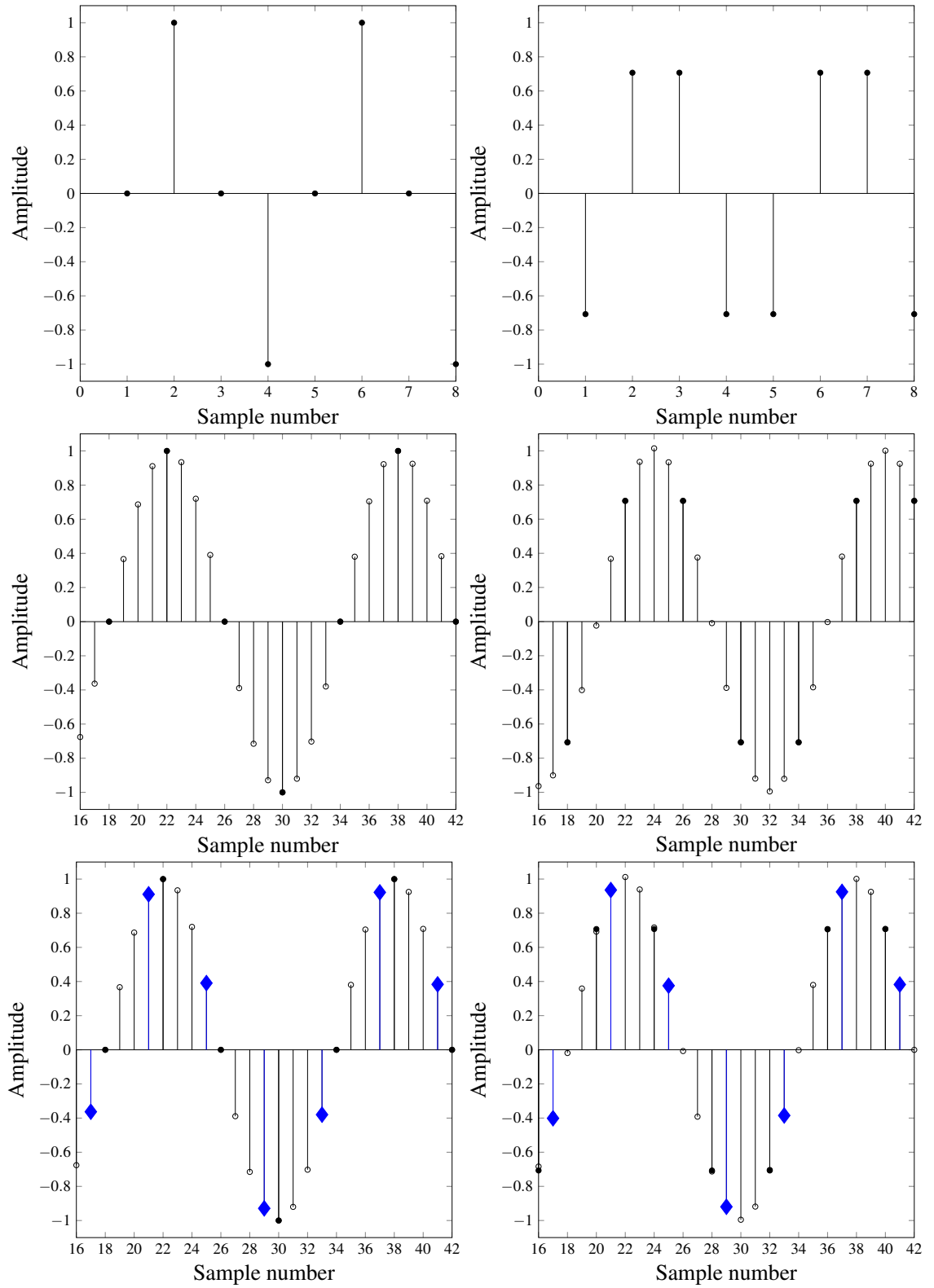


**Figure 4.17:** The steps in the interpolation process with polyphase decomposition. The top panels show two signals, where one is lagging the first by  $\omega T_s/2$ . In the middle panels, show two signals after interpolation. The bottom right panel, shows the delayed signal after delay adjustment. The blue diamonds indicate the samples left after the decimation stage. Original samples are marked with black circles.

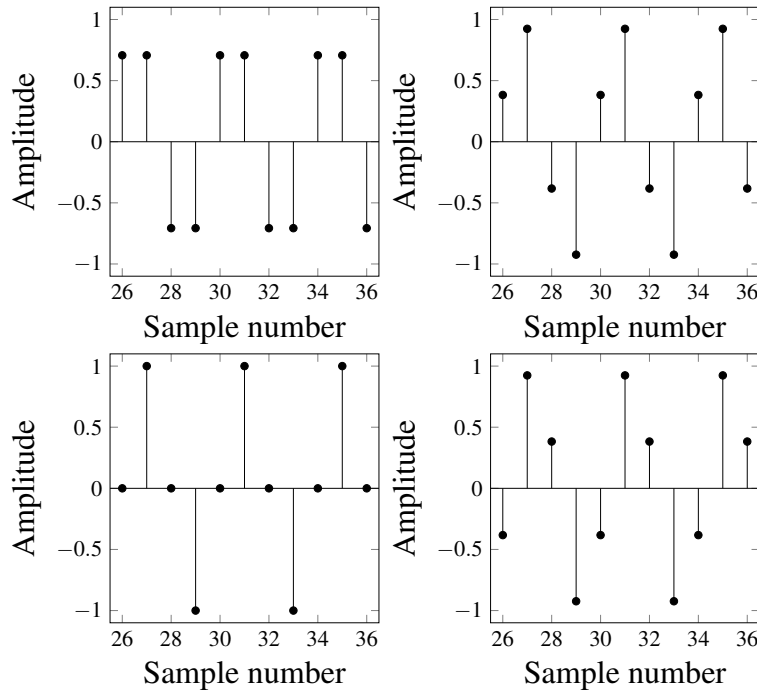


**Figure 4.18:** Polyphase components of the signal in the top right panel in Figure 4.17.

decimating is marked with blue diamonds. It is claimed that the polyphase filtering can be placed at the end of this chain, so that the fine delaying is performed on the zero-padded sequence, decimated and finally filtered. This is equivalent to choosing one of the polyphase filters and delaying over  $rT_s$ , where  $r = \lceil \tau_m/T_s \rceil$ . The total number of multiplications for this method is equal to  $M N_E N_B f_s/L$ , see Table 4.1 for a comparison with the pre-beamforming interpolation. This can be justified by studying Figure 4.18 depicting the polyphase components for the delayed signal. Since each polyphase filter computes the desired sample and only every  $L^{\text{th}}$  sample is used in the beamforming process, increasing the sampling rate can be avoided. As there is no follow up to this study, as far as the author is aware, a further development of this method could be useful for radio astronomy applications.

Another area, where the complexity of the implementation can be lowered is the fractional delay filter. It was shown in §4.4, that implementation of an FDF pass-band that closely resembles an all-pass filter requires a large number of coefficients. It has been proposed, e.g. Yli-Kaakinen & Saramaki (2006), that the coefficients of the modified Farrow structure (Vesma & Saramaki, 2000) can be efficiently quantised so that the implementation cost are minimised. This method includes setting to zero value

coefficients that have negligible effect on the overall system and the non-zero value coefficients are quantised to a few signed powers of two terms. Effectively, the implementation cost is only the number of adders and subtracters to implement the sub filters in the modified Farrow structure.

By combining the two methods, proposed above, of minimising the implementation costs of the interpolation and/or the FDF, an efficient structure for radio astronomy signal processing can be obtained.

We have also shown that the taps number per filter component in a polyphase filter bank can have an adverse effect on the pulse shape. This appears to be true for pulsars with a shorter pulse period. Increasing number of taps can improve the pulse shape recovery, but again for shorter pulse periods, the pulse shape is distorted. Moreover, changing the number of taps can lead to an offset, that is also demonstrated in the middle panel in Figure 4.16. Keeping track of such changes will be essential for high precision timing analysis. This effect has to be further investigated with a range of pulsars and with different techniques for shaping each channel of a polyphase filter bank.

# Chapter 5

## FRBs and Interferometric Arrays

The observed large dispersion measure values of the FRBs along the line of sight implies large integrated electron density values that greatly exceed the modelled predictions for the contribution from our Galaxy. This suggests an extragalactic origin for FRBs. Follow up radio observations have failed to find further bursts at the same location. As FRBs might represent a new class of highly compact and extreme events in the Universe, it is vital to pin down the source location with an arcsecond precision using only the one available burst in order to identify, for example, a host galaxy at redshift greater than one. This is especially true if there is no afterglow, or other associated emission, at any other wavelength that might help to reveal the location sufficiently precisely. This chapter presents a new method that utilises the additional spectral and comparative spatial information from multiple overlapping tied array beams to estimate a source location with up to arcsecond accuracy in almost real time without imaging.

### 5.1 Spectral sensitivity of interferometric arrays

A single antenna is the main building block of every interferometer. Nearly all characteristics describing antenna performance are frequency dependent. For example, the antenna beam pattern gets narrower with increasing frequency and the sidelobes move closer to the beam centre, as illustrated in Figure 2.4. Furthermore, the sensitivity of a TAB will vary not only due to the frequency but also with the steering direction as it is affected by the primary beam shape and foreshortening, as seen in Figure 2.4. Therefore, the sensitivity of a TAB is frequency and steering direction dependent. These



frequency-dependent variations in a telescope beam shape can be used to create a sensitivity  $\mathcal{S}$  map at different frequencies e.g. at the upper  $\nu_H$  and lower  $\nu_L$  frequencies in the observing band, as shown in Figure 3.23 for the MUST array. It follows that observations at two different frequencies of the same source will yield different values for the apparent flux density. Moreover, the apparent flux density will vary with the source position in a TAB, as demonstrated in Figure 2.3. With the current techniques, the location of a variable source detected with a single-beam telescope can be approximated only to an area defined by the HPBW<sup>1</sup>. In the case of an interferometer, the source position can be determined to be within the HPBW of a TAB<sup>2</sup>, §2.2.2.

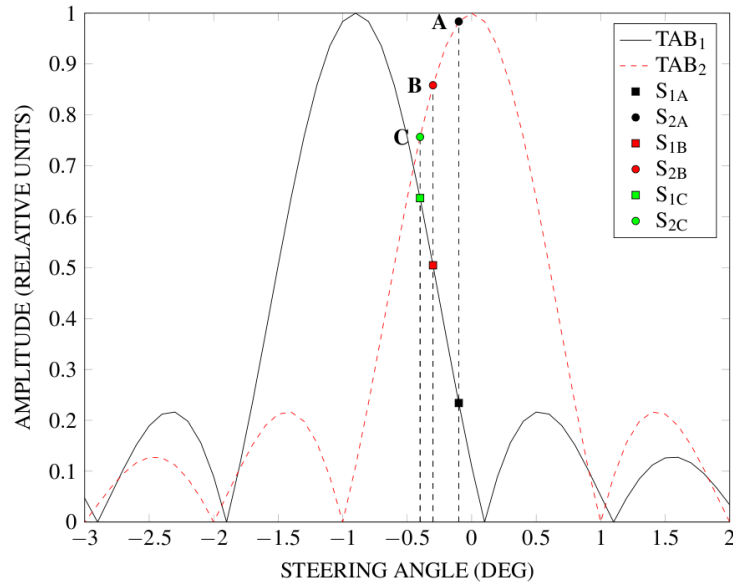


**Figure 5.1:** Flux ratio of two overlapping TABs plotted with normalised units. Three hypothetical strong sources are detected in two TABs, their positions are marked as A (black), B (red) and C (green). Note that the primary beam shape is ignored for clarity.

When a source is detected in multiple TABs from an interferometer, the SNR pattern can be used to further constrain the source position. The idea is that the detection pattern of the SNR across the multiple TABs can be generated based on our knowledge of the interferometer being used. From that corresponding values of the observed (apparent) flux density  $S_v$  can be calculated. The value of the observed  $S_v$  depends on the

<sup>1</sup>In this work, an area on the sky illuminated by a HPBW contour of a TAB is described by a symbol  $\Omega_{HPBW_L}$  in degree square.  $\Omega_{HPBW_L}$  can be thought of as a beam solid angle of an antenna but it does not include sidelobes

<sup>2</sup>This is only an assumption as a strong source can be detected in a sidelobe.

source location within the TABs, as the sensitivity decreases away from the phase centre. Using Figure 5.1 as an illustration of a hypothetical scenario when three sources are detected in two overlapping TABs at positions marked with A, B and C. Each position is located further away from the phase centre of each TAB, i.e. the most sensitive region in the beam pattern. For TAB<sub>1</sub>, location C is the most sensitive position and for TAB<sub>2</sub> location A is the most sensitive. The resulting ratios of the arbitrary fluxes from both TABs are then:

$$S_{1A}/S_{2A} = 0.24, S_{1B}/S_{2B} = 0.56 \text{ and } S_{1C}/S_{2C} = 0.84.$$

All fluxes are assumed to be above the detection threshold. As the decrease in sensitivity of the TABs falls off rapidly, the flux ratios from each position differ substantially. The ratio of the observed fluxes in the two TABs,  $S_{1A}/S_{2A}$ , can be compared with the ratio of the calculated sensitivity  $s_1/s_2$  across the TABs ratio map  $S_1/S_2$  (in the case of Figure 5.1 these have been normalised to peak at 1). By identifying the locations where the observed and calculated sensitivities are the same, the source location can be estimated with higher precision than from a TAB on its own. An example of the *flux density ratio map*  $S_1/S_2$  can be seen in the bottom panel in Figure 5.2 for the two overlapping TABs of the simulated MUST array, the top panel. When considering the 2-dimensional distribution of  $s_1/s_2$ , the  $S_1/S_2$  is not enough to constrain a source location as its value might repeat or be a part of a constant contour on the flux density ratio map in different areas of the FoV. Thus, another metric is needed.

In our analysis we assumed that the beam dependent spectral index is described by a power law, §2.1.3. If observations at two distinct frequencies  $\nu_L$  and  $\nu_H$  are available, the spectral index  $\alpha$  can be calculated via Equation 2.5:

$$\alpha = \frac{\log\left(\frac{S_L}{S_H}\right)}{\log\left(\frac{\nu_L}{\nu_H}\right)}, \quad (5.1)$$

where  $S_L$  and  $S_H$  are the apparent flux densities from observations at frequencies  $\nu_L$  and  $\nu_H$ . Due to the frequency-dependent gain pattern of a telescope, sources detected off-axis can have their spectral index distorted substantially. In our analysis we have assumed that the beam dependent spectral index is also described by a power law. Using 2-D sensitivity  $S$  maps for frequencies  $\nu_L$  and  $\nu_H$  and Equation 5.1, a 2-D *instrumental spectral index*  $\mathcal{A}$  map of a telescope beam pattern can be created, as illustrated in the

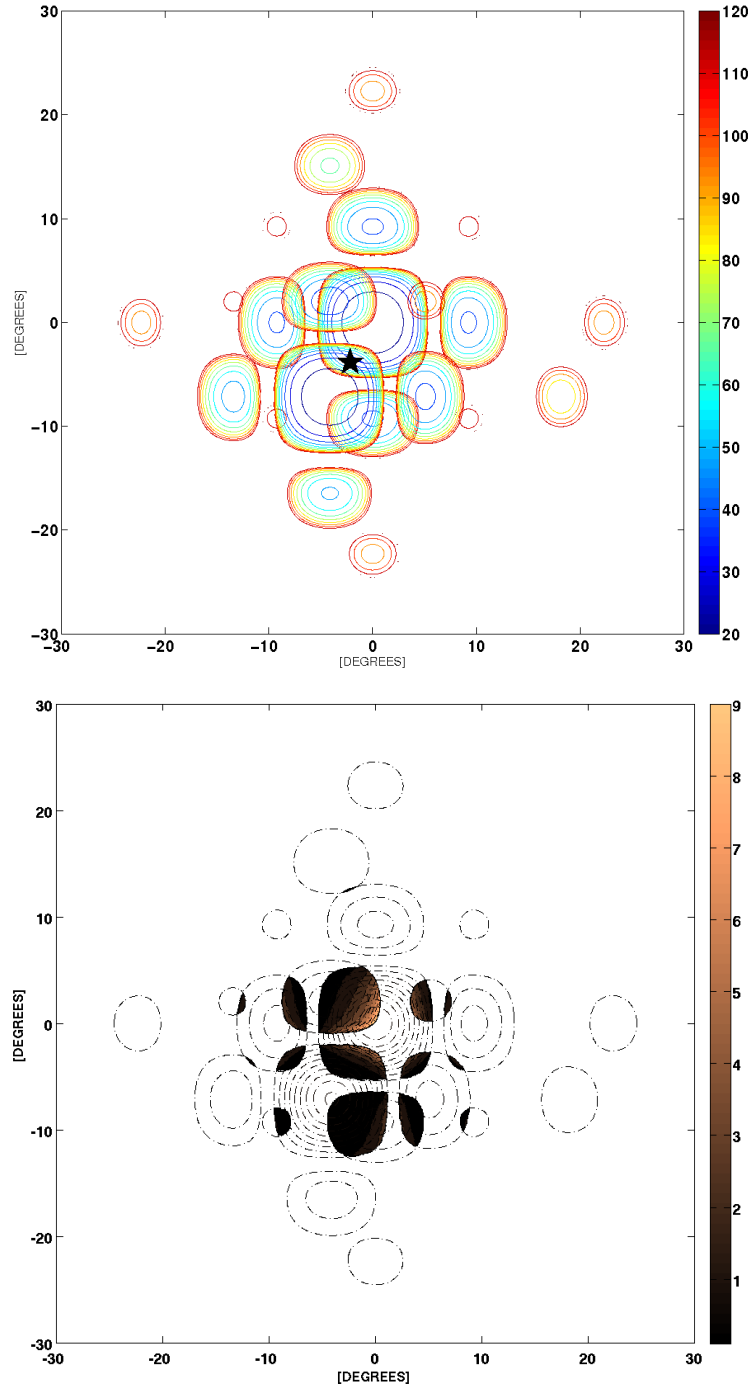


**Figure 5.2:** An example of the sensitivity  $S$  maps of two TABs in units of Jy for the MUST array. The TABs (top) are plotted on a linear scale and normalised to the minimum sensitivity  $S_{v,min}$  (Jy) for each pointing direction. A hypothetical source detected in the two overlapping TABs at a position  $[-2.1^\circ, -3.8^\circ]$  is shown as a black star. (Bottom) shows the flux density ratio  $S_1/S_2$  map. The ratio values are limited to the range  $[0, 1]$  for clarity.

top panel in Figure 5.3. The  $\mathcal{A}$  map describes an apparent (instrumental) spectral index contribution from a TAB. In this work, the main assumption is that a telescope imparts an instrumental spectral index on a detected source.

In contrast to Spitler et al. (2014), the instrumental spectral index  $\mathcal{A}$  map is created using the sensitivity of the telescope at a given observing frequency rather than the telescope's gain. This is in order to include the beam shape variation with steering direction as well as the contribution from the sky<sup>3</sup>. This explains why the apparent variation away from the phase centre has the opposite sign, positive rather than negative, to that of Spitler et al. (2014). We assume that the observed spectral index  $\alpha_O$  of a detected source is a combination of its intrinsic spectral index  $\alpha_I$  and the instrumental spectral index  $\alpha$  imposed by the  $\mathcal{A}$  map. It can be described with the following equation:

$$\alpha_I = \alpha_O + \alpha \quad (5.2)$$

Using Figure 5.1 as an illustration again, a source observed at position A, with normalised flux density  $S_{1A}$  from TAB<sub>1</sub> and  $S_{2A}$  from TAB<sub>2</sub>, is also observed at the low and high frequency,  $\nu_L$  and  $\nu_H$ . This yields four different values of flux density. Namely,  $S_{1A,\nu_L}$  and  $S_{1A,\nu_H}$  for TAB<sub>1</sub> and  $S_{2A,\nu_L}$  and  $S_{2A,\nu_H}$  for TAB<sub>2</sub>. Now, the observed spectral index  $\alpha_{O_1}$  can be calculated, Equation 5.1, for source A detected in TAB<sub>1</sub> and  $\alpha_{O_2}$  for source A detected in TAB<sub>2</sub>. As both TABs detected the same source A, Equation 5.2 can be written as follows (omitting subscript A for generality):

$$\begin{aligned} \alpha_{O_1} &= \alpha_I - \alpha_1, \\ \alpha_{O_2} &= \alpha_I - \alpha_2. \end{aligned} \quad (5.3)$$

These two equalities yield the relationship:

$$\alpha_{O_1} - \alpha_{O_2} = \alpha_2 - \alpha_1, \quad (5.4)$$

and the left side of this equality is known from the observation. To connect the calculated difference  $(\alpha_2 - \alpha_1)$  to a position within a TAB we need to subtract the instrumental spectral index  $\mathcal{A}_2$  map of TAB<sub>2</sub> from the instrumental spectral index  $\mathcal{A}_1$  map of TAB<sub>1</sub>. An example of such a manipulation is illustrated in the bottom panel in Figure 5.3 for the MUST array.

---

<sup>3</sup>The beam broadens with the elevation.

**Table 5.1:** Glossary of symbols.

|                  | Flux density   | Spectral index |
|------------------|----------------|----------------|
| Observed (1-D)   | $S$            | $\alpha$       |
| Map (2-D)        | $\mathcal{S}$  | $\mathcal{A}$  |
| Map values (1-D) | $\mathfrak{s}$ | $\mathfrak{a}$ |

The difference of the observed spectral indices ( $\alpha_{O_1} - \alpha_{O_2}$ ) together with the observed flux density ratio  $S_1/S_2$ , can be used to constrain the position of a source within a TAB with an accuracy significantly better than a beam width. A by-product of an accurate position estimation is the possibility of recovering the intrinsic spectral index  $\alpha_i$  of a source. The spectral index contribution from the beam pattern can be corrected for if the position of the source within a TAB can be estimated with good accuracy. The glossary of symbols used in this work are listed in Table 5.1.

The above two-TAB detection analysis of the observed flux density ratio and spectral index difference produces a single or a set of possible locations for a source. If a transient source was detected in  $N$  TABs, this process can be repeated for *all*  $C_2^N$  pair combinations. To identify the pair combinations a subscript  $(i, j)$  is used. The  $S/N$  of the detected source from every TAB is used to estimate the apparent flux density. This step will produce  $2 \times N$  apparent flux densities (one apparent flux density  $S$  for each frequency):

$$(S_{1,v}, S_{2,v}, \dots, S_{N,v}) = ([S_{1,v_L}, S_{1,v_H}], \dots, [S_{N,v_L}, S_{N,v_H}]), \quad (5.5)$$

Then each pair  $[S_{N,v_L}, S_{N,v_H}]$  is used in Equation 5.1 to calculate the observed spectral index  $\alpha_{O,N}$  for each TAB:

$$(\alpha_{O,1}, \alpha_{O,2}, \dots, \alpha_{O,N}). \quad (5.6)$$

Next we create different pair combination according to  $C_2^N$  of flux density ratio  $(S_1/S_2)_{(i,j)}$  and corresponding  $(\alpha_{O_1} - \alpha_{O_2})_{(i,j)}$ . The values of the flux density ratio and the spectral index difference are then compared with a 2-D flux density ratio  $(\mathcal{S}_1/\mathcal{S}_2)_{(i,j)}$  map and the 2-D spectral index difference  $(\mathcal{A}_2 - \mathcal{A}_1)_{(i,j)}$  map, within an error bound. The matching indices from both 2-D arrays, that point to the corresponding values of  $(\mathfrak{s}_1/\mathfrak{s}_2)_{(i,j)}$  and  $(\mathfrak{a}_2 - \mathfrak{a}_1)_{(i,j)}$ , are examined against each other. *Only locations common for all pairs are chosen for the estimated true source position.* As we are looking

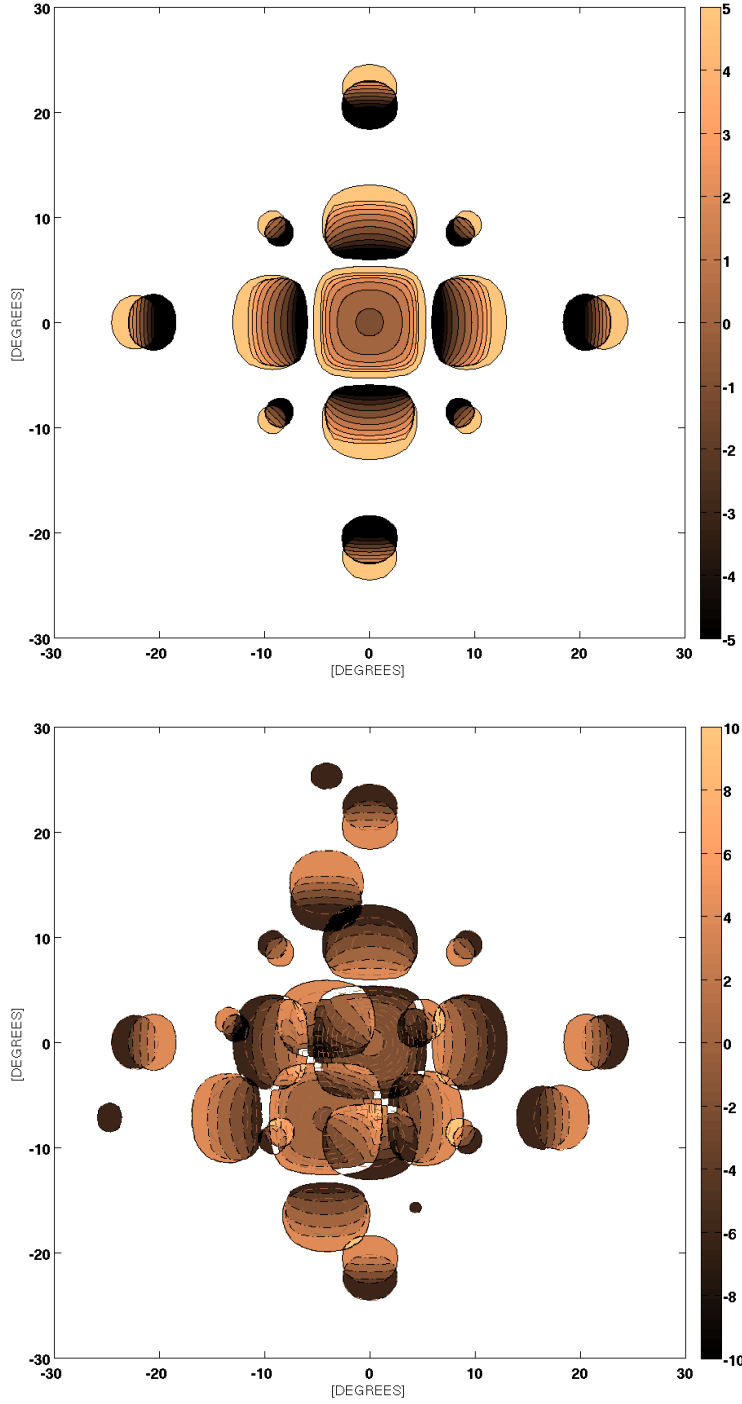


**Figure 5.3:** (Top) the instrumental spectral index map  $\mathcal{A}$  for the MUST array. The values of spectral index are limited to the range  $(-5, 5)$  and only pixels with sensitivity  $10 \times S_{v,\min}$  are displayed for clarity. (Bottom) the spectral index difference  $(\mathcal{A}_2 - \mathcal{A}_1)$  map of TABs from Figure 5.2 (top) and (bottom).

for dimensionless quantities even very small features in the map can yield the ratio we are looking for. For that reason, only the coordinates common for both,  $(\mathfrak{s}_1/\mathfrak{s}_2)_{(i,j)}$  and  $(\mathfrak{a}_2 - \mathfrak{a}_1)_{(i,j)}$ , are treated as a possible source location.

This is illustrated in Figure 5.4, for a five TAB scenario where each colour depicts overlapping regions of  $(\mathfrak{s}_1/\mathfrak{s}_2)_{(i,j)}$  and  $(\mathfrak{a}_2 - \mathfrak{a}_1)_{(i,j)}$  from each TAB pair. For example, orange represents overlapping regions of  $(\mathfrak{s}_1/\mathfrak{s}_2)_{(11,17)}$  and  $(\mathfrak{a}_2 - \mathfrak{a}_1)_{(11,17)}$  for the TAB<sub>11</sub> and TAB<sub>17</sub> pair. Crucially, only regions where all "colours" overlap are treated as a possible source location.

In our simulations we have assumed a perfectly calibrated array where all the antenna gains are uniform and our beam model is ideal. In a real telescope, each antenna will have uncalibrated errors in gain and phase. This inevitably will affect the performance of our method, but for this proof-of-concept analysis we assume perfect calibration. A simplified example is given next.

### 5.1.1 Simple Example

The following example illustrates a scenario described by Figure 5.1 but for the 2-dimensional case depicted in Figure 5.2, where a source is simulated at the position  $[-2.1^\circ, -3.8^\circ]$  in two overlapping TABs, marked with a black star in the top panel in Figure 5.2. The source is detected in both TABs and at upper  $\nu_H$  and lower  $\nu_L$  frequencies. The observed SNR pattern yields  $S_1/S_2 = 0.86$  and  $(\alpha_{O_1} - \alpha_{O_2}) = -0.52$ , for the observed flux density ratio and the observed spectral index difference respectively. The top panel in Figure 5.5 shows the repeating values of  $\mathfrak{s}_1/\mathfrak{s}_2$  from the flux density ratio map  $S_1/S_2$  equal to  $S_1/S_2 \pm 1\%$ . The values of the flux density ratio  $\mathfrak{s}_1/\mathfrak{s}_2$  are plotted along with the TABs flux contours as to aid visualisation. The middle panel in Figure 5.5 shows all locations where values  $(\mathfrak{a}_2 - \mathfrak{a}_1)$  from the instrumental spectral index difference  $(\mathcal{A}_2 - \mathcal{A}_1)$  map are equal to  $(\alpha_{O_1} - \alpha_{O_2}) \pm 1\%$ . When we overlay the regions identified in the top and middle panels, as the bottom panel in Figure 5.5, a position where both these allowed regions of the spectral index difference  $(\mathfrak{a}_2 - \mathfrak{a}_1)$  and the flux density ratio  $\mathfrak{s}_1/\mathfrak{s}_2$  overlap can be established. In this example, there is only one common coordinate for both values of  $(\mathfrak{a}_2 - \mathfrak{a}_1)$  and  $\mathfrak{s}_1/\mathfrak{s}_2$  at  $[-1.95^\circ, -3.9^\circ]$ , marked with a red dot in the bottom panel in Figure 5.5. Using the above technique, the source location was estimated to within 2% of the HPBW of a TAB, where the true

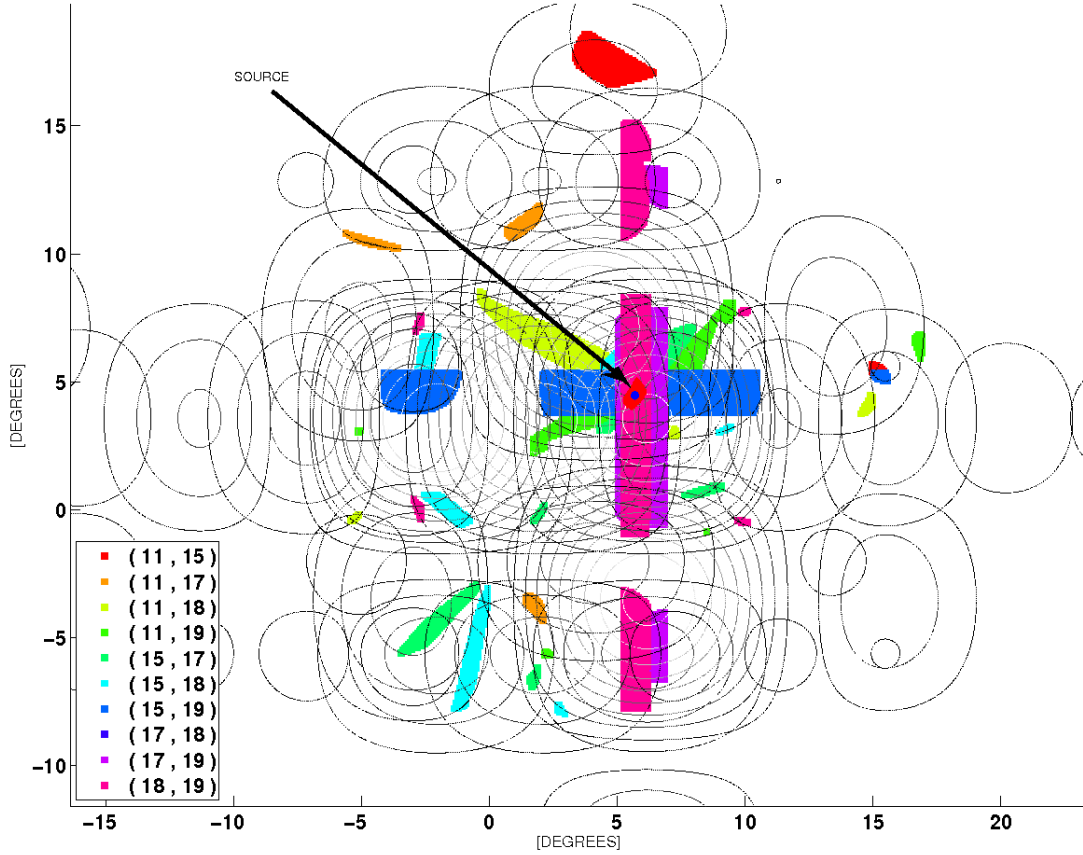


**Figure 5.4:** Illustration of a detection made with five TABs resulting in 10 pair combinations. Each colour depicts overlapping regions of  $(s_1/s_2)_{(i,j)}$  and  $(a_2 - a_1)_{(i,j)}$  from each  $(i, j)$  TAB pair.

source position is marked with a red star.

To summarise the methodology for a TAB pair:

- Create the sensitivity map  $S_1$  of  $TAB_1$  at frequency  $\nu_1$  and  $\nu_2$ , Figure 3.23;
- Create the instrumental spectral index  $\mathcal{A}_1$  map of  $TAB_1$ , the top panel in Figure 5.3;
- Repeat (a) and (b) for  $TAB_2$ ;
- Create the flux density ratio map  $S_1/S_2$ , the bottom panel in Figure 5.2;
- Create the spectral index difference map  $(\mathcal{A}_2 - \mathcal{A}_1)$ , the bottom panel in Figure 5.3;
- Find  $s_1/s_2$  in (d), the top panel in Figure 5.5;
- Find  $(a_2 - a_1)$  in (e), the middle panel in Figure 5.5;
- Compare results of (f) and (g) and find source location, the bottom panel in



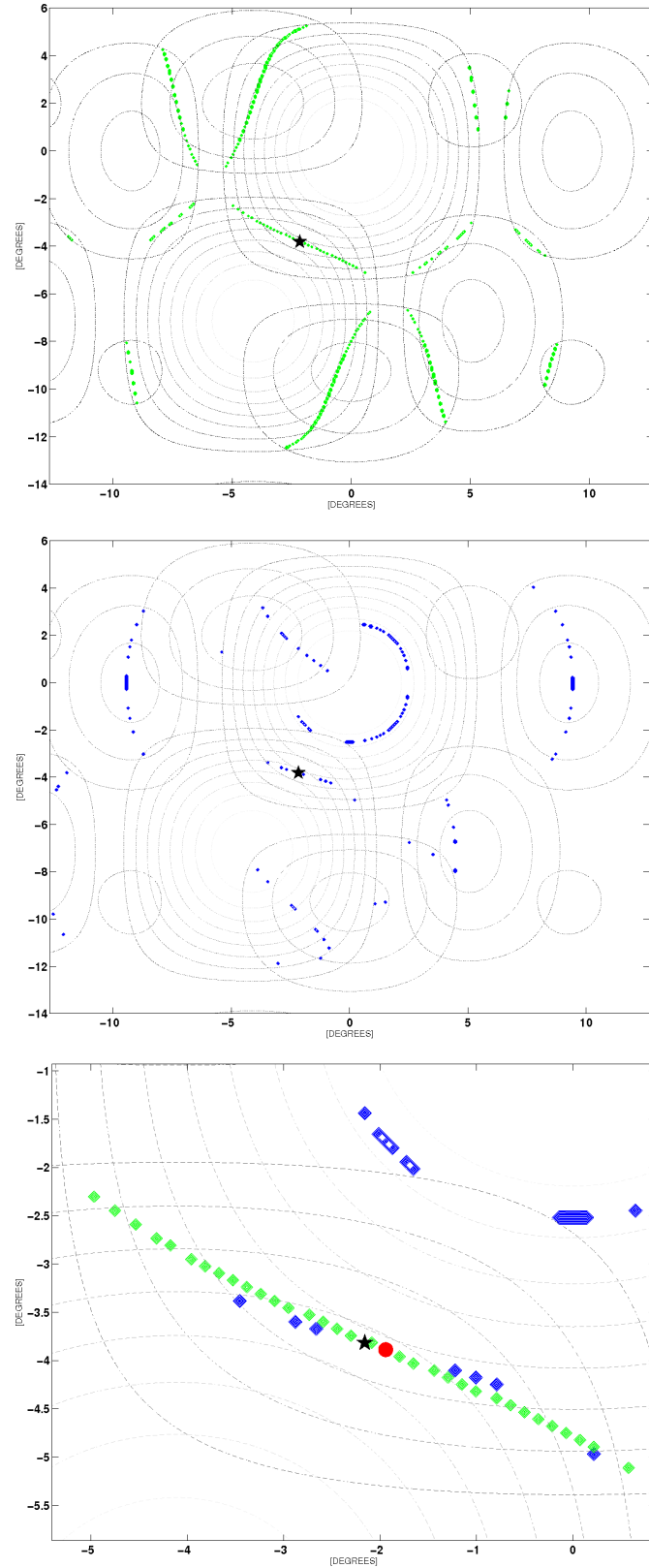


**Figure 5.5:** Example  $s_1/s_2$  and  $(a_2 - a_1)$  maps for the MUST array. The top figure shows the values of  $s_1/s_2 = S_1/S_2 \pm 1\%$ , plotted on top of the TABs contours. The middle figure shows values of  $(a_2 - a_1) = (\alpha_{O_1} - \alpha_{O_2}) \pm 1\%$ . The bottom figure shows both  $(a_2 - a_1)$  and  $s_1/s_2$  overlaid. The red circle at a position  $[-1.95^\circ, -3.9^\circ]$  indicates the best estimated position and the red star indicates the true source position.

Figure 5.5.

## 5.2 Simulation Parameters

In this section the detailed methodology for finding the location of a source within a TAB is presented. The arrays considered in this analysis are:

- The MUST-4 array in rectangular configuration §3.5.1;
- LOFAR Superterp §2.3.1;
- The MeerKAT core §2.3.2.

All three arrays are assumed to have multibeaming capabilities, although the MUST and the MeerKAT array are under construction at the moment of writing. Each array operates at different frequencies, different baseline lengths, number of elements and finally the type of antennas used, to demonstrate the flexibility of this method. The theoretical HPBWs, at  $\nu_L$  and  $\nu_H$ , were calculated with Equation 2.8 and are listed in Table 5.4 and Table 3.3 together with the maximum baselines  $B_{max}$ .

To explore the capabilities of the method presented here, three different spatial sampling methods are tested to determine how important the TAB separation is for the accuracy of determining a source location:

- undersampling: TAB separation is equal to HPBW at the lower edge  $\nu_L$  of the observed frequency band  $(HPBW_L)^4$ ;
- Nyquist sampling: TAB separation is equal to half HPBW at the lower edge of the frequency band  $(HPBW_L/2)$ , i.e. undersampling at  $\nu_H$ ;
- oversampling: TAB separation is equal to half HPBW at the upper edge of the frequency band  $(HPBW_H/2)$ , i.e. Nyquist sampling at  $\nu_H$ .

We are using undersampled TABs as this layout is common for pulsar observations while the Nyquist sampling provides uniform sensitivity of the combined FoV. The oversampling is used as a control to determine if there are any benefits to oversample the FoV. The number of TABs used in each simulation is given in Table 5.3. To accurately test different spatial sampling methods the TABs HPBW are taken from the simulations done with MATLAB and the OSKAR-2 software<sup>5</sup>.

---

<sup>4</sup>Half Power Beamwidth. In some sources also called Full Width Half Maximum (FWHM)

<sup>5</sup><http://www.oerc.ox.ac.uk/~ska/oskar2/>

**Table 5.2:** Values used in Equation 2.7.

|                   | MUST               | LOFAR              | MeerKAT            |
|-------------------|--------------------|--------------------|--------------------|
| $\beta$           | 0.99               | 0.66               | 0.66               |
| $A_{eff} [m^2]$   | 36                 | 8064               | 22902              |
| $\tau [s]$        | $5 \times 10^{-3}$ | $5 \times 10^{-3}$ | $5 \times 10^{-3}$ |
| $\Delta\nu [MHz]$ | 50                 | 32                 | 300                |
| $n_p$             | 2                  | 2                  | 2                  |
| $T [K]$           | 207                | 907                | 500                |

To make the comparison between different arrays and different sampling methods simple, the independent TABs are simulated to occupy a circle with a diameter equal to  $3 \times \text{HPBW}_L$ . The centre of the circle is located at the zenith for a particular epoch MJD 56772.5629376499. The zenith coordinates are given in Table 5.4 and Table 3.3 together with the geographical location of the array. A set of 60 strong<sup>6</sup> point sources, with identical characteristics, is randomly distributed on a square with the length of a side equal to  $3 \times \text{HPBW}_L$  and overlapping with the TAB circle. A separate set is generated for each array. Refer to Figure 5.8, Figure 5.12 and Figure 5.16 for a detailed illustration on beam position and source location for the MUST, LOFAR and MeerKAT arrays respectively. We also assume that the transient sources are very short, therefore we can neglect the Earth's movement.

The procedure of calculating the minimum array sensitivity  $S_{v,\min}$  is described in §3.6 for the MUST array as an example. The values of the parameters used are listed in Table 5.2. The sky temperature  $T_{\text{sky}}$  is scaled to frequencies listed in Table 5.4 and Table 3.3. To ensure detection with sidelobes the flux density of each source is made several times stronger than the minimum detectable flux density  $S_{v,\min}$  at the lower frequency  $\nu_L$  in the observing band. A source with the  $S/N$  above threshold  $(S/N)_{\min} = 8$ , is further processed only if the two following conditions are met:

A source was "detected"

- a) with at least 2 independent TABs and
- b) at two frequencies,  $\nu_L$  and  $\nu_H$  in each independent TAB.

<sup>6</sup>This value is equal to detections at  $20\sigma$ .

A source can be detected in a traditional way in one beam or at one frequency only. The definition of detection is therefore quite restrictive but is required to provide better positional accuracy. However, for wide bandwidths we can use multiple frequency values across the band, for strong sources, even if the source is not detected at the furthest frequencies.

As mentioned in the previous section, the flux density ratio  $S$  maps used to create the spectral index map  $\mathcal{A}$  are normalised to the minimum sensitivity  $S_{v,\min}$  at the phase centre. The  $S_{v,\min}$  is frequency dependent and has a different value for the same TAB at different frequencies, Figure 2.3. Due to this dependency the instrumental spectral index  $\alpha$  at the phase centre is not zero. That value might be large depending on the extent of the fractional bandwidth. It has no effect for the location finding, but affects the estimated intrinsic spectral index  $\alpha_I$  of a source. To force  $\alpha$  to be zero at the phase centre we had to subtract a constant<sup>7</sup>:

$$\alpha_{\text{Const}} = \frac{\log\left(\frac{s_{v_L,\min}}{s_{v_H,\min}}\right)}{\log\left(\frac{v_L}{v_H}\right)}, \quad (5.7)$$

where values of  $s_{v_L,\min}$ ,  $s_{v_H,\min}$ ,  $v_L$  and  $v_H$  are listed in Table 5.4. Moreover, we also discount locations on the map that are too noisy to detect even a strong source. A detection is said to be successful if only one small area was estimated for that source, preferably even a single pixel<sup>8</sup>. The uncertainty of the estimated location increases when more than one location was estimated for a source.

### 5.2.1 Uncertainties and Error Propagation

In the simplified example shown in §5.1.1, highly significant detections (i.e. SNR of 100) are assumed simply to illustrate the method. These do not reflect likely SNRs in actual observations so here we consider that, to qualify as a detection, a transient source must have  $\text{SNR} \geq 8$  and thus a related flux error of  $\delta S \leq 12.5\%$ . The question of whether the errors between TABs are correlated or independent is a non-trivial combination of several factors. For example there may be a degree of non-independent noise, depending on the relative contribution of the sky and receiver temperatures; these will

<sup>7</sup> $\alpha_{\text{Const}}$  is subtracted from the final estimated  $\alpha_I$ .

<sup>8</sup>Pixel is the smallest resolution element of the simulated beam pattern. A single pixel covers an area of 0.32 square arcminute for the MUST array, 0.23 square arc seconds for the LOFAR Superterp and  $2.25 \times 10^{-4}$  square arc seconds for MeerKAT.

be quite different in the LOFAR and MeerKAT arrays. For the present discussion the worst case scenario is assumed for all three arrays where the errors are taken to be highly correlated and hence combine linearly rather than quadratically.

The error  $\delta(S_1/S_2)_v$  on the observed flux density ratio  $(S_1/S_2)$  comes from the SNR detection and the ratio itself. It is expressed as:

$$\delta(S_1/S_2)_v = \left( \frac{\delta S_1}{S_1} + \frac{\delta S_2}{S_2} \right)_v. \quad (5.8)$$

Then the observed  $(S_1/S_2)$  and the modelled  $s_1/s_2$  ratios obtained from the 2-D flux density ratio  $S_1/S_2$  map can be compared as we are looking for regions where the modelled  $s_1/s_2$  fall within the range:

$$S_1/S_2 \pm \delta(S_1/S_2). \quad (5.9)$$

For the sources simulated in this study, the cumulative error on the flux ratio  $(S_1/S_2)$  is typically 20%. An example of the flux ratio error  $\delta(S_1/S_2)$  range for the LOFAR array, using the oversampled method is plotted in the top panel in Figure 5.6.

The measured flux density  $S$  is also used via Equation 5.1 to estimate the observed spectral index  $\alpha_O$ . The cumulative error  $\delta\alpha_O$  is as follows:

$$\delta\alpha_O = \frac{0.43}{\log\left(\frac{v_L}{v_H}\right)} \left( \frac{\frac{\delta S_{v_L}}{S_{v_L}} + \frac{\delta S_{v_H}}{S_{v_H}}}{\frac{S_{v_L}}{S_{v_H}}} \right). \quad (5.10)$$

The error then propagates further as we are considering the observed spectral index difference from two TABs (Equation 5.4):

$$\delta(\alpha_{O_2} - \alpha_{O_1}) = \delta\alpha_{O_2} + \delta\alpha_{O_1}. \quad (5.11)$$

The calculated  $(\alpha_{O_2} - \alpha_{O_1})$  and modelled  $(a_2 - a_1)$  from the 2-D the spectral index difference  $(\mathcal{A}_2 - \mathcal{A}_1)$  map are then compared as we are looking for regions where the modelled  $(a_2 - a_1)$  fall within the range:

$$(\alpha_{O_2} - \alpha_{O_1}) \pm \delta(\alpha_{O_2} - \alpha_{O_1}). \quad (5.12)$$

The cumulative error on the spectral index difference  $\delta(\alpha_{O_2} - \alpha_{O_1})$  is at least 60%

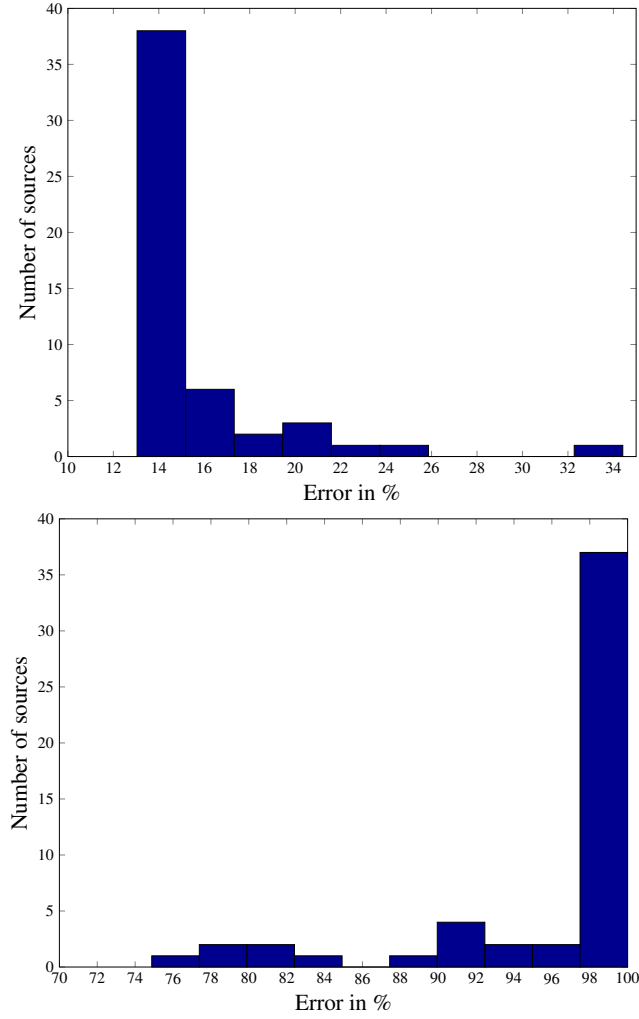


**Figure 5.6:** An example of the cumulative error range for the LOFAR array using the over-sampled method; (top)  $\delta(S_1/S_2)$ ; (bottom)  $\delta(\alpha_{O_2} - \alpha_{O_1})$ .

and for the present purpose we have limited it to 100%. A representative for the error  $\delta(\alpha_{O_2} - \alpha_{O_1})$  range is plotted in the bottom panel in Figure 5.6. It is important to note that these errors refer only to the simulated sources presented in this work and are not generic to the method. A way to reduce these error is to use large fractional bandwidths but that can make a detection at two frequencies difficult. We also note that stronger detections will reduce the errors significantly.

### 5.3 Simulation Results

The results of the simulations are presented in a separate table for all sources detected with each sampling method. Each table lists a source true position in RA and Dec, the

number of locations  $P$ , or patches, that were estimated for that source to illustrate the location uncertainty. To show the benefits of detection with many TABs, the number of TABs,  $B$ , the source was detected in is also listed. Next, the minimum ( $\delta D_{Min}$ ), maximum ( $\delta D_{Max}$ ) and mean ( $\bar{D}$ ) value of the total area  $D$  covered by the overlapping values of  $\mathfrak{s}_1/\mathfrak{s}_2$  and  $(\mathfrak{a}_2 - \mathfrak{a}_1)$ , normalised to the  $\Omega_{HPBW_L}$  is shown. The total area  $D$  represents the area that would need to be sampled in follow up, or archival, observations to be sure that the actual position of the source was observed. The minimum ( $\delta\phi_{Min}$ ), maximum ( $\delta\phi_{Max}$ ) and mean ( $\bar{\Delta\phi}$ ) value of the total angular distances  $\Delta\phi$  between the true and the estimated source position, normalised to  $\Omega_{HPBW_L}$ , is listed to illustrate how far, or how close, the estimated position is in relation to the true source position.

For the purpose of illustration, Figure 5.7 shows the estimated locations for source A with  $P = 2$  and source B with  $P = 3$  plotted in green and red respectively. The true source position is marked with a blue dot. It is clear that the total area  $D_B$  for source B is considerably larger than the total area  $D_A$  for source A. However, the patch areas,  $\delta D_{B1}$  and  $\delta D_{B3}$ , are small and still within a FoV of an optical telescope. Out of the two sources, source A position estimation is more accurate in comparison to source B, as the total area  $D_A$  is smaller.

**Table 5.3:** Number of TABs per spatial sampling for each array.

|         | Undersampling | Nyquist sampling | Oversampling | Source      |
|---------|---------------|------------------|--------------|-------------|
| MUST    | 7             | 19               | 19           | Figure 5.8  |
| LOFAR   | 7             | 19               | 31           | Figure 5.12 |
| MeerKAT | 7             | 19               | 31           | Figure 5.16 |

**Table 5.4:** Calculated and simulated values of the Half Power Beamwidth (HPBW) for the LOFAR Superterp and the MeerKAT array core, where  $HPBW_T$  and  $HPBW_S$  are the theoretical and simulated half power beamwidths respectively,  $B_{max}$  is the maximum baseline,  $\nu_L$  and  $\nu_H$  are the lowest and the highest operating frequencies and  $S_{min}$  is the minimum detectable flux.

| Array   | $B_{max}$ [m] | Frequency [MHz] | $HPBW_T$ | $HPBW_S$ | $S_{min}$ [Jy] | Location [Lat,Long] |
|---------|---------------|-----------------|----------|----------|----------------|---------------------|
| LOFAR   | 307.6         | $\nu_L$ 119     | 0.47°    | 0.43°    | 7.9m           | +52°54'28.32"       |
|         |               | $\nu_H$ 150     | 0.37°    | 0.35°    | 6.4m           | +06°52'00.99"       |
| MeerKAT | 883.2         | $\nu_L$ 1400    | 0.50'    | 0.52'    | 538.24 $\mu$   | 21°23' E            |
|         |               | $\nu_H$ 1700    | 0.41'    | 0.43'    | 538.13 $\mu$   | 30°42' S            |

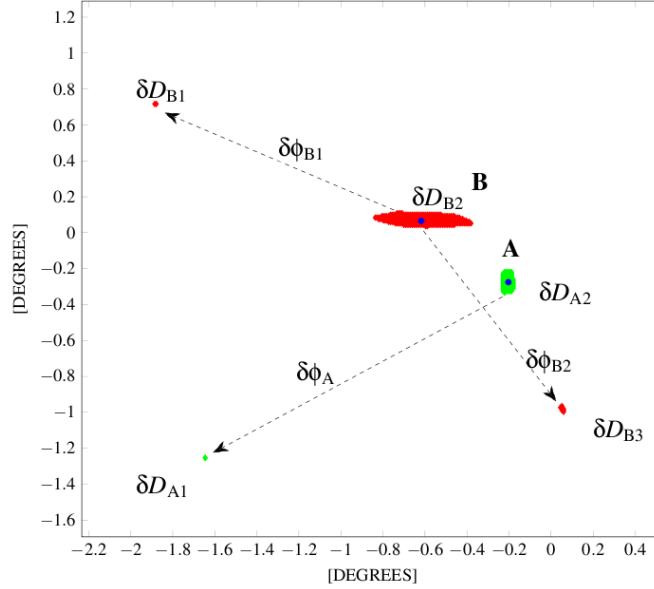


**Figure 5.7:** Graphical representation of locations  $P$ , the total area  $D$  and the angular distance  $\delta\phi$  from the true source position. Green patches ( $P = 2$ ) represent the two estimated locations for source A. Red patches ( $P = 3$ ) represent the three estimated locations for source B. While there may be a significant angular distance between the estimated locations, the areas to search at these locations may be quite small.

### 5.3.1 The MUST array

The top and the bottom left panels in Figure 5.8 illustrate the position of the MUST TABs, plotted as HPBW<sub>L</sub> contours, in relation to the 60 randomly generated point sources, marked with small circles. We summarise here the detection rates with different spatial TAB sampling illustrated in the bottom right panel in Figure 5.8:

- Undersampling of the FoV, top left panel in Figure 5.8, yields the lowest detection rate out of the three sampling methods with only 14 detected sources,  $\circ$  symbol in the bottom right panel;
  - All sources detected with undersampling were also detected by the Nyquist sampled and oversampled methods;
- Both, Nyquist sampled and oversampled methods, the top right and the bottom left panel respectively, detected 40 of the simulated sources, marked with  $\square$  symbol in the bottom right panel;
- Although the detection rates for both Nyquist and oversampled methods are the same, i.e. 40 detected sources, two of those detected sources are different. In the bottom right panel, sources detected in the Nyquist sampled TABs are marked with the  $\diamond$  symbol and sources detected in the oversampled TABs are marked



with the  $\diamond$  symbol;

- There were 20 sources not detected with any sampling method marked with  $\diamond$  in the bottom right panel;
  - The majority of not detected sources lay outside of the TAB test area with the exception of source #60, marked with a red circle in the bottom right panel, which is located inside the test area.

By inspecting panel the top right and the bottom left panels, it is clear that source #60 was not detected in two independent TABs. In contrast, source #37 located next to source #60 was detected with the oversampling TABs where it just falls in the side-lobe<sup>9</sup> of a TAB. Refer to Table 5.5, Table 5.6 and Table 5.7 for more details.

**Table 5.5:** Summary of results for the MUST array using undersampled TABs. Source input RA and Dec are calculated for MJD 56772.5629376499. Below we list the minimum ( $\delta D_{Min}$ ), maximum ( $\delta D_{Max}$ ) and mean ( $\bar{D}$ ) value of the total area  $D$  covered by the overlapping values of  $s_1/s_2$  and  $(a_2 - a_1)$ , normalised to  $\Omega_{HPBW_L}$ . We also list the minimum ( $\delta\phi_{Min}$ ), maximum ( $\delta\phi_{Max}$ ) and mean ( $\bar{\Delta\phi}$ ) value of the total angular distances  $\Delta\phi$  between the true and the estimated source position, normalised to the  $HPBW_L$ .  $\bar{\alpha}_I$  is the mean estimated intrinsic spectral index from all possible locations, where the error is the standard deviation from that mean. The assigned value of  $\bar{\alpha}_I$  is -2. The two last columns list the number of areas of possible source locations  $P$  and the number of TABs in which a source was detected  $B$ . Sources for which location was estimated with a single pixel are marked with asterisk (\*).

| Undersampling |              |              |  |  |                       |   |   |
|---------------|--------------|--------------|--|--|-----------------------|---|---|
|               | Input RA     | Input Dec    | $[\delta D_{Min}, \delta D_{Max}, \overline{D}]$ | $[\delta \phi_{Min}, \delta \phi_{Max}, \overline{\Delta \phi}]$ | $\overline{\alpha_I}$ | P | B |
| Source 5      | 03:03:32.301 | +50:23:48.65 | [0.1, 0.3, 0.2]                                  | [0.004, 1, 0.5]  | $-1.4 \pm 1.1$        | 2 | 2 |
| Source 8      | 03:19:46.373 | +52:02:30.43 | [0.005, 0.2, 0.07]                               | [0.004, 0.8, 0.2]  | $-1.8 \pm 0.3$        | 3 | 2 |
| Source 10     | 03:24:12.682 | +49:31:02.64 | [0.0002, 0.2, 0.05]                              | [0.005, 0.9, 0.3]  | $-1.6 \pm 0.8$        | 7 | 2 |
| Source 19     | 03:43:35.369 | +52:29:30.08 | 0.08   | [0.003, 0.1, 0.05]   | $-2.0 \pm 0.4$        | 1 | 3 |
| Source 20     | 03:38:37.080 | +49:35:13.99 | [0.007, 0.2, 0.06]                               | [0.006, 0.9, 0.2]  | $-1.8 \pm 1.1$        | 4 | 2 |
| Source 25     | 04:10:29.535 | +55:54:21.19 | [0.1, 0.3, 0.2]                                  | [0.003, 1, 0.5]  | $-1.4 \pm 1.1$        | 2 | 2 |
| Source 28     | 03:39:22.483 | +52:10:08.14 | [0.0005, 0.1, 0.04]                              | [0.004, 0.8, 0.09]   | $-1.9 \pm 0.8$        | 3 | 3 |
| Source 30     | 04:12:25.038 | +58:12:27.15 | 0.2  | [0.002, 0.2, 0.1]  | $-1.7 \pm 0.9$        | 1 | 2 |
| Source 36     | 04:07:40.818 | +55:22:51.73 | [0.2, 0.8, 0.5]                                  | [0.003, 1, 0.4]  | $-1.1 \pm 1.1$        | 2 | 2 |
| Source 38     | 04:15:57.856 | +52:08:13.05 | 0.03   | [0.005, 0.07, 0.03]  | $-2.0 \pm 0.3$        | 1 | 2 |
| Source 41     | 02:54:57.607 | +55:08:58.03 | [0.2, 0.8, 0.5]                                  | [0.003, 1, 0.5]  | $-1.3 \pm 1.1$        | 2 | 2 |
| Source 42     | 03:06:57.849 | +50:55:26.94 | [0.2, 0.7, 0.4]                                  | [0.005, 1, 0.4]  | $-1.1 \pm 1.1$        | 2 | 2 |
| Source 46     | 03:48:40.993 | +55:06:17.42 | [0.0002, 0.1, 0.06]                              | [0.004, 0.9, 0.4]  | $-1.7 \pm 0.6$        | 3 | 2 |
| Source 56     | 03:53:34.228 | +54:31:20.11 | [0.03, 0.3, 0.1]                                 | [0.003, 0.9, 0.4]  | $-1.8 \pm 0.5$        | 3 | 2 |
|               | Input RA     | Input Dec    | $[\delta D_{Min}, \delta D_{Max}, \overline{D}]$ | $[\delta \phi_{Min}, \delta \phi_{Max}, \overline{\Delta \phi}]$ | $\overline{\alpha_I}$ | P | B |

Figure 5.9 shows the mean total area  $\bar{D}$  covered by the estimated positions for the undersampled, top panel, Nyquist sampled, the middle panel, and the oversampled

<sup>9</sup>Sidelobe contours are not plotted for clarity.

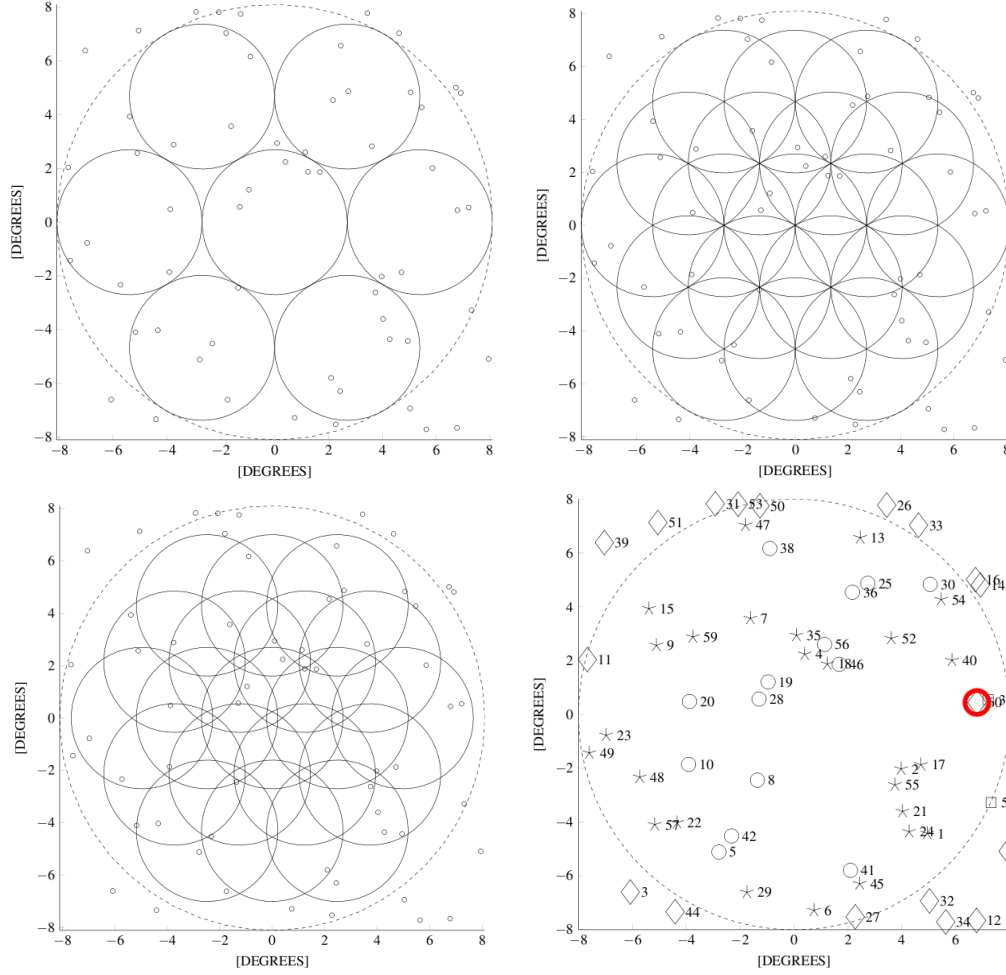


**Figure 5.8:** The MUST array spatial TAB sampling. The dashed circle of diameter  $3 \times \text{HPBW}_L$  represents a test area for different methods of spatial sampling ( $\text{HPBW}_L = 5.39^\circ$ ). The position of randomly placed sources are shown as small circles. (Top left) undersampling: 7 independent TABs are separated by  $\text{HPBW}_L$ ; (top right) Nyquist sampling: 19 independent beams are separated by  $\text{HPBW}_L/2 = 2.69^\circ$ ; (bottom left) oversampling: 19 independent beams are separated by  $\text{HPBW}_H/2 = 2.48^\circ$ . (Bottom right) graphical representation of source detection success using different sampling methods;  $\circ$ : sources detected with undersampling, Nyquist sampling and oversampling;  $\square$ : sources detected with Nyquist sampling and oversampling;  $\diamond$ : no detection with any sampling method;  $\nabla$ : sources detected with Nyquist sampling only;  $\ominus$ : sources detected with oversampling only.

methods, the bottom panel. We summarise the results below:

- For the majority of sources detected in the undersampled TABs, the top panel, the mean total area  $\bar{D}$  is less than 20% of a single TAB area, i.e.  $\Omega_{HPBW_L}$ ;
  - For five sources,  $\bar{D}$  is less than 5% of  $\Omega_{HPBW_L}$  and for two sources  $\bar{D}$  is less than 10%;
  - The mean angular distance  $\overline{\Delta\phi}$  from a source true location for four sources is less than 10% of  $HPBW_L$ , i.e.  $0.54^\circ$ ;
  - For two sources  $\overline{\Delta\phi}$  is less than 5% of  $HPBW_L$ , i.e.  $0.27^\circ$ ;
- For the majority of sources detected in the Nyquist sampled TABs, the middle panel, the mean total area  $\bar{D}$  is less than 8% of  $\Omega_{HPBW_L}$ . For four sources  $\bar{D}$  is less than 1%;
  - For 31 sources the mean angular distance  $\overline{\Delta\phi}$  is 0.15 of  $HPBW_L$ , i.e.  $0.8^\circ$ . Out of those, for 17 sources  $\overline{\Delta\phi}$  is less than 1% of  $HPBW_L$ , i.e. 3.2 arcminute;
- For 17 sources detected in the oversampled TABs, (bottom) panel, the mean total area  $\bar{D}$  is less than 1% of  $\Omega_{HPBW_L}$ ;
  - For 25 sources the mean angular distance  $\overline{\Delta\phi}$  is less than 5% of  $HPBW_L$ ;
  - For 8 sources  $\overline{\Delta\phi}$  is less than 1% of  $HPBW_L$ .

As the sources detected in the Nyquist sampled and oversampled TABs are almost the same, comparing the middle and the bottom panels in Figure 5.9, it is clear that the Nyquist sampling the FoV resulted in better location estimation.

Figure 5.10 presents examples of the estimated source positions for representative cases with low (one location only) and high (many possible locations) positional uncertainty for the undersampling, Nyquist sampling and oversampling methods. The top panel shows a detection of source #5, marked with a blue circle, in TAB<sub>4</sub> and in a side-lobe of TAB<sub>5</sub>. It demonstrates that a detection in only two TABs, while still helping to limit the search area, produces a large area of uncertainty, illustrated by a red patch that indicates the overlapping values of  $\mathfrak{s}_1/\mathfrak{s}_2$  and  $(\mathfrak{a}_2 - \mathfrak{a}_1)$  for that particular source from both TABs. The middle panel shows a detection of source #52 in five Nyquist sampled TABs. The green squares indicate overlapping values of  $(\mathfrak{s}_1/\mathfrak{s}_2)_{(i,j)}$  and  $(\mathfrak{a}_2 - \mathfrak{a}_1)_{(i,j)}$  from each TAB pair. Only the region marked with red diamonds shows an area where  $(\mathfrak{s}_1/\mathfrak{s}_2)_{(i,j)}$  and  $(\mathfrak{a}_2 - \mathfrak{a}_1)_{(i,j)}$  values from all TAB pairs overlap. Bottom panel shows the detection of source #46 in eight oversampled TABs. The total area  $D$  covered by the red patch is only half of that for the Nyquist sampled TABs and the true source

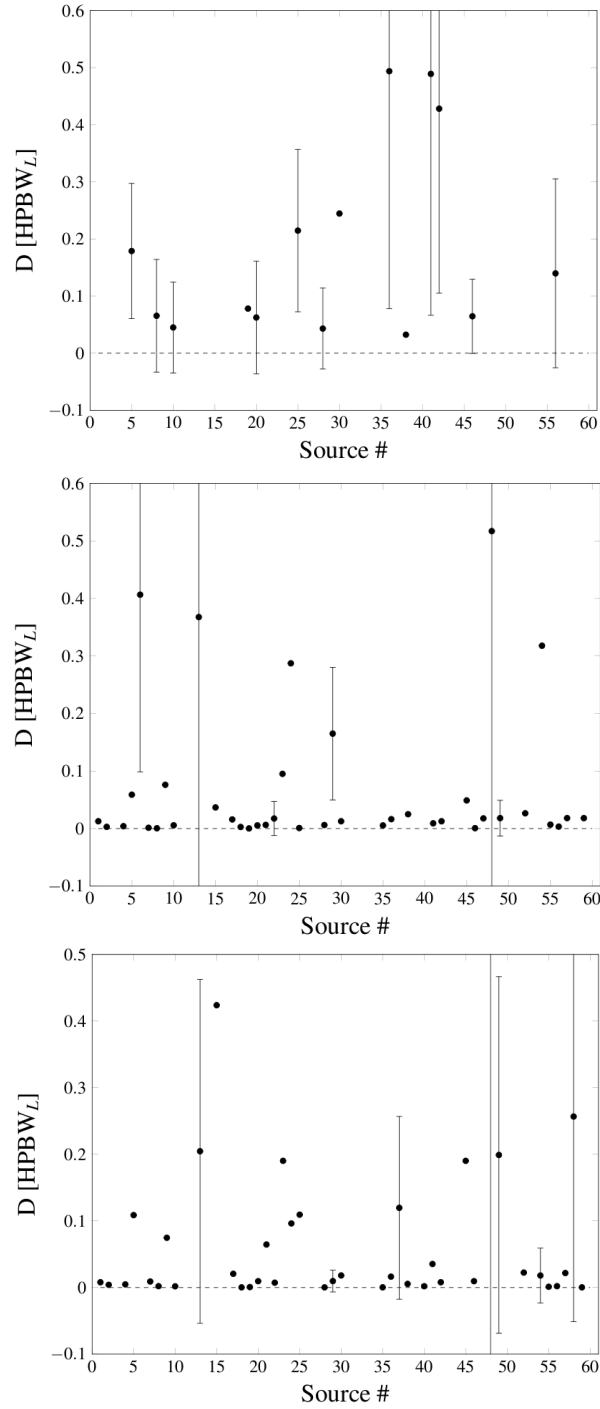


**Figure 5.9:** The mean total area  $\bar{D}$  covered by the estimated positions for the MUST TABs. The plot shows the mean  $\bar{D}$  value of the total area  $D$  covered by the overlapping values of the flux density ratio  $s_1/s_2$  and the spectral index difference  $(\alpha_2 - \alpha_1)$  normalised to  $\Omega_{\text{HPBW}_L}$ . The error corresponds to one standard deviation from that mean; (top) undersampling; (middle) Nyquist sampling; (bottom) oversampling.

position is only  $0.3^\circ$  away from the estimated location.

**Table 5.6:** Summary of results for the MUST array using Nyquist sampled TABs. Source input RA and Dec are calculated for MJD 56772.5629376499. Below we list the minimum ( $\delta D_{Min}$ ), maximum ( $\delta D_{Max}$ ) and mean ( $\bar{D}$ ) value of the total area  $D$  covered by the overlapping values of  $\mathfrak{s}_1/\mathfrak{s}_2$  and  $(\mathfrak{a}_2 - \mathfrak{a}_1)$ , normalised to the  $\Omega_{HPBW_L}$ . We also list the minimum ( $\delta\phi_{Min}$ ), maximum ( $\delta\phi_{Max}$ ) and mean ( $\bar{\Delta\phi}$ ) value of the total angular distances  $\Delta\phi$  between the true and the estimated source position, normalised to the  $HPBW_L$ .  $\bar{\alpha}_I$  is the mean estimated intrinsic spectral index from all possible locations, where the error is the standard deviation from that mean. The assigned value of  $\bar{\alpha}_I$  is -2. The two last columns list the number of areas of possible source locations  $P$  and the number of TABs in which a source was detected  $B$ . Sources for which location was estimated with a single pixel are marked with asterisk (\*).

| Nyquist sampling |              |              |  |  |                       |    |   |
|------------------|--------------|--------------|--|--|-----------------------|----|---|
|                  | Input RA     | Input Dec    | $[\delta D_{Min}, \delta D_{Max}, \overline{D}]$ | $[\delta \phi_{Min}, \delta \phi_{Max}, \overline{\Delta \phi}]$ | $\overline{\alpha_I}$ | P  | B |
| Source 1         | 03:02:06.451 | +58:08:58.16 | 0.01   | [0.003, 0.04, 0.02]  | $-2.0 \pm 0.2$        | 1  | 3 |
| Source 2         | 03:20:38.528 | +57:23:29.77 | 0.003  | [0.003, 0.05, 0.03]  | $-2.01 \pm 0.03$      | 1  | 5 |
| Source 4         | 03:50:50.836 | +53:48:31.53 | 0.004  | [0.002, 0.03, 0.01]  | $-2.0 \pm 0.1$        | 1  | 7 |
| Source 5         | 03:03:32.301 | +50:23:48.65 | 0.06   | [0.004, 0.1, 0.05]   | $-1.8 \pm 0.4$        | 1  | 3 |
| Source 6         | 02:46:21.930 | +53:34:45.72 | [0.04, 0.7, 0.4]                                 | [0.004, 3, 1]  | $-1.5 \pm 2.1$        | 5  | 2 |
| Source 7         | 03:58:43.394 | +51:42:23.46 | 0.001  | [0.003, 0.01, 0.007]   | $-2.01 \pm 0.04$      | 1  | 6 |
| Source 8         | 03:19:46.373 | +52:02:30.43 | 0.0005   | [0.004, 0.007, 0.005]  | $-2.001 \pm 0.002$    | 1  | 9 |
| Source 9         | 03:51:05.369 | +48:17:29.93 | 0.08   | [0.002, 0.1, 0.05]   | $-2.0 \pm 0.4$        | 1  | 4 |
| Source 10        | 03:24:12.682 | +49:31:02.64 | 0.006  | [0.005, 0.03, 0.02]  | $-2.0 \pm 0.2$        | 1  | 6 |
| Source 13        | 04:22:06.782 | +55:23:08.72 | [0.02, 0.9, 0.4]                                 | [0.004, 1, 0.3]  | $-1.3 \pm 1.1$        | 3  | 2 |
| Source 15        | 03:59:07.336 | +47:55:33.43 | 0.04   | [0.004, 0.08, 0.04]  | $-2.1 \pm 0.4$        | 1  | 4 |
| Source 17        | 03:21:30.964 | +58:08:06.59 | 0.02   | [0.004, 0.04, 0.02]  | $-2.0 \pm 0.2$        | 1  | 4 |
| Source 18        | 03:48:38.067 | +54:39:47.63 | 0.003  | [0.0006, 0.02, 0.01]   | $-2.0 \pm 0.1$        | 1  | 6 |
| Source 19        | 03:43:35.369 | +52:29:30.08 | [0.0002, 0.0002, 0.0002]                         | [0.05, 2, 0.7]   | $-0.28 \pm 3.01$      | 20 | 8 |
| Source 20        | 03:38:37.080 | +49:35:13.99 | 0.005  | [0.006, 0.03, 0.02]  | $-1.9 \pm 0.3$        | 1  | 6 |
| Source 21        | 03:08:57.968 | +57:19:39.49 | 0.006  | [0.004, 0.06, 0.03]  | $-2.0 \pm 0.2$        | 1  | 4 |
| Source 22        | 03:11:08.982 | +48:57:25.21 | [0.0002, 0.06, 0.02]                             | [0.005, 0.2, 0.08]   | $-2.0 \pm 0.6$        | 4  | 3 |
| Source 23        | 03:31:10.135 | +46:29:20.22 | 0.1  | [0.003, 0.1, 0.05]   | $-2.0 \pm 0.3$        | 1  | 2 |
| Source 24        | 03:03:10.785 | +57:29:32.62 | 0.3  | [0.002, 0.3, 0.1]  | $-2.2 \pm 0.7$        | 1  | 3 |
| Source 25        | 04:10:29.535 | +55:54:21.19 | 0.0009   | [0.003, 0.02, 0.01]  | $-2.1 \pm 0.2$        | 1  | 6 |
| Source 28        | 03:39:22.483 | +52:10:08.14 | 0.006  | [0.004, 0.04, 0.02]  | $-2.0 \pm 0.2$        | 1  | 7 |
| Source 29        | 02:53:18.461 | +51:13:58.62 | [0.08, 0.2, 0.2]                                 | [0.002, 2, 0.6]  | $-2.3 \pm 1.1$        | 2  | 2 |
| Source 30        | 04:12:25.038 | +58:12:27.15 | 0.01   | [0.002, 0.04, 0.02]  | $-2.0 \pm 0.3$        | 1  | 4 |
| Source 35        | 03:55:25.737 | +53:27:21.65 | 0.005  | [0.001, 0.03, 0.02]  | $-2.0 \pm 0.1$        | 1  | 5 |
| Source 36        | 04:07:40.818 | +55:22:51.73 | 0.02   | [0.003, 0.04, 0.02]  | $-2.0 \pm 0.2$        | 1  | 5 |
| Source 38        | 04:15:57.856 | +52:08:13.05 | 0.02   | [0.005, 0.06, 0.03]  | $-2.0 \pm 0.2$        | 1  | 3 |
| Source 40        | 03:51:24.741 | +59:16:43.58 | 1  | [0.002, 0.7, 0.3]  | $-2.1 \pm 0.7$        | 1  | 2 |
| Source 41        | 02:54:57.607 | +55:08:58.03 | 0.009  | [0.003, 0.04, 0.02]  | $-2.0 \pm 0.1$        | 1  | 4 |
| Source 42        | 03:06:57.849 | +50:55:26.94 | 0.01   | [0.005, 0.04, 0.02]  | $-2.0 \pm 0.2$        | 1  | 5 |
| Source 45        | 02:51:09.850 | +55:24:39.34 | 0.05   | [0.001, 0.09, 0.05]  | $-1.9 \pm 0.4$        | 1  | 3 |
| Source 46        | 03:48:40.993 | +55:06:17.42 | 0.0007   | [0.004, 0.01, 0.008]   | $-2.01 \pm 0.01$      | 1  | 6 |
| Source 47        | 04:20:38.595 | +51:06:46.24 | 0.02   | [0.002, 0.06, 0.03]  | $-2.1 \pm 0.2$        | 1  | 3 |
| Source 48        | 03:21:50.079 | +47:41:16.18 | [0.01, 2, 0.5]                                   | [0.004, 2, 0.4]  | $-1.8 \pm 1.1$        | 3  | 2 |
| Source 49        | 03:27:27.897 | +45:51:00.58 | [0.0002, 0.05, 0.02]                             | [0.02, 0.9, 0.08]  | $-2.4 \pm 0.4$        | 3  | 2 |
|                  | Input RA     | Input Dec    | $[\delta D_{Min}, \delta D_{Max}, \overline{D}]$ | $[\delta \phi_{Min}, \delta \phi_{Max}, \overline{\Delta \phi}]$ | $\overline{\alpha_I}$ | P  | B |

**Table 5.6:** (continued)

| Nyquist sampling |              |              |   |   |                  |   |   |
|------------------|--------------|--------------|---|---|------------------|---|---|
|                  | Input RA     | Input Dec    | $[\delta D_{Min}, \delta D_{Max}, \bar{D}]$ | $[\delta \phi_{Min}, \delta \phi_{Max}, \bar{\Delta \phi}]$ | $\bar{\alpha}_I$ | P | B |
| Source 52        | 03:56:24.212 | +56:58:32.97 | 0.03  | [0.004, 0.06, 0.03]   | $-2.0 \pm 0.2$   | 1 | 5 |
| Source 54        | 04:08:32.344 | +58:40:50.63 | 0.3   | [0.0009, 0.3, 0.1]  | $-1.6 \pm 0.8$   | 1 | 2 |
| Source 55        | 03:16:23.803 | +57:07:33.19 | 0.007                                       | [0.003, 0.03, 0.01]   | $-2.0 \pm 0.2$   | 1 | 6 |
| Source 56        | 03:53:34.228 | +54:31:20.11 | 0.003                                       | [0.003, 0.02, 0.01]   | $-2.0 \pm 0.2$   | 1 | 7 |
| Source 57        | 03:11:07.885 | +48:07:31.67 | 0.02  | [0.004, 0.05, 0.02]   | $-2.0 \pm 0.3$   | 1 | 4 |
| Source 59        | 03:53:27.130 | +49:37:28.22 | 0.02  | [0.002, 0.05, 0.02]   | $-2.0 \pm 0.2$   | 1 | 5 |
|                  | Input RA     | Input Dec    | $[\delta D_{Min}, \delta D_{Max}, \bar{D}]$ | $[\delta \phi_{Min}, \delta \phi_{Max}, \bar{\Delta \phi}]$ | $\bar{\alpha}_I$ | P | B |

**Table 5.7:** Summary of results for the MUST array using oversampled TABs. Source input RA and Dec are calculated for MJD 56772.5629376499. Below we list the minimum ( $\delta D_{Min}$ ), maximum ( $\delta D_{Max}$ ) and mean ( $\bar{D}$ ) value of the total area  $D$  covered by the overlapping values of  $\mathfrak{s}_1/\mathfrak{s}_2$  and  $(\mathfrak{a}_2 - \mathfrak{a}_1)$ , normalised to the  $\Omega_{HPBW_L}$ . We also list the minimum ( $\delta \phi_{Min}$ ), maximum ( $\delta \phi_{Max}$ ) and mean ( $\bar{\Delta \phi}$ ) value of the total angular distances  $\Delta \phi$  between the true and the estimated source position, normalised to the  $HPBW_L$ .  $\bar{\alpha}_I$  is the mean estimated intrinsic spectral index from all possible locations, where the error is the standard deviation from that mean. The assigned value of  $\bar{\alpha}_I$  is -2. The two last columns list the number of areas of possible source locations  $P$  and the number of TABs in which a source was detected  $B$ . Sources for which location was estimated with a single pixel are marked with asterisk (\*).

| Oversampling |              |              |   |   |                  |    |    |
|--------------|--------------|--------------|---|---|------------------|----|----|
|              | Input RA     | Input Dec    | $[\delta D_{Min}, \delta D_{Max}, \bar{D}]$ | $[\delta \phi_{Min}, \delta \phi_{Max}, \bar{\Delta \phi}]$ | $\bar{\alpha}_I$ | P  | B  |
| Source 1     | 03:02:06.451 | +58:08:58.16 | 0.008                                       | [0.003, 0.04, 0.02]   | $-2.1 \pm 0.2$   | 1  | 3  |
| Source 2     | 03:20:38.528 | +57:23:29.77 | 0.004                                       | [0.003, 0.02, 0.01]   | $-2.0 \pm 0.2$   | 1  | 6  |
| Source 4     | 03:50:50.836 | +53:48:31.53 | 0.005                                       | [0.002, 0.03, 0.02]   | $-2.01 \pm 0.07$ | 1  | 7  |
| Source 5     | 03:03:32.301 | +50:23:48.65 | 0.1   | [0.004, 0.1, 0.06]  | $-1.8 \pm 0.5$   | 1  | 3  |
| Source 7     | 03:58:43.394 | +51:42:23.46 | 0.009                                       | [0.003, 0.04, 0.02]   | $-2.0 \pm 0.2$   | 1  | 6  |
| Source 8     | 03:19:46.373 | +52:02:30.43 | 0.002                                       | [0.004, 0.01, 0.01]   | $-2.0 \pm 0.1$   | 1  | 9  |
| Source 9     | 03:51:05.369 | +48:17:29.93 | 0.07  | [0.002, 0.1, 0.05]  | $-2.0 \pm 0.5$   | 1  | 3  |
| Source 10    | 03:24:12.682 | +49:31:02.64 | 0.002                                       | [0.005, 0.02, 0.01]   | $-2.1 \pm 0.1$   | 1  | 7  |
| Source 13    | 04:22:06.782 | +55:23:08.72 | [0.02, 0.4, 0.2]                            | [0.004, 0.9, 0.2]   | $-1.9 \pm 0.5$   | 2  | 2  |
| Source 15    | 03:59:07.336 | +47:55:33.43 | 0.4   | [0.004, 0.4, 0.1]   | $-1.5 \pm 0.8$   | 1  | 2  |
| Source 17    | 03:21:30.964 | +58:08:06.59 | 0.02  | [0.004, 0.05, 0.03]   | $-2.0 \pm 0.3$   | 1  | 4  |
| Source 18    | 03:48:38.067 | +54:39:47.63 | [0.0002, 0.0005, 0.0002]                    | [0.05, 1, 0.6]  | $-0.6 \pm 3.1$   | 34 | 10 |
| Source 19    | 03:43:35.369 | +52:29:30.08 | 0.0007                                      | [0.003, 0.01, 0.007]  | $-2.01 \pm 0.07$ | 1  | 8  |
| Source 20    | 03:38:37.080 | +49:35:13.99 | 0.01  | [0.006, 0.04, 0.02]   | $-2.0 \pm 0.1$   | 1  | 7  |
| Source 21    | 03:08:57.968 | +57:19:39.49 | 0.06  | [0.004, 0.1, 0.05]  | $-1.9 \pm 0.4$   | 1  | 5  |
| Source 22    | 03:11:08.982 | +48:57:25.21 | 0.007                                       | [0.005, 0.04, 0.02]   | $-1.9 \pm 0.1$   | 1  | 3  |
| Source 23    | 03:31:10.135 | +46:29:20.22 | 0.2   | [0.003, 0.2, 0.07]  | $-1.8 \pm 0.7$   | 1  | 2  |
| Source 24    | 03:03:10.785 | +57:29:32.62 | 0.1   | [0.002, 0.1, 0.06]  | $-2.1 \pm 0.5$   | 1  | 4  |
| Source 25    | 04:10:29.535 | +55:54:21.19 | 0.1   | [0.003, 0.1, 0.07]  | $-1.8 \pm 0.4$   | 1  | 3  |
| Source 28    | 03:39:22.483 | +52:10:08.14 | 0.0002*                                     | 0.004*  | -2*              | 1  | 10 |
| Source 29    | 02:53:18.461 | +51:13:58.62 | [0.0002, 0.03, 0.01]                        | [0.002, 0.8, 0.05]  | $-2.0 \pm 0.4$   | 3  | 3  |
| Source 30    | 04:12:25.038 | +58:12:27.15 | 0.02  | [0.002, 0.04, 0.02]   | $-2.0 \pm 0.3$   | 1  | 3  |
| Source 35    | 03:55:25.737 | +53:27:21.65 | [0.0002, 0.0009, 0.0003]                    | [0.04, 0.5, 0.2]  | $-1 \pm 2$       | 17 | 7  |
| Source 36    | 04:07:40.818 | +55:22:51.73 | 0.02  | [0.003, 0.05, 0.02]   | $-2.0 \pm 0.1$   | 1  | 6  |
| Source 37    | 03:40:06.194 | +60:40:39.98 | [0.02, 0.2, 0.1]                            | [0.001, 2, 0.3]   | $-2.1 \pm 0.6$   | 2  | 2  |
|              | Input RA     | Input Dec    | $[\delta D_{Min}, \delta D_{Max}, \bar{D}]$ | $[\delta \phi_{Min}, \delta \phi_{Max}, \bar{\Delta \phi}]$ | $\bar{\alpha}_I$ | P  | B  |

Table 5.7: (continued)

|           | Input RA     | Input Dec    | Oversampling                                     |  | $\overline{\alpha_I}$ | P | B |
|-----------|--------------|--------------|--|--|-----------------------|---|---|
|           |              |              | $[\delta D_{Min}, \delta D_{Max}, \overline{D}]$ | $[\delta \phi_{Min}, \delta \phi_{Max}, \overline{\Delta \phi}]$ |                       |   |   |
| Source 38 | 04:15:57.856 | +52:08:13.05 | 0.005  | [0.005, 0.06, 0.03]  | $-2.0 \pm 0.1$        | 1 | 3 |
| Source 40 | 03:51:24.741 | +59:16:43.58 | [0.0002, 0.004, 0.002]                           | [0.002, 0.03, 0.02]  | $-2.0 \pm 0.3$        | 2 | 3 |
| Source 41 | 02:54:57.607 | +55:08:58.03 | 0.04   | [0.003, 0.07, 0.04]  | $-1.9 \pm 0.2$        | 1 | 3 |
| Source 42 | 03:06:57.849 | +50:55:26.94 | 0.008  | [0.005, 0.03, 0.02]  | $-2.0 \pm 0.1$        | 1 | 5 |
| Source 45 | 02:51:09.850 | +55:24:39.34 | 0.2  | [0.001, 0.4, 0.2]  | $-1.4 \pm 0.5$        | 1 | 2 |
| Source 46 | 03:48:40.993 | +55:06:17.42 | 0.01   | [0.03, 0.08, 0.06]   | $-2.0 \pm 0.4$        | 1 | 8 |
| Source 48 | 03:21:50.079 | +47:41:16.18 | [0.003, 2, 0.8]                                  | [0.004, 0.9, 0.4]  | $-2.4 \pm 0.8$        | 2 | 2 |
| Source 49 | 03:27:27.897 | +45:51:00.58 | [0.0002, 0.7, 0.2]                               | [0.002, 3, 0.7]  | $-0.9 \pm 2.1$        | 5 | 2 |
| Source 52 | 03:56:24.212 | +56:58:32.97 | 0.02   | [0.004, 0.05, 0.03]  | $-2.0 \pm 0.3$        | 1 | 6 |
| Source 54 | 04:08:32.344 | +58:40:50.63 | [0.0002, 0.1, 0.02]                              | [0.06, 0.9, 0.7]   | $-1.2 \pm 0.5$        | 6 | 2 |
| Source 55 | 03:16:23.803 | +57:07:33.19 | 0.001  | [0.003, 0.02, 0.01]  | $-2.0 \pm 0.2$        | 1 | 7 |
| Source 56 | 03:53:34.228 | +54:31:20.11 | 0.002  | [0.003, 0.01, 0.008]   | $-2.0 \pm 0.1$        | 1 | 9 |
| Source 57 | 03:11:07.885 | +48:07:31.67 | 0.02   | [0.004, 0.08, 0.03]  | $-2.0 \pm 0.3$        | 1 | 3 |
| Source 58 | 03:08:59.819 | +60:37:41.54 | [0.002, 0.8, 0.3]                                | [0.002, 2, 0.9]  | $-0.5 \pm 2.1$        | 6 | 2 |
| Source 59 | 03:53:27.130 | +49:37:28.22 | 0.0002*  | 0.01*  | $-1.9^*$              | 1 | 6 |
|           | Input RA     | Input Dec    | $[\delta D_{Min}, \delta D_{Max}, \overline{D}]$ | $[\delta \phi_{Min}, \delta \phi_{Max}, \overline{\Delta \phi}]$ | $\overline{\alpha_I}$ | P | B |

Figure 5.11 shows the mean value of the estimated intrinsic spectral index  $\overline{\alpha_I}$  from all combined estimated locations for that source detected with the undersampled, the Nyquist sampled and the oversampled methods. We summarise the results next:

- All but two sources detected in the undersampled TABs, the top panel, were detected in two TABs only;
  - The value of the estimated  $\overline{\alpha_I}$  is close to the assigned value of -2, but the deviation, for the majority of sources as around 50% of the  $\overline{\alpha_I}$  value;
- For sources detected in the Nyquist sampled TABs, the middle panel, position of 32 sources were estimated with a single location;
  - As a result, the value of the estimated  $\overline{\alpha_I}$  is close to -2 for the majority of sources with deviation of less than 20% of the  $\overline{\alpha_I}$  value.
- For sources detected in the oversampled TABs, the bottom panel, the value of the estimated  $\overline{\alpha_I}$  also oscillates around -2.
  - The deviation of the mean are much higher than for the Nyquist sampled method with at least 30% of the  $\overline{\alpha_I}$  value.

A clear relationship can be observed between the number of estimated locations and the accuracy of the  $\overline{\alpha_I}$  estimation.

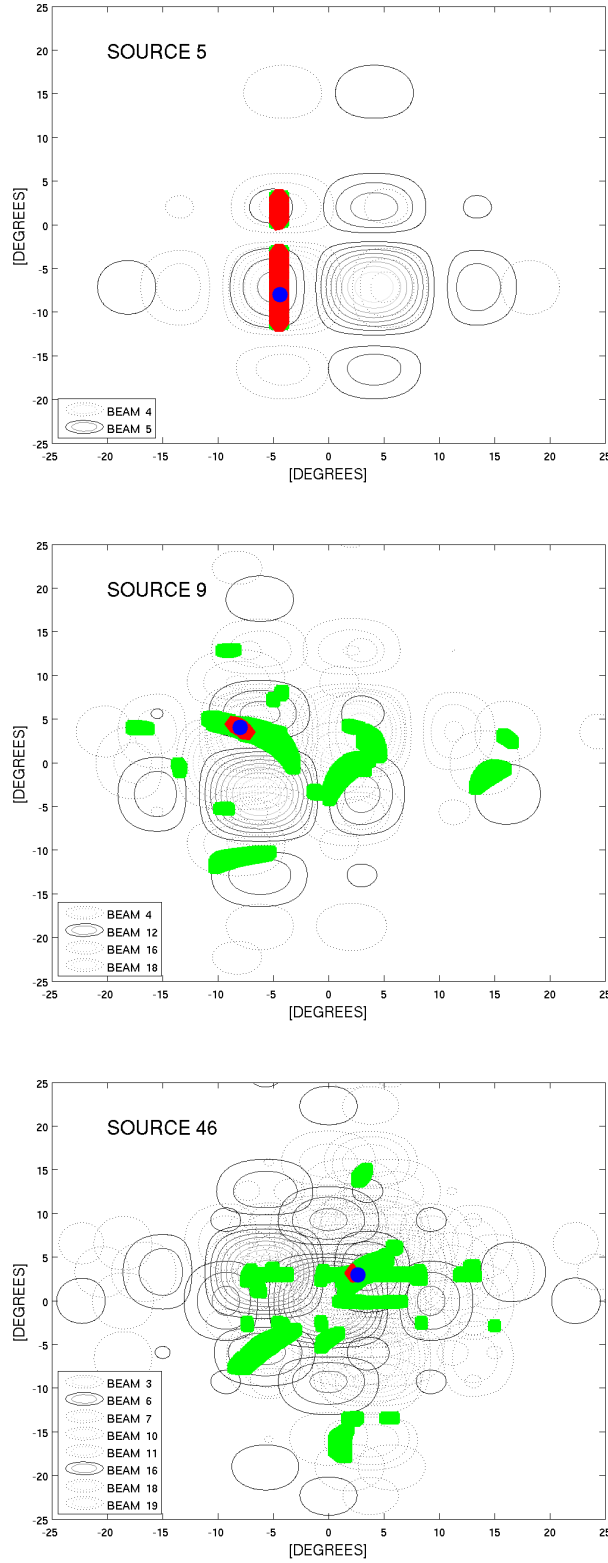


**Figure 5.10:** Detection examples for the MUST array with undersampling, Nyquist sampling and oversampling the FoV. Green squares correspond to overlapping values of  $\mathfrak{s}_1/\mathfrak{s}_2$  and  $(\mathfrak{a}_2 - \mathfrak{a}_1)$  from TAB pairs, red diamonds represent overlapping coordinates of  $\mathfrak{s}_1/\mathfrak{s}_2$  and  $(\mathfrak{a}_2 - \mathfrak{a}_1)$  from all TABs and the blue circle shows the true position of a source; (top) undersampling; (middle) Nyquist sampling; (bottom) oversampling.



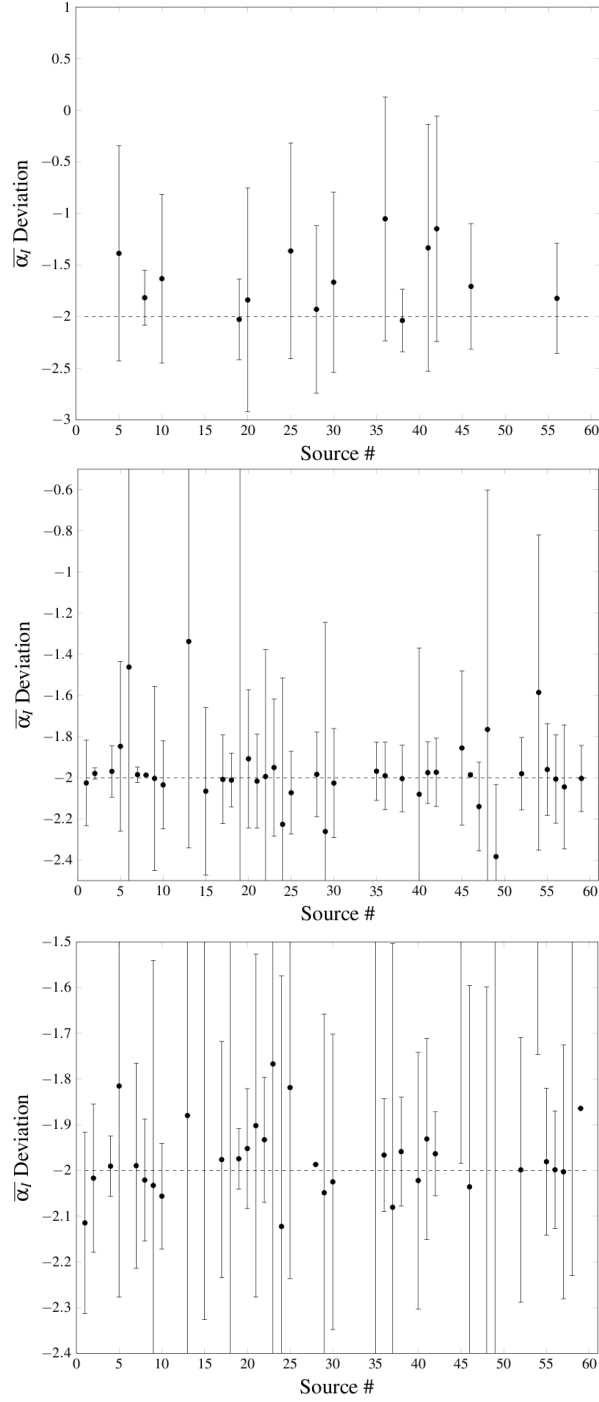


**Figure 5.11:** The estimated  $\bar{\alpha}_I$  for sources detected in the MUST TABs. The error bars show the standard deviation of the mean  $\bar{\alpha}_I$  from all estimated source positions. The assigned value of the intrinsic spectral index  $\alpha_I = -2$ ; (top) undersampling; (middle) Nyquist sampling; (bottom) oversampling.

### 5.3.2 LOFAR Superterp

The top and the bottom left panels in Figure 5.12 illustrate the position of the LOFAR TABs relative to the randomly generated point sources. We summarise here the detection rates with different spatial TAB sampling illustrated in the bottom right panel in Figure 5.12:

- Oversampling of the FoV, bottom left panel, gives the highest detection rate with 55 detected sources, marked with the  $\diamond$ , the  $\circ$  and the  $\square$  symbols in the bottom right panel;
- When Nyquist sampling the Fov, the top right panel, 48 sources were detected, the  $\circ$  and the  $\square$  symbols in the bottom right panel;
- Undersampling detected only three, the  $\circ$  symbol in the bottom right panel;
- The  $\diamond$  symbol, in the bottom right panel, represents sources not detected with any spatial sampling method. All five sources lay outside of the test area, where the requirements for detection are more difficult to meet;
- All sources, apart from source #56, detected outside of the test area were detected in the oversampled TABs.

Source #6, marked with a red circle in the bottom left panel, illustrates the impact of fractional bandwidth<sup>10</sup> on the detection rates. It is clear that source #6 is not detected when the FoV is Nyquist sampled as the second condition for successful detection is not satisfied. Refer to Table 5.8, Table 5.9 and Table 5.10 for more details.

**Table 5.8:** Summary of results for the LOFAR array using undersampled TABs. Source input RA and Dec are calculated for MJD 56772.5629376499. Below we list the minimum ( $\delta D_{Min}$ ), maximum ( $\delta D_{Max}$ ) and mean ( $\overline{D}$ ) value of the total area  $D$  covered by the overlapping values of  $\mathfrak{s}_1/\mathfrak{s}_2$  and  $(\mathfrak{a}_2 - \mathfrak{a}_1)$ , normalised to the  $\Omega_{HPBW_L}$ . We also list the minimum ( $\delta\phi_{Min}$ ), maximum ( $\delta\phi_{Max}$ ) and mean ( $\overline{\Delta\phi}$ ) value of the total angular distances  $\Delta\phi$  between the true and the estimated source position, normalised to the  $HPBW_L$ .  $\overline{\alpha_I}$  is the mean estimated intrinsic spectral index from all possible locations, where the error is the standard deviation from that mean. The assigned value of  $\overline{\alpha_I}$  is -2. The two last columns list the number of areas of possible source locations  $P$  and the number of TABs in which a source was detected  $B$ . Sources for which location was estimated with a single pixel are marked with asterisk (\*).

| Undersampling |              |              |  |  |                       |   |       |
|---------------|--------------|--------------|--|--|-----------------------|---|-------|
|               | Input RA     | Input Dec    | $[\delta D_{Min}, \delta D_{Max}, \overline{D}]$ | $[\delta \phi_{Min}, \delta \phi_{Max}, \overline{\Delta \phi}]$ | $\overline{\alpha_I}$ | P | Beams |
| Source 23     | 04:12:28.618 | +52:17:24.61 | [0.009, 0.6, 0.1]                                | [0.009, 6, 1]  | $-1.2 \pm 0.9$        | 7 | 2     |
|               | Input RA     | Input Dec    | $[\delta D_{Min}, \delta D_{Max}, \overline{D}]$ | $[\delta \phi_{Min}, \delta \phi_{Max}, \overline{\Delta \phi}]$ | $\overline{\alpha_I}$ | P | Beams |

<sup>10</sup>Fractional bandwidth indicates how wide the bandwidth is and is given as  $(v_H - v_L)/v_c$ , where  $v_c$  is a centre frequency in the band.

**Table 5.8:** (continued)

|                  | Undersampling   |                  |   |   |                  |          | <b>P</b>     | <b>Beams</b> |
|------------------|-----------------|------------------|---|---|------------------|----------|--------------|--------------|
|                  | <b>Input RA</b> | <b>Input Dec</b> | $[\delta D_{Min}, \delta D_{Max}, \bar{D}]$ | $[\delta \phi_{Min}, \delta \phi_{Max}, \bar{\Delta \phi}]$ | $\bar{\alpha}_I$ |          |              |              |
| <b>Source 34</b> | 04:10:36.472    | +52:52:44.27     | [0.004, 0.3, 0.1]                           | [0.007, 3, 0.4]   | $-1.4 \pm 0.7$   | 3        | 2            |              |
| <b>Source 44</b> | 04:13:05.224    | +52:53:40.87     | [0.005, 0.5, 0.1]                           | [0.003, 6, 1]   | $-1.2 \pm 0.9$   | 7        | 2            |              |
|                  | <b>Input RA</b> | <b>Input Dec</b> | $[\delta D_{Min}, \delta D_{Max}, \bar{D}]$ | $[\delta \phi_{Min}, \delta \phi_{Max}, \bar{\Delta \phi}]$ | $\bar{\alpha}_I$ | <b>P</b> | <b>Beams</b> |              |

Figure 5.13 shows the mean total area  $\bar{D}$  covered by the estimated positions for the undersampled, top panel, Nyquist sampled, the middle panel, and the oversampled methods, the bottom panel. We summarise the results below:

- For sources detected in the undersampled TABs, the top left panel, the mean total area  $\bar{D}$  for all three sources is 10% of  $\Omega_{HPBW_L}$ ;
  - The mean angular distance  $\bar{\Delta \phi}$  for two sources is one  $HPBW_L$ ;
- For 41 sources detected in the Nyquist sampled TABs, the top right panel,  $\bar{D}$  is less than 10% of  $\Omega_{HPBW_L}$ ;
  - For 10 sources  $\bar{D}$  is less than 1% of  $\Omega_{HPBW_L}$ ;
  - For 6 sources the mean angular distance  $\bar{\Delta \phi}$  is less than 1% of  $HPBW_L$ ;
  - For 15 sources  $\bar{\Delta \phi}$  is less than 50% of  $HPBW_L$ ;
  - A single pixel location was estimated for three sources with  $\delta \phi$  of 1% of  $HPBW_L$ , i.e. 15.5 arcsecond;
- For 45 sources detected with the oversampled TABs, the bottom left panel, the  $\bar{D}$  is less than 10% of  $\Omega_{HPBW_L}$ ;
  - For 16 sources,  $\bar{D}$  is less than 5% of  $\Omega_{HPBW_L}$ ;
  - For 24 sources,  $\bar{D}$  is less than 1% of  $\Omega_{HPBW_L}$ ;
  - For 21 sources the mean angular distance  $\bar{\Delta \phi}$  is less than 10% of  $HPBW_L$ ;
  - For three sources  $\bar{\Delta \phi}$  is less than 5% of  $HPBW_L$ , i.e. 1.3 arcminute, and for 17 sources  $\bar{\Delta \phi}$  is less than 1% of  $HPBW_L$ .

A single pixel location was estimated for five sources with angular distance  $\delta \phi$  from the true source positions of 1% of  $HPBW_L$ .

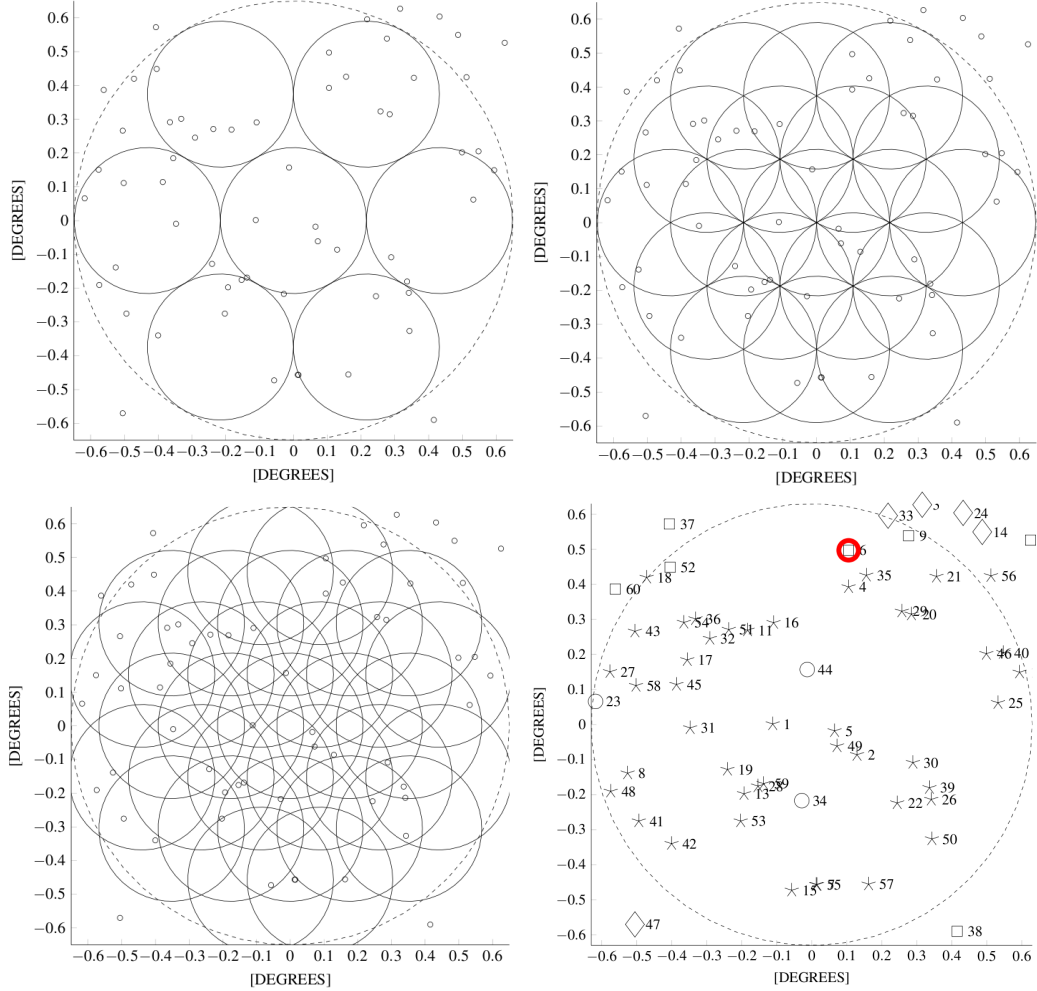


**Figure 5.12:** The LOFAR Superterp TABs spatial TAB sampling. The dashed circle of diameter  $3 \times \text{HPBW}_L$  represents a test area for different methods of spatial sampling ( $\text{HPBW}_L = 0.43^\circ$ ). The position of randomly placed sources are shown as small circles. (Top left) undersampling: 7 independent TABs are separated by  $\text{HPBW}_L$ ; (top right) Nyquist sampling: 19 independent beams are separated by  $\text{HPBW}_L/2 = 0.215^\circ$ ; (bottom left) oversampling: 31 independent beams are separated by  $\text{HPBW}_H/2 = 0.175^\circ$ . (Bottom right) graphical representation of source detection success using different sampling methods;  $\circ$ : sources detected with undersampling, Nyquist sampling and oversampling;  $\square$ : sources detected with Nyquist sampling and oversampling;  $\diamond$ : no detection with any sampling method;  $\nabla$ : sources detected with Nyquist sampling only;  $\circ$  (with a dot): sources detected with oversampling only.

**Table 5.9:** Summary of results for the LOFAR array using Nyquist sampled TABs. Source input RA and Dec are calculated for MJD 56772.5629376499. Below we list the minimum ( $\delta D_{Min}$ ), maximum ( $\delta D_{Max}$ ) and mean ( $\bar{D}$ ) value of the total area  $D$  covered by the overlapping values of  $\mathfrak{s}_1/\mathfrak{s}_2$  and  $(\mathfrak{a}_2 - \mathfrak{a}_1)$ , normalised to the  $\Omega_{HPBW_L}$ . We also list the minimum ( $\delta\phi_{Min}$ ), maximum ( $\delta\phi_{Max}$ ) and mean ( $\bar{\Delta\phi}$ ) value of the total angular distances  $\Delta\phi$  between the true and the estimated source position, normalised to the  $HPBW_L$ .  $\bar{\alpha}_I$  is the mean estimated intrinsic spectral index from all possible locations, where the error is the standard deviation from that mean. The assigned value of  $\bar{\alpha}_I$  is -2. The two last columns list the number of areas of possible source locations  $P$  and the number of TABs in which a source was detected  $B$ . Sources for which location was estimated with a single pixel are marked with asterisk (\*).

|                  | Nyquist sampling |                  |   |  |                  |          | <b>P</b> | <b>B</b> |
|------------------|------------------|------------------|---|--|------------------|----------|----------|----------|
|                  | <b>Input RA</b>  | <b>Input Dec</b> | $[\delta D_{Min}, \delta D_{Max}, \bar{D}]$ | $[\delta\phi_{Min}, \delta\phi_{Max}, \bar{\Delta\phi}]$ | $\bar{\alpha}_I$ |          |          |          |
| <b>Source 1</b>  | 04:12:03.422     | +52:47:47.31     | 0.0004*                                     | 0.009*   | -2*              | 1        | 5        |          |
| <b>Source 2</b>  | 04:11:28.443     | +53:02:13.58     | 0.009                                       | [0.008, 0.06, 0.04]                                      | $-2.01 \pm 0.05$ | 1        | 3        |          |
| <b>Source 4</b>  | 04:14:39.398     | +53:00:40.80     | [0.06, 0.06, 0.06]                          | [0.01, 3, 0.9]   | $-1.9 \pm 0.2$   | 2        | 3        |          |
| <b>Source 5</b>  | 04:11:55.576     | +52:58:23.24     | [0.0004, 0.2, 0.04]                         | [0.008, 4, 0.6]  | $-1.7 \pm 0.4$   | 6        | 3        |          |
| <b>Source 7</b>  | 04:09:00.987     | +52:55:13.27     | [0.0004, 1, 0.1]                            | [0.01, 8, 2]   | $-0.6 \pm 2.1$   | 31       | 2        |          |
| <b>Source 8</b>  | 04:11:08.288     | +52:22:54.18     | [0.02, 0.02, 0.02]                          | [0.005, 2, 0.7]  | $-1.9 \pm 0.2$   | 2        | 3        |          |
| <b>Source 11</b> | 04:13:49.417     | +52:43:25.49     | [0.0009, 0.002, 0.001]                      | [0.007, 2, 0.5]  | $-2.01 \pm 0.09$ | 4        | 3        |          |
| <b>Source 12</b> | 04:13:02.943     | +53:30:05.01     | [0.0004, 0.7, 0.05]                         | [0.007, 7, 2]  | $-1.1 \pm 1.1$   | 37       | 2        |          |
| <b>Source 13</b> | 04:10:44.553     | +52:42:50.20     | [0.01, 0.02, 0.02]                          | [0.007, 2, 0.9]  | $-1.9 \pm 0.2$   | 2        | 3        |          |
| <b>Source 15</b> | 04:08:54.893     | +52:50:53.54     | [0.0004, 0.7, 0.2]                          | [0.01, 3, 0.5]   | $-1.6 \pm 0.7$   | 5        | 3        |          |
| <b>Source 16</b> | 04:13:58.107     | +52:47:52.13     | [0.03, 0.03, 0.03]                          | [0.005, 2, 0.9]  | $-1.9 \pm 0.2$   | 2        | 3        |          |
| <b>Source 17</b> | 04:13:15.629     | +52:33:06.55     | [0.0004, 0.5, 0.04]                         | [0.009, 6, 2]  | $-1.3 \pm 1.1$   | 24       | 2        |          |
| <b>Source 18</b> | 04:14:48.026     | +52:26:03.06     | [0.02, 1, 0.4]                              | [0.008, 3, 0.7]  | $-1.5 \pm 0.8$   | 3        | 2        |          |
| <b>Source 19</b> | 04:11:12.060     | +52:40:00.88     | [0.0009, 0.2, 0.04]                         | [0.01, 4, 0.5]   | $-1.7 \pm 0.4$   | 6        | 3        |          |
| <b>Source 20</b> | 04:14:08.872     | +53:11:29.78     | [0.0004, 1, 0.08]                           | [0.004, 8, 2]  | $-0.7 \pm 2.1$   | 39       | 2        |          |
| <b>Source 21</b> | 04:14:52.255     | +53:15:43.94     | [0.0004, 3, 0.4]                            | [0.005, 6, 1]  | $-1 \pm 1$       | 14       | 2        |          |
| <b>Source 22</b> | 04:10:33.256     | +53:09:05.25     | [0.0004, 0.7, 0.04]                         | [0.008, 4, 1]  | $-1.4 \pm 1.1$   | 20       | 2        |          |
| <b>Source 23</b> | 04:12:28.618     | +52:17:24.61     | [0.0009, 0.3, 0.09]                         | [0.009, 3, 0.3]  | $-1.7 \pm 0.4$   | 3        | 3        |          |
| <b>Source 25</b> | 04:12:27.813     | +53:26:23.86     | [0.0004, 0.07, 0.02]                        | [0.005, 6, 1]  | $-1.8 \pm 0.5$   | 6        | 3        |          |
| <b>Source 26</b> | 04:10:37.078     | +53:14:55.45     | [0.0004, 0.002, 0.0007]                     | [0.09, 4, 2]   | $-1.4 \pm 1.1$   | 16       | 2        |          |
| <b>Source 27</b> | 04:13:01.900     | +52:19:52.90     | [0.0004, 0.7, 0.05]                         | [0.01, 6, 2]   | $-1.3 \pm 1.1$   | 28       | 2        |          |
| <b>Source 28</b> | 04:10:53.149     | +52:45:14.50     | 0.0004*                                     | 0.01*  | -2*              | 1        | 4        |          |
| <b>Source 29</b> | 04:14:12.165     | +53:09:50.83     | [0.0004, 1, 0.08]                           | [0.007, 8, 2]  | $-0.7 \pm 1.9$   | 37       | 2        |          |
| <b>Source 30</b> | 04:11:19.319     | +53:11:48.90     | [0.0004, 0.04, 0.006]                       | [0.007, 4, 0.5]  | $-1.6 \pm 0.4$   | 7        | 3        |          |
| <b>Source 31</b> | 04:11:58.973     | +52:33:37.64     | [0.0004, 0.6, 0.03]                         | [0.006, 6, 1]  | $-1.3 \pm 1.1$   | 28       | 2        |          |
| <b>Source 32</b> | 04:13:39.775     | +52:36:58.27     | [0.0004, 0.5, 0.03]                         | [0.004, 7, 2]  | $-1.2 \pm 1.1$   | 34       | 2        |          |
| <b>Source 34</b> | 04:10:36.472     | +52:52:44.27     | [0.0004, 0.2, 0.03]                         | [0.007, 4, 0.7]  | $-1.7 \pm 0.4$   | 5        | 3        |          |
| <b>Source 35</b> | 04:14:52.765     | +53:03:41.94     | [0.0004, 0.6, 0.3]                          | [0.007, 1, 0.4]  | $-1.4 \pm 0.7$   | 2        | 2        |          |
| <b>Source 36</b> | 04:14:01.742     | +52:34:29.10     | [0.0004, 0.8, 0.06]                         | [0.002, 8, 2]  | $-0.8 \pm 1.1$   | 40       | 2        |          |
| <b>Source 39</b> | 04:10:50.451     | +53:14:37.71     | [0.0004, 0.2, 0.07]                         | [0.009, 4, 0.3]  | $-1.7 \pm 0.4$   | 3        | 3        |          |
| <b>Source 40</b> | 04:13:25.383     | +53:27:17.34     | [0.0004, 1, 0.1]                            | [0.003, 8, 2]  | $-0.8 \pm 2.1$   | 28       | 2        |          |
| <b>Source 41</b> | 04:10:14.457     | +52:24:46.60     | [0.0004, 0.9, 0.1]                          | [0.004, 6, 0.7]  | $-1.3 \pm 0.9$   | 7        | 2        |          |
| <b>Source 42</b> | 04:09:48.831     | +52:30:22.16     | [0.002, 1, 0.1]                             | [0.009, 6, 2]  | $-0.9 \pm 1.1$   | 21       | 2        |          |
| <b>Source 43</b> | 04:13:47.424     | +52:24:06.92     | [0.0004, 1, 0.1]                            | [0.009, 6, 1]  | $-0.7 \pm 1.1$   | 12       | 2        |          |
| <b>Source 44</b> | 04:13:05.224     | +52:53:40.87     | [0.0004, 0.3, 0.07]                         | [0.003, 4, 0.4]  | $-1.7 \pm 0.3$   | 4        | 3        |          |
| <b>Source 45</b> | 04:12:47.812     | +52:31:16.35     | [0.0004, 0.02, 0.005]                       | [0.006, 4, 0.5]  | $-1.7 \pm 0.5$   | 6        | 3        |          |
| <b>Source 46</b> | 04:13:24.165     | +53:24:22.36     | 0.0004*                                     | 0.006*   | -2*              | 1        | 4        |          |
|                  | <b>Input RA</b>  | <b>Input Dec</b> | $[\delta D_{Min}, \delta D_{Max}, \bar{D}]$ | $[\delta\phi_{Min}, \delta\phi_{Max}, \bar{\Delta\phi}]$ | $\bar{\alpha}_I$ | <b>P</b> | <b>B</b> |          |

**Table 5.9:** (continued)

|                  | Input RA     | Input Dec    | Nyquist sampling                                 |  | $\overline{\alpha_I}$ | <b>P</b> | <b>B</b> |
|------------------|--------------|--------------|--|--|-----------------------|----------|----------|
|                  |              |              | $[\delta D_{Min}, \delta D_{Max}, \overline{D}]$ | $[\delta \phi_{Min}, \delta \phi_{Max}, \overline{\Delta \phi}]$ |                       |          |          |
| <b>Source 48</b> | 04:10:47.950 | +52:19:59.17 | [0.0004, 0.9, 0.06]                              | [0.007, 8, 2]  | $-0.9 \pm 0.9$        | 39       | 2        |
| <b>Source 49</b> | 04:11:38.342 | +52:58:48.06 | [0.0004, 0.3, 0.08]                              | [0.009, 4, 0.3]  | $-1.8 \pm 0.4$        | 4        | 3        |
| <b>Source 50</b> | 04:09:51.831 | +53:14:59.89 | [0.0004, 1, 0.09]                                | [0.009, 8, 2]  | $-0.6 \pm 2.1$        | 34       | 2        |
| <b>Source 51</b> | 04:13:50.019 | +52:40:12.25 | [0.0004, 0.6, 0.04]                              | [0.006, 6, 2]  | $-1.3 \pm 1.1$        | 29       | 2        |
| <b>Source 53</b> | 04:10:13.738 | +52:42:14.69 | [0.0004, 0.05, 0.02]                             | [0.004, 4, 0.1]  | $-2.0 \pm 0.3$        | 2        | 3        |
| <b>Source 54</b> | 04:13:57.663 | +52:32:30.06 | [0.0004, 0.8, 0.06]                              | [0.003, 8, 2]  | $-1 \pm 1$            | 37       | 2        |
| <b>Source 55</b> | 04:09:01.104 | +52:55:05.71 | [0.0004, 1, 0.1]                                 | [0.009, 8, 2]  | $-0.5 \pm 2.1$        | 31       | 2        |
| <b>Source 56</b> | 04:14:53.636 | +53:25:04.00 | 0.6  | [0.01, 1, 0.5]   | $-1.7 \pm 0.7$        | 1        | 2        |
| <b>Source 57</b> | 04:09:00.896 | +53:04:04.47 | [0.004, 0.7, 0.2]                                | [0.008, 3, 0.6]  | $-1.3 \pm 0.8$        | 3        | 2        |
| <b>Source 58</b> | 04:12:46.504 | +52:24:20.37 | 0.006  | [0.008, 0.06, 0.04]  | $-2.0 \pm 0.1$        | 1        | 3        |
| <b>Source 59</b> | 04:10:55.883 | +52:46:12.06 | 0.007  | [0.01, 0.05, 0.03]   | $-2.01 \pm 0.04$      | 1        | 4        |
|                  | Input RA     | Input Dec    | $[\delta D_{Min}, \delta D_{Max}, \overline{D}]$ | $[\delta \phi_{Min}, \delta \phi_{Max}, \overline{\Delta \phi}]$ | $\overline{\alpha_I}$ | <b>P</b> | <b>B</b> |

Figure 5.14 presents examples of the estimated source positions for representative cases with low (one location only) and high (many possible locations) positional uncertainty with the undersampling, Nyquist sampling and oversampling method. The top panel shows another example for a two TAB detection and the high positional uncertainty it produces. Here, source #23 was detected in two TABs, six different locations were estimated as a result, where five small patches are located in sidelobes and one extensive patch is produced in the TAB. Poor location estimation is a trend that repeats for every sampling method when only two TABs are used to estimate a source location. The middle panel shows a detection in three Nyquist sampled TABs of source #11. Only two small patches of overlapping  $\mathfrak{s}_1/\mathfrak{s}_2$  and  $(\alpha_2 - \alpha_1)$  values from all TABs, which is a substantial improvement from a two beam detection. In the case of the oversampled TABs, the bottom panel, where the conditions for detection in multiple TABs can be more easily met, the positional uncertainty is lower. For example, as demonstrated for a detection of source #25, the estimated location covers 20% of the  $\Omega_{HPBW_L}$  despite detection in four TABs.

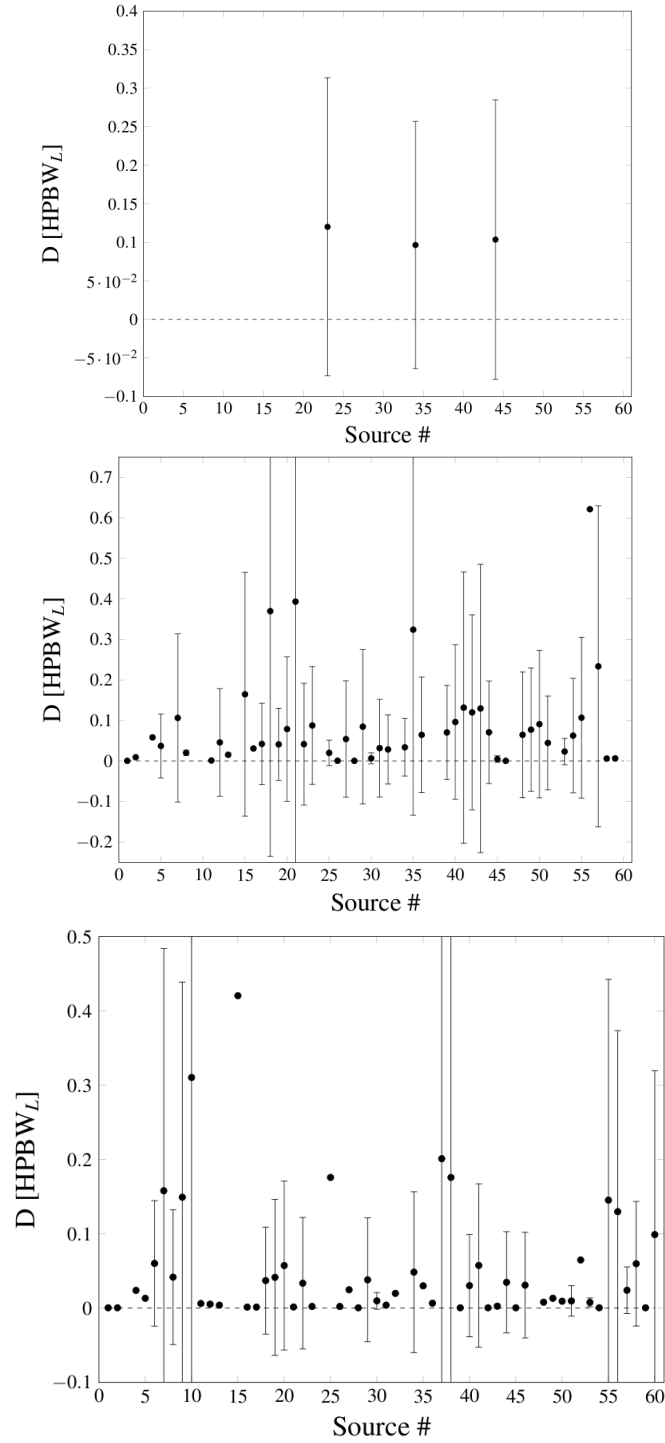


**Figure 5.13:** The mean total area  $\bar{D}$  covered by the estimated positions for the LOFAR TABs. The plot shows the mean  $\bar{D}$  value of the total area  $D$  covered by the overlapping values of the flux density ratio  $s_1/s_2$  and the spectral index difference  $(\alpha_2 - \alpha_1)$  normalised to  $\Omega_{\text{HPBW}_L}$ . The error corresponds to one standard deviation from that mean; (top) undersampling; (middle) Nyquist sampling; (bottom) oversampling.

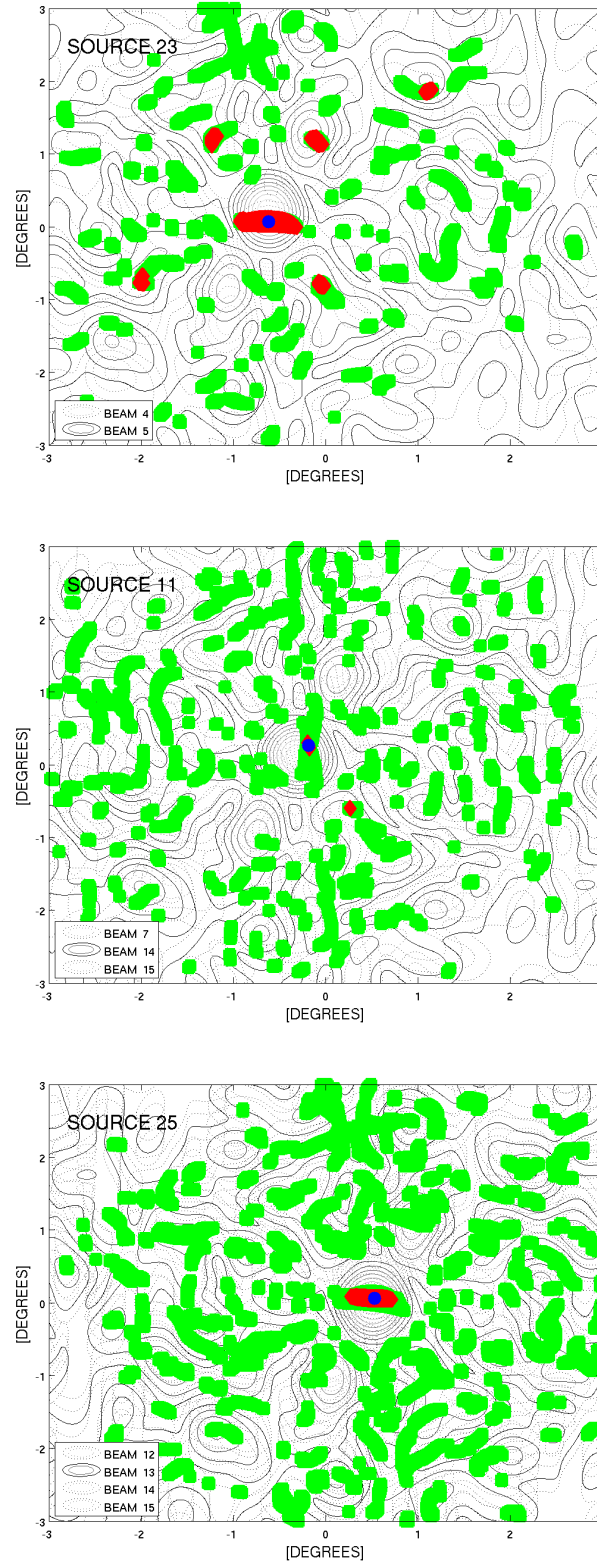


**Figure 5.14:** Detection examples for the LOFAR array with different spatial sampling. Green squares correspond to overlapping values of  $s_1/s_2$  and  $(a_2 - a_1)$  from TAB pairs, red diamonds represent overlapping coordinates of  $s_1/s_2$  and  $(a_2 - a_1)$  from all TABs and the blue circle shows the true position of a source; (top) undersampling; (middle) Nyquist sampling; (bottom) oversampling.



**Table 5.10:** Summary of results for the LOFAR array using oversampled TABs. Source input RA and Dec are calculated for MJD 56772.5629376499. Below we list the minimum ( $\delta D_{Min}$ ), maximum ( $\delta D_{Max}$ ) and mean ( $\bar{D}$ ) value of the total area  $D$  covered by the overlapping values of  $\mathfrak{s}_1/\mathfrak{s}_2$  and  $(\mathfrak{a}_2 - \mathfrak{a}_1)$ , normalised to the  $\Omega_{HPBW_L}$ . We also list the minimum ( $\delta\phi_{Min}$ ), maximum ( $\delta\phi_{Max}$ ) and mean ( $\bar{\Delta\phi}$ ) value of the total angular distances  $\Delta\phi$  between the true and the estimated source position, normalised to the  $HPBW_L$ .  $\bar{\alpha}_I$  is the mean estimated intrinsic spectral index from all possible locations, where the error is the standard deviation from that mean. The assigned value of  $\bar{\alpha}_I$  is -2. The two last columns list the number of areas of possible source locations  $P$  and the number of TABs in which a source was detected  $B$ . Sources for which location was estimated with a single pixel are marked with asterisk (\*).

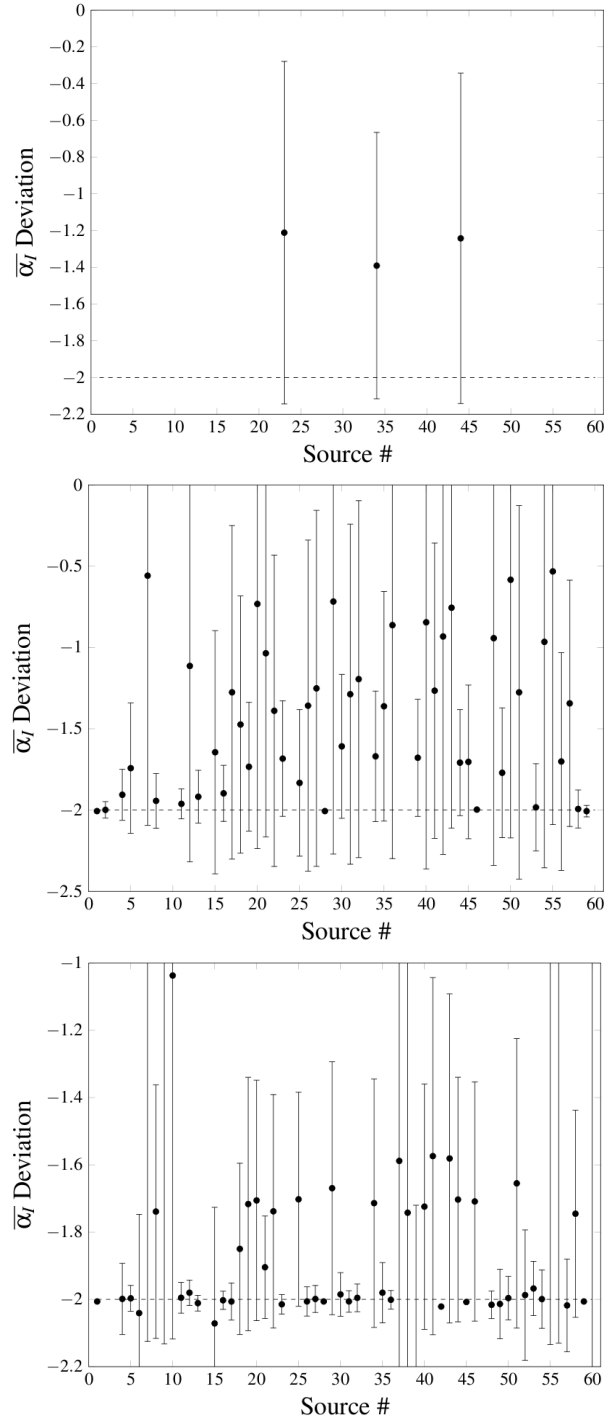
| Oversampling |              |              |  |  |                       |    |   |
|--------------|--------------|--------------|--|--|-----------------------|----|---|
|              | Input RA     | Input Dec    | $[\delta D_{Min}, \delta D_{Max}, \overline{D}]$ | $[\delta \phi_{Min}, \delta \phi_{Max}, \overline{\Delta \phi}]$ | $\overline{\alpha}_I$ | P  | B |
| Source 1     | 04:12:03.422 | +52:47:47.31 | 0.0004*  | 0.009*   | -2*                   | 1  | 5 |
| Source 2     | 04:11:28.443 | +53:02:13.58 | [0.0004, 0.0004, 0.0004]                         | [6, 7, 7]  | $1.9 \pm 1.1$         | 9  | 5 |
| Source 4     | 04:14:39.398 | +53:00:40.80 | 0.02   | [0.01, 0.09, 0.05]   | $-2.0 \pm 0.1$        | 1  | 5 |
| Source 5     | 04:11:55.576 | +52:58:23.24 | 0.01   | [0.008, 0.06, 0.03]  | $-2.01 \pm 0.04$      | 1  | 5 |
| Source 6     | 04:15:21.034 | +53:00:37.10 | [0.0004, 0.1, 0.06]                              | [0.01, 0.4, 0.2]   | $-2.0 \pm 0.3$        | 2  | 3 |
| Source 7     | 04:09:00.987 | +52:55:13.27 | [0.001, 1, 0.2]                                  | [0.01, 6, 2]   | $-0.8 \pm 1.1$        | 18 | 2 |
| Source 8     | 04:11:08.288 | +52:22:54.18 | [0.0004, 0.2, 0.04]                              | [0.005, 4, 0.6]  | $-1.7 \pm 0.4$        | 7  | 3 |
| Source 9     | 04:15:38.429 | +53:10:52.15 | [0.0004, 1, 0.1]                                 | [0.005, 8, 2]  | $-0.7 \pm 1.1$        | 23 | 2 |
| Source 10    | 04:15:35.180 | +53:31:47.19 | [0.005, 2, 0.3]                                  | [0.009, 6, 1]  | $-1 \pm 1$            | 8  | 2 |
| Source 11    | 04:13:49.417 | +52:43:25.49 | 0.006  | [0.007, 0.06, 0.03]  | $-2.01 \pm 0.05$      | 1  | 5 |
| Source 12    | 04:13:02.943 | +53:30:05.01 | [0.004, 0.007, 0.005]                            | [0.007, 3, 0.9]  | $-2.01 \pm 0.04$      | 2  | 4 |
| Source 13    | 04:10:44.553 | +52:42:50.20 | 0.004  | [0.007, 0.03, 0.02]  | $-2.01 \pm 0.02$      | 1  | 5 |
| Source 15    | 04:08:54.893 | +52:50:53.54 | 0.4  | [0.01, 0.7, 0.3]   | $-2.1 \pm 0.3$        | 1  | 3 |
| Source 16    | 04:13:58.107 | +52:47:52.13 | 0.001  | [0.005, 0.02, 0.01]  | $-2.01 \pm 0.03$      | 1  | 5 |
| Source 17    | 04:13:15.629 | +52:33:06.55 | 0.001  | [0.009, 0.02, 0.02]  | $-2.01 \pm 0.06$      | 1  | 5 |
| Source 18    | 04:14:48.026 | +52:26:03.06 | [0.0004, 0.2, 0.04]                              | [0.008, 6, 1]  | $-1.8 \pm 0.3$        | 6  | 3 |
| Source 19    | 04:11:12.060 | +52:40:00.88 | [0.0004, 0.3, 0.04]                              | [0.01, 4, 0.5]   | $-1.7 \pm 0.4$        | 8  | 3 |
| Source 20    | 04:14:08.872 | +53:11:29.78 | [0.0004, 0.3, 0.06]                              | [0.004, 4, 0.5]  | $-1.7 \pm 0.4$        | 5  | 3 |
| Source 21    | 04:14:52.255 | +53:15:43.94 | [0.0009, 0.004, 0.001]                           | [0.005, 3, 0.8]  | $-1.9 \pm 0.2$        | 5  | 3 |
| Source 22    | 04:10:33.256 | +53:09:05.25 | [0.0004, 0.3, 0.03]                              | [0.008, 4, 0.6]  | $-1.7 \pm 0.3$        | 9  | 3 |
| Source 23    | 04:12:28.618 | +52:17:24.61 | 0.002  | [0.009, 0.04, 0.02]  | $-2.01 \pm 0.03$      | 1  | 4 |
| Source 25    | 04:12:27.813 | +53:26:23.86 | 0.2  | [0.005, 0.6, 0.2]  | $-1.7 \pm 0.3$        | 1  | 4 |
| Source 26    | 04:10:37.078 | +53:14:55.45 | 0.002  | [0.004, 0.04, 0.02]  | $-2.01 \pm 0.04$      | 1  | 5 |
| Source 27    | 04:13:01.900 | +52:19:52.90 | 0.02   | [0.01, 0.09, 0.05]   | $-2.01 \pm 0.04$      | 1  | 4 |
| Source 28    | 04:10:53.149 | +52:45:14.50 | 0.0004*  | 0.01*  | -2*                   | 1  | 7 |
| Source 29    | 04:14:12.165 | +53:09:50.83 | [0.0004, 0.2, 0.04]                              | [0.007, 4, 0.5]  | $-1.7 \pm 0.4$        | 6  | 3 |
| Source 30    | 04:11:19.319 | +53:11:48.90 | [0.002, 0.02, 0.01]                              | [0.007, 3, 0.3]  | $-2.01 \pm 0.06$      | 2  | 4 |
| Source 31    | 04:11:58.973 | +52:33:37.64 | 0.004  | [0.006, 0.03, 0.02]  | $-2.01 \pm 0.03$      | 1  | 6 |
| Source 32    | 04:13:39.775 | +52:36:58.27 | 0.02   | [0.004, 0.08, 0.05]  | $-2.01 \pm 0.04$      | 1  | 4 |
| Source 34    | 04:10:36.472 | +52:52:44.27 | [0.0004, 0.3, 0.05]                              | [0.007, 4, 0.4]  | $-1.7 \pm 0.4$        | 6  | 3 |
| Source 35    | 04:14:52.765 | +53:03:41.94 | 0.03   | [0.007, 0.2, 0.08]   | $-2.0 \pm 0.1$        | 1  | 4 |
| Source 36    | 04:14:01.742 | +52:34:29.10 | 0.007  | [0.002, 0.04, 0.03]  | $-2.01 \pm 0.03$      | 1  | 5 |
| Source 37    | 04:15:48.381 | +52:29:50.30 | [0.0004, 0.8, 0.2]                               | [0.006, 4, 0.8]  | $-1.6 \pm 0.8$        | 4  | 2 |
| Source 38    | 04:08:05.821 | +53:19:08.96 | [0.0004, 0.7, 0.2]                               | [0.007, 4, 0.8]  | $-1.7 \pm 0.8$        | 4  | 2 |
| Source 39    | 04:10:50.451 | +53:14:37.71 | [0.0004, 0.0004, 0.0004]                         | [6, 8, 7]  | $-3.3 \pm 2.1$        | 13 | 6 |
| Source 40    | 04:13:25.383 | +53:27:17.34 | [0.0004, 0.2, 0.03]                              | [0.003, 4, 0.8]  | $-1.7 \pm 0.4$        | 9  | 3 |
| Source 41    | 04:10:14.457 | +52:24:46.60 | [0.0004, 0.2, 0.06]                              | [0.004, 3, 0.5]  | $-1.6 \pm 0.5$        | 4  | 3 |
|              | Input RA     | Input Dec    | $[\delta D_{Min}, \delta D_{Max}, \overline{D}]$ | $[\delta \phi_{Min}, \delta \phi_{Max}, \overline{\Delta \phi}]$ | $\overline{\alpha}_I$ | P  | B |

Table 5.10: (continued)

|           | Input RA     | Input Dec    | Oversampling                                     |  | $\overline{\alpha_I}$ | P  | B |
|-----------|--------------|--------------|--|--|-----------------------|----|---|
|           |              |              | $[\delta D_{Min}, \delta D_{Max}, \overline{D}]$ | $[\delta \phi_{Min}, \delta \phi_{Max}, \overline{\Delta \phi}]$ |                       |    |   |
| Source 42 | 04:09:48.831 | +52:30:22.16 | 0.0004*  | 0.009*   | -2*                   | 1  | 4 |
| Source 43 | 04:13:47.424 | +52:24:06.92 | [0.0004, 0.009, 0.003]                           | [0.009, 3, 0.6]  | $-1.6 \pm 0.5$        | 10 | 3 |
| Source 44 | 04:13:05.224 | +52:53:40.87 | [0.0009, 0.2, 0.03]                              | [0.003, 4, 1]  | $-1.7 \pm 0.4$        | 7  | 3 |
| Source 45 | 04:12:47.812 | +52:31:16.35 | 0.0004*  | 0.006*   | -2*                   | 1  | 6 |
| Source 46 | 04:13:24.165 | +53:24:22.36 | [0.0004, 0.2, 0.03]                              | [0.006, 4, 0.8]  | $-1.7 \pm 0.4$        | 9  | 3 |
| Source 48 | 04:10:47.950 | +52:19:59.17 | 0.008  | [0.007, 0.06, 0.03]  | $-2.01 \pm 0.04$      | 1  | 4 |
| Source 49 | 04:11:38.342 | +52:58:48.06 | 0.01   | [0.009, 0.07, 0.04]  | $-2.0 \pm 0.1$        | 1  | 5 |
| Source 50 | 04:09:51.831 | +53:14:59.89 | 0.009  | [0.009, 0.06, 0.04]  | $-2.01 \pm 0.06$      | 1  | 5 |
| Source 51 | 04:13:50.019 | +52:40:12.25 | [0.0004, 0.06, 0.01]                             | [0.006, 4, 1]  | $-1.7 \pm 0.4$        | 9  | 3 |
| Source 52 | 04:14:59.719 | +52:30:03.91 | 0.06   | [0.009, 0.2, 0.09]   | $-2.0 \pm 0.2$        | 1  | 3 |
| Source 53 | 04:10:13.738 | +52:42:14.69 | [0.004, 0.01, 0.008]                             | [0.004, 3, 0.6]  | $-2.01 \pm 0.08$      | 2  | 4 |
| Source 54 | 04:13:57.663 | +52:32:30.06 | [0.0004, 0.0004, 0.0004]                         | [0.003, 0.04, 0.03]  | $-2.0 \pm 0.1$        | 3  | 5 |
| Source 55 | 04:09:01.104 | +52:55:05.71 | [0.0004, 1, 0.1]                                 | [0.009, 8, 2]  | $-0.8 \pm 1.1$        | 21 | 2 |
| Source 56 | 04:14:53.636 | +53:25:04.00 | [0.0004, 1, 0.1]                                 | [0.01, 8, 2]   | $-0.6 \pm 2.1$        | 31 | 2 |
| Source 57 | 04:09:00.896 | +53:04:04.47 | [0.002, 0.05, 0.02]                              | [0.008, 2, 0.3]  | $-2.0 \pm 0.1$        | 2  | 4 |
| Source 58 | 04:12:46.504 | +52:24:20.37 | [0.0004, 0.1, 0.06]                              | [0.008, 0.5, 0.2]  | $-1.7 \pm 0.3$        | 2  | 4 |
| Source 59 | 04:10:55.883 | +52:46:12.06 | 0.0004*  | 0.01*  | -2*                   | 1  | 5 |
| Source 60 | 04:14:34.627 | +52:20:41.95 | [0.0004, 1, 0.1]                                 | [0.009, 8, 2]  | $-0.7 \pm 1.1$        | 34 | 2 |
|           | Input RA     | Input Dec    | $[\delta D_{Min}, \delta D_{Max}, \overline{D}]$ | $[\delta \phi_{Min}, \delta \phi_{Max}, \overline{\Delta \phi}]$ | $\overline{\alpha_I}$ | P  | B |

Figure 5.15 shows the mean value of the estimated intrinsic spectral index  $\overline{\alpha_I}$  from all combined estimated locations for that source detected with the undersampled, the Nyquist sampled and the oversampled methods. We summarise the results next:

- All three sources detected in the undersampled TABs, the top panel, were detected with two TABs only and the minimum number of estimated locations is three;
  - The mean value of the estimated  $\overline{\alpha_I}$  from all locations is -1.2 with deviation from the mean value of at least 0.7;
- The majority of sources detected in the Nyquist sampled TABs, the middle panel, were detected with two or three TABs;
  - As a result, the mean value of the estimated  $\overline{\alpha_I}$  oscillates around -2 with large deviation from the mean value;
  - Only sources with a single estimated location have  $\overline{\alpha_I}$  equal to -2 with small deviation of less than 0.1.
- For sources detected in the oversampled TABs, the bottom panel, the number of TABs per detection is at least four;
  - Almost half of the detected sources have  $\overline{\alpha_I}$  estimated at -2 with deviation of less than 0.2.



**Figure 5.15:** The estimated  $\bar{\alpha}_I$  for sources detected in the LOFAR TABs. The error bars show the standard deviation of the mean  $\bar{\alpha}_I$  from all estimated source positions. The assigned value of the intrinsic spectral index  $\alpha_I = -2$ ; (top) undersampling; (middle) Nyquist sampling; (bottom) oversampling.

### 5.3.3 The MeerKAT Core

The top and the bottom left panels in Figure 5.16 illustrate the position of the LOFAR TABs relative to the randomly generated point sources. We summarise here the detection rates with different spatial TAB sampling illustrated in the bottom right panel in Figure 5.16:

- Oversampling of the FoV, the bottom left panel, gives the highest detection rate with 43 detected sources, the  $\diamond$ , the  $\circ$  and the  $\square$  symbols in the bottom right panel;
- The Nyquist sampling detected 33 sources, the top right panel, the  $\circ$  and the  $\square$  symbols in the bottom right panel;
- Undersampling detected only two sources, the top left panel, the  $\circ$  symbol in the bottom right panel;
- The  $\diamond$  symbol, in the bottom right panel, represent 17 sources not detected with any sampling method. Those 17 sources lie outside, or on, the dashed circle, i.e. the boundaries of the test area;
- Sources detected only with the oversampling method, the  $\diamond$  symbol in the bottom right panel, are located close to the test boundary and are covered, but not detected, by the Nyquist sampled beams.

For example, source #58 marked with a red circle in the bottom left panel, is detected in the oversampling TABs but not in the Nyquist sampled TABs. It is clear that source #58 was detected in the Nyquist sampled TAB in the traditional sense but according to the restrictive definition of detection in this text at least two TABs are needed for detection. Refer to Table 5.11, Table 5.12 and Table 5.13 for more details.

**Table 5.11:** Summary of results for the MeerKAT array using undersampled TABs. Source input RA and Dec are calculated for MJD 56772.5629376499. Below we list the minimum ( $\delta D_{Min}$ ), maximum ( $\delta D_{Max}$ ) and mean ( $\bar{D}$ ) value of the total area  $D$  covered by the overlapping values of  $\mathfrak{s}_1/\mathfrak{s}_2$  and  $(\mathfrak{a}_2 - \mathfrak{a}_1)$ , normalised to the  $\Omega_{HPBW_L}$ . We also list the minimum ( $\delta\phi_{Min}$ ), maximum ( $\delta\phi_{Max}$ ) and mean ( $\bar{\Delta\phi}$ ) value of the total angular distances  $\Delta\phi$  between the true and the estimated source position, normalised to the  $HPBW_L$ .  $\bar{\alpha}_I$  is the mean estimated intrinsic spectral index from all possible locations, where the error is the standard deviation from that mean. The assigned value of  $\bar{\alpha}_I$  is -2. The two last columns list the number of areas of possible source locations  $P$  and the number of TABs in which a source was detected  $B$ . Sources for which location was estimated with a single pixel are marked with asterisk (\*).

|                  | Undersampling |              |   |  |                  |            |
|------------------|---------------|--------------|---|--|------------------|------------|
|                  | Input RA      | Input Dec    | $[\delta D_{Min}, \delta D_{Max}, \bar{D}]$ | $[\delta\phi_{Min}, \delta\phi_{Max}, \bar{\Delta\phi}]$ | $\bar{\alpha}_I$ | <b>P B</b> |
| <b>Source 30</b> | 05:09:29.869  | +30:25:53.43 | 0.3   | [0.008, 0.1, 0.06]                                       | $-1.5 \pm 0.5$   | 1 2        |
| <b>Source 56</b> | 05:09:27.722  | +30:25:04.13 | 0.4   | [0.009, 0.1, 0.05]                                       | $-1.4 \pm 0.6$   | 1 2        |
|                  | Input RA      | Input Dec    | $[\delta D_{Min}, \delta D_{Max}, \bar{D}]$ | $[\delta\phi_{Min}, \delta\phi_{Max}, \bar{\Delta\phi}]$ | $\bar{\alpha}_I$ | <b>P B</b> |

Figure 5.17 shows the mean total area  $\bar{D}$  covered by the estimated positions for the undersampled, top panel, Nyquist sampled, the middle panel, and the oversampled methods, the bottom panel. We summarise the results below:

- For sources detected in the undersampled TABs, the top panel in Figure 5.17, the mean total area  $\bar{D}$  is below 40% of  $\Omega_{HPBW_L}$ ;
  - The mean angular distance  $\bar{\Delta\phi}$  from the true source position is 6% of  $HPBW_L$ , i.e. 3 arcsecond;
- For 28 sources detected in the Nyquist sampled TABs, the middle panel, the  $\bar{D}$  is less than 10% of  $\Omega_{HPBW_L}$ ;
  - For four sources,  $\bar{D}$  is less than 1% of  $\Omega_{HPBW_L}$ ;
  - The mean angular distance  $\bar{\Delta\phi}$  for 19 sources is less than 5% of  $HPBW_L$ ;
  - For three source  $\bar{\Delta\phi}$  is less than 1% of  $HPBW_L$ , i.e. 0.52 arcsecond, for 14 sources  $\bar{\Delta\phi}$  is less than 5% and for 7 sources  $\bar{\Delta\phi}$  is less than 10% of  $HPBW_L$ ;
  - A single pixel location was estimated for two sources with a mean  $\delta\phi$  distance from the source true positions is less than 1% of a  $HPBW_L$ ;
- For the majority of sources detected in the oversampled TABs, the bottom panel, the mean total area  $\bar{D}$  is less than 10% of  $\Omega_{HPBW_L}$ ;
  - For 28 sources,  $\bar{D}$  is less than 1% of  $\Omega_{HPBW_L}$ ;
  - For 10 sources,  $\bar{D}$  is less than 10% of  $\Omega_{HPBW_L}$ ;
  - The mean angular distance  $\bar{\Delta\phi}$  is 10% of  $HPBW_L$ , i.e. 5.2 arcsecond;
  - For 17 source  $\bar{\Delta\phi}$  is less than 5% of  $HPBW_L$  and for 12 it less than 1% of

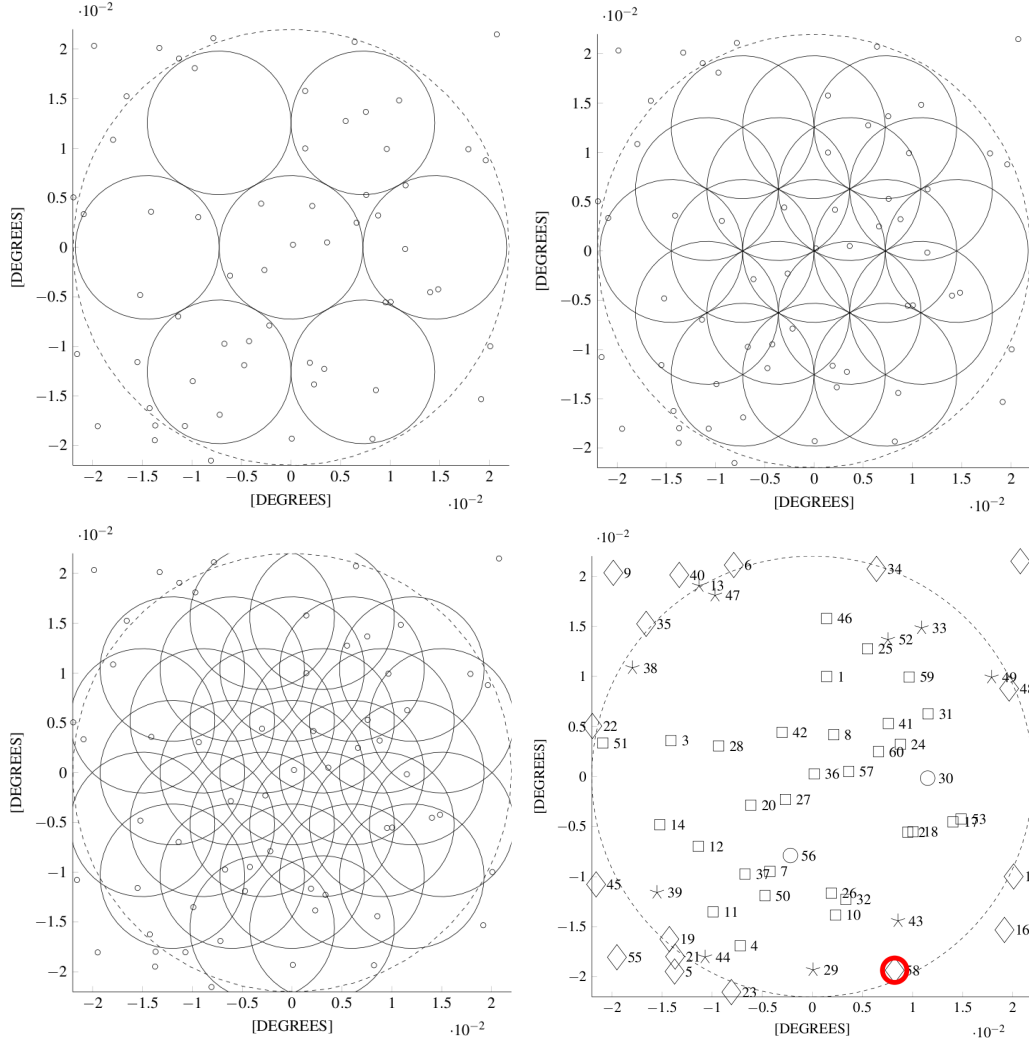


**Figure 5.16:** The MeerKAT Core TABs spatial TAB sampling. The dashed circle of diameter  $3 \times \text{HPBW}_L$  represents a test area for different methods of spatial sampling ( $\text{HPBW}_L = 0.52'$ ). The position of randomly placed sources are shown as small circles. (Top left) undersampling: 7 independent TABs are separated by  $\text{HPBW}_L$ ; (top right) Nyquist sampling: 19 independent beams are separated by  $\text{HPBW}_L/2 = 0.26'$ ; (bottom left) oversampling: 31 independent beams are separated by  $\text{HPBW}_H/2 = 0.21'$ . (Bottom right) graphical representation of source detection success using different sampling methods;  $\circ$ : sources detected with undersampling, Nyquist sampling and oversampling;  $\square$ : sources detected with Nyquist sampling and oversampling;  $\diamond$ : no detection with any sampling method;  $\nabla$ : sources detected with Nyquist sampling only;  $\circ$ : sources detected with oversampling only.

HPBW<sub>L</sub>.

A single pixel location was estimated for 13 sources with  $\delta\phi$  distance from the source true positions is 0.5% of HPBW<sub>L</sub>, .i.e. 0.26 arcsecond).

**Table 5.12:** Summary of results for the MeerKAT array using Nyquist sampled TAB. Source input RA and Dec are calculated for MJD 56772.5629376499. Below we list the minimum ( $\delta D_{Min}$ ), maximum ( $\delta D_{Max}$ ) and mean ( $\bar{D}$ ) value of the total area  $D$  covered by the overlapping values of  $\mathfrak{s}_1/\mathfrak{s}_2$  and  $(\mathfrak{a}_2 - \mathfrak{a}_1)$ , normalised to the  $\Omega_{HPBW_L}$ . We also list the minimum ( $\delta\phi_{Min}$ ), maximum ( $\delta\phi_{Max}$ ) and mean ( $\bar{\Delta\phi}$ ) value of the total angular distances  $\Delta\phi$  between the true and the estimated source position, normalised to the HPBW<sub>L</sub>.  $\bar{\alpha}_I$  is the mean estimated intrinsic spectral index from all possible locations, where the error is the standard deviation from that mean. The assigned value of  $\bar{\alpha}_I$  is -2. The two last columns list the number of areas of possible source locations  $P$  and the number of TABs in which a source was detected  $B$ . Sources for which location was estimated with a single pixel are marked with asterisk (\*).

| Nyquist sampling |              |              |  |  |                       |    |   |
|------------------|--------------|--------------|--|--|-----------------------|----|---|
|                  | Input RA     | Input Dec    | $[\delta D_{Min}, \delta D_{Max}, \overline{D}]$ | $[\delta \phi_{Min}, \delta \phi_{Max}, \overline{\Delta \phi}]$ | $\overline{\alpha}_I$ | P  | B |
| Source 1         | 05:09:32.694 | +30:25:17.13 | 0.04   | [0.008, 0.1, 0.06]   | $-2.0 \pm 0.1$        | 1  | 3 |
| Source 2         | 05:09:28.370 | +30:25:46.29 | 0.03   | [0.009, 0.1, 0.05]   | $-2.01 \pm 0.07$      | 1  | 4 |
| Source 3         | 05:09:30.914 | +30:24:21.20 | 0.001  | [0.003, 0.02, 0.01]  | $-2.01 \pm 0.03$      | 1  | 3 |
| Source 4         | 05:09:25.214 | +30:24:46.10 | 2  | [0.004, 1, 0.6]  | $-1.6 \pm 0.6$        | 1  | 2 |
| Source 7         | 05:09:27.280 | +30:24:56.77 | 0.003  | [0.009, 0.03, 0.02]  | $-2.01 \pm 0.02$      | 1  | 4 |
| Source 8         | 05:09:31.078 | +30:25:19.69 | 0.008  | [0.003, 0.06, 0.03]  | $-2.01 \pm 0.06$      | 1  | 3 |
| Source 10        | 05:09:26.067 | +30:25:20.35 | 0.05   | [0.006, 0.2, 0.07]   | $-2.01 \pm 0.09$      | 1  | 3 |
| Source 11        | 05:09:26.156 | +30:24:36.33 | [0.0004, 2, 0.6]                                 | [0.008, 6, 0.7]  | $-1.2 \pm 0.8$        | 4  | 2 |
| Source 12        | 05:09:27.976 | +30:24:31.05 | 0.01   | [0.006, 0.07, 0.04]  | $-2.01 \pm 0.06$      | 1  | 4 |
| Source 14        | 05:09:28.576 | +30:24:17.22 | [0.0004, 0.8, 0.08]                              | [0.007, 10, 1]   | $-0.8 \pm 1.1$        | 12 | 2 |
| Source 17        | 05:09:28.655 | +30:26:02.48 | 0.04   | [0.01, 0.1, 0.06]  | $-2.0 \pm 0.1$        | 1  | 3 |
| Source 18        | 05:09:28.381 | +30:25:48.16 | 0.02   | [0.01, 0.09, 0.04]   | $-2.01 \pm 0.06$      | 1  | 4 |
| Source 20        | 05:09:29.120 | +30:24:49.88 | 0.003  | [0.002, 0.03, 0.02]  | $-2.01 \pm 0.03$      | 1  | 5 |
| Source 24        | 05:09:30.812 | +30:25:43.62 | 0.0004*  | 0.01*  | -2*                   | 1  | 5 |
| Source 25        | 05:09:33.463 | +30:25:31.84 | 0.06   | [0.01, 0.1, 0.08]  | $-2.0 \pm 0.1$        | 1  | 3 |
| Source 26        | 05:09:26.674 | +30:25:18.82 | 0.03   | [0.001, 0.1, 0.05]   | $-2.01 \pm 0.08$      | 1  | 3 |
| Source 27        | 05:09:29.278 | +30:25:02.34 | 0.0004*  | 0.007*   | -2*                   | 1  | 4 |
| Source 28        | 05:09:30.764 | +30:24:38.33 | 0.003  | [0.006, 0.03, 0.02]  | $-2.01 \pm 0.02$      | 1  | 5 |
| Source 30        | 05:09:29.869 | +30:25:53.43 | 0.008  | [0.009, 0.06, 0.03]  | $-2.01 \pm 0.05$      | 1  | 5 |
| Source 31        | 05:09:31.658 | +30:25:53.56 | 0.01   | [0.01, 0.07, 0.03]   | $-2.01 \pm 0.04$      | 1  | 4 |
| Source 32        | 05:09:26.501 | +30:25:24.04 | 0.03   | [0.009, 0.1, 0.05]   | $-2.01 \pm 0.07$      | 1  | 3 |
| Source 36        | 05:09:29.988 | +30:25:12.70 | 0.4  | [0.009, 0.8, 0.5]  | $-1.1 \pm 0.7$        | 1  | 3 |
| Source 37        | 05:09:27.207 | +30:24:47.80 | [0.0008, 0.07, 0.03]                             | [0.009, 10, 0.5]   | $-1.8 \pm 0.6$        | 3  | 3 |
| Source 41        | 05:09:31.388 | +30:25:39.29 | [0.0004, 0.08, 0.02]                             | [0.007, 10, 0.6]   | $-1.8 \pm 0.8$        | 4  | 3 |
| Source 42        | 05:09:31.143 | +30:25:01.15 | 0.003  | [0.008, 0.04, 0.02]  | $-2.01 \pm 0.03$      | 1  | 4 |
| Source 46        | 05:09:34.306 | +30:25:17.11 | [0.002, 2, 0.3]                                  | [0.008, 10, 1]   | $-1 \pm 1$            | 7  | 2 |
| Source 50        | 05:09:26.607 | +30:24:55.00 | [0.0004, 0.04, 0.02]                             | [0.006, 6, 0.1]  | $-1.9 \pm 0.5$        | 2  | 3 |
| Source 51        | 05:09:30.846 | +30:23:56.74 | [0.005, 0.7, 0.3]                                | [0.002, 1, 0.6]  | $-1.5 \pm 0.8$        | 2  | 2 |
| Source 53        | 05:09:28.737 | +30:26:05.41 | 0.02   | [0.008, 0.1, 0.05]   | $-2.0 \pm 0.1$        | 1  | 3 |
| Source 56        | 05:09:27.722 | +30:25:04.13 | 0.006  | [0.004, 0.04, 0.02]  | $-2.01 \pm 0.03$      | 1  | 5 |
| Source 57        | 05:09:30.055 | +30:25:25.06 | 0.009  | [0.008, 0.06, 0.03]  | $-2.01 \pm 0.05$      | 1  | 5 |
|                  | Input RA     | Input Dec    | $[\delta D_{Min}, \delta D_{Max}, \overline{D}]$ | $[\delta \phi_{Min}, \delta \phi_{Max}, \overline{\Delta \phi}]$ | $\overline{\alpha}_I$ | P  | B |

**Table 5.12:** (continued)

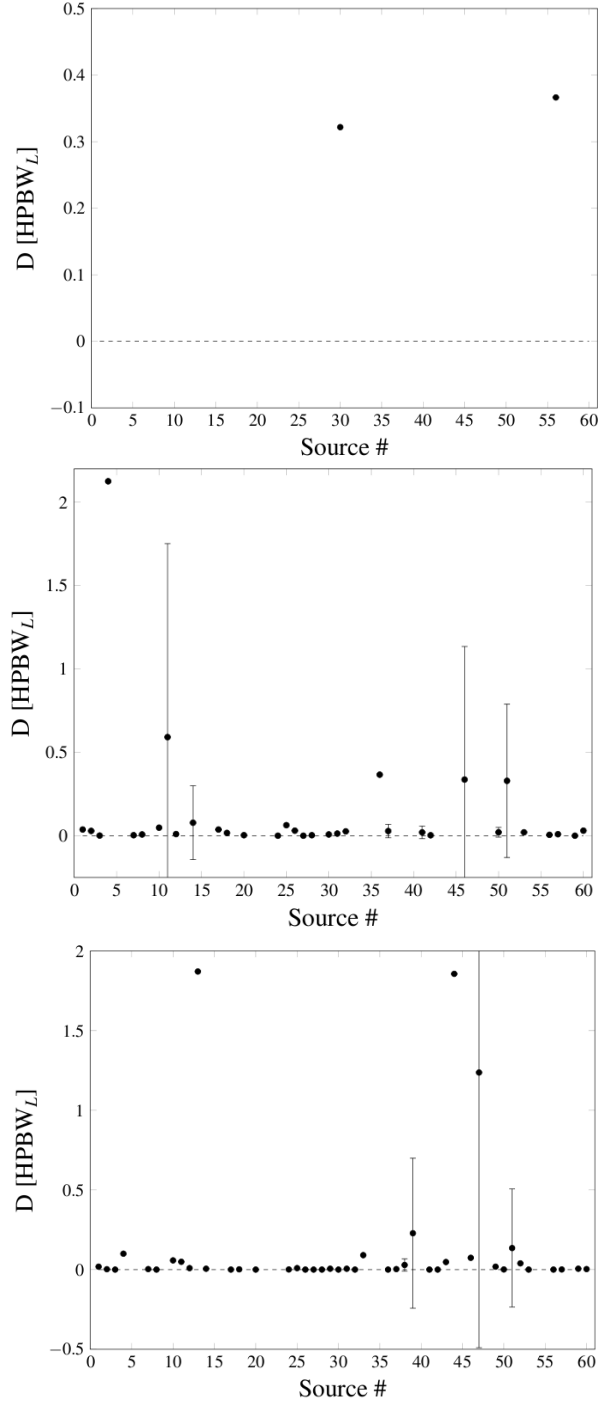
|           | Nyquist sampling |              |  |  |                       |     |
|-----------|------------------|--------------|--|--|-----------------------|-----|
|           | Input RA         | Input Dec    | $[\delta D_{Min}, \delta D_{Max}, \overline{D}]$ | $[\delta \phi_{Min}, \delta \phi_{Max}, \overline{\Delta \phi}]$ | $\overline{\alpha_I}$ | P B |
| Source 59 | 05:09:32.679     | +30:25:46.76 | [0.0004, 0.0004, 0.0004]                         | [0.003, 6, 3]  | $0.2 \pm 3.1$         | 2 3 |
| Source 60 | 05:09:30.608     | +30:25:35.77 | 0.03   | [0.008, 0.1, 0.05]   | $-2.01 \pm 0.05$      | 1 4 |
|           | Input RA         | Input Dec    | $[\delta D_{Min}, \delta D_{Max}, \overline{D}]$ | $[\delta \phi_{Min}, \delta \phi_{Max}, \overline{\Delta \phi}]$ | $\overline{\alpha_I}$ | P B |

Figure 5.18 presents examples of the estimated source positions for representative cases with low (one location only) and high (many possible locations) positional uncertainty the undersampling, Nyquist sampling and oversampling method. In the top panel, source #30 is detected in two undersampled TABs. The area covered by the overlapping  $\mathfrak{s}_1/\mathfrak{s}_2$  and  $(\mathfrak{a}_2 - \mathfrak{a}_1)$  values from all TABs amounts to almost 30% of  $\Omega_{HPBW_L}$ . As with all arrays, only two TAB detections produces the poorest position estimation. For a three TAB detection of source #59, the middle panel, in Nyquist sampled TABs, only two positions with a combined area of less than 1% of  $\Omega_{HPBW_L}$  were estimated. Finally, a detection in three oversampled TABs of source #43, the bottom panel, shows that a location with low level of uncertainty can be achieved if oversampling is used. The total area  $\delta D$  in this case is only 5% of a  $\Omega_{HPBW_L}$ .

Figure 5.19 shows the mean value of the estimated intrinsic spectral index  $\overline{\alpha_I}$  from all combined estimated locations for that source detected with the undersampled, the Nyquist sampled and the oversampled methods. We summarise the results next:

- For two sources detected in the undersampled TABs, the top panel, all were detected with at least two TABs and within a single patch;
  - The estimated value of  $\overline{\alpha_I}$  is -1.5 and -1.4;
  - The value  $\overline{\alpha_I}$  is distorted, despite a single estimated position, as the total area  $D$  for each source is at least 0.3 of  $\Omega_{HPBW_L}$ ;
- The majority of sources detected in the Nyquist sampled TABs, the middle panel, were detected with at least three TABs and a single location was estimated for 25 sources;
  - The mean value of the estimated  $\overline{\alpha_I}$  is -2 with deviation from the mean value much lower than 0.1;
  - Only sources detected in two TABs and with many estimated position exhibit large variations from the mean  $\overline{\alpha_I}$ ;
- For sources detected in the oversampled TABs, the bottom panel, the number of TABs per detection is at least four and a single location was estimated for 38 sources;





**Figure 5.17:** The mean total area  $\bar{D}$  covered by the estimated positions for the MeerKAT TABs. The plot shows the mean  $\bar{D}$  value of the total area  $D$  covered by the overlapping values of the flux density ratio  $s_1/s_2$  and the spectral index difference  $(\alpha_2 - \alpha_1)$  normalised to  $\Omega_{\text{HPBW}_L}$ . The error corresponds to one standard deviation from that mean; (top) undersampling; (middle) Nyquist sampling; (bottom) oversampling.

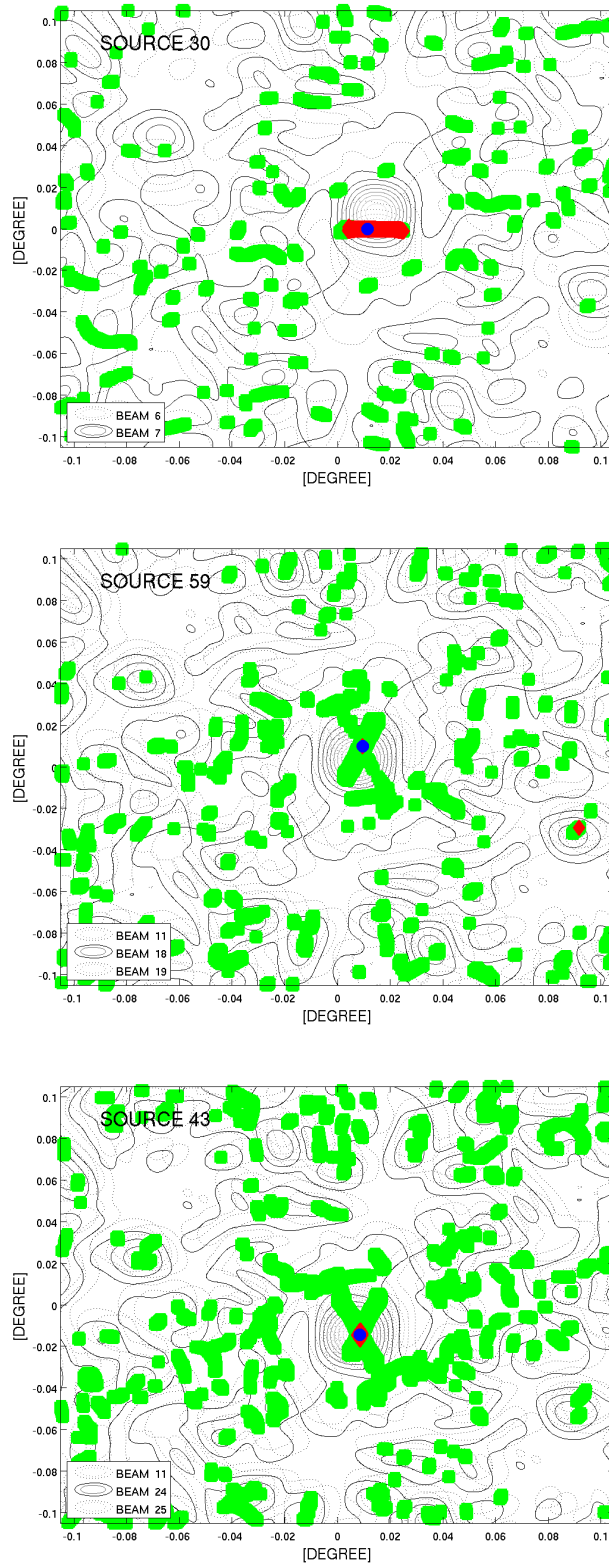


**Figure 5.18:** Detection examples for the MeerKAT array with different spatial sampling. Green squares correspond to overlapping values of  $s_1/s_2$  and  $(a_2 - a_1)$  from TAB pairs, red diamonds represent overlapping coordinates of  $s_1/s_2$  and  $(a_2 - a_1)$  from all TABs and the blue circle shows the true position of a source; (top) undersampling; (middle) Nyquist sampling; (bottom) oversampling.

- The mean value of the estimated  $\overline{\alpha_I}$  is -2 with deviation from the mean value for majority of sources is 0.05.

**Table 5.13:** Summary of results for the MeerKAT array using oversampled TABs. Source input RA and Dec are calculated for MJD 56772.5629376499. Below we list the minimum ( $\delta D_{Min}$ ), maximum ( $\delta D_{Max}$ ) and mean ( $\overline{D}$ ) value of the total area  $D$  covered by the overlapping values of  $s_1/s_2$  and  $(a_2 - a_1)$ , normalised to the  $\Omega_{HPBW_L}$ . We also list the minimum ( $\delta\phi_{Min}$ ), maximum ( $\delta\phi_{Max}$ ) and mean ( $\overline{\Delta\phi}$ ) value of the total angular distances  $\Delta\phi$  between the true and the estimated source position, normalised to the  $HPBW_L$ .  $\overline{\alpha_I}$  is the mean estimated intrinsic spectral index from all possible locations, where the error is the standard deviation from that mean. The assigned value of  $\overline{\alpha_I}$  is -2. The two last columns list the number of areas of possible source locations  $P$  and the number of TABs in which a source was detected  $B$ . Sources for which location was estimated with a single pixel are marked with asterisk (\*).

| Oversampling |              |              |  |   |                       |          |          |
|--------------|--------------|--------------|--|---|-----------------------|----------|----------|
|              | Input RA     | Input Dec    | $[\delta D_{Min}, \delta D_{Max}, \overline{D}]$ | $[\delta\phi_{Min}, \delta\phi_{Max}, \overline{\Delta\phi}]$ | $\overline{\alpha_I}$ | <b>P</b> | <b>B</b> |
| Source 1     | 05:09:32.694 | +30:25:17.13 | 0.02   | [0.008, 0.08, 0.04]   | -2.01 $\pm$ 0.07      | 1        | 5        |
| Source 2     | 05:09:28.370 | +30:25:46.29 | 0.003  | [0.009, 0.06, 0.03]   | -2.01 $\pm$ 0.04      | 1        | 5        |
| Source 3     | 05:09:30.914 | +30:24:21.20 | 0.0004*  | 0.003*  | -2*                   | 1        | 5        |
| Source 4     | 05:09:25.214 | +30:24:46.10 | 0.1  | [0.004, 0.2, 0.1]   | -2.0 $\pm$ 0.2        | 1        | 3        |
| Source 7     | 05:09:27.280 | +30:24:56.77 | 0.003  | [0.009, 0.03, 0.02]   | -2.01 $\pm$ 0.03      | 1        | 5        |
| Source 8     | 05:09:31.078 | +30:25:19.69 | 0.0004*  | 0.003*  | -2*                   | 1        | 6        |
| Source 10    | 05:09:26.067 | +30:25:20.35 | 0.06   | [0.006, 0.2, 0.08]  | -2.0 $\pm$ 0.1        | 1        | 4        |
| Source 11    | 05:09:26.156 | +30:24:36.33 | 0.05   | [0.008, 0.1, 0.07]  | -2.01 $\pm$ 0.09      | 1        | 4        |
| Source 12    | 05:09:27.976 | +30:24:31.05 | 0.009  | [0.006, 0.05, 0.03]   | -2.01 $\pm$ 0.02      | 1        | 5        |
| Source 13    | 05:09:35.215 | +30:24:31.31 | 2  | [0.009, 1, 0.6]   | -1.7 $\pm$ 0.6        | 1        | 2        |
| Source 14    | 05:09:28.576 | +30:24:17.22 | 0.006  | [0.007, 0.04, 0.02]   | -2.01 $\pm$ 0.03      | 1        | 5        |
| Source 17    | 05:09:28.655 | +30:26:02.48 | 0.0004*  | 0.01*   | -2*                   | 1        | 4        |
| Source 18    | 05:09:28.381 | +30:25:48.16 | 0.002  | [0.01, 0.04, 0.02]  | -2.01 $\pm$ 0.02      | 1        | 5        |
| Source 20    | 05:09:29.120 | +30:24:49.88 | 0.0004*  | 0.002*  | -2*                   | 1        | 7        |
| Source 24    | 05:09:30.812 | +30:25:43.62 | 0.001  | [0.01, 0.03, 0.02]  | -2.01 $\pm$ 0.02      | 1        | 5        |
| Source 25    | 05:09:33.463 | +30:25:31.84 | 0.009  | [0.01, 0.06, 0.03]  | -2.01 $\pm$ 0.05      | 1        | 4        |
| Source 26    | 05:09:26.674 | +30:25:18.82 | 0.0004*  | 0.001*  | -2*                   | 1        | 4        |
| Source 27    | 05:09:29.278 | +30:25:02.34 | 0.0004*  | 0.007*  | -2*                   | 1        | 5        |
| Source 28    | 05:09:30.764 | +30:24:38.33 | 0.0004*  | 0.006*  | -2*                   | 1        | 5        |
| Source 29    | 05:09:24.544 | +30:25:12.26 | 0.006  | [0.008, 0.1, 0.07]  | -2.0 $\pm$ 0.1        | 1        | 3        |
| Source 30    | 05:09:29.869 | +30:25:53.43 | 0.0004*  | 0.009*  | -2*                   | 1        | 7        |
| Source 31    | 05:09:31.658 | +30:25:53.56 | 0.006  | [0.01, 0.05, 0.02]  | -2.01 $\pm$ 0.02      | 1        | 6        |
| Source 32    | 05:09:26.501 | +30:25:24.04 | 0.0004*  | 0.009*  | -2*                   | 1        | 4        |
| Source 33    | 05:09:34.043 | +30:25:51.23 | 0.09   | [0.004, 0.2, 0.09]  | -2.0 $\pm$ 0.2        | 1        | 3        |
| Source 36    | 05:09:29.988 | +30:25:12.70 | 0.0004*  | 0.009*  | -2*                   | 1        | 7        |
| Source 37    | 05:09:27.207 | +30:24:47.80 | 0.003  | [0.009, 0.03, 0.02]   | -2.01 $\pm$ 0.02      | 1        | 7        |
| Source 38    | 05:09:32.934 | +30:24:07.39 | [0.002, 0.06, 0.03]                              | [0.004, 0.2, 0.07]  | -1.9 $\pm$ 0.2        | 2        | 3        |
| Source 39    | 05:09:26.694 | +30:24:16.22 | [0.0008, 1, 0.2]                                 | [0.008, 10, 0.7]  | -1.2 $\pm$ 1.1        | 5        | 2        |
| Source 41    | 05:09:31.388 | +30:25:39.29 | [0.0004, 0.0004, 0.0004]                         | [0.007, 0.04, 0.03]   | -2.01 $\pm$ 0.05      | 3        | 6        |
| Source 42    | 05:09:31.143 | +30:25:01.15 | 0.0004*  | 0.008*  | -2*                   | 1        | 6        |
| Source 43    | 05:09:25.905 | +30:25:42.79 | 0.05   | [0.006, 0.2, 0.07]  | -2.01 $\pm$ 0.08      | 1        | 3        |
| Source 44    | 05:09:24.899 | +30:24:33.47 | 2  | [0.009, 1, 0.6]   | -1.4 $\pm$ 0.7        | 1        | 2        |
| Source 46    | 05:09:34.306 | +30:25:17.11 | 0.07   | [0.008, 0.3, 0.1]   | -2.0 $\pm$ 0.1        | 1        | 3        |
| Source 47    | 05:09:34.948 | +30:24:37.05 | [0.02, 2, 1]                                     | [0.006, 6, 0.6]   | -1.4 $\pm$ 0.8        | 2        | 2        |
|              | Input RA     | Input Dec    | $[\delta D_{Min}, \delta D_{Max}, \overline{D}]$ | $[\delta\phi_{Min}, \delta\phi_{Max}, \overline{\Delta\phi}]$ | $\overline{\alpha_I}$ | <b>P</b> | <b>B</b> |

**Table 5.13:** (continued)

|                  | Oversampling    |                  |  |  |                       |          | <b>P</b> | <b>B</b> |
|------------------|-----------------|------------------|--|--|-----------------------|----------|----------|----------|
|                  | <b>Input RA</b> | <b>Input Dec</b> | $[\delta D_{Min}, \delta D_{Max}, \overline{D}]$ | $[\delta \phi_{Min}, \delta \phi_{Max}, \overline{\Delta \phi}]$ | $\overline{\alpha_I}$ |          |          |          |
| <b>Source 49</b> | 05:09:32.673    | +30:26:16.38     | 0.02   | [0.002, 0.07, 0.04]  | $-2.0 \pm 0.1$        | 1        | 3        |          |
| <b>Source 50</b> | 05:09:26.607    | +30:24:55.00     | 0.001  | [0.006, 0.02, 0.01]  | $-2.01 \pm 0.04$      | 1        | 5        |          |
| <b>Source 51</b> | 05:09:30.846    | +30:23:56.74     | [0.0004, 1, 0.1]                                 | [0.002, 10, 0.9]   | $-1.1 \pm 1.1$        | 9        | 2        |          |
| <b>Source 52</b> | 05:09:33.719    | +30:25:39.15     | 0.04   | [0.007, 0.1, 0.06]   | $-2.01 \pm 0.07$      | 1        | 3        |          |
| <b>Source 53</b> | 05:09:28.737    | +30:26:05.41     | 0.0004*  | 0.008*   | -2*                   | 1        | 5        |          |
| <b>Source 56</b> | 05:09:27.722    | +30:25:04.13     | 0.0004*  | 0.004*   | -2*                   | 1        | 6        |          |
| <b>Source 57</b> | 05:09:30.055    | +30:25:25.06     | 0.001  | [0.008, 0.03, 0.01]  | $-2.01 \pm 0.02$      | 1        | 5        |          |
| <b>Source 59</b> | 05:09:32.679    | +30:25:46.76     | 0.006  | [0.003, 0.04, 0.02]  | $-2.01 \pm 0.03$      | 1        | 5        |          |
| <b>Source 60</b> | 05:09:30.608    | +30:25:35.77     | 0.003  | [0.008, 0.03, 0.02]  | $-2.01 \pm 0.02$      | 1        | 7        |          |
|                  | <b>Input RA</b> | <b>Input Dec</b> | $[\delta D_{Min}, \delta D_{Max}, \overline{D}]$ | $[\delta \phi_{Min}, \delta \phi_{Max}, \overline{\Delta \phi}]$ | $\overline{\alpha_I}$ | <b>P</b> | <b>B</b> |          |

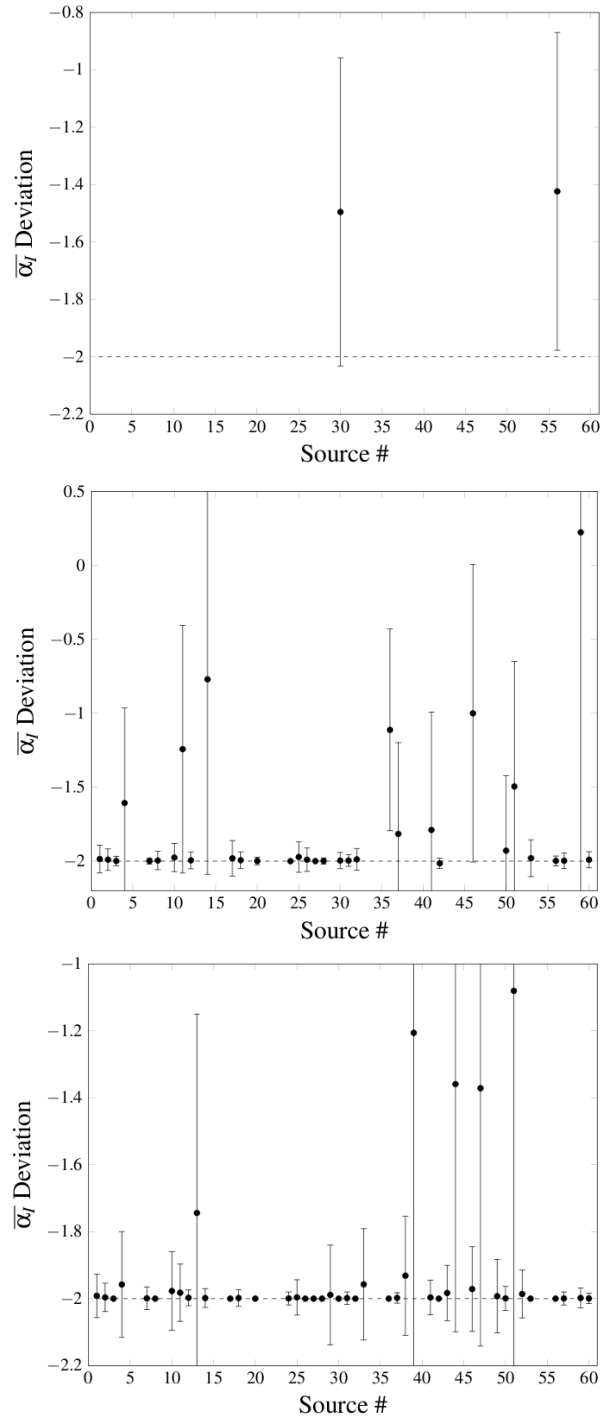


**Figure 5.19:** The estimated  $\bar{\alpha}_I$  for sources detected in the MeerKAT TABs. The error bars show the standard deviation of the mean  $\bar{\alpha}_I$  from all estimated source positions. The assigned value of the intrinsic spectral index  $\alpha_I = -2$ ; (top) undersampling; (middle) Nyquist sampling; (bottom) oversampling.

## 5.4 Discussion

A review of the results of this localisation technique will now be given starting with the detection rates. Then, an estimation of the accuracy of recovery of the true source position is discussed followed by the intrinsic spectral index recovery analysis.

### 5.4.1 Detection Rates

The number of detected sources that meet the restrictive criteria for detection are summarised in Table 5.14 and reviewed below.

#### Undersampling of the FoV

In the analysis the definition of detection is restricted to encompass only sources detected in at least two TABs and at two frequencies in each TAB. Consequently, the lowest detection rates occur, common for all arrays, when undersampling the FoV. This is because in the undersampled method, the TABs only touch at the half-power point, the detection in two TABs condition can only be met if a source is very strong or is detected in a sidelobe of a second TAB. The MUST array exhibits the highest detection rate for the undersampled TAB out of the three arrays because, in addition to having four strong sidelobes close to the main beam it also has a small fractional bandwidth, see the top left panel in Figure 5.20. Thus, the source is more easily detected at the highest and the lowest frequencies then for the other arrays.

The detection rates for the undersampled LOFAR and MeerKAT arrays are much lower than for the MUST array, three and two sources respectively, as the fractional bandwidths for both arrays are twice that of the MUST array, the top right and bottom panels in Figure 5.20. For example, for the LOTAAS survey (§2.3.1), the HPBW at 119 MHz is almost 20% wider than the HPBW at 150 MHz. The same difference in beamwidth applies to the MeerKAT array. Therefore, detection with undersampled TABs is difficult as only sources close to the beam centre can be detected at  $\nu_L$  and

**Table 5.14:** Detection rates for the MUST, LOFAR and MeerKAT arrays.

|         | Undersampling | Nyquist | Oversampling |
|---------|---------------|---------|--------------|
| MUST    | 14            | 40      | 40           |
| LOFAR   | 3             | 48      | 55           |
| MeerKAT | 2             | 33      | 43           |

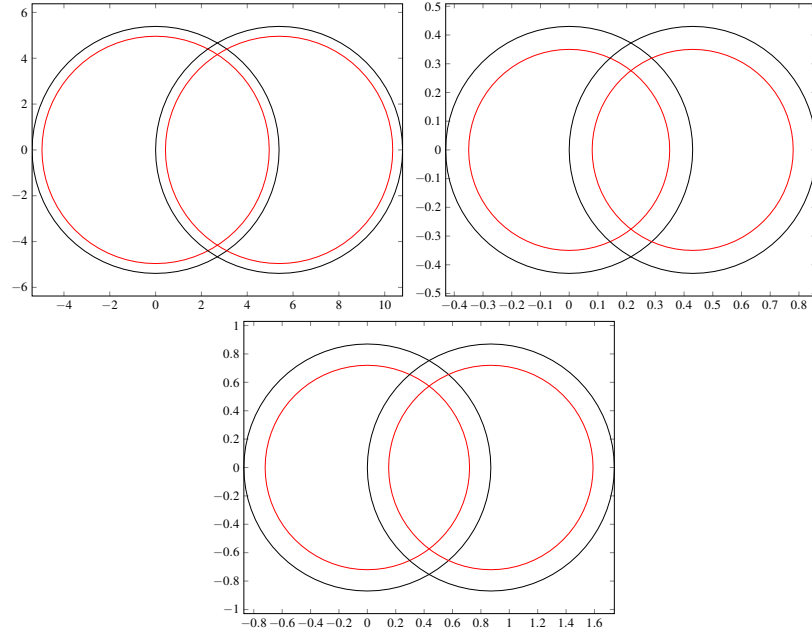


**Figure 5.20:** 3-dB beam contours of the MUST, LOFAR and MeerKAT arrays. 3-dB beam size are plotted for the lowest  $\nu_L$  (black) and the highest  $\nu_H$  (red) frequency in the observing band. The TABs are Nyquist sampled at  $\nu_L$ ; (top left) the MUST array; (top right) The LOFAR array; (bottom) the MeerKAT array.

$\nu_H$ . The lowest detection rate, when undersampling is considered, is produced for the MeerKAT array. Unlike LOFAR, MeerKAT's beam pattern is much smoother and does not exhibit too many strong sidelobes close to the main lobe, in the bottom panel in Figure 5.21. Hence, the detection with at least two TABs is more difficult due to the absence of strong sidelobes.

### Nyquist sampling of the FoV

Nyquist sampling of the FoV increased the detection rates dramatically for all arrays. The highest increase is observed for the LOFAR array that detected 48 sources. This again can be explained by the complicated beam pattern, in the top panel in Figure 5.21, which allows for the detection in sidelobes. The lowest detection rates, when the Nyquist sampling is considered, is achieved with the MeerKAT array recovering only 33 sources. The high fractional bandwidth and relatively clean beam pattern prevent one or both conditions for detection to be realised.

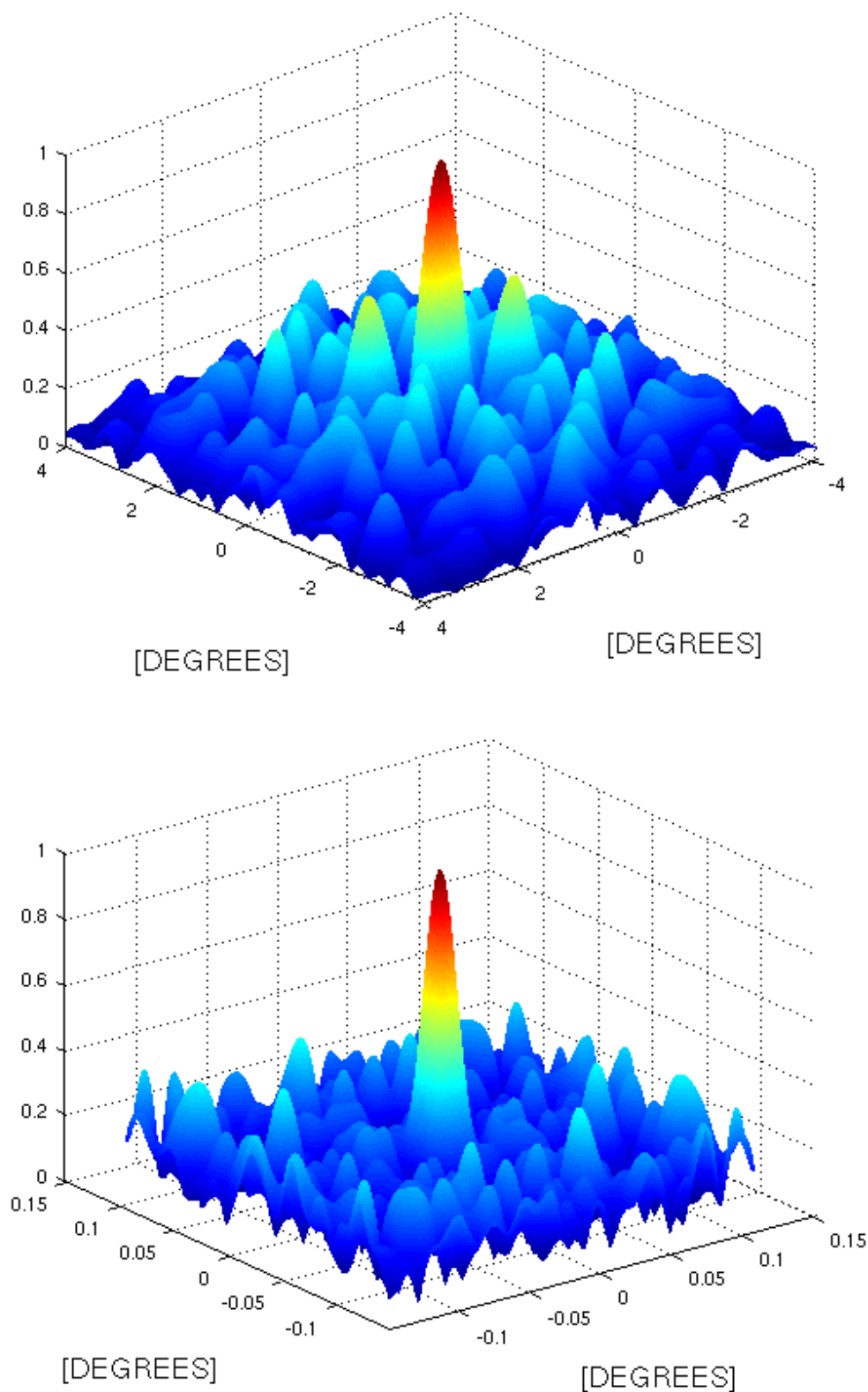


**Figure 5.21:** The LOFAR and MeerKAT normalised beam patterns; (top) LOFAR Superterp; (bottom) MeerKAT core.



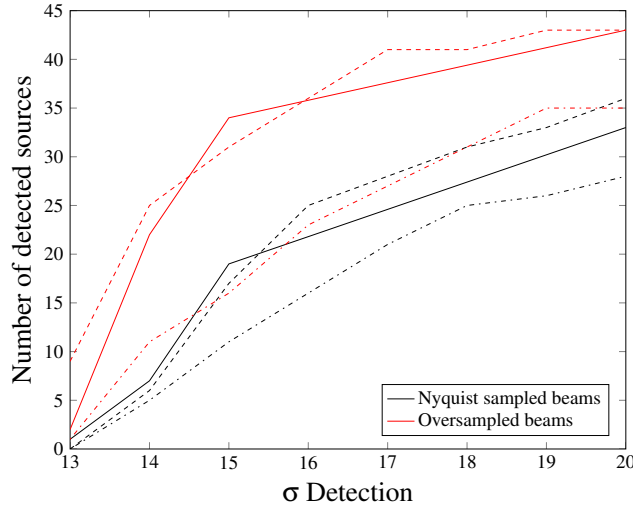


**Figure 5.22:** Detection rates for the MeerKAT array for three different sets of 60 random point sources. Only detection rates for the Nyquist sampled and oversampled beams are shown. Line styles indicate different sets of random sources. The detection rates for Nyquist sampling are shown in red, for oversampling in black.

### Oversampling of the FoV

The above discussion suggests that spacing TABs even closer together would increase the detection rates. However, the fractional bandwidth still has to be taken into consideration, as for the MUST array with a small fractional bandwidth, decreasing the TAB spacing does not improve detection rate but rather it stays constant. From the simulations, oversampling is only beneficial for arrays with large fractional bandwidths, like the LOFAR and MeerKAT arrays. For example, Figure 5.22 shows detection rates for the MeerKAT array, where three different sets of random sources with increasing strength were simulated. For each set the oversampled TABs detected more sources in comparison to the Nyquist sampled FoV, irrespective of their strength. A beam pattern with high number of low level fluctuations, like LOFAR, can contribute to a higher detection rate, via detection in sidelobes, but also to a higher number of "false positions". On the other hand, a clean beam pattern, as produced by MeerKAT, results in lower detection rates but good location accuracy. The increase in the detection rate would be even sharper for the LOFAR array as it has two strong sidelobes that help detect a source in more than one beam.

While the oversampling of the FoV yields superior results for both the LOFAR and MeerKAT arrays there is a limit on how many TABs can be synthesised with a given

telescope. Some coverage of the FoV may therefore have to be sacrificed if a high location accuracy is desired and this has a trade-off in the survey speed. For example, say that a FoV is undersampled with  $N$  TABs, with  $N$  being the maximum number of TABs that can be synthesised. If we survey the same FoV with the Nyquist sampled TABs, the survey would take approximately 3.5 times longer. If we were to tile the FoV with the oversampled TABs, the survey would take approximately 4 times longer, for an array with 10% fractional bandwidth. For an array with 20% fractional bandwidth it would take 5 times longer.

In our analysis, the telescope under test is always pointing at or close to the Zenith. This preserves the beam shape, i.e. there is no broadening as the elevation is low. However, for pointing directions, where the broadening of the beam is substantial, the sampling of the FoV should be considered carefully not to heavily oversample the FoV. We plan to address this in the future work, i.e. to determine the optimum FoV sampling for directions off-boresight.

### 5.4.2 Location Estimation Accuracy

Not only are the detection rates heavily dependant on the TAB spacing, it also affects the mean total area  $\bar{D}$  covered by the estimated positions and the mean angular distance  $\bar{\Delta\phi}$  from the true source position. For clarity, only the Nyquist sampled and oversampled methods will be reviewed here for all arrays.

Results from Table 5.6, Table 5.7, Table 5.9, Table 5.10, Table 5.12 and Table 5.13 are summarised in in the top and the middle panels in Figure 5.24. To present the results of this simulations in a compact form, data is divided according to how many locations  $P$  were estimated per detected source. The top panel shows the mean total area  $\bar{D}$  covered by the estimated positions normalised to  $\Omega_{HPBW_L}$ , where the error corresponds to one standard deviation from that mean for each  $P$ . The middle panel plots the mean angular distance  $\bar{\Delta\phi}$  between the estimated and the true source position. The smaller the mean angular distance  $\bar{\Delta\phi}$  the more accurate the estimated location is. The accuracy of the method described here can be best appreciated when the top and middle panels are examined together. For example for sources in group  $P = 1$ , the mean total area  $\bar{D}$  for the MeerKAT array has a size of almost a full  $\Omega_{HPBW_L}$ , but the mean angular distance  $\bar{\Delta\phi}$  is very small. This can be explained with the help of the top panel in Figure 5.18. When a source is detected with two TABs the estimated

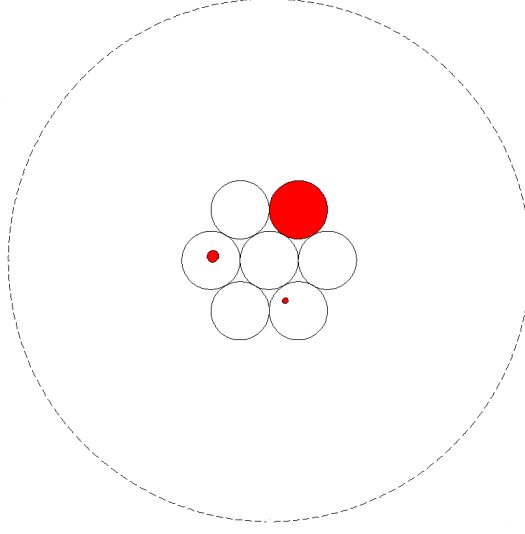


**Figure 5.23:** Hierarchy of positional accuracy within a TAB. A primary beam (dashed line, not to scale) and seven undersampled TABs (black circles) are plotted. A TAB coloured in red signifies the accuracy level  $\sim 1 \times \text{HPBW}$ . The red dots of decreasing size signify the accuracy level of  $\sim 0.1 \times \text{HPBW}$  and  $\sim 0.01 \times \text{HPBW}$  respectively.

area  $D$  can cover an area of up to  $1/2\Omega_{\text{HPBW}_L}$ . Consequently, the mean total area  $\bar{D}$  is artificially inflated. Looking at the other end of the scale, the mean total area  $\bar{D}$  for the sources in group  $P > 5$  is smaller than for sources in group  $P = 1$  for all arrays. However, the mean angular distance  $\bar{\Delta\phi}$  suggests that the estimated locations are at least half a  $\text{HPBW}_L$  away from the true source location. This is because the possible locations now include strong sidelobes as well, as illustrated in the top panel in Figure 5.14.

Overall it can be seen that the mean angular distance  $\bar{\Delta\phi}$  deteriorates with increasing  $P$ . Neither is particularly bad as long as the total area covered by the estimated locations is small compared to the FoV of any follow up instrument. Moreover, if the detection has a small error on location, this will allow for better possible host identification than a single detection with a large position uncertainty. In summary, we can broadly distinguish three basic levels in a hierarchy of positional accuracy within a TAB that can be achieved with the method presented here:

- (i)  $\sim 1 \times \text{HPBW}$  accuracy;
- (ii)  $\sim 0.1 \times \text{HPBW}$  accuracy;
- (iii)  $\sim 0.01 \times \text{HPBW}$  accuracy or better.

For sources that fall into category (i) a detection can be constrained to a single or small group of TABs. The accuracies of (i) and (ii) may however be more than sufficient if

the observations are conducted in parallel with follow-up telescopes with higher positional accuracy. On the other hand the angular position of accuracy of (iii), depending on the maximum baseline, may already be sufficient to identify a host galaxy, or other related object without reference to other simultaneous observations. This is illustrated in Figure 5.23, where a primary beam of the MeerKAT dish<sup>11</sup>.

### The MeerKAT array analysis

The results of the method for finding a source location in a TAB, for the array configurations analysed here, favoured the MeerKAT core configuration. This is not unexpected since the MUST array is a small test array and the LOFAR Superterp with a poor instantaneous UV coverage, due to a small number of baselines, would need a further development of this method<sup>12</sup>. A detailed analysis of only the MeerKAT results will therefore now be presented.

The oversampling of the MeerKAT TABs gives the best results in terms of small mean total area  $\bar{D}$  and the mean angular distance  $\bar{\Delta\phi}$ . Figure 5.25 plots the mean  $\bar{\Delta\phi}$  (black dots) and uses the mean  $\bar{D}$  as error bars of 38 sources detected in oversampled TABs with  $\bar{\Delta\phi} < 0.5$  of  $\text{HPBW}_L$ . From that group, locations of 13 sources were estimated with a single pixel. The mean angular distance  $\bar{\Delta\phi}$  for single-pixel sources is 0.03 arc second (0.006  $\text{HPBW}_L$ ) from the true source position. For the 38 sources from Figure 5.25, a detection can be constrained to a single or small group, if on the edge, of TABs, i.e. condition (i). Moreover, the mean  $\bar{\Delta\phi}$  for all 38 sources from the true source location meets condition (ii). The third degree of accuracy is achieved for 12 sources. The accuracies of (i) and (ii) are more than satisfactory if the observations are conducted in parallel with the majority of follow-up telescopes. The accuracy of (iii) is already sufficient to identify a host galaxy or other object of a transient. Imaging is still useful in case (i) and also for undersampling the radio environment.

---

<sup>11</sup>The primary beam shape is not to scale.

<sup>12</sup>Due to very complicated beam pattern of the LOFAR Superterp, an additional metric would need to be developed to limit the number of estimated source locations and to better constrain the true position.

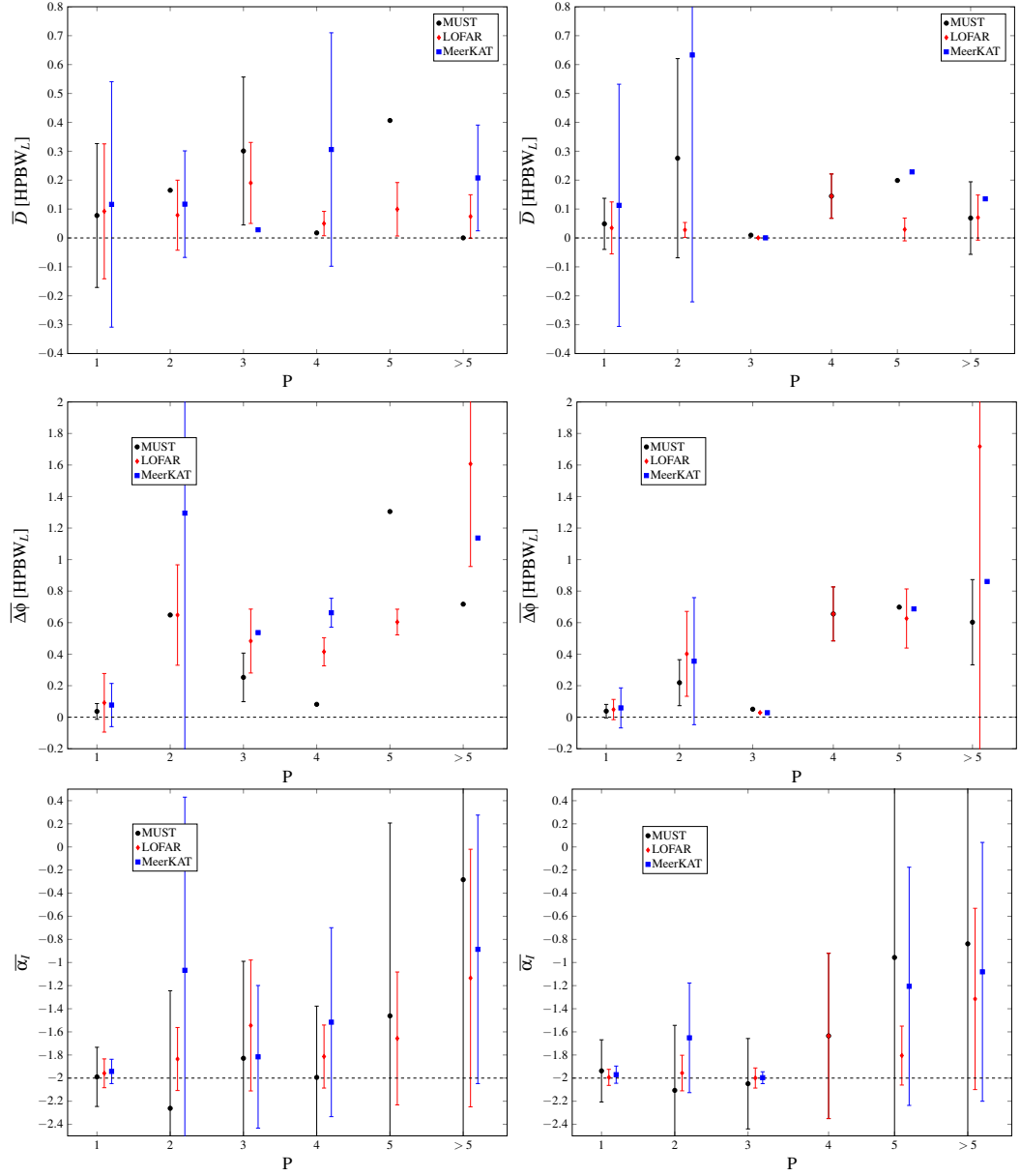


**Figure 5.24:** Summary of results. (top) The mean total area  $\bar{D}$  covered by the estimated positions normalised to  $\Omega_{HPBW_L}$ , where the error corresponds to one standard deviation  $\sigma$  from that mean for each  $P$ ; (middle) The mean angular distance  $\Delta\phi$  between the estimated and the true source position; (bottom) The mean estimated intrinsic spectral index  $\bar{\alpha}_l$  for combined sources in each  $P$ .

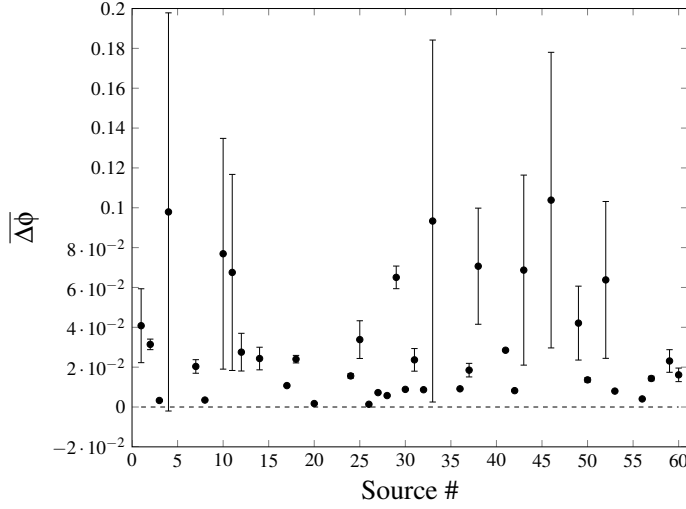


**Figure 5.25:** The mean  $\overline{\Delta\phi}$  (black dots) and the mean  $\overline{D}$  as error bars of 38 sources detected in MeerKAT oversampled TABs with  $\overline{\Delta\phi} < 0.5$ .

### 5.4.3 Intrinsic Spectral Index Recovery

A by-product of an accurate position estimation is the recovery of the intrinsic spectral index  $\alpha_l$ . Results from Table 5.6, Table 5.7, Table 5.9, Table 5.10, Table 5.12 and Table 5.13 are summarised in the bottom panel in Figure 5.24, that shows the mean estimated intrinsic spectral index  $\overline{\alpha_l}$  and the standard deviation  $\sigma$  from that mean from all estimated locations for sources detected when the FoV is Nyquist sampled and oversampled. The correlation between the number of estimated positions and the recovery of  $\alpha_l$  is clear. For example, for the LOFAR array the mean intrinsic spectral index  $\overline{\alpha_l}$  is  $-2.0 \pm 0.1$  for sources in group  $P = 1$ . Whereas, estimated  $\overline{\alpha_l}$  for sources in group  $P < 5$  is  $-1.1 \pm 1.1$ . This is also shown in the bottom panel in Figure 5.24, where the mean estimated intrinsic spectral index  $\overline{\alpha_l}$ , for combined sources in each  $P$ , is plotted for the MUST, LOFAR and MeerKAT arrays. For all arrays where only one small mean area  $\overline{D}$  and small  $\overline{\Delta\phi}$  were estimated, the recovered  $\alpha_l$  is close to its assigned value of -2. Not unexpectedly, there is a clear correlation between the small angular offset  $\delta\phi$  from the true source position and the accuracy of estimated  $\alpha_l$ . The more accurate the estimated position is the smaller the  $\alpha_l$  error. In addition, Figure 5.26 shows the accuracy of the intrinsic spectral index  $\alpha_l$  recovery in relation to the number of TABs a source was detected in for the LOFAR in the top panel and MeerKAT array in the bottom panel. For both arrays the standard deviation  $\sigma$  decreases with the increasing number of TABs.

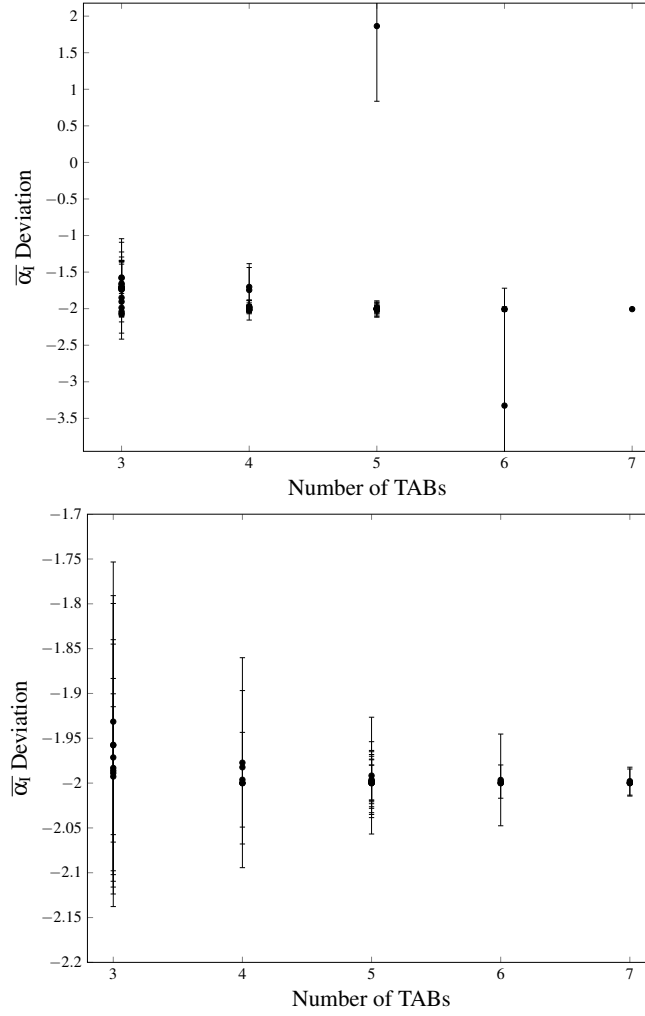


**Figure 5.26:** The mean estimated intrinsic spectral index  $\bar{\alpha}_l$  and the standard deviation  $\sigma$  from that mean from all estimated locations for sources detected when the FoV is oversampled; (top) LOFAR; (bottom) MeerKAT.

# Chapter 6

## Conclusions

### **The Manchester University Student Telescope**

The development and construction of a prototype phased array capable of multi-beam operation was described in this thesis. The approach to the construction was to exploit low-cost components available from the broadcast TV industry. The initial RFI tests identified a commercially unused band between 565 MHz and 620 MHz allowing for a bandwidth of 50 MHz. Further, more sophisticated RFI test determined the specification for the bandpass filter used in the array front-end. Regular RFI checks ensured that the appearance of new TV signals could be dealt with promptly which resulted in re-engineering of the original bandpass filter to a narrower band of 35 MHz.

A performance comparison between different tiles in the array was made possible with a field tested heterodyne receiver adapted from the 42 foot telescope back-end at the Jodrell Bank Observatory. In the lab tests showed that the system is capable of providing 50 dB of amplification, sufficient to sample a signal. Furthermore, a simultaneous observation with the MUST heterodyne receiver and a standard 42 foot telescope set-up of the Crab pulsar, confirmed satisfactory operation of the receiver. An observation with 25% lower bandwidth of the heterodyne receiver in comparison to the 42 foot telescope, resulted in only 28% lower signal to noise ratio.

The optimum separation between the custom made Yagi antennas was examined quantitatively by extensive test observations of different Yagi arrays configuration to minimise the mutual coupling. After also considering the physical size of each Yagi, a separation of 0.8 m was chosen, in part for practical reasons associated with the available GRP sections.



The use of low-cost, off-the-shelf components enabled the development of the digital back-end in a platform-independent way that used the open-source hardware from the Centre for Astronomy Signal Processing and Electronics Research (CASPER). Certain receiver functionality can thus be performed in software without limiting the flexibility of the instrument. By employing sub-sampling techniques, the sampling rate could be lowered easing the requirements on the analog to digital converter (ADC) boards from 1.2 GHz to 182.46 MHz.

The optimum array configuration was determined by extensive beam pattern simulations in MATLAB. The spacing between the tiles was partly dictated by the size of suitable standing area available and to avoid grating lobes in the FoV of the primary element. The array configuration suggested by the simulations is a regular 4 m by 4 m, centre to centre of a tile, rectangular array with the longest baseline of 5.65 m with the simulated half-power-beam-width of  $5.39^\circ$ . The array beam pattern exhibits four strong sidelobes close to the main lobe. The beam pattern simulations were also used to develop a new method for estimating locations of transient sources to an accuracy better than a beamwidth.

### **Time-domain beamforming**

In terms of implementation, the beamforming operation can be performed in either the time or frequency domain. We discussed and demonstrated how each approach has its own advantages and disadvantages. For example, frequency domain beamforming has lower computational cost than the time-domain implementation when one considers the number of simultaneous beams.

The sampling frequency used in the MUST project, allows the formation of up to five synchronous beams in steps of  $24.3^\circ$ . As the MUST array design requirements are 10 beams for the initial four elements and an uniform sampling of the field of view, implementations of an interpolation filter to increase the number of synchronous beams were reviewed. The ROACH-1 board, used in the project, can be clocked at up to 550 MHz, thus with the sampling frequency of 182.46 MHz an interpolation by a factor of three already reaches the theoretical limit of the clock speed. An interpolation-by-4 filter for a lower bandwidth was successfully implemented on the ROACH-1 board.

To overcome this limitation we propose the use of a fractional delay filter to align the samples. In addition we present efficient multiplication-free implementations that can reduce the cost of the filter. The saved resources could then be used to implement more filters, i.e. to synchronise more beams.

The future work in developing a digital back-end system using hardware from the Center for Astronomy Signal Processing and Electronics Research (CASPER) for a MUST beamformer involves integrating the interpolation filter into the beamformer design. A reduction in bandwidth for the initial implementation would enable a higher order of interpolation and thus an increased number of synthesised beams. As the current beamformer design has not been tested with the hardware in a real-time regime the above step would verify the multibeam operation. After a successful verification of the beamformer operations the next step would be to develop a multiplierless fractional delay filter using the CASPER blocks and slowly increase the system bandwidth.

### **Source position estimation using beamformed data**

A new population of sources emitting fast and bright transient radio bursts (FRBs) has recently been identified. The observed large dispersion measure values of FRBs suggests an extragalactic origin and an accurate determination of their positions and distances will provide a unique opportunity to study the magneto-ionic properties of the intergalactic medium. In a beamforming approach to interferometry, where many narrow tied array beams are produced, the advantages of single dishes and interferometers can be combined. We present a proof-of-concept analysis of a new non-imaging method that utilises the additional spectral and comparative spatial information obtained from multiple overlapping TABs to estimate a transient source location with up to arcsecond accuracy in almost real time.

We considered three different parts of new and upcoming telescopes with multi-beaming capabilities; *(i)* the MUST array; *(ii)* the LOFAR Superterp; and *(iii)* the MeerKAT array core. The results of the method for finding a source location in a TAB, for the array configurations analysed here, favoured the MeerKAT core configuration due to greater number of baselines, and hence clean<sup>1</sup> beam pattern. In all cases, transient sources can be localised to small fractions of a HPBW of a TAB. In the case of MeerKAT, which has the narrowest TABs, the method is sufficient to localise a source

---

<sup>1</sup>With low level of fluctuations.

to arcsecond accuracy. Even if the estimated position of given transient is less certain, it is still useful if there is a parallel transient search in the same field at a different wavelength.

It is clear, from our results, that a high fractional bandwidth in the case of Nyquist sampling can prevent one or both of our conditions for detection to be realised. When the TABs Nyquist sample the FoV, the HPBW contours at  $\nu_H$  are spaced further apart making one or both our conditions difficult to meet. For such arrays oversampling of the FoV will clearly give higher detection rates. A beam pattern with high number of low level fluctuations, like LOFAR, can contribute to a higher detection rate, via detection in sidelobes, but also to a higher number of "false positions". On the other hand, a clean beam pattern, as produced by MeerKAT, results in lower detection rates but good location accuracy.

However, as this is a proof-of-concept, certain caveats will have to be addressed in the future work. For example, in this work it is assumed that:

- the beam pattern has been measured and is known to a good accuracy;
- there is no scintillation and the sensitivity as a function of bandwidth is described by a simple function.

In addition, an investigation on how other available scientific data, like DM or polarisation, can be utilised in the next iterations of this method. Moreover, the simulation assumed a strict two frequency regime i.e.  $\nu_L$  and  $\nu_H$ , but in reality the bandwidth can be split into many bands increasing the detection rates and positively contributing to the accuracy of the estimated location if many bands can be compared. Those steps would increase the usability of this method for arrays with complicated beam patterns, like the LOFAR Superterp.

For a real-time transient detection and localisation, the spatial information measured with sub-second resolution with a correlator interferometer requires high data rates. The current and the next generation radio telescopes typically provide both the beamforming mode and the correlation mode of observation. In that sense, the method we have described can provide high time resolution and highly useful, sometimes excellent, positional accuracy without increasing the computational burden of creating an image. Additionally, there is no significant delay between the detection and localisation. It is however still of high value to have a transient buffer available on all dishes in

an array, because it will allow for greater sensitivity by making use of dishes outside of the core. In addition, the longer baselines will allow even further improvement determination of the source location. Being able to trigger and store the raw data from the dishes, and then use the position determined by our methods we can go back and form a higher sensitivity beamformed data set. This will consist of the raw complex data which can then be used for coherent dedispersion, in non-scattering-limited situations, to obtain the true width of the pulse. The raw complex data can also be used so that the full polarisation calibration, necessary to achieve the scientific goals mentioned in the introduction, can be achieved.

Finally, this method gives access to the intrinsic spectral index, true flux density and polarisation properties for which an accurate localisation is essential. Those three properties are fundamental to the understanding of what generates FRBs and how we can use them for cosmology.

# Appendix A

## The derivation of Equation 2.1

The derivation of Equation 2.1 follows notes from Prof. Peter Wilkinson.

The receiver produces a voltage that is proportional to the intensity of radiation within the field of view. The intensity is often measured in units of brightness temperature  $T$  given by:

$$T = \frac{B_{\nu}\lambda^2}{2k}, \quad (\text{A.1})$$

where  $k$  is Boltzmann's constant,  $B_{\nu}$  is the source brightness at frequency  $\nu$  and  $\lambda$  is the corresponding wavelength. By rearranging above formula, we obtain:

$$B_{\nu} = \frac{2kT}{\lambda^2}. \quad (\text{A.2})$$

The flux density  $S$  is the received energy from a radio source per second, per unit frequency interval per unit surface area. The source brightness  $B_{\nu}$  and flux density  $S$  are related by:

$$\frac{S}{\Omega} = B, \quad (\text{A.3})$$

where  $\Omega$  is the solid angle of the source in steradians. Thus, from Equation A.2 and Equation A.3:

$$\frac{S}{\Omega} = \frac{2kT}{\lambda^2} \quad \text{or} \quad \frac{Sc^2}{2kT\nu^2} = \Omega. \quad (\text{A.4})$$

To estimate  $\Omega$  we have to know the source dimension  $r$ . The source dimension can be estimated from how long it takes the light to travel across it, i.e. from the centre to the "edge". Hence, the pulse width  $W$  gives an estimate of the source radius  $r$  as:

$$r \sim Wc, \quad (\text{A.5})$$

where,  $c$  is the speed of light. The surface area  $A$  of a disk with radius  $r$  is equal to:

$$A = \pi r^2 \sim \pi W^2 c^2. \quad (\text{A.6})$$

The solid angle subtended  $\Omega$  is related to the area  $A$  as:

$$\Omega = \frac{A}{D^2}, \quad (\text{A.7})$$

where  $D$  is the source distance from the observer, thus:

$$\Omega \sim \frac{\pi W^2 c^2}{D^2}. \quad (\text{A.8})$$

Combining Equation A.4 and Equation A.8 we get

$$\frac{Sc^2}{2kTv^2} \sim \frac{\pi W^2 c^2}{D^2}, \quad (\text{A.9})$$

and:

$$v^2 W^2 \sim \frac{1}{2\pi k} \frac{SD^2}{T} \quad (\text{A.10})$$

# Appendix B

## Position Estimation Methodology

### B.1 Simulation

The simulation is written in MATLAB language, where the code is vectorised to operate on many arrays simultaneously. The purpose of the script is to simulate a detection of a transient source in multiple TABs and output a SNR pattern and the sensitivity  $\mathcal{S}$  and the instrumental spectral index  $\mathcal{A}$  maps for each TAB.

#### B.1.1 Input File

The script accepts two input text files, one describing telescope parameters and the second one describing the source. Details are given in Table B.1.

**Table B.1:** Input files description.

| Telescope  | Input Format | Source                        | Input Format |
|------------|--------------|-------------------------------|--------------|
| RA         | HH:MM:SS.S   | RA                            | HH:MM:SS.S   |
| Dec        | +DD:MM:SS.S  | Dec                           | +DD:MM:SS.S  |
| Latitude   | Degrees      | Flux <sub>v<sub>H</sub></sub> | Value        |
| Longitude  | Degrees      | Flux <sub>v<sub>L</sub></sub> | Value        |
| Stationary | 0/1          | Spectral index                | Value        |
| Geometry   | 0/1          |                               |              |
| Year       | YYYY         |                               |              |
| Month      | MM           |                               |              |
| Day        | DD           |                               |              |
| Hour       | HH           |                               |              |
| Minute     | mm           |                               |              |
| Second     | ss.sss       |                               |              |

### B.1.2 Beam Pattern

A normalised beam pattern for each TAB is generated using MATLAB for the MUST array and using the OSKAR-2 package for the LOFAR and the MeerKAT arrays. The OSKAR-2 produces a FITS file<sup>1</sup> from which an array with the beam pattern has to be extracted. In addition, the MUST beam pattern is also multiplied with an element factor. This step is omitted for the LOFAR and the MeerKAT arrays as the test area used in the data analysis is too small to be affected by the element beam shape.

```

1  %----- PATTERN MULT -----
2  for uu = 1:lRA % loop over all pointings
3      indAa = indAr(:, :, :, uu);
4      indTa = indT(:, :, :, uu);
5      for ii = 1:length(f)
6          indA(:, :, ii, uu) = ...
              indAa(:, :, ii) .* indTa(:, :, ii) .* element(:, :, uu);
7      end
8  end

```

### B.1.3 Sensitivity $\mathcal{S}$ Map

The sensitivity  $\mathcal{S}$  map is created by scaling the normalised beam pattern calculated in §B.1.2 to the minimum sensitivity  $S_{min}$  at the phase centre.

```

1  for uu = 1:lRA % loop over all pointings
2      for ii = 1:length(f) % for each frequency
3          sensF = sensitivity(uu, ii) ./ indA(:, :, ii, uu);
4          sensF(isinf(SNRf)) = 10000;
5          sensF(sensF ≥ 10*sensitivity(uu, ii)) = 10000;
6          arraySensitivity(:, :, ii, uu) = SNRf;
7      end
8  end

```

### B.1.4 Instrumental Spectral Index $\mathcal{A}$ Map

The instrumental spectral index  $\mathcal{A}$  map is created using the sensitivity  $\mathcal{S}$  maps at frequency  $\nu_L$  and  $\nu_H$ .

---

<sup>1</sup>Flexible Image Transport System.



```

1 for uu = 1:lRA % loop over all pointings
2     alphaF = log10(arraySensitivity(:,:,1,uu)./ ...
3         arraySensitivity(:,:,2,uu))./ratiof;
4     alpha(:,:,uu) = alphaF;
5 end

```

### B.1.5 Output file

The output file is saved as a MAT-file object that contains following variables (arrays):

1.  $\mathcal{S}$  map for each TAB;
2.  $\mathcal{A}$  map for each TAB;
3. Normalised beam pattern for each TAB;
4. SNR detection;
5. Actual flux density for each source;
6. Estimated flux density for each source;
7. Actual spectral index for each source;
8. Estimated spectral index for each source;
9. Source coordinates<sup>2</sup>;
10. Minimum sensitivity  $S_{min}$  at the phase centre for each TAB.

Half of listed variables were used for debugging purposes and only (1), (2), (4) and (10) are passed to the location estimation routine described next.

## B.2 Data Analysis

After the simulation is complete, only sources that satisfy conditions 5.2 are further processed to estimate their position. A visual representation of the steps is shown in Figure B.1. The SNR pattern, (4) in §B.1.5, is passed through a routine, where for each  $(i, j)$  pair combination a set of overlapping coordinates is produced. At the end of the routine, coordinates from all pairs are compared against each other and eventually a source position is estimated. The input to the for loop are the  $\mathcal{S}$  map and  $\mathcal{A}$  map for each  $(i, j)$  pair, (1) and (2) respectively in §B.1.5. In addition, the minimum sensitivity  $S_{min}$  at the phase centre for each TAB in  $(i, j)$  pair is also used to estimate the flux density, (10) in §B.1.5, but was omitted from the diagram for clarity.

---

<sup>2</sup>Used for comparison and for plotting the results.

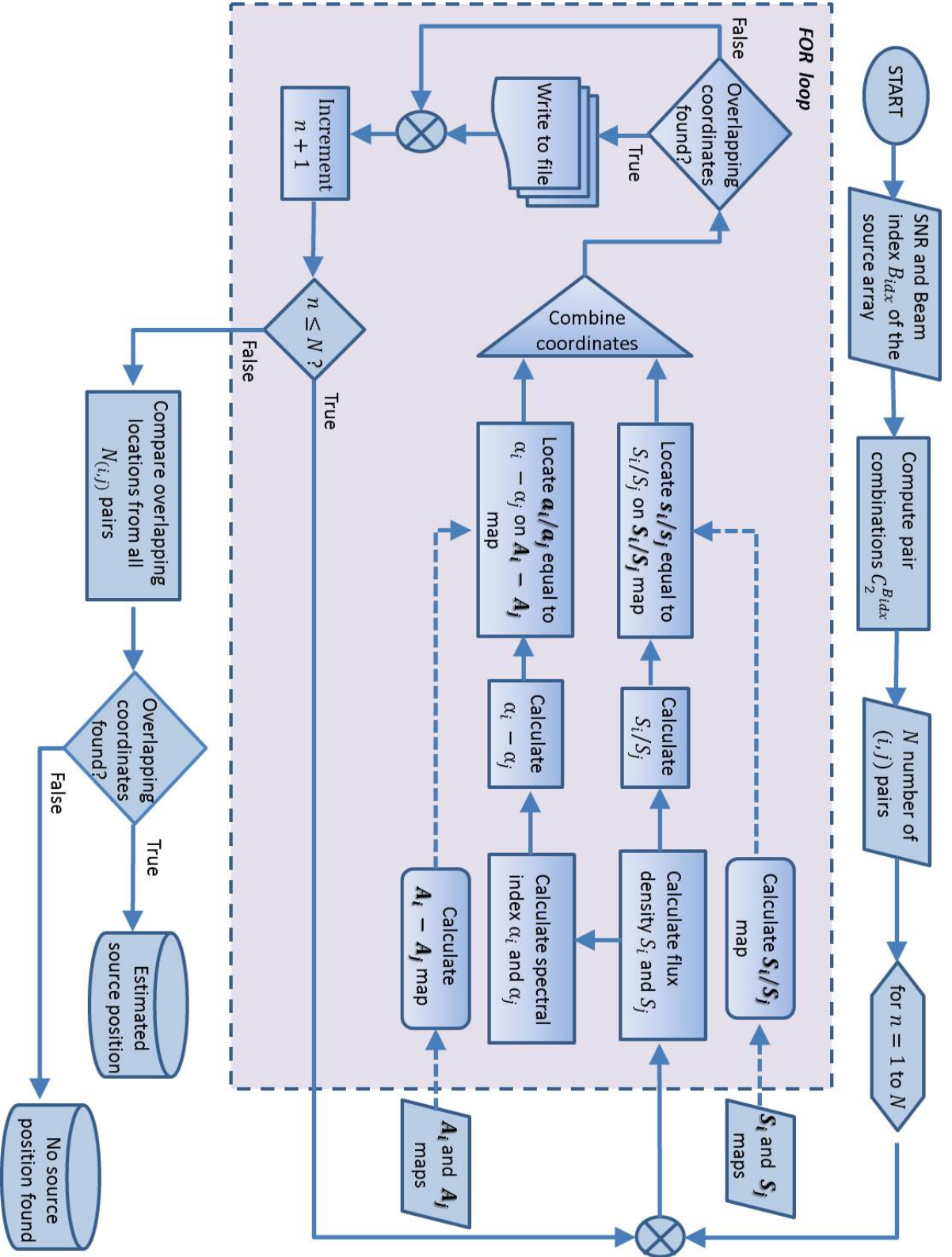


**Figure B.1:** A visual representation of the steps in the location estimation methodology. The flow chart describes location estimation steps for a single source detected in multiple TABs. The dashed area represents a for loop. Bold letters indicate either a map or values from a map while the non-bold indicates source values.

## Appendix C

### The MUST array beam pattern without the primary element

The actual MUST-4 array TAB pattern is a product of the radiation pattern of a tile factor of the  $4 \times 4$  Yagi array ( $AF_{\text{Tile}}$ ) and the array factor of  $2 \times 2$  tile array ( $AF_{\text{Array}}$ ):

$$AF_{\text{MUST-4}} = AF_{\text{Tile}} \times AF_{\text{Array}}. \quad (\text{C.1})$$

Due to the absence of the Yagi radiation pattern, modelled as a Gaussian beam with a HPBW of  $27^\circ$  with no sidelobes present, there are eight grating lobes present.

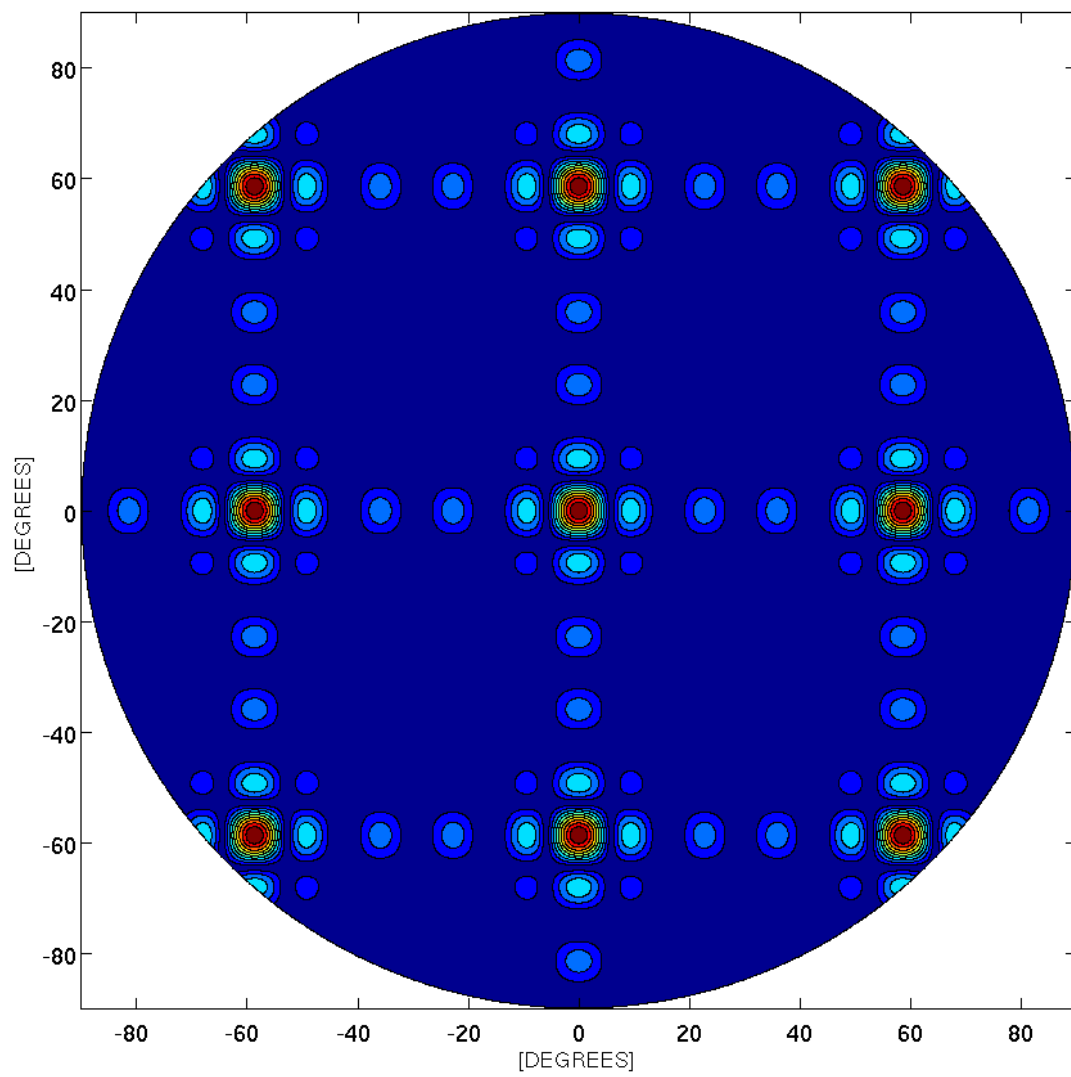


**Figure C.1:** The MUST-4 array beam pattern without the primary element

# Bibliography

- Baade W., Zwicky F., 1934, Proc. Nat. Acad. Sci., 20, 254
- Bannister K. W., Cornwell T. J., 2011, ApJS, 196, 16
- Bannister K. W., Madsen G. J., 2014, MNRAS, 440, 353
- Bates S. D., Lorimer D. R., Verbiest J. P. W., 2013, MNRAS, 431, 1352
- Beskin V. S., Philippov A. A., 2012, MNRAS, 425, 814
- Bhat N. D. R., 2011, ArXiv e-prints
- Booth R. S., de Blok W. J. G., Jonas J. L., Fanaroff B., 2009, ArXiv e-prints
- Booth R. S., Jonas J. L., 2012, African Skies, 16, 101
- Bosse S., Barth S., Torchinsky S., Da Silva B., 2010, in Microwave Integrated Circuits Conference (EuMIC), 2010 European, p. 106
- Briskin W. F., Benson J. M., Beasley A. J., Fomalont E. M., Goss W. M., Thorsett S. E., 2000, ApJ, 541, 959
- Burke-Spolaor S., Bailes M., Ekers R., Macquart J.-P., Crawford F., III, 2011, ApJ, 727, 18
- Cen R., Ostriker J. P., 1999, ApJ, 514, 1
- Coenen T. et al., 2014, ArXiv e-prints
- Cooley J., Tukey J., 1965, Mathematics of Computation, 19, 297
- Cordes J. M., Lazio T. J. W., 2002, ArXiv Astrophysics e-prints
- Cordes J. M., Lazio T. J. W., McLaughlin M. A., 2004, New Astronomy Review, 48, 1459

- Crawford F., Kaspi V. M., Manchester R. N., Lyne A. G., Camilo F., D'Amico N., 2001, *ApJ*, 553, 367
- Davidson A., 2013, Master's thesis, School of Physics and Astronomy
- Deneva J. S. et al., 2009, *ApJ*, 703, 2259
- Deng W., Zhang B., 2014, *ApJ*, 783, L35
- Dewdney P., Hall P., Schilizzi R., Lazio T., 2009, *Proceedings of the IEEE*, 97, 1482
- Ellingson S. W., Clarke T. E., Cohen A., Craig J., Kassim N. E., Pihlstrom Y., Rickard L. J., Taylor G. B., 2009, *IEEE Proceedings*, 97, 1421
- Ellingson S. W. et al., 2013, *IEEE Transactions on Antennas and Propagation*, 61, 2540
- Farrow C., 1988, in *Circuits and Systems, 1988.*, *IEEE International Symposium on*, p. 2641
- Fender R. P., Bell M. E., 2011, *Bulletin of the Astronomical Society of India*, 39, 315
- Gokhale, S. D. , 2011, Master's thesis, School of Mechanical, Aerospace and Civil Engineering
- Gold T., 1968, *Nature*, 218, 731
- Hankins T. H., Rickett B. J., 1975, in *Methods in Computational Physics Volume 14 — Radio Astronomy*. Academic Press, New York, p. 55
- Haslam C. G. T., Stoffel H., Salter C. J., Wilson W. E., 1982, *A&AS*, 47, 1
- Hassall T. E., Keane E. F., Fender R. P., 2013, *MNRAS*, 436, 371
- Hewish A., Bell S. J., Pilkington J. D. H., Scott P. F., Collins R. A., 1968, *Nature*, 217, 709
- Janssen G. H., Stappers B. W., Braun R., van Straten W., Edwards R. T., Rubio-Herrera E., van Leeuwen J., Weltevrede P., 2009, *A&A*, 498, 223
- Keane E. F., Kramer M., Lyne A. G., Stappers B. W., McLaughlin M. A., 2011, *MNRAS*, 415, 3065
- Keane E. F., Stappers B. W., Kramer M., Lyne A. G., 2012, *MNRAS*, 425, L71

- Keith M. J. et al., 2010, MNRAS, 409, 619
- Kontorovich V. M., Flanchik A. B., 2013, Ap&SS, 345, 169
- Kopeikin S. M., 1997, Phys. Rev. D, 56, 4455
- Kouwenhoven M. L. A., Voûte J. L. L., 2001, A&A, 378, 700
- Kramer M., Lyne A. G., O'Brien J. T., Jordan C. A., Lorimer D. R., 2006, Science, 312, 549
- Laakso T., Valimäki V., Karjalainen M., Laine U., 1996, Signal Processing Magazine, IEEE, 13, 30
- Law C. J., Bower G. C., 2014, in Exascale Radio Astronomy, p. 20303
- Law C. J. et al., 2014, ArXiv e-prints
- Law C. J., Jones G., Backer D. C., Barott W. C., Bower G. C., Gutierrez-Kraybill C., Williams P. K. G., Werthimer D., 2011, ApJ, 742, 12
- Lorimer D. R., Bailes M., McLaughlin M. A., Narkevic D. J., Crawford F., 2007, Science, 318, 777
- Lorimer D. R. et al., 2006, MNRAS, 372, 777
- Lorimer D. R., Karastergiou A., McLaughlin M. A., Johnston S., 2013, ArXiv e-prints
- Lorimer D. R., Kramer M., 2004, Handbook of Pulsar Astronomy. Cambridge University Press
- Lorimer D. R., Yates J. A., Lyne A. G., Gould D. M., 1995, MNRAS, 273, 411
- Lundgren S. C., Cordes J. M., Ulmer M., Matz S. M., Lomatch S., Foster R. S., Hankins T., 1995, ApJ, 453, 433
- Lyons R. G., 2010, Understanding Digital Signal Processing (3rd Edition) (3 ed.). Prentice Hall
- Macquart J.-P., Koay J. Y., 2013, ApJ, 776, 125
- Manchester R. N., 2009, in Astrophysics and Space Science Library, Vol. 357, Becker W., ed, Astrophysics and Space Science Library, p. 19

- Manchester R. N., Fan G., Lyne A. G., Kaspi V. M., Crawford F., 2006, *ApJ*, 649, 235
- Manchester R. N. et al., 2001, *MNRAS*, 328, 17
- Maron O., Kijak J., Kramer M., Wielebinski R., 2000, *A&AS*, 147, 195
- McLaughlin M. A., Cordes J. M., 2003, *ApJ*, 596, 982
- McLaughlin M. A. et al., 2006, *Nature*, 439, 817
- Mitola J., 1995, *Communications Magazine, IEEE*, 33, 26
- Mol J. D., Romein J. W., 2011, *ArXiv e-prints*
- Nan R. et al., 2011, *International Journal of Modern Physics D*, 20, 989
- Papadopoulos C., Nikias C., 1988, in *Acoustics, Speech, and Signal Processing*, 1988. ICASSP-88., 1988 International Conference on, p. 2404
- Pridham R. G., Mucci R. A., 1978, *Acoustical Society of America Journal*, 63, 425
- Pridham R. G., Mucci R. A., 1979a, *Proceedings of the IEEE*, 67, 904
- Pridham R. G., Mucci R. A., 1979b, *Acoustics, Speech and Signal Processing, IEEE Transactions on*, 27, 713
- Ransom S. M., Eikenberry S. S., Middleditch J., 2002, *AJ*, 124, 1788
- Reich P., Reich W., 1988, *A&A*, 196, 211
- Rickett B. J., 1990, *Ann. Rev. Astr. Ap.*, 28, 561
- Romein J. W., Mol J. D., van Nieuwpoort R. V., Broekema P. C., 2011, in *General Assembly and Scientific Symposium, 2011 XXXth URSI*, p. 1
- Roy J., Bhattacharyya B., 2013, *ApJ*, 765, L45
- Saint-Hilaire P., Benz A. O., Monstein C., 2014, *ApJ*, 795, 19
- Schobben D., Sommen P., 1996, in *Statistical Signal and Array Processing*, 1996. Proceedings., 8th IEEE Signal Processing Workshop on (Cat. No.96TB10004, p. 117
- Shannon C. E., 1949, *IEEE Proceedings*, 37, 10
- Siemion A. P. V. et al., 2012, *ApJ*, 744, 109



- Soriano M., Navarro R., D'Addario L., Sigman E., Wang D., 2011, in Aerospace Conference, 2011 IEEE, p. 1
- Spitler L. G. et al., 2014, ArXiv e-prints
- Stappers B. W. et al., 2011, A&A, 530, A80
- Taylor J. H., Wolszczan A., Damour T., Weisberg J. M., 1992, Nature, 355, 132
- Thornton D. et al., 2013, Science, 341, 53
- Tingay S. J. et al., 2013, PASA, 30, 7
- van Haarlem M. P. et al., 2013, A&A, 556, A2
- van Straten W., Bailes M., Britton M., Kulkarni S. R., Anderson S. B., Manchester R. N., Sarkissian J., 2001, Nature, 412, 158
- Vesma J., Saramaki T., 2000, in Circuits and Systems, 2000. Proceedings. ISCAS 2000 Geneva. The 2000 IEEE International Symposium on, Vol. 1, p. 104
- Wayth R. B., Brisken W. F., Deller A. T., Majid W. A., Thompson D. R., Tingay S. J., Wagstaff K. L., 2011, ApJ, 735, 97
- Yli-Kaakinen J., Saramaki T., 2006, Circuits, Systems and Signal Processing, 25, 265